



**HAL**  
open science

# Electron and multielectron reaction characterizations in molecular photosystems by laser flash photolysis, towards energy production by artificial photosynthesis

Thu-Trang Tran

► **To cite this version:**

Thu-Trang Tran. Electron and multielectron reaction characterizations in molecular photosystems by laser flash photolysis, towards energy production by artificial photosynthesis. Chemical Physics [physics.chem-ph]. Université Paris Saclay (COmUE), 2019. English. NNT : 2019SACLS320 . tel-03092295

**HAL Id: tel-03092295**

**<https://theses.hal.science/tel-03092295>**

Submitted on 2 Jan 2021

**HAL** is a multi-disciplinary open access archive for the deposit and dissemination of scientific research documents, whether they are published or not. The documents may come from teaching and research institutions in France or abroad, or from public or private research centers.

L'archive ouverte pluridisciplinaire **HAL**, est destinée au dépôt et à la diffusion de documents scientifiques de niveau recherche, publiés ou non, émanant des établissements d'enseignement et de recherche français ou étrangers, des laboratoires publics ou privés.

# Electron and multielectron reaction characterizations in molecular photosystems by laser flash photolysis, towards energy production by artificial photosynthesis

Thèse de doctorat de l'Université Paris-Saclay  
préparée à l'Université Paris Sud

École doctorale n°572 Ondes et matière (EDOM)

Spécialité de doctorat : Physique et chimie de la matière et des matériaux

Thèse présentée et soutenue à Orsay, le 27 Septembre 2019

**Thu-Trang Tran**

Composition du Jury:

Talal Mallah Professeur des Universités, Université Paris-Sud (ICMMO)	Président
Michel Sliwa Chargé de Recherche CNRS, Université de Lille 1 (LASIR)	Rapporteur
Yann Pellegrin Chargé de Recherche CNRS, Université de Nantes (CEISAM)	Rapporteur
Murielle Chavarot-Kerlidou Chargée de Recherche CNRS, Université Grenoble Alpes (LCBM)	Examinatrice
Thomas Pino Directeur de recherche CNRS, Université Paris-Sud (ISMO)	Directeur de thèse
Rachel Méallet-Renault Professeure des Universités, Université Paris-Sud (ISMO)	Co-Directrice de thèse
Minh-Huong Ha-Thi Maître de Conférences, Université Paris-Sud (ISMO)	Co-Encadrante de thèse (Absente)



# Résumé

La demande en énergie de l'humanité augmente rapidement et ne montre aucun signe de ralentissement. Cependant, les combustibles fossiles n'existent qu'en quantités limitées et non renouvelables, et les ressources sont en train de s'épuiser. De plus, l'utilisation continue de combustibles fossiles est l'une des principales causes de l'accumulation de CO<sub>2</sub> dans l'atmosphère terrestre. Il est temps de trouver de nouvelles sources d'énergie renouvelables et respectueuses de l'environnement. L'énergie solaire est une des sources d'énergie renouvelables. Le soleil fournit environ 10 000 fois nos besoins quotidiens en énergie. Cependant, la lumière du soleil présente deux limites principales. Premièrement, le rayonnement est diffus, de sorte que pour collecter efficacement l'énergie solaire, il faut des dispositifs de collection à grande échelle. De plus, la lumière est intermittente et n'éclaire en moyenne que 6 heures par jour.

De nos jours, l'énergie solaire a été principalement exploitée à l'aide de cellules solaires photovoltaïques offrant un rendement de plus en plus performant. Cette technologie montre des progrès remarquables dans l'efficacité de la conversion solaire grâce au développement de cellules solaires variées. Néanmoins, l'électricité produite doit pouvoir être stockée pour compenser l'intermittence et l'électricité ne couvre qu'une partie de nos besoins énergétiques. Pour que le rayonnement solaire soit une source d'énergie renouvelable permettant de remplacer les combustibles fossiles, il faut pouvoir stocker l'énergie solaire. Les combustibles solaires sont un moyen prometteur d'y parvenir. Les réactions de photosynthèse dans les feuilles, les bactéries et d'autres systèmes photosynthétiques dans la nature sont parfaitement adaptées à l'utilisation de la lumière solaire. Par conséquent, nous devons créer des systèmes photosynthétiques artificiels pour imiter les réactions photosynthétiques naturelles dans lesquelles la lumière du soleil est capturée, convertie et stockée sous forme d'énergie chimique. L'eau et le CO<sub>2</sub> sont des sources universelles et abondantes sur notre planète. Produire des énergies renouvelables à base d'eau et de CO<sub>2</sub> utilisant l'énergie solaire pour obtenir de l'hydrogène et des hydrocarbures est un défi de taille. À l'heure actuelle, la photolyse solaire de l'eau a atteint un certain niveau de succès, le rendement de conversion de l'énergie solaire en énergie chimique stockée dans H<sub>2</sub> le plus élevé atteignant environ 18%. Toutefois, de nombreuses recherches sont encore nécessaires pour que les combustibles solaires deviennent viables. Pour atteindre cet objectif, certaines difficultés doivent être surmontées.

Les transferts d'électrons et les transferts d'énergie jouent un rôle important dans les systèmes de photosynthèse. Fondamentalement, un seul transfert d'électron est nécessaire pour réaliser des cellules solaires photovoltaïques. En revanche, pour construire du combustible solaire, des processus de transfert multi-électrons doivent être requis. Dans ce contexte, l'objectif de la thèse s'articule autour de deux thèmes principaux: (i) L'étude du transfert d'électron unique dans les systèmes de dyades donneur-accepteur en vue d'optimiser l'efficacité de la séparation des charges et de son éventuelle application dans les cellules solaires organiques photovoltaïques. (ii) Etudier les transferts d'électrons multiples dans des systèmes modèles en vue d'élucider les processus de transfert d'électrons dans des photosystèmes artificiels.

Pour le premier thème de cette thèse, les propriétés photophysiques du transfert d'électron dans différentes dyades composées de dérivés du bore-dipyrométhène (BDP) et du fullerène  $C_{60}$  ont été étudiées à l'aide de spectroscopies d'absorption rapides et ultra-rapides. Sous excitation sélective du fragment BDP dans la dyade BDP- $C_{60}$ , deux mécanismes ultra-rapides de transfert d'électron photo-induits (100 *fs* et 4 *ps*) ont été mis en évidence. De plus, une longue durée de vie inattendue de séparation des charges a été observée. Ces résultats indiquent clairement l'efficacité du transfert d'électron du BDP au  $C_{60}$ . Les systèmes de dyades composées d'assemblage BDP- $C_{60}$  (dyade alkyle et dyade peptide) ont également été étudiés. Ces dyades avec leurs chaînes peptidiques et alkyles peuvent être ancrées pour former des monocouches auto-assemblées sur des surfaces d'or, ce qui ouvre la voie vers la mise au point de dispositifs photovoltaïques moléculaires.

Le second thème de la thèse portait sur l'étude du transfert multiélectronique dans différents systèmes impliquant soit des molécules modèles (méthylviologène et naphthalène diimide), soit des molécules catalytiques (Porphyrine) en utilisant la spectroscopie d'absorption transitoire pompe-pompe-sonde. L'accumulation de charge a été démontrée avec succès dans deux systèmes multi-composants différents (méthylviologène et naphthalène diimide) qui impliquent l'ascorbate comme donneur d'électrons et le photosensibilisateur  $[Ru(bpy)_3]^{2+}$ . Nous avons atteint des rendements globaux relativement bons pour l'accumulation de charges sur ces molécules modèles. Nos résultats permettent donc d'interroger des processus photocatalytiques multiélectroniques plus sophistiqués.

Des efforts pour étudier l'accumulation de charge dans des photocatalyseurs dans la configuration à plusieurs composants ont été mis en œuvre en utilisant la spectroscopie d'absorption transitoire pompe-pompe-sonde. Différents catalyseurs à base de porphyrine ont été explorés pour étudier les processus photo-induits avec l'ascorbate ou le 1,4-diazabicyclo[2.2.2]octane (DABCO) comme donneur d'électron. Nous pouvons en déduire que les processus photoinduits dépendent fortement de la nature de ce donneur, l'utilisation de DABCO semblant faciliter le transfert d'électron. Pour la première fois un

état doublement réduit de la porphyrine de zinc a été observé sous excitations séquentielles. En outre, un modèle du photosystème II - porphyrine-imidazole-phénol a été étudié en présence de l'accepteur d'électrons  $MV^{2+}$  et seul le premier transfert d'électron couplé au proton a pu être clairement observé dans ce système.

En résumé, cette thèse a été consacrée à l'exploration de différents photosystèmes, tels que les dyades et les systèmes moléculaires à plusieurs composants, dans le but de déterminer les propriétés les plus pertinentes pour obtenir un rendement élevé du transfert de charge simple et double. Ces travaux ont ainsi permis de suggérer des stratégies permettant d'optimiser l'efficacité de la réaction de transfert de charge pour chaque étape après une et deux excitations lumineuses. En conclusion, ces travaux fondamentaux ont permis de contribuer à une meilleure compréhension des processus photophysiques susceptibles de se produire dans les systèmes photocatalytiques et les cellules photoélectrochimiques.

# Acknowledgements

First of all, I would like to thank the Vietnamese government for giving me the scholarship to come to a beautiful country, France, to study.

I am deeply grateful for the support I have received from my supervisors. I would like to express my special thanks to Dr. Thomas Pino for your guidance and inspiring me in research. You always facilitated the best conditions for me to improve and increase my knowledge and experience as well. It is my pleasure to study under your supervision and learn your expertise. I would like to send my sincere thanks to Prof. Rachel Méallet-Renault for your care and encouragement me during the time I studied. You always gave me your warm kindness and responsibility in my thesis. My special thank sends to Dr. Minh Huong Ha Thi, my supervisor and my dear older sister as well. Thank you for your patient teaching and guiding me from the first days. Thank you for your care and motivating me not only in work but in my life as well.

I would like to thank my collaborators, whom I have chanced to work with:

- Stéphane Aloise at LASIR Lab in University Lille, who gave me a lot of enthusiastic in teaching me data treatment as well as knowledge in Femtosecond transient absorption spectroscopy.
- Emmanuel Allard at Institut Lavoisier de Versailles gave us samples to study, Gilles Clavier and Fabien Miomandre at PPSM Cachan were welcome and help us measuring spectroelectrochemistry.
- Gortard Burdzinski at Adam Mickiewicz University in Poznan, who helped us measuring Femtosecond transient absorption spectra.
- Ally Aukauloo, Zakaria Halime at ICMMO Lab, Winfried Leibl, Annamaria Quaranta, Philipp Gotico at CEA Lab for giving us samples and sharing knowledges in the discussion meetings.

I would not have completed my PhD in time without the enthusiastic support from the scientific instruments and electronic groups. Christophe Lefumeux, Catherine Le Bris supported me a lot for optics, Thierry Chamaillé for mechanical designs, Christophe Charrière for electronics. Especially, I would like to send many thanks to Christophe Lefumeux. You were always ready to help me with any trouble of lasers and optical instruments. I am also sorry for not frequently keep cleaning the laboratory room.

I would like to thank all members of the research group “Molecular System, Astrophysics and Environment” for your kindness and warmth, especially, thank Mrs. Karine Beroff for your helping me to prepare a delicious cake for my party’s defence. Thank my friends: Mark Hammonds for spending your tea time to help me to correct my faults in English for my thesis and indicated me many useful things. Thank you so much, my friends, in my research group, Oliver Happer, Ozan Lacinbala, Joffrey Fréreau, Mark Hammonds, Olivia Chitarra, Anam Fatima, Yevheniia Smortsova for special gift as well as for all the funny moments in our office.

I am thankful Director of EDOM Ondes et Matière - Jean-Jacques Greffet, Director of ISMO - Bernard Bourguignon, and the staff of human resource at ISMO for helping me through administrative paper works.

I would like to thank all members of the jury committee for your valuable assessments for the thesis: Michel Sliwa, Yann Pellegrin, Talal Mallah, Murielle Chavarot-Kerlidou, and Jerome Chauvin. I would like to express my sincere acknowledgement of your open and communicative atmosphere that you made. Your behaviour helped me feeling more warm and confident to answer and discussed in all the defence’s time. I am thankful Michel Sliwa for also sending us many valuable contributions for our next publication.

I would like to thank my Vietnamese friends. Thank Minh Chau Nguyen, Ngoc Ha Nguyen, Thanh Loan Truong, Khoa Truong Nguyen, Hang Au, Lan Anh Nguyen, Hoang Yen Tran for sharing and helping me in my life.

The last acknowledgements, I would like to thank my beloved family. All you always accompany and motivate me to complete the thesis. I would not have done my PhD without support from my family. Thank my parents, my parents in law for supporting and helping me taking care of my daughter. I want to say to my husband thank you so much. Thank you for always supporting, motivating, and loving me. I love you so much. Finally, send to the most important person in my life, my dear daughter, thank you for your love and your sympathy with my absence in three years. I love you so much.

# Table of contents

<b>RESUME .....</b>	<b>I-1</b>
<b>ACKNOWLEDGEMENTS.....</b>	<b>I</b>
<b>TABLE OF CONTENTS .....</b>	<b>III</b>
<b>LIST OF FIGURES.....</b>	<b>VI</b>
<b>LIST OF TABLES.....</b>	<b>XI</b>
<b>LIST OF ABBREVIATIONS.....</b>	<b>XII</b>
<b>CHAPTER 1. BACKGROUND .....</b>	<b>1</b>
<b>1.1 INTRODUCTION .....</b>	<b>1</b>
<b>1.2 PHOTOVOLTAIC ORGANIC SOLAR CELLS.....</b>	<b>2</b>
1.2.1 Introduction .....	2
1.2.2. The principal mechanism of photovoltaic organic solar cells .....	3
<b>1.3 PHOTOSYNTHESIS REACTIONS .....</b>	<b>4</b>
1.3.1 Natural photosynthesis .....	4
1.3.2 Artificial photosynthesis.....	5
<b>1.4 THEORETICAL BACKGROUND .....</b>	<b>6</b>
1.4.1 Photoinduced quenching processes .....	6
1.4.1.1 Photoinduced energy transfer .....	7
1.4.1.2 Photoinduced electron transfer .....	9
1.4.2 Accumulative electron transfer.....	13
1.4.2.1 Difficulties and solutions in accumulative electron transfer.....	15
1.4.2.2 The context of studying photoinduced the accumulative electron transfer .....	18
<b>REFERENCES .....</b>	<b>25</b>
<b>CHAPTER 2. MATERIALS AND METHODS.....</b>	<b>31</b>
<b>2.1 MATERIALS.....</b>	<b>31</b>
2.1.1 Dyads and their derivatives study in chapter 3.....	31
2.1.2 Molecular complexes on multicomponent systems study in chapter 4, 5, and 6.....	32
<b>2.2 METHODS .....</b>	<b>33</b>
2.2.1 Nanosecond pump-pump-probe transient experiment.....	34
2.2.2 Femtosecond transient absorption spectroscopy .....	39

2.2.3	Nanosecond time-resolved resonance Raman spectroscopy .....	39
2.2.4	Time-correlated single-photon counting .....	41
2.2.5	Steady-state spectroscopy.....	41
2.2.6	Cyclic voltammetry measurements .....	42
2.2.7	Spectroelectrochemical absorption measurements.....	42
<b>REFERENCES .....</b>		<b>43</b>
<b>CHAPTER 3. ENERGY TRANSFER AND ELECTRON TRANSFER IN BODIPY-C<sub>60</sub> DYAD SYSTEMS.....</b>		<b>44</b>
3.1	<b>INTRODUCTION.....</b>	<b>44</b>
3.2	<b>LIGHT-INDUCED ELECTRON TRANSFER AND ENERGY TRANSFER PROCESSES IN A NEW BODIPY-C<sub>60</sub> DYAD (MANUSCRIPT PREPARED) .....</b>	<b>46</b>
3.3	<b>RESULTS AND DISCUSSION IN STUDYING PHOTOPHYSICAL PROPERTIES OF THE BDP-C<sub>60</sub> DYAD SYSTEM.....</b>	<b>84</b>
3.4	<b>RESULTS AND DISCUSSION IN STUDYING PHOTOPHYSICAL PROPERTIES OF DYAD PEPTIDE AND DYAD ALKYL SYSTEMS .....</b>	<b>91</b>
3.4.1	Absorption and fluorescence measurements .....	91
3.4.2	Femtosecond and nanosecond TA studies.....	93
3.4.2.1	<i>Femtosecond TA spectra .....</i>	<i>93</i>
3.4.2.2	<i>Nanosecond TA spectra.....</i>	<i>96</i>
3.5	<b>PERSPECTIVE .....</b>	<b>98</b>
<b>REFERENCES .....</b>		<b>98</b>
<b>CHAPTER 4. CHARGE ACCUMULATION ON MULTICOMPONENT SYSTEMS</b>		<b>104</b>
4.1	<b>INTRODUCTION.....</b>	<b>104</b>
4.2	<b>COMPONENTS FOR CONSTRUCTING CHARGE ACCUMULATION SYSTEMS – A MODEL PHOTOCATALYTIC SYSTEM.....</b>	<b>105</b>
4.2.1	Photosensitizer (PS) and reductant.....	105
4.2.2	Model complexes for studying charge accumulation .....	107
4.3	<b>SNAPSHOTS OF LIGHT-INDUCED ACCUMULATION OF TWO CHARGES ON METHYLVIologen USING A SEQUENTIAL NANOSECOND PUMP- PUMP PHOTOEXCITATION (THE JOURNAL OF PHYSICAL CHEMISTRY LETTERS).....</b>	<b>108</b>
4.4	<b>WATCHING INTERMOLECULAR LIGHT-INDUCED CHARGE ACCUMULATION ON NAPHTHALENE DIIMIDE BY TRIS(BIPYRIDYL) RUTHENIUM (II) PHOTOSENSITIZER (MANUSCRIPT IN PREPARATION) .....</b>	<b>121</b>

<b>REFERENCES .....</b>	<b>143</b>
<b>CHAPTER 5. PHOTOINDUCED CHARGE TRANSFER PROCESSES ON TETRAPHENYLPORPHYRINS AS A CATALYST FOR CO<sub>2</sub> PHOTOREDUCTION AND A PORPHYRIN DYAD AS MODELS FOR PHOTOSYSTEM II .....</b>	<b>150</b>
<b>5.1 INTRODUCTION .....</b>	<b>150</b>
<b>5.2 METAL COMPLEX APPROACH TO PHOTOCATALYTIC SYSTEMS .....</b>	<b>151</b>
<b>5.3 PHOTOPHYSICAL STUDY OF IRON PORPHYRIN COMPLEXES IN PHOTOCATALYTIC SYSTEMS .....</b>	<b>152</b>
5.3.1 Introduction .....	152
5.3.2 Results and discussion .....	153
<b>5.4 PHOTOPHYSICAL STUDY OF ZINC PORPHYRIN COMPLEX IN PHOTOCATALYTIC SYSTEMS .....</b>	<b>158</b>
5.4.1 Introduction .....	158
5.4.2 Results and discussion .....	159
<b>5.5 PHOTOINDUCED PROCESSES IN A PORPHYRIN-IMIDAZOLE-PHENOL COMPOUND..</b>	<b>169</b>
5.5.1 Porphyrin-imidazole-phenol – a model of photosystem II .....	169
5.5.2 Results and discussion .....	171
<b>REFERENCES .....</b>	<b>175</b>
<b>CHAPTER 6. TIME-RESOLVED RESONANCE RAMAN SPECTROSCOPIC STUDY OF CHARGE TRANSFER REACTION FROM RUTHENIUM (II) TRIS- BIPYRIDINE TO METHYL VIOLOGEN .....</b>	<b>179</b>
<b>6.1 INTRODUCTION .....</b>	<b>180</b>
<b>6.2 TIME-RESOLVED RESONANCE RAMAN SPECTROSCOPY OF THE PHOTO-INDUCED ELECTRON TRANSFER FROM RUTHENIUM (II) TRIS-BIPYRIDINE TO METHYL VIOLOGEN (MANUSCRIPT PREPARED) .....</b>	<b>180</b>
<b>REFERENCES .....</b>	<b>201</b>
<b>CHAPTER 7. CONCLUSIONS AND PERSPECTIVES.....</b>	<b>205</b>
<b>7.1 CONCLUSIONS.....</b>	<b>205</b>
<b>7.2 PERSPECTIVES .....</b>	<b>210</b>
<b>REFERENCES .....</b>	<b>211</b>

# List of figures

Figure 1.1 Simplified schematic mechanism of OCSs.....	3
Figure 1.2. Illustration of the photosynthetic reaction of Photosystem II.....	4
Figure 1.3. The schematic reaction mechanism for CO <sub>2</sub> reduction reaction by using the photocatalytic systems. <sup>26</sup> .....	6
Figure 1.4. The mechanism of Dexter (a) and Forster (b) energy transfer .....	8
Figure 1.5. Illustration of two parabolas, which correspond to the energy of the reactants and the products .....	10
Figure 1.6. Illustration of the reactions regions of electron transfer is predicted by the Marcus theory. In the A-C regions, the rate of electron transfer increases as $\Delta G^0$ decreases. In the inverted region (D), the rate of electron transfer decreases as it becomes more energetically favorable .....	12
Figure 1.7 <sup>40</sup> . A schematic picture for artificial photosynthesis that converts solar energy into fuel by charge separation coupled to catalytic water oxidation and fuel production.....	14
Figure 1.8. <sup>40</sup> Schematic diagram of reaction and state energy of a donor-photosensitizer-acceptor (D-P-A) triad under absorbing two sequential photons. Solid arrows describe productive reaction; dash line arrows describe recombination reactions. Energy transfer reactions between P* and D are not shown for clarity.....	16
Figure 1. 9. Structure of the triad <sup>69</sup> $[\text{Ru}(\text{bpy})_3]^{2+}$ -NDI- $[\text{Ru}(\text{bpy})_3]^{2+}$ .....	20
Figure 1.10. Structure of porphyrin-PDI-porphyrin system <sup>70</sup> .....	21
Figure 1.11. Chemical structure of the Anthraquinone- $[\text{Ru}(\text{bpy})_3]^{2+}$ -Oligotriarylamine- $[\text{Ru}(\text{bpy})_3]^{2+}$ -Anthraquinone <sup>73</sup> .....	22
Figure 1.12. Chemical structure of the Triarylamine- $[\text{Ru}(\text{bpy})_3]^{2+}$ -Anthraquinone- $[\text{Ru}(\text{bpy})_3]^{2+}$ -Triarylamine <sup>71</sup> .....	23
Figure 1.13. Chemical structure of the Heptad and its reference compounds <sup>73</sup> .....	23
Figure 1.14 <sup>74</sup> . Scheme of Oligotriarylamine- $[\text{Ru}(\text{bpy})_2(\text{CN})_2]^{2+}$ -TiO <sub>2</sub> .....	24
Figure 1.15. <sup>75</sup> Molecular structure of dyad $[\text{Ru}(\text{bpy})_3]^{2+}$ -NDI .....	24
Figure 2.1. Simplified representation of a pump-probe assembly with the superimposition of the probe and pump lasers .....	34
Figure 2.2. Simplified optical setup of the pump-pump-probe system <sup>75</sup> .....	35

Figure 2.3. Synchronization and timing control. Left side (blue part): shows device block diagrams and how they are synchronized. The right side indicates the approach of timing control and acquisition.....	38
Figure 2.5. Simple schematic diagram of nanosecond pump-probe TR3 system.....	40
Figure 2.5. Schematic presentation of the TCSPC experimental setup. Abbreviation: Light pulses are collected; PD: photodiode; D: discriminator; m: monochromator; PM: photomultiplier; TAC: time-amplitude convertor; ADC: analogic-digital converter; TCSPC: TCSPC module.....	41
Figure 3.1. The molecular structures of a) BDP-C <sub>60</sub> Dyad, b) <b>BDP</b> , and c) <b>C<sub>60</sub></b> .....	45
Figure 3.2. The molecular structures of a) BDP-C <sub>60</sub> -peptide assembly Dyad and b) BDP-peptide derivative .....	45
Figure 3.3. The molecular structures of a) BDP-C <sub>60</sub> -alkyl assembly Dyad and b) BDP-alkyl derivative .....	45
Figure 3.4. Femtosecond transient absorption spectra of the <b>BDP</b> and <b>C<sub>60</sub></b> pristine in benzonitrile at the indicated delay times .....	85
Figure 3.5. Three conformers with the distance of 8.8 Å corresponding to the folded conformer and two distances of 17.5 and 20.5 Å for stretched conformers. ....	86
Figure 3.6. Femtosecond transient absorption spectra of the BDP-C <sub>60</sub> Dyad ( $5.5 \times 10^{-5}$ M) in argon-saturated benzonitrile at the indicated delay times, $\lambda_{exc}$ 380 nm. ....	88
Figure 3.7. Basic kinetic fits at specific characterization bands. ....	89
<i>Figure 3.8. Energy level diagram presents the photoinduced processes obtained following laser excitation (<math>\lambda_{exc}</math> 380 nm) in the two conformations of the BDP-C<sub>60</sub> Dyad in benzonitrile. Abbreviations: EnT= Energy transfer, CT = charge transfer, Back CT = back charge transfer, ISC = intersystem crossing, energies: <math>^1\mathbf{BDP}^* = 2.33eV</math>, <math>^1\mathbf{C}_{60}^* = 1.75eV</math>, <math>^3\mathbf{C}_{60}^* = 1.55eV</math><sup>25,59</sup>.</i> ....	90
Figure3.9. Red and black lines: Normalized absorption (solid line) and fluorescence (dash line) spectra in benzonitrile of the BDP-peptide and Dyad-peptide ( $1.4 \times 10^{-6}$ M), $\lambda_{exc}$ =510 nm. Green line: the normalized absorption spectrum of the <b>C<sub>60</sub></b> fragment in benzonitrile. ....	91
Figure 3.10. Fluorescence spectra (a) and fluorescence decays (b) of the Dyad-peptide and BDP-peptide ( $1.4 \times 10^{-6}$ M) excited at 490 nm in benzonitrile, $\lambda_{exc}$ 527 nm. ....	92
Figure 3.11. Femtosecond transient absorption spectra of the BDP-peptide ( $4.6 \times 10^{-5}$ M) in benzonitrile at the indicated delay times ( $\lambda_{exc}$ 527 nm).....	94

Figure 3.12. Femtosecond transient absorption spectra of the BDP-C <sub>60</sub> -peptide assembly Dyad (4.6 × 10 <sup>-5</sup> M) in benzonitrile at the indicated delay times, λ <sub>exc</sub> 527 nm; inset: Spectrum of BDP after oxidization by spectroelectrochemistry, presented for comparison.....	94
Figure 3.13. The kinetic traces of the peaks at 445 and 390 nm of the Dyad-peptide in benzonitrile, λ <sub>exc</sub> 527 nm. ....	95
Figure 3.14. Femtosecond transient absorption spectra of the Dyad-alkyl assembly Dyad (5.9 × 10 <sup>-5</sup> M) in benzonitrile at the indicated delay times, λ <sub>exc</sub> 527 nm.....	96
Figure 3.15. Kinetic trace at 390 nm corresponding the singlet-excited state of the BDP.....	96
Figure 3.16. a) Nanosecond transient absorption spectra of the C <sub>60</sub> in Argon-saturated benzonitrile at the indicated delay times; b) Kinetic traces (scattered points) of the C <sub>60</sub> at 710 nm in the comparison between argon-saturated and air in benzonitrile .....	97
Figure 3.17. (a) Nanosecond transient absorption spectra of the Dyad-peptide (5.1 × 10 <sup>-6</sup> M) in argon-saturated benzonitrile at the indicated delay times. (b) Kinetic traces of the Dyad-peptide assembly at 700 nm corresponding to the <sup>3</sup> C <sub>60</sub> <sup>*</sup> , λ <sub>exc</sub> 527 nm .....	97
Figure 3.18. (a) Nanosecond transient absorption spectra of the Dyad-alkyl assembly (5 × 10 <sup>-6</sup> M) in argon-saturated benzonitrile at the indicated delay times. (b) Kinetic traces of the Dyad-alkyl assembly at 700 nm corresponding to the <sup>3</sup> C <sub>60</sub> <sup>*</sup> , λ <sub>exc</sub> 527 nm .....	98
Figure 4.1. Ground-state absorption spectra of neutral (NDI), first reduced (NDI <sup>•-</sup> ) and second reduced state of NDI (NDI <sup>2-</sup> ) <sup>15</sup> . Inset: structure of NDI .....	109
Figure 5.1. Metal porphyrin derivatives studied for reduction of CO <sub>2</sub> : metalloporphyrins (MP) <sup>5</sup> , metallocorrins (MN), metallophthalocyanines (MPc), and metallocorroles (MC) <sup>7</sup> ...	153
Figure 5.2. Iron porphyrins and iAscH <sup>-</sup> (reversible electron donor) studied for nanosecond transient absorption .....	154
Figure 5.3. Cyclic voltammograms of 1mM of FeTPPCl (red) and FeTPPF <sub>8</sub> OH (blue) in argon-degassed acetonitrile containing 0.1 M [Bu <sub>4</sub> N]PF <sub>6</sub> at 25 °C and recorded using a glassy carbon working electrode, a platinum mesh as the counter electrode and a saturated calomel electrode (SCE) as the reference electrode .....	155
Figure 5.4. Absorption spectra of FeTPPF <sub>8</sub> OH (0.02 mM)- iAscH <sup>-</sup> (100 mM) (black curve) and FeTPPF <sub>8</sub> OH-0.02 mM (red curve) in argon-saturated acetonitrile. Inset: spectrum of FeTPPF <sub>8</sub> OH (9 μM) .....	156
Figure 5.5. Nanosecond TA spectra at the indicated delay times of the FeTPPF <sub>8</sub> OH (0.02 mM) – iAscH <sup>-</sup> (100 mM) in argon-saturated acetonitrile, λ <sub>exc</sub> 430 nm .....	157

Figure 5.6. Kinetic traces and their fits at 524 and 562 nm of the FeTPPF <sub>8</sub> OH (0.02 mM) – iAscH <sup>-</sup> (100 mM) in argon-saturated acetonitrile, $\lambda_{exc}$ 430 nm.....	157
Figure 5.7. Absorption spectra of FeTPPcI (0.15 mM)– iAscH <sup>-</sup> (100 mM) (black curve) and FeTPPcI (red curve) in argon-saturated acetonitrile; (b) Zoom Q- region .....	158
Figure 5.8. Nanosecond TA spectra at the indicated delay times of FeTPPcI (0.15 mM)– iAscH <sup>-</sup> (100 mM) in argon-saturated acetonitrile, $\lambda_{exc}$ 430 nm.....	158
Figure 5.9 Kinetic traces and their fits at 569 and 543 nm of FeTPPcI (0.15 mM)– iAscH <sup>-</sup> (100 mM) in argon-saturated acetonitrile, $\lambda_{exc}$ 430 nm.....	159
Figure 5.10. Functionalized ZnTTPF20 porphyrin studied for nanosecond transient absorption.....	160
Figure 5.11. Cyclic voltammogram of 1mM of ZnTPPF20 in argon-deaerated acetonitrile containing 0.1 M [Bu <sub>4</sub> N]PF <sub>6</sub> at 25°C, and recorded using a glassy carbon working electrode, a platinum mesh as the counter electrode and a SCE as the reference electrode .....	161
Figure 5.12. The absorption spectrum of ZnTPPF20 (6.2 $\mu$ M) in argon-saturated acetonitrile .....	161
Figure 5.13 a) Nanosecond TA spectra at the indicated delay times of ZnTPPF20 (6.2 $\mu$ M) in acetonitrile and in air, $\lambda_{exc}$ = 430 nm; b) Kinetic traces and their fits at 454 and 555 nm .....	162
Figure 5.14. a) Nanosecond TA spectra at the indicated delay times of ZnTPPF20 in argon-saturated acetonitrile solution, $\lambda_{exc}$ = 430 nm, 6.2 $\mu$ M; b) Kinetic traces and their fits at 454 and 555 nm.....	162
Figure 5.15. The absorption spectrum of ZnTPPF20 (6.2 $\mu$ M)– iAscH <sup>-</sup> (100 mM) (black curve) in comparison with the absorption spectrum of ZnTPPF20-6.2 $\mu$ M (red curve) and iAscH <sup>-</sup> -100 mM (green curve) in acetonitrile. ....	163
Figure 5.16. Nanosecond TA spectra of ZnTPPF20 (6.2 $\mu$ M) and iAscH <sup>-</sup> (100 mM) in argon-saturated acetonitrile at indicated delay times, $\lambda_{exc}$ = 430 nm.....	164
Figure 5.17. Nanosecond TA global fit kinetic traces of ZnTPPF20 (6.2 $\mu$ M) and iAscH <sup>-</sup> (100 mM) in argon-saturated acetonitrile, $\lambda_{exc}$ = 430 nm.....	164
Figure 5.18. The absorption spectrum of ZnTPPF20 (6.2 $\mu$ M) and DABCO (100 mM) (black curve) in comparison with the absorption spectrum of ZnTPPF20-6.2 $\mu$ M (red curve) and DABCO-100 mM (green curve) in acetonitrile. ....	165
Figure 5.19. Nanosecond TA spectra of ZnTPPF20(6.2 $\mu$ M)– DABCO (100 mM) in argon-saturated acetonitrile at indicated delay times, $\lambda_{exc}$ = 430 nm. ....	165

Figure 5.20. Nanosecond TA global fit kinetic traces of ZnTPPF20 (6.2 $\mu$ M)– DABCO (100 mM) in argon-saturated acetonitrile, $\lambda_{exc} = 430$ nm.....	166
Figure 5.21. Nanosecond TA spectra of ZnTPPF20 (6.2 $\mu$ M)– DABCO (100 mM) in argon-saturated acetonitrile at indicated delay times, $\lambda_{exc} = 450$ nm.....	167
Figure 5.22. Nanosecond TA global fit kinetic traces of ZnTPPF20 (6.2 $\mu$ M)– DABCO (100 mM) in argon-saturated acetonitrile, single pulse excitation $\lambda_{exc} = 450$ nm .....	167
Figure 5.23. TA spectra (a) and corrected TA spectra (b) of the solution ZnTPPF20 (6.2 $\mu$ M)– DABCO (100 mM) in argon-deaerated acetonitrile, upon double-pulse excitation: first pulse at 430 nm, 20 Hz and second pulse at 450 nm, 10 Hz; separated by 0.8 $\mu$ s.....	168
Figure 5.24. a) Nanosecond TA global fit kinetic traces of ZnTPPF20-DABCO in argon-saturated acetonitrile, double-pulse excitation $\lambda_{exc1} = 430$ nm, $\lambda_{exc2} = 450$ nm. b) Decay Associated different spectra (DADS) obtained from global fits.....	169
<i>Figure 5.25. Left: Molecular drawing of porphyrin-imidazole-phenol (denoted as P-Im-ArOH) , right X-ray crystal structure of P-Im-ArOH<sup>37</sup> .....</i>	<i>171</i>
Figure 5.26. Cyclic (CV) and square wave (SW) voltammograms (a) and spectroelectrochemistry in benzonitrile/tetrabutylammonium hexafluorophosphate (0.1 M) of P-Im-ArOH <sup>38</sup> .....	171
Figure 5.27. Absorption spectra of P-Im-ArOH 11 $\mu$ M and P-Im-ArOH (11 $\mu$ M) + MV <sup>2+</sup> (10 mM) in dry argon-saturated acetonitrile .....	172
Figure 5.28. Nanosecond TA spectra (a) and kinetic trace at 455 nm (b) of P-Im-ArOH 11 $\mu$ M in dry argon-saturated acetonitrile. Absorbance of the initial solution $A_{517\text{ nm}} = 0.2$ , $\lambda_{exc} = 517$ nm.....	173
Figure 5.29. Nanosecond TA spectra of P-Im-ArOH (11 $\mu$ M) + MV <sup>2+</sup> (10 mM) in dry argon-saturated acetonitrile at indicated delay times, $\lambda_{exc} = 517$ nm. Inset: normalized spectrum at 10 $\mu$ s in comparison with spectrum at 1 $\mu$ s .....	174
Figure 7.1. 1 Scheme of second charge transfer on photosystems (a) photosensitizer – acceptor and donor, (b) photocatalyst and donor .....	206

# List of tables

Table 1.1. Chemical structures of referent molecules .....	19
Table 2.1 Molecular structure, chemical formula and molar mass of the dyads and their derivatives under study .....	31
Table 2.2. Molecular structures under studying charge accumulation on multicomponent systems in chapter 4, 5, and 6 .....	32
Table 3.1 . Basic kinetic traces were fitting at the specific bands. The singlet excited state of $C_{60}$ ( $^1C_{60}^*$ ), singlet excited state of BDP ( $^1BDP^*$ ), triplet excited state of $C_{60}$ ( $^3C_{60}^*$ ), the first reduced-state of $C_{60}$ ( $C_{60}^{\bullet-}$ ), decay time (d), rising time (r) .....	90
Table 3.2. Photophysical properties of the BDP- $C_{60}$ -peptide, BDP- $C_{60}$ -alkyl Dyad assembly, BDP-peptide and BDP-alkyl in Benzonitrile. Absorption band $\lambda_{abs}$ (nm) and emission band $\lambda_{em}$ (nm), fluorescence quantum yield $\Phi_F$ , fluorescence lifetime $\tau$ (ns), radiative $k_r$ ( $s^{-1}$ ) and nonradiative rate $k_{nr}$ ( $s^{-1}$ ) constants. ....	93
Table 4.1. $CO_2$ reduction potentials vs NHE. ....	104
Table 5.1. Standard redox potentials in V versus SCE of Figure 5.3.....	154

# List of abbreviations

- BODIPY Boron-dipyrromethene
- C<sub>60</sub> Fullerene
- CCD Charge-couple device
- CV Cyclic voltammetry
- CSS1 First charge separated state
- CSS2 Second charge-separated state
- CuAAC Copper(I)-catalyzed alkyne-azide cycloaddition
- DABCO Diazabicyclo[2.2.2]octane
- DADS Decay Associated different spectra
- DBU 1,8-biazabicyclo(5.4.0) undec-7-ene
- DFT Density functional theory
- EnT Energy transfer
- ET Electron transfer
- FRET Förster resonant energy transfer
- FeTPPCl Iron tetraphenylporphyrin
- FeTPPF<sub>8</sub>OH Iron tetra-2,6-difluorophenylporphyrin hydroxide
- HOMO Highest occupied molecular orbital
- ICCD Intensified CCD
- iAscH<sup>-</sup> 5,6-iso propylidene-L-ascorbate
- iAscH<sub>2</sub> 5,6-iso propylidene-L-ascorbic acid
- LUMO Lowest unoccupied molecular orbital
- MLCT Metal-to-ligand charge transfer
- MV<sup>2+</sup> Methyl viologen
- MN Metallocorrins
- MP Metalloporphyrins
- MPc Metallophthalocyanines
- MC metallocorroles
- NDI Naphthalene diimide

- NHE Normal hydrogen electrode
- OSCs Photovoltaic organic solar cells
- OERS One-electron-reduced species
- OEOS One-electron-oxidized species
- P-Im-Ar-OH Porphyrin-imidazole-phenol
- PCET Proton-coupled electron transfer
- Pcat Photocatalyst
- PSII Photosystem II
- Pheo Pheophytin
- Q<sub>A</sub> Quinone protein
- PS Photosensitizer
- PET Photoinduced electron transfer
- [Ru(bpy)<sub>3</sub>]<sup>2+</sup> Ruthenium(II) Tris-bipyridine
- SAMs Self-assembled monolayers
- SCE Saturated calomel electrode
- SW Square wave
- TA Transient absorption
- TR3 Nanosecond time-resolved resonance Raman
- TCSPC Time-correlated single-photon counting
- TDDFT Time-Dependent Density Functional Theory
- ZnTPPF20 Zinc porphyrins

## Math symbols

- Driving force  $\Delta G^0$
- Electronic coupling  $V_{DA}$
- Förster radius  $R_0$
- Free energy of activation  $\Delta G^\ddagger$
- Rate of electron transfe  $k_{ET}$
- Reorganisation energy  $\lambda$
- Rate of FRET  $k_T$

# Chapter 1. Background

## 1.1 Introduction

The energy demand of humanity is increasing rapidly, and shows no signs of slowing. Statistically, energy consumption in 2012 ( $5.8 \times 10^{20}$  J) was higher than that in 2001 ( $4.3 \times 10^{20}$  J)<sup>1,2</sup> and by 2050, consumption might be two times higher than in 2001, possibly increasing to three times higher by 2100.<sup>3</sup> Fossil resources supplied most of this demand (86 %) in 2001. However, fossil fuels only exist in limited, non-renewable amounts, which are being depleted. Furthermore, the continuous use of fossil fuels is a leading cause of CO<sub>2</sub> accumulation in the Earth's atmosphere.

It is time to look ahead to find a new future for energy: one possibility is to use environmentally friendly renewable energy sources. One renewable energy source is the sun. Solar energy supplies approximately 10,000 times our daily energy needs.<sup>4</sup> However, sunlight itself possesses two main limitations. Firstly, it is diffuse, so collecting solar energy efficiently would require to collect solar energy on a large scale. Moreover, the light is intermittent, illuminating on average only ~ 6 hours per day.

Nowadays, solar energy has mainly been collected using photovoltaic solar cells with better and better efficiency. This research direction shows outstanding progress in solar conversion efficiency and development of varieties of solar cells. Nevertheless, we cannot use photovoltaic solar cells at nighttime. To make solar energy a perfect renewable energy source, solar energy needs to be stored. A promising means of accomplishing this is with solar fuels. Photosynthesis reactions in leaves, bacteria, and other photosynthetic systems in nature are excellently adapted to use sunlight. Therefore, what we need to do is to create artificial photosynthetic systems to mimic natural photosynthetic reactions in which sunlight is captured, converted, and stored as chemical energy. Water and CO<sub>2</sub> are universally available, abundant sources on our planet. Building renewable energy based on water and CO<sub>2</sub> using solar energy to obtain hydrogen and hydrocarbons is a big challenge. Currently, water splitting has attained a certain level of success, with the highest efficiency reaching ~18 %.<sup>5</sup> However, much research is still required before solar fuels become viable, so to achieve this goal, some difficulties have to be overcome.

Electron transfer and energy transfer play an important role in photosynthesis systems. Fundamentally, a single electron transfer is needed to perform photovoltaic solar cells. In contrast, to construct solar fuel, multielectron transfer processes have to require.

In this context, the aim of the thesis focuses on two main themes: (i) Studying single electron transfer in Donor-Acceptor Dyad systems towards optimization efficiency of charge separation and application in photovoltaic organic solar cells. (ii) Studying multiple electron transfers in models of artificial photosynthesis systems towards elucidating the electron transfer processes in artificial systems.

## **1.2 Photovoltaic organic solar cells**

To have an overview about the meaning of studying single electron transfer in donor-acceptor systems, this section will briefly provide the development progress of photovoltaic organic solar cells (OSCs), in which creating electron-hole pairs are necessary. The principal mechanism of photovoltaic OSCs is also introduced.

### **1.2.1 Introduction**

Photovoltaic OSCs have found widespread use in the global market. Photovoltaics are one of the most rapidly developing technologies in the world, with above 35 % growth rates per year.<sup>6</sup> The development of inorganic photovoltaic cells, such as single-junction GaAs, monocrystalline Silicon, thin film, etc, shows a large variety of materials with steadily increasing efficiency. Additionally, the price of inorganic solar cells has fallen drastically in recent years. However, the price of fossil-based energy sources is still cheaper in comparison with the production cost of inorganic solar cells. Higher efficiency inorganic solar cells require correspondingly higher production costs. However, a renewable energy source requires a reasonable price to become widespread.

Photovoltaic organic solar cells (OSCs) were first studied in the 1950s, until 1977 marked a milestone for the OSCs with the discovery of conductivity of conjugation polymers.<sup>7</sup> The researchers were awarded the Nobel Prize in Chemistry for their discovery in 2000. To date, a variety of materials has been developed in the field of OSCs, such as dye-sensitizers, polymers, and molecular donor-acceptor systems. OSCs offer some outstanding features. Almost all materials used to fabricate OSCs are abundant and low-cost materials. They use simple manufacturing techniques, with low environmental impact. Today, the efficiency of OSCs has increased sufficiently to be able to compete with inorganic solar cells.<sup>8</sup> Nevertheless, OSCs also

possess some disadvantages, which need to be solved, such as the reproducibility and lifetime. Currently, research on OSCs has concentrated on the development in designing new structures, new materials, and the fundamental mechanism of photoinduced processes.

### **1.2.2. The principal mechanism of photovoltaic organic solar cells**

The principal mechanism of photovoltaic OSCs is different from the mechanism of conventional photovoltaic solar cells. In inorganic photovoltaic cells, free conduction band electrons and valence band holes are generated upon photon excitation. In contrast, the mechanism of OSCs is based on the generation of electron and hole pairs bound under photon excitations. These charges are so-called excitons.<sup>9</sup> The mechanism of OSCs is being actively researched in an attempt to find a theoretical description, which can be applied in all kind of OSCs substances. In general, an OSC system is blended by two components, donor and acceptor, in which both highest occupied molecular orbital (HOMO) and lowest unoccupied molecular orbital (LUMO) of the electron donor are at higher energy than those, respectively, of the electron acceptor. Following light excitation, an excited electron in the LUMO of the donor transfers to the LUMO of the acceptor leading to charge transfer states (Figure 1.1). The charge transfer states of OSCs are diverse and might be defined differently in each OSC. For example, charge transfer states may be variously referred to as polaron pairs,<sup>10</sup> intermolecular radical pairs,<sup>11</sup> charge transfer excitons,<sup>12</sup> charge separation,<sup>13</sup> exciplexes,<sup>14</sup> and interfacial charge pairs.<sup>15</sup> Current in OSCs is based on charge separation by applying an external electric field. However, charge transfer states can also be lost by charge recombination to the ground state.

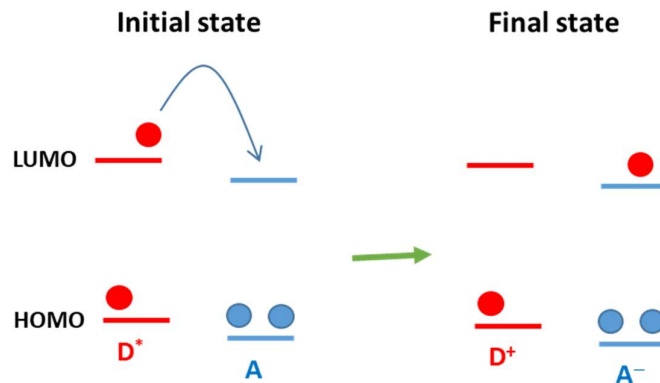


*Figure 1.1 Simplified schematic mechanism of OSCs.*

In the framework of the thesis, I focus on studying the principal mechanism of electron transfer in donor-acceptor dyad systems incorporating the C<sub>60</sub> fullerene, in solution, which

could contribute to construction of photovoltaic OSCs. Moreover, this donor-acceptor dyad system could be associated with a helical peptide that can be in favor of immobilizing them on surfaces to develop photoelectrochemical devices. Therefore, studying photophysical characterizations of the dyad system have to address first. The theory, which has been used to explain electron transfer dynamics in these systems, is considered in term of Marcus non-adiabatic electron-transfer theory.

### 1.3 Photosynthesis reactions

Photosynthetic reactions are the basis for all life on Earth, using the principle of harvesting light to acquire energy. They support the life and development of all creatures on the Earth, and without it, life might be different. In general, plants use antenna proteins which contain many chromophores to absorb light, then transfer this energy to reaction center proteins, in which the energy is converted into a chemical bond by electron-transfer reactions.<sup>16</sup>

#### 1.3.1 Natural photosynthesis

The photosynthetic reactions of green plants are the most crucial model to mimic for converting solar energy into solar fuel, with photosystem II (PSII) being key for all photosynthetic processes in green plants. Solar energy is used by PSII to drive the oxidation of water and the reduction of plastoquinone reactions.<sup>17,18</sup> The components of PSII contain a light-harvesting antenna system, in which photons are captured, and this excitation energy is transferred to the second component, the reaction centre, where primary charge transfers are occurring. The photosynthetic process of PSII is illustrated in Figure 1.2.

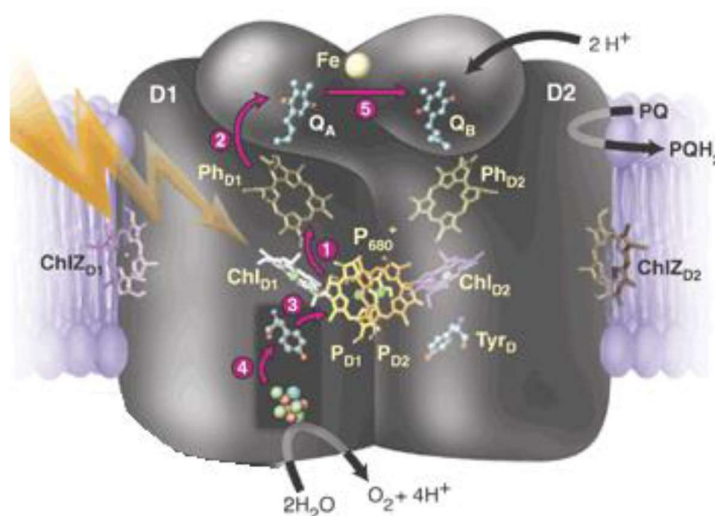


Figure 1.2. Illustration of the photosynthetic reaction of Photosystem II<sup>19</sup>

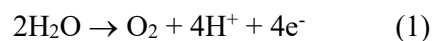
## Chapter 1. Background

The reactions in PSII are described in more detail in the following processes. Firstly, antenna components absorb light and rapidly ( $\sim 100$  fs)<sup>20</sup> transfer energy to the chlorophyll unit P<sub>680</sub>. The excited state of P<sub>680</sub> (P<sub>680</sub><sup>\*</sup>) is quickly quenched (1-30 ps) by electron transfer to the acceptor systems. Then, electrons transfer from P<sub>680</sub><sup>\*</sup> to the initial acceptor pheophytin (Pheo) (label 1 in Figure 1.2) to create a reduced state of Pheo (Pheo<sup>-</sup>) and oxidized state of P<sub>680</sub> (P<sub>680</sub><sup>+</sup>). The electron transfer process from Pheo<sup>-</sup> to the quinone protein (Q<sub>A</sub>) has been done rapidly (300 ps) (process 2 in Figure 1.2). After that, electron transfer to another quinone bound at Q<sub>B</sub> site (process 5 in Figure 1.2) occurs. After two successive excitations and charge separation, Q<sub>B</sub> accumulates fully two electrons and protonate, forming PQH<sub>2</sub> (in which PQ is a pool of quinone molecules). Meanwhile, P<sub>680</sub><sup>+</sup> is one of the most oxidizing species in nature (potential +1.2 V relative to NHE). Therefore, during electron transfer to the quinone, P<sub>680</sub><sup>+</sup> simultaneously receives an electron from a tyrosine molecule (Tyr<sub>Z</sub>), on a timescale of 20-35  $\mu$ s, depending on the state of the Mn<sub>4</sub>Ca cluster,<sup>21</sup> to form P<sub>680</sub> and oxidized Tyr<sub>Z</sub><sup>\*</sup> (process 3 in Figure 1.2). Oxidized Tyr<sub>Z</sub><sup>\*</sup> is reduced by the Mn<sub>4</sub>Ca cluster, which is the centre of water oxidation reaction (process 4 in Figure 1.2). Water oxidation can be implemented by four successive excitations of the regenerated P<sub>680</sub> to accumulate four holes on Mn<sub>4</sub>Ca<sup>21</sup>.

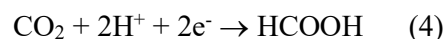
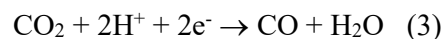
### **1.3.2 Artificial photosynthesis**

To convert solar energy into fuel, using artificial photosynthesis by mimicking natural systems is vital but challenging. For the production of solar fuel to become practical and economical, a system of artificial photosynthesis must be constructed from abundant, inexpensive, and non-toxic raw materials. Natural synthesis systems can start with low energy inorganic materials such as water and carbon dioxide to form oxygen and carbohydrates via redox chemistry. An artificial photosynthesis system attempts to emulate this process, producing high-energy substances from low energy materials.

In PSII, the water oxidation reaction proceeds by successive accumulative holes on Mn<sub>4</sub>Ca cluster:



Consequently, the electrons from equation (1) can also be used to reduce carbon dioxide.



Natural photosynthesis achieves water oxidation by accumulating multiple charges on specific molecular sites. Charge accumulation is also necessary for the formation of solar fuels.

As with natural photosynthesis, the artificial photosynthesis systems also require these characteristics. Firstly, sunlight is efficiently absorbed by an antenna. Secondly, a centre reaction is required for the charge-separated state. The first two functions are relatively easy to fulfill. Additionally, multi-electron catalysis is a crucial component to perform oxidation and reduction reactions. It is noted that most fuel forming reactions require more than a single electron, for example, equations (2) and (3). Therefore, a suitable catalyst should be able to provide several narrow spans of redox potential for different catalyst steps.

In the framework of the thesis, I focus on studying charge accumulation towards applications to reduce CO<sub>2</sub> using photocatalytic molecular systems. Herein, I will briefly discuss a system for CO<sub>2</sub> reduction but the same conceptual approach for water oxidation<sup>22,23</sup> or hydrogen evolution.<sup>24</sup> Molecular photocatalytic systems for CO<sub>2</sub> reduction are generally composed of three components: a redox photosensitizer (PS) which facilitates photoinduced electron transfer from a reductant (D) to a catalyst (Cat). The catalyst accepts the electron from the PS and accumulates an electron upon successive excitations of the photosensitizer. These electrons are used to reduce the CO<sub>2</sub> molecule. These processes are illustrated in Figure 1.3.

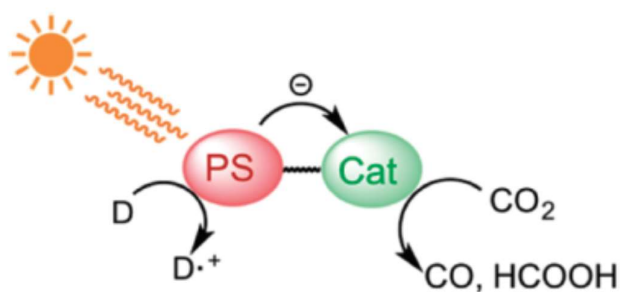


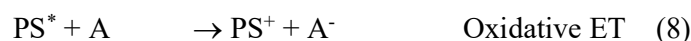
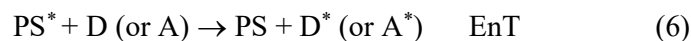
*Figure 1.3. The schematic reaction mechanism for CO<sub>2</sub> reduction reaction by using the photocatalytic systems.<sup>25</sup>*

## **1.4 Theoretical background**

The purpose of this section is to introduce the basic concepts of photoinduced processes that are related to the knowledge in the thesis. Some other basic concepts can be found in the textbook and articles such as electronically excited states, radiative and non-radiative transitions.<sup>26,27</sup>

### **1.4.1 Photoinduced quenching processes**

Quenching fluorescence is the decrease in intensity upon interaction with another molecule in solution. In the framework of the thesis, photoinduced quenching processes are photoinduced energy transfer (EnT) and photoinduced electron transfer (ET). Photoinduced energy transfer and electron transfer are the most pivotal processes in photosynthesis reactions and optoelectronic devices. The understanding of these processes lead to further insight on the reactions in natural systems, photocatalytic reactions, and optimization of the efficiency of OSCs as well. The initial step for both energy transfer and electron transfer starts with the excited state of a photosensitizer (PS\*) in the presence of reductant (D) or oxidant (A). Orbital interactions can induce both energy transfer and electron transfer between PS\* and reductant (or oxidant) (equations 5-7). However, several different factors will decide particularly the way of quenching processes.



To be more convenient in reading the chapter 3 in the thesis, the reactions (6-8) will be transformed into the reactions (9-10)<sup>28</sup> which refer to a donor (D) and acceptor (A) system under excitation of the donor.



#### **1.4.1.1 Photoinduced energy transfer**

The equation (9) presents the energy transfer process from the excited state of the donor to the ground state of the acceptor. In general, the condition required for energy transfer is spectral overlap between the emission spectrum of the donor and the absorption spectrum of the acceptor. There are two different types of interaction between donor excited state (D\*) and acceptor (A), leading to two mechanisms of energy transfer.

Dexter energy transfer mechanism is based on exchange electrons between the D\* and acceptor. Figure 1.4(a) illustrates the Dexter energy transfer mechanism. The electron promoted to the LUMO of the excited state of the donor is transferred to the LUMO of the acceptor,

simultaneously with the electron transfer from the HOMO of the acceptor to the HOMO of the donor. Therefore, Dexter energy transfer mechanism requires electrons exchange, so it is also called “exchange mechanism”. To have electrons exchange, a strong D-A orbitals overlap is required; this means a short-range D-A interaction ( $< 10\text{\AA}$ ).

Förster resonant energy transfer<sup>29</sup> (FRET) is the results from the interaction of the oscillating dipole of the donor excited state ( $D^*$ ) with that of the acceptor. Therefore, this type of energy transfer is also called “dipole-dipole”, “coulombic”, or “resonance” energy transfer. Figure 1.4(b) shows the mechanism of FRET. There is no electrons transfer or exchange. Therefore, this mechanism does not require the overlap of the orbitals and can take place even at long distances ( $\sim 100\text{\AA}$ ). The FRET will be discussed in more detail because of the relevance in this thesis.

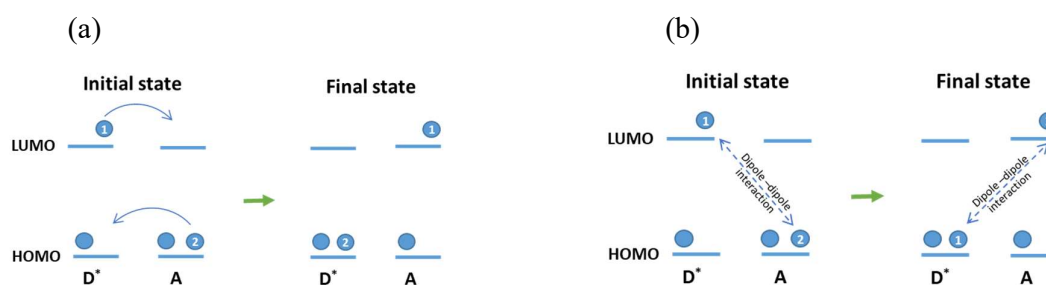


*Figure 1.4. The mechanism of Dexter (a) and Förster (b) energy transfer*

The rate of FRET from the donor to the acceptor can be estimated by:  $k_T = \frac{1}{\tau_D} \left( \frac{R_0}{r} \right)^6$  (11)

Where  $\tau_D$  is the fluorescence lifetime of the donor in the absence of the acceptor,  $r$  is the distance centre to centre of the donor and the acceptor,  $R_0$  is the Förster radius. The FRET rate is thus affected by the D-A distance. Therefore, the FRET measurement can be used to estimate the effects of conformation changes in the donor-acceptor dyad.<sup>30</sup> The Förster radius  $R_0$  were estimated, according to the equation:<sup>29</sup>

$$R_0 = 0.2108 * [n^4 * \Phi_d * k^2 * \int_0^\infty I_D(\lambda) \epsilon_A(\lambda) \lambda^4 d\lambda]^{1/6} \text{ (in \AA)} \quad (12)$$

Where  $n$  is the refractive index of the solvent.  $\Phi_d$  is the emission quantum yield of the donor chromophore in the absence of the acceptor.  $k^2$  is the orientation factor. For a random distribution of dipole-dipole interaction,  $k^2$  is equal to  $2/3$ .  $I_D(\lambda)$  is the entire emission intensity normalised to unity.  $\epsilon_A(\lambda)$  is the extinction coefficient of the acceptor.

**1.4.1.2 Photoinduced electron transfer**

Electron transfer that is described in the equation (10) is known as a cause for fluorescence quenching of donor-excited state in solution. In electron transfer reactions, no bond is formed or broken, except the change of ownership of an electron, which is moved from one orbital to another. Electron transfer processes will be favorable if the reaction is an exothermic process. The modern theory of electron transfer was pointed out by Marcus in the 1950s<sup>31,32,33</sup> It has been extended to adapt a variety of transformations that known as the semi-classical Marcus theory.<sup>31,34</sup> According to this theory, the electron transfer process can be illustrated by parabolas according to the reaction coordinate, which presents for the nuclear coordinate of the whole system undergoing the electron transfer reaction. One parabola presents for the energy of reactants and the other for the energy of products (Figure 1.5).

Following this theory, the rate of electron transfer ( $k_{ET}$ ) is described as a function of three parameters: the reorganization energy ( $\lambda$ ), the driving force ( $\Delta G^0$ ), and the electronic coupling ( $V_{DA}$ ). The equation (13)<sup>35</sup> shows the relation of these parameters. These parameters will be discussed in more details.

$$k_{ET} = \frac{2\pi}{\hbar} |V_{DA}|^2 \frac{1}{\sqrt{4\pi\lambda k_B T}} \exp\left(\frac{-(\Delta G^0 + \lambda)^2}{4\lambda k_B T}\right) \quad (13)$$

In which: T is temperature,  $k_B$  is the Boltzmann constant, and  $\Delta G^0$  is expressed by involving the reorganisation energy and free energy of activation ( $\Delta G^\ddagger$ ) for electron transfer.

$$\Delta G^\ddagger = \frac{(\Delta G^0 + \lambda)^2}{4\lambda} \quad (14)$$

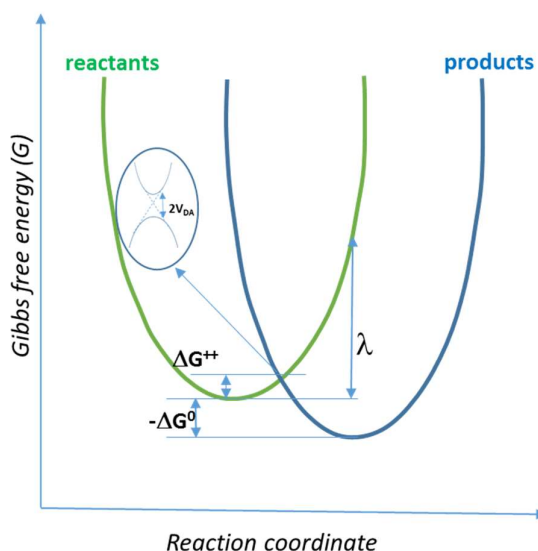


Figure 1.5. Illustration of two parabolas, which correspond to the energy of the reactants and the products.

### Reorganisation energy ( $\lambda$ )

The reorganisation energy is the energy needed to move all nuclei of the reactions and solvent into the place of the products without electron transfer. This energy is divided into two types, inner and outer reorganization as equation (15).

$$\lambda = \lambda_{\text{inner}} + \lambda_{\text{outer}} \quad (15)$$

$$\lambda_{\text{in}} = \frac{1}{2} \sum (k_i \Delta q_i^2) \quad (16)$$

$$\lambda_{\text{out}} = \frac{\Delta e^2}{4\pi\epsilon_0} \left( \frac{1}{\epsilon_{\text{op}}} - \frac{1}{\epsilon_s} \right) \left( \frac{1}{2a_D} + \frac{1}{2a_A} - \frac{1}{r_{DA}} \right) \quad (17)$$

The inner reorganisation refers to the internal changes in bond lengths, angles between and within the structures of the reactants and the products. The value of inner reorganisation can be evaluated using equation (16).<sup>31,36</sup> In which,  $k_i$  is the force constant of the normal mode vibration and  $\Delta q_i$  is the nuclear deviations of the normal vibrations. The outer reorganisation is the contribution from the changes in solvent orientation coordinated to local changes. Theory of the dielectric continuum was used to be a more simple expression for the contribution of  $\lambda_{\text{out}}$ . According to (17) equation, the value of  $\lambda_{\text{out}}$  depends on the donor-acceptor distance ( $r_{DA}$ ), the polarity of the solvent which is presented by the optical ( $\epsilon_{\text{op}}$ ) and static ( $\epsilon_s$ ) dielectric constants. Additionally,  $\lambda_{\text{out}}$  is also affected by the radii of the donor ( $a_D$ ) and acceptor ( $a_C$ ) which are

described as hard spheres. In general, the value of  $\lambda_{\text{out}}$  is minimal in a non-polar solvent, whereas it is quite significant in polar solvent for 0.5-1.0 eV.<sup>36</sup>

***Driving force ( $\Delta G^0$ )***

Driving force (or free energy change) is determined by the free energy required to reach the product state from the minimum of the reactant potential energy (Figure 1.5). An assumption is that the reaction coordinate does not change significantly in reaction exothermicity, the behavior of the two parabolas in Figure 1.6 leads to a remarkable and non-intuitive expectation. Marcus related the reorganisation energy to the activation free energy by equation (14). At the thermoneutral condition ( $\Delta G^0 = 0$ ), the kinetic barrier ( $\Delta G^\ddagger$ ) equals  $\lambda/4$  (Figure 1.6A). The barrier to electron transfer decreases from  $\lambda/4$  to zero as the reaction becomes more exothermic,  $\Delta G^0$  decreases, and rate constant of electron transfer increases as expected (Figure 1.6B; 6C). In Figure 1.6C,  $\Delta G^0 = -\lambda$  where the transition from reaction state to product state is barrierless ( $\Delta G^\ddagger = 0$ ). For more exothermic reaction ( $\Delta G^0 \ll 0$ ), the barrier starts increasing again (Figure 1.6D). Thus, the rate of electron transfer decreases with increasing driving force. This region is called the inverted region. Inverted region can be explained by nuclear tunneling effects.<sup>31</sup> The nuclear tunneling is a process to move the whole system from the reactant state to the product state in which does not require energy to surmount the barrier  $\Delta G^\ddagger$ . Therefore, the electron transfer is independent on the transition of  $\Delta G^\ddagger$ . The nuclear tunneling occurs preferentially at low temperature, where the smaller probability of the reaction system has enough energy to overcome the barrier. The nuclear tunneling effect can be neglected if the intersection point can be reached thermally and the frequencies of the vibrations are small ( $k_B T \gg h\omega$ ).

## Chapter 1. Background

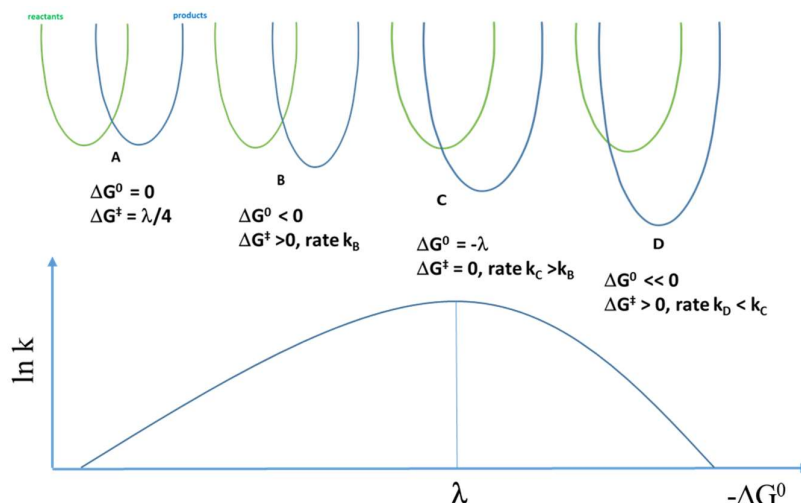


Figure 1.6. Illustration of the reactions regions of electron transfer is predicted by the Marcus theory. In the A-C regions, the rate of electron transfer increases as  $\Delta G^0$  decreases. In the inverted region (D), the rate of electron transfer decreases as it becomes more energetically favorable.

Although the inverted region was anticipated by the Marcus theory, it was hard to probe the inverted region in experiments. Until 1984, it was observed for the first time by G. Closs and J. Miller who designed and studied intramolecular electron transfer processes on series of donor-acceptor dyads.<sup>37-38</sup> A strategy to observe the inverted region required to avoid the problem of limited diffusion reaction. For this reason, G. Closs and J. Miller have chosen intramolecular processes to test the Marcus theory, in which diffusion is not required.

The driving force of electron transfer can be estimated from experimental data. The free energy changes for charge recombination ( $-\Delta G_{CR}$ ) and charge separation ( $-\Delta G_{CS}$ ) were estimated by using the Rehm-Weller approach, according to two equations (18-19):

$$-\Delta G_{CR} = e[E_{ox}^{1/2} - E_{red}^{1/2}] - \Delta G_s \quad (18)$$

$$-\Delta G_{CS} = E_{0,0} - (-\Delta G_{CR}) \quad (19)$$

$$\text{In which: } \Delta G_s = \frac{e^2}{4\pi\epsilon_0} \left[ \left( \frac{1}{2R_+} + \frac{1}{2R_-} \right) \Delta \left( \frac{1}{\epsilon_R} \right) - \frac{1}{R_{CC}\epsilon_R} \right]$$

Where  $\Delta G_s$  is the solvation energy,  $E_{OX}$  is the half-wave potential for one-electron oxidation of the electron-donor unit,  $E_{red}$  is the half-wave potential for one-electron reduction of the electron acceptor unit,  $E_{0,0}$  is the energy associated with the 0-0 optical transition (the midpoint of

absorption and emission corresponding to 0-0 transition). The symbols  $\epsilon_0$  and  $\epsilon_R$  refer to vacuum permittivity and dielectric constant of the employed solvent, respectively. The symbols  $R_+$  and  $R_-$  refer to radii of the radical cation and radical anion species, respectively.  $R_{CC}$  is the centre-to-centre distance.

### ***Electronic coupling ( $V_{DA}$ )***

The last parameter we will discuss is electronic coupling ( $V_{DA}$ ). The electronic coupling depends on the states of the donor, acceptor, and spatial distance ( $r_{DA}$ ), which is expressed in the equation (20).

$$V_{DA} = V_0 \exp\left(\frac{-\beta}{2} r_{DA}\right) \quad (20)$$

Where  $V_0$  is the coupling at the centre-to-centre distance of the donor and acceptor, limited by the radii of the donor and acceptor. The attenuation factor  $\beta$  depends on the system.

The electronic coupling is the essential parameter to understand the interaction between the donor and the acceptor. The origin of the electronic coupling is the orbital overlap between donor and acceptor. From the equation (13) and (20), the rate of electron transfer will fall rapidly with distance centre-to-centre of donor-acceptor.

It has to be emphasised that these discussions are valid for weakly electronic coupling, at high enough temperature, and when a classical theory of reaction coordinate is applicable. The small electronic coupling is satisfied for non-adiabatic conditions, when  $V_{DA} < k_B T$ .

### **1.4.2 Accumulative electron transfer**

The natural photosynthesis reactions require multiple charge transfers. Meanwhile, absorption of one photon only releases a single electron. Therefore, multiple charge separations created by sequential multi-photon absorptions are required.

Fundamentally, single electron transfer is well understood in various systems by Marcus Theory. However, multiple electron transfer processes may not have a full description yet. The

reactions of natural photosynthesis systems have been studied and are fairly well understood.<sup>39,40</sup> Today, efforts are towards fully understanding artificial photosynthesis systems, with the goal of duplicating the functional characteristics of natural photosynthesis.

Accumulative electron transfer is a vital process in the reactions, which occur in photocatalyst to split water or produce fuel. Stemming from the photosynthesis reaction, the concept of artificial photosynthesis has been defined and manipulated to store and use of solar energy as a solar fuel.

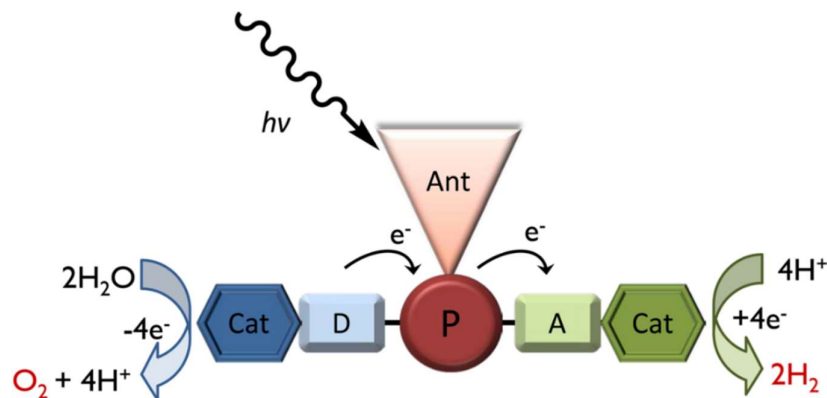


*Figure 1.7<sup>41</sup>. A schematic picture for artificial photosynthesis that converts solar energy into fuel by charge separation coupled to catalytic water oxidation and fuel production.*

Figure 1.7<sup>41</sup> shows a schematic picture of a molecular system for artificial photosynthesis. This system works based on the coupling of electrons and holes to catalysts for water oxidation and fuel production, via photoinduced charge separation in a donor-photosensitizer-acceptor (D-P-A). A full system has not yet been realized. Instead, the separate half-reaction of water oxidation or fuel production by addition of sacrificial agents (oxidants or reductants) to provide accumulative holes or electrons have been performed.<sup>42-45</sup> Using sacrificial donor or acceptor helps to complement redox equivalent for these reactions and avoid competing reactions as well. Therefore, this is not easy to replace the sacrificial agents in these half-reactions. However, using sacrificial agents are only of fundamental interest in studying half reactions.

To date, there are different techniques that have been performed to study charge accumulation in artificial photosynthesis systems, such as photo continuous irradiation or successive photoexcitation spectroscopies. However, the nature of charge accumulation processes in photosynthetic reactions are due to the sequential absorption of several photons. Therefore, studying accumulative electron transfer by sequential photon excitation is necessary

to understand deeply the mechanisms at work, which in turn will help to improve the efficiency of charge transfer processes.

There are many reports on P-A systems, which were shown to produce solar fuels, where the principle of charge accumulation in explaining the results have been invoked.<sup>42, 46-51</sup> However, there was no clear evidence for the formation of accumulative charge separation in those systems. Nevertheless, probing accumulative charge separation in a realistic photocatalytic system remains a challenge. Therefore, for fundamental studies of charge accumulation by using sequential photoexcitation, photosystems might involved catalyst molecules or model molecules, in which several potentials are provided.

#### ***1.4.2.1 Difficulties and solutions in accumulative electron transfer***

##### ***Difficulties***

From the scheme of Figure 1.7, some difficulties of charge accumulation can be pointed out immediately. Firstly, accumulative electron transfer on catalyst will be implemented by sequential absorption of several photons on the photosensitizer molecule. Therefore, an efficiency light-harvesting antenna is required to increase the probability of accumulation on catalyst molecule before charge recombination occurs. Secondly, the rate of water oxidation has to match that of fuel production. Thirdly, there is no separation between water oxidation and fuel production to separate oxygen and fuels. Using two half-reactions instead for the whole reaction can solve these two last difficulties.

In term of energy, there are other significant difficulties for the investigation of accumulative electron transfer. To accumulate charges on the catalyst, energetic requirements are sharper than for single electron transfer. Charge accumulation requires a narrow range of redox potentials for successive oxidising or reducing steps. The range of redox potentials may be compressed by delocalisation of charges on a large molecule. However, it also means an increase in difficulty to use them for coordinated multielectron catalysis.<sup>41</sup>

Figure 1.8 shows a schematic diagram of the reaction and state energy of a donor-photosensitizer-acceptor (D-P-A) triad under successive absorption of two photons.<sup>41, 52</sup> Accumulative charge transfer processes appear as new competing and wasted energetic reactions, which are not involved on the single electron level.<sup>42, 53</sup> This issue will be discussed in more details in the following part.

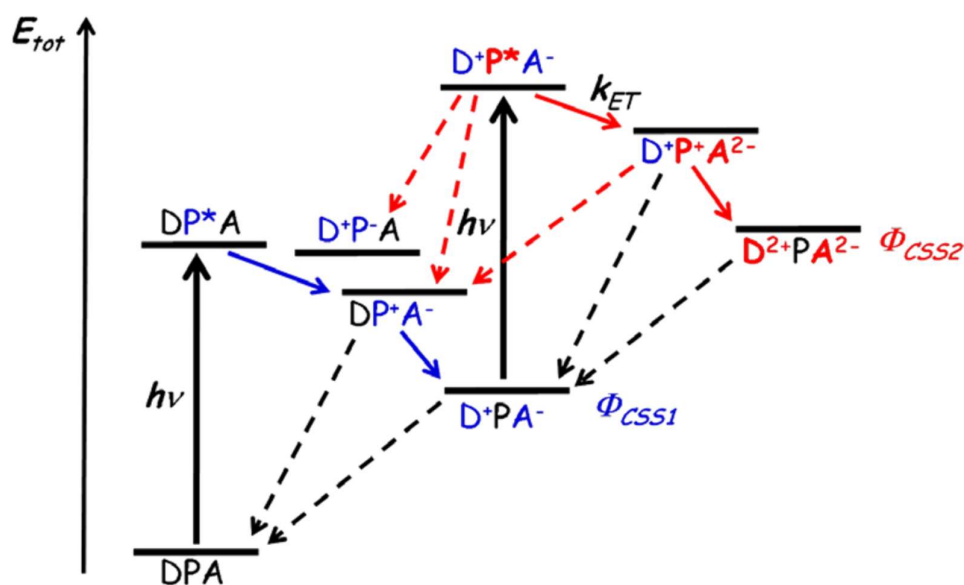


Figure 1.8<sup>41</sup> Schematic diagram of reaction and state energy of a donor-photosensitizer-acceptor (D-P-A) triad under absorbing two sequential photons. Solid arrows describe productive reaction; dash line arrows describe recombination reactions. Energy transfer reactions between  $P^*$  and D are not shown for clarity.

The left side of the diagram in Figure 1.8 describes the photoinduced processes of the first charge separated state (CSS1). In these steps, donor and acceptor should be chosen to have the charge separated state ( $D^+PA^-$ ) forming faster than that of charge recombination reactions. Furthermore, the excited state of photosensitizer should be lower than that of donor and acceptor to avoid energy transfer quenching. Under the second photon absorption, the double charge separated state ( $D^{2+}PA^{2-}$ ) is much more challenging to obtain.

The first difficulty is that the first charge separated states of donor and acceptor ( $D^+$  and  $A^-$ ) have relatively low excited states, and the photosensitizer excited state ( $P^*$ ) is usually both a strong reductant and oxidant. Therefore,  $P^*$  is likely to be quenched by either the oxidized state of the donor ( $D^+$ ) or reduced state of the acceptor ( $A^-$ ). These processes are presented in red dash arrows in Figure 1.8. These processes are named “reverse electron transfer” to distinguish it from the back electron transfer, which resets the system to the ground state by recombination of the electron and hole. Secondly, other unexpected processes, such as the intermediate states  $D^+P^+A^{2-}$  may recombine directly between the second reduced state of the acceptor ( $A^{2-}$ ) and  $D^+ / P^+$  states. Therefore, the electronic coupling between the different units has to be controlled. In overall, control of the second charge separated states yield ( $D^{2+}PA^{2-}$ ) is even more critical than the control efficiency of the first charge-separated state.

## Chapter 1. Background

A third difficulty is that the  $P^*$  may suffer from paramagnetic quenching by the presence of unpaired spin of  $D^+$  and  $A^-$ . The states of  $D^+$  and  $A^-$  can affect the rate of intersystem crossing,<sup>27</sup> resulting in competing with, or promoting, the formation of  $D^+P^+A^{2-}$ ,  $D^{2+}P^+A^{2-}$ , and  $D^{2+}PA^{2-}$ . Therefore, in the D-P-A system, unproductive energy transfer needs to be avoided for both the first charge separated state and the double charge-separated state.

Besides, the accumulation of charges will suffer from an electrostatic problem. The repulsion of the second same charge in one molecule explains why charge accumulation requires typically more energy than the first.<sup>54</sup>

### ***Solutions***

The difficulties discussed above arise from the accumulation of two separated charges. Solutions to solve the deleterious problems can be found in the design of molecular systems. In this part, some strategies are proposed to limit unproductive processes and promote the accumulation of charge separated state.

#### *Donor and acceptor choices*

The starting step in the design of a molecular system is the choice of donor and acceptor units. The donors or acceptors have to be able to donate or accept two or more electrons from the  $P^*$ . Therefore, an ideal donor and acceptor for studying charge accumulation should be able to oxidise or reduce in several narrow potential steps.

#### *Coupled electron transfers*

The Coulomb repulsion energy may be partially compensated in the case of electron transfer coupled to a structural rearrangement or charge compensation, such as proton transfer. These changes could also prevent back electron transfer from the separation state.

This strategy is examined in Photosystem II, where structural changes in the  $CaMn_4$  oxygen-evolving-complex upon oxidation can be related to the accumulation of four holes on this site within a narrow potential range.<sup>55</sup>

#### *Rapid Electron transfer in the initial step*

To limit the unproductive processes in Figure 1.8, a strategy is employed, which consists of a rapid electron transfer from  $D^+P^*A^-$  state to overcome the reverse electron transfer. In photosystem II, the initial charge transfer between  $P_{680}$  and the pheophytin (Pheo) is very rapid ( $\sim$ ps).

*Electronic decoupling of donor-acceptor*

Recombination mechanisms in the intermediate charge separated states are available. To limit these unproductive pathways, the electron and hole need to be decoupled. This requirement can be solved by increasing donor-acceptor distance or structural changes.

*Additional intermediate donors and acceptors*

In photosystem II, charge recombination is avoided by intermediate acceptors. An intermediate acceptor supports fast forward electron transfer and prevents recombination by reverse electron transfer. Additionally, a cascade electron transfer between different cofactors leads to an increase in the electron-hole distance, decreasing electronic coupling, so increasing the rate of electron transfer.

**1.4.2.2 The context of studying photoinduced the accumulative electron transfer**

The natural photosynthesis may be the most famous example of photoinduced accumulative charge transfer. To date, there are not many articles that describe photoinduced charge accumulation in an artificial system. Some of the most relevant examples of studying charge accumulations in both irreversible and reversible systems will be presented in this section.

First, Brewer and co-workers have presented the formation of double charge accumulation in Ru-Ir-Ru and Ru-Rh-Ru systems in the presence of a sacrificial electron donor under irradiation.<sup>53, 56</sup> They succeeded in reducing Rh<sup>III</sup> to Rh<sup>I</sup> by using continuous irradiation experiment. These systems have been used to study photocatalytic hydrogen production.<sup>44</sup>

L. Hammarstrom, S. String and co-workers have reported the hole accumulation in a Ru-Mn<sub>2</sub> dyad. Under the excitation of the Ru moiety in the presence of a sacrificial acceptor, they indicated the hole accumulation on the Mn-site.<sup>57</sup>

From 2002, F. MacDonnell team worked on dinuclear Ru-complexes, in which the ligand is reduced in four separate steps in the presence of a triethylamine sacrificial donor.<sup>44, 58</sup> Under the irradiation, the electrons were accumulated at the bridging ligand. When studying in aqueous media, they observed proton-coupled electron transfer processes.

Another example was presented by A. Harriman, F. Odobel and co-workers about a system in which multiporphyrinic clusters were covalently attached to a polyoxometalate (POM).<sup>59</sup> The charge accumulation takes place on the POM under irradiation in the presence of a sacrificial electron donor.

## Chapter 1. Background

In the literature, there are also examples of studying charge accumulation that has not worked. However, those studies supported to identify and understand the unproductive processes that prevented the accumulation charge transfer. For example, M. Borgstrom and co-workers have reported a zero charge separation efficiency for the second electron transfer step in a Ru(II)-Ru(II)-PI (PI = pyromellitimide) triad under two successive photoexcitations.<sup>60</sup>

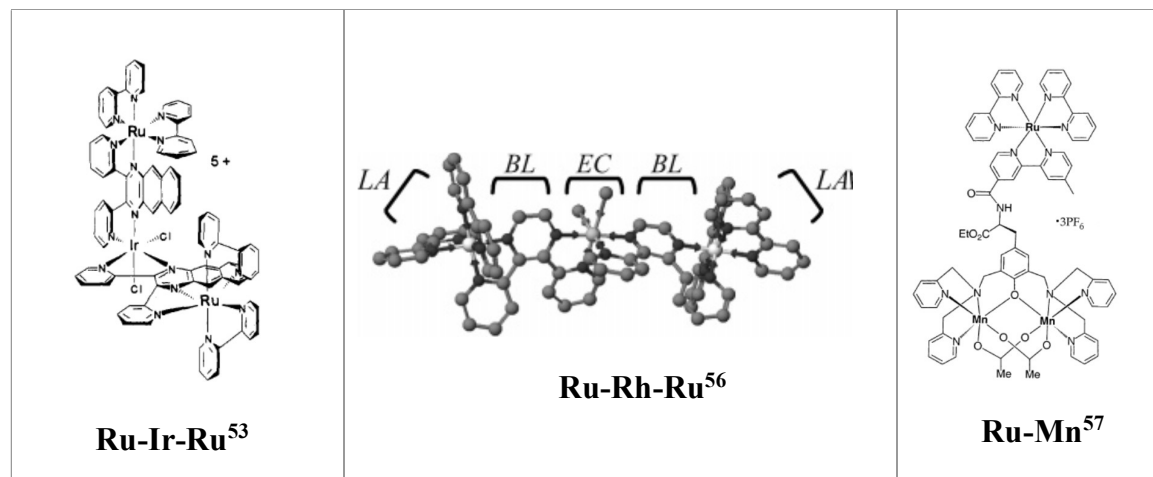
In 2015, The LCI team reported the study of two successive photoinduced electron transfer in a Ru-Fe system in the presence of an irreversible electron acceptor.<sup>61</sup> This system comprises a  $[\text{Ru}(\text{bpy})_3]^{2+}$  chromophore covalently linked to a  $\text{Fe}^{\text{II}}(\text{OH}_2)$  catalyst. The first charge separated state was identified by nanosecond transient absorption spectroscopy. For the double oxidation species,  $\text{Ru}^{\text{II}}-\text{Fe}^{\text{IV}}$  was obtained by studying the ESI (electrospray ionization) mass spectroscopy and UV-visible spectroscopy.

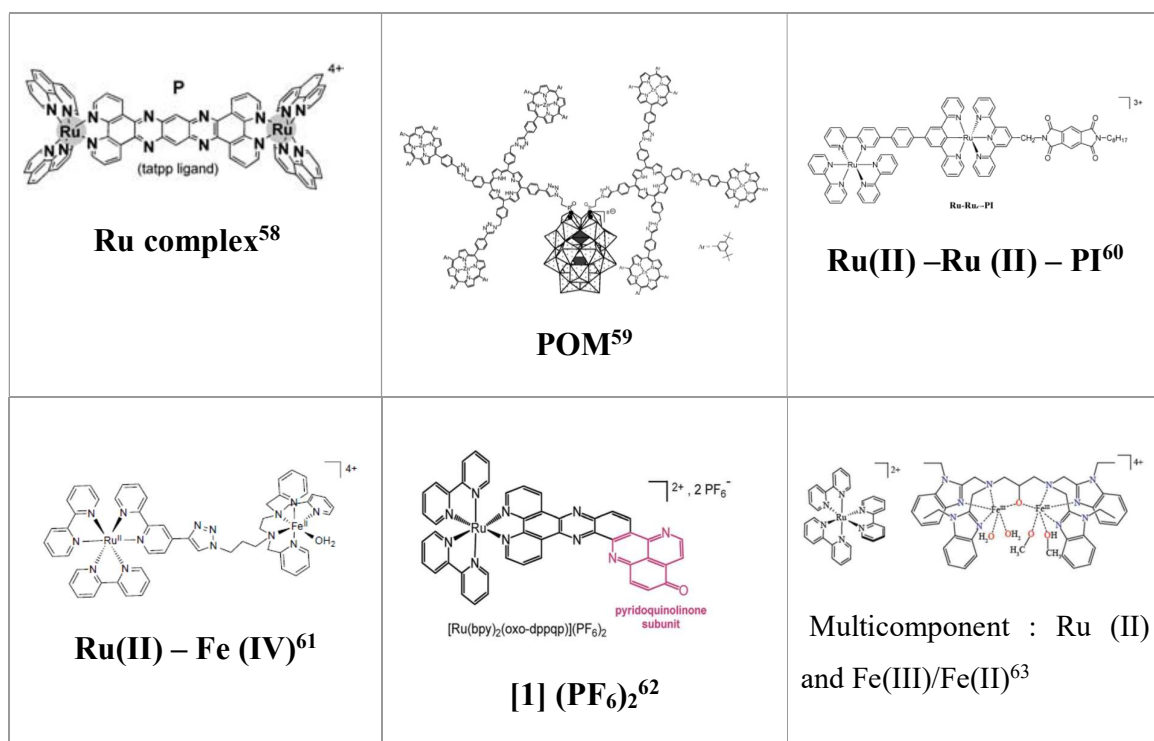
Recently, Chavarot-Kerlidou et al.<sup>62</sup> have presented charge accumulation, couple to protonation, on a fuse dipyridophenazine-pyridoquinolinone ligand (denoted as  $[1](\text{PF}_6)_2$ ) using visible-light irradiation in the presence of a sacrificial electron donor. Electron storage sites are indicated to locate on the p-extend ligand by the combination of resonance Raman and EPR spectroscopies with DFT calculation.

D. Moonshiram and co-workers have reported a time-resolved X-ray absorption spectroscopy investigation in the ns- $\mu\text{s}$  time scale to monitor the light-induced two electron transfer in a multicomponent photocatalytic system.<sup>63</sup> This system includes a chromophore  $[\text{Ru}(\text{bpy})_3]^{2+}$ , a dimer of Fe(III)/Fe(II), in the presence of a sacrificial electron donor, triethylamine.

Table 1.1 presents the structures of those molecules, which are mentioned above.

Table 1.1. Chemical structures of referent molecules





O.S. Wenger's team developed a triad that is shown in Figure 1.9.<sup>64</sup> The authors managed to accumulate two negative charges on one NDI (naphthalene diimide) unit in a triad with two chromophores  $[\text{Ru}(\text{bpy})_3]^{2+}$ , under continuous irradiation of light and in the presence of an irreversible electron donor.

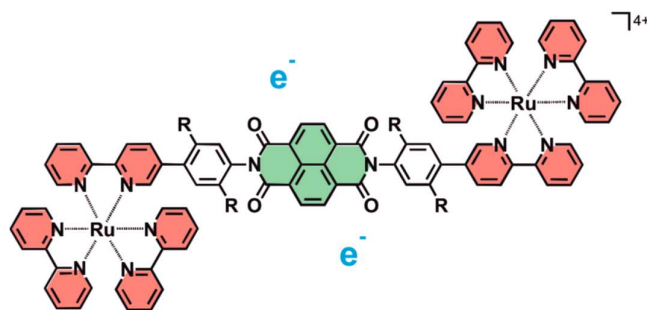
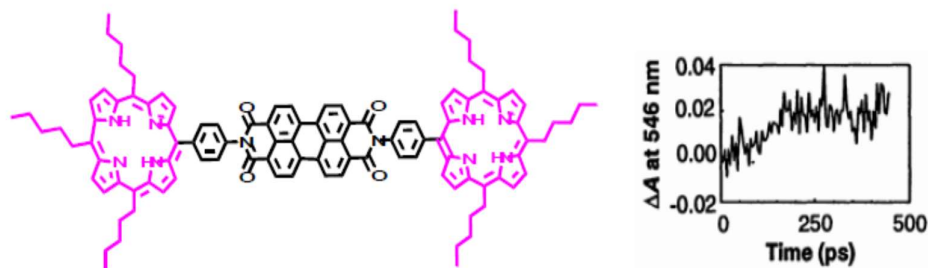


Figure 1. 9<sup>64</sup> Structure of the triad  $[\text{Ru}(\text{bpy})_3]^{2+}$ -NDI- $[\text{Ru}(\text{bpy})_3]^{2+}$

Unfortunately, using transient absorption experiment, they were not able to detect the formation of the doubly reduced  $\text{NDI}^{2-}$  species.

The few examples of studies carried out on the accumulation of two charge separations by photoinduced electron transfer in the reversible system will be described below.

The first relevant example was presented by Wasielewski's team in 1992. This system is shown in Figure 1.10.<sup>65</sup> This system was composed of two porphyrin chromophores (H<sub>2</sub>P) covalently bound to the two electron acceptor unit (PBDCI). In this system, porphyrin was excited with subpicosecond laser pulses, resulting in the formation of single or double reduced acceptors depending on the light intensity. The monitoring of the charge accumulated state has been made by transient absorption. This technique saw that double charge separation recombined in about 5ns.



*Figure 1.10. Structure of porphyrin-PDI-porphyrin system<sup>65</sup>*

A few years later, Zhang investigated multiple photoinduced electron transfers in a D<sub>n</sub>-A complex. These systems include several electron donors, phthalocyanines, bound to the surface of a carbon nanotube acceptor.<sup>66-67</sup> D<sub>n</sub> (amino-phthalocyanines) can transfer multiple electrons to the carbon nanotube to create (D<sup>•+</sup>)<sub>n</sub>-A<sup>n•-</sup> as demonstrated by nanosecond laser flash photolysis. Thanks to the study of a model quite different from conventional systems comprising a donor and an acceptor, the researchers were able to reveal the existence of different types of photo-induced electron transfers.

Currently, the most prolific group in the field of the accumulation charge separated states is Wenger's team. They studied different pentads, DP<sub>2</sub>A<sub>2</sub> or D<sub>2</sub>P<sub>2</sub>A, for the accumulation of two photoinduced charge separations. The first system is illustrated in Figure 1.11. It was composed of two anthraquinone electron acceptors (AQ), each was connected to a chromophore [Ru(bpy)<sub>3</sub>]<sup>2+</sup>, and these two chromophores were linked to an electron donor (OTA).<sup>68</sup>

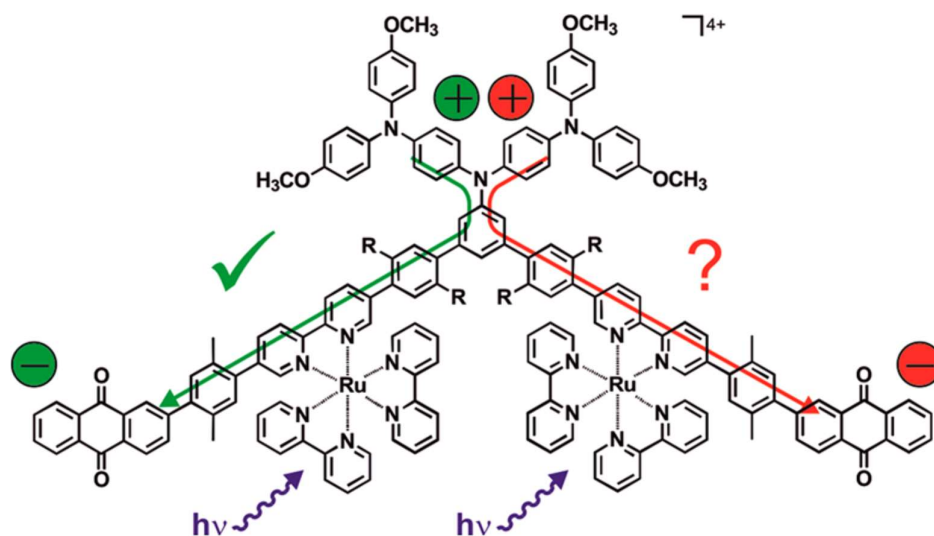


Figure 1.11. Chemical structure of the Anthraquinone- $[Ru(bpy)_3]^{2+}$ -Oligotriarylamine- $[Ru(bpy)_3]^{2+}$ -Anthraquinone<sup>68</sup>

The purpose of studying this molecule is the accumulation of two positive charges at OTA placed by photoexcitation of both  $[Ru(bpy)_3]^{2+}$  units, through reducing two AQ units. However, the signal, which can be attributed to the formation of the double oxidised of  $OTA^{2+}$  was not enough to be sure that it corresponded to this species. It was also impossible to follow its temporal evolution and to establish the kinetics of formation and disappearance of  $OTA^{2+}$ .

The Wenger's team also developed another system based on the pentad model and with the same subunits, it is shown in Figure 1.12.<sup>69-70</sup> Each electron donors amines are connected to one of the two chromophores  $[Ru(bpy)_3]^{2+}$ , they are covalently linked to an electron acceptor, an anthraquinone. This linear arrangement aims to force the two photoinduced electron transfer of each amine to the centre where the electron acceptor is located. The studies were carried out by infrared and UV-visible spectroscopies. A long-lived charge separation state was detected ( $TAA^+-Ru-AQ^{2-}-Ru-TAA^+$ ) where two electrons were accumulated on the anthraquinone AQ. The addition of an acid in the medium made a possible to protonate the  $AQ^{2-}$  to  $AQH_2$ .

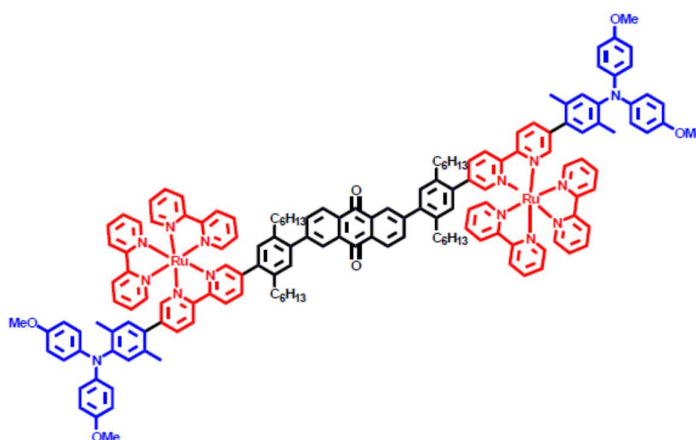


Figure 1.12. Chemical structure of the Triarylamine-[Ru(bpy)<sub>3</sub>]<sup>2+</sup>-Anthraquinone-[Ru(bpy)<sub>3</sub>]<sup>2+</sup>-Triarylamine<sup>69</sup>

Recently, Wenger's team has also reported photoinduced multielectron transfer and accumulation on a molecular heptad. The molecular structure is composed of four donors (TAA), two photosensitizers (Ru(bpy)<sub>3</sub><sup>2+</sup>), and one acceptor (PhSSPh), and is described in Figure 1.13.<sup>71</sup>

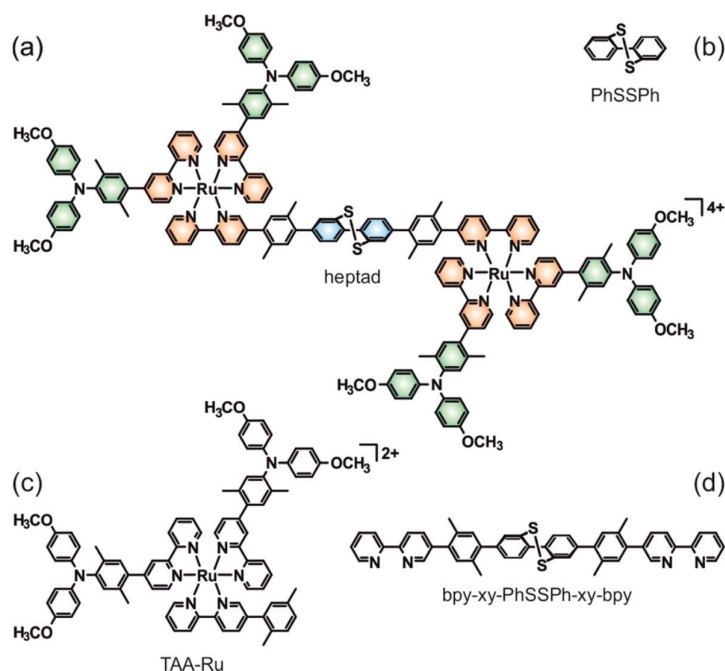


Figure 1.13. Chemical structure of the Heptad and its reference compounds<sup>71</sup>

## Chapter 1. Background

A two-electron reduced state of PhSSPh was obtained under simultaneous excitation of the two  $[\text{Ru}(\text{bpy})_3]^{2+}$ . The lifetime of the charge-accumulated state is 66ns, and the quantum yield for the formation of this double charge-separated state was 0.5%. These two systems above allowed studying multiple electron transfer without the use of a sacrificial electron donor.

All the examples cited above use several chromophores to induce the accumulation of two charges. There are only a few examples of studying charge accumulation using sequential nanosecond photon excitations of the same chromophore. Hammarstrom and Odobel teams developed the first system. A hybrid system comprises of an oligo (triarylamine) as an electron donor, connected to a chromophore  $[\text{Ru}(\text{bpy})_3(\text{CN})_2]^{2+}$ , and anchored onto titanium dioxide nanoparticle surface which serves as a good electron acceptor. This system is shown in Figure 1.14.<sup>72</sup>

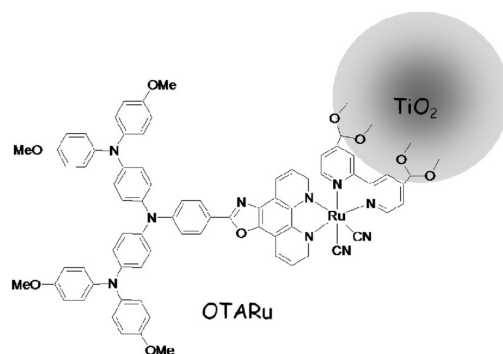


Figure 1.14<sup>72</sup>. Scheme of Oligotriarylamine- $[\text{Ru}(\text{bpy})_3(\text{CN})_2]^{2+}$ - $\text{TiO}_2$

The charge accumulation of this system was observed by the pump-pump-probe transient absorption technique. The species of double charge separation,  $\text{OTA}^{2+}\text{-Ru-TiO}_2^{2-}$ , was formed with an overall yield of about 10%. Without using a sacrificial agent, this is the first system comprising a single chromophore that allowed two charge separations by successive absorption of two photons.

The second example was implemented by our team. A dyad system comprised a naphthalene diimide (NDI) linked to a  $[\text{Ru}(\text{bpy})_3]^{2+}$  was studied using sequential nanosecond excitation in the presence of a reversible electron donor.<sup>73</sup> Figure 1.15 describes the molecular structure of the dyad system. This system indicated an unprecedented long-lived charge accumulative on NDI moiety (200  $\mu\text{s}$ ).

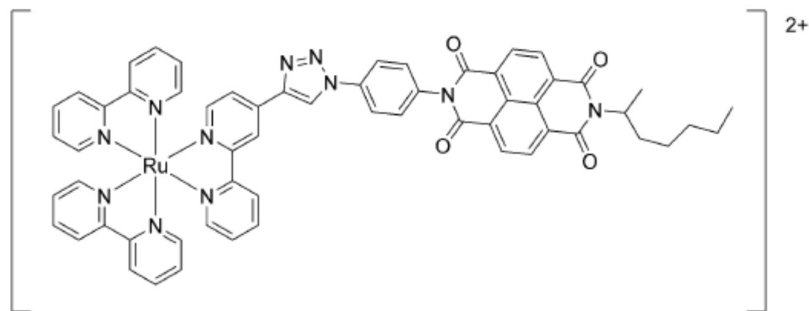


Figure 1.15.<sup>73</sup> Molecular structure of dyad  $[Ru(bpy)_3]^{2+}$ -NDI

These are two typical examples of studying light-induced charge accumulation by using sequential laser excitation transient absorption. A more recent example using this technique was reported by our team. It will be presented as a part of the thesis in chapter 4.

## REFERENCES

1. EIA, U. *Energy Information Administration. International Energy Outlook 2016 with Projections to 2040*; DOE/EIA-0484: 2016.
2. Van der Hoeven, M., *World energy outlook 2012. International Energy Agency: Tokyo, Japan 2013.*
3. Lewis, N. S.; Nocera, D. G., Powering the planet: Chemical challenges in solar energy utilization. *Proceedings of the National Academy of Sciences*. **2006**, *103* (43), 15729-15735.
4. Concepcion, J. J.; House, R. L.; Papanikolas, J. M.; Meyer, T. J., Chemical approaches to artificial photosynthesis. *Proceedings of the National Academy of Sciences*. **2012**, *109* (39), 15560-15564.
5. Ager, J. W.; Shaner, M. R.; Walczak, K. A.; Sharp, I. D.; Ardo, S., Experimental demonstrations of spontaneous, solar-driven photoelectrochemical water splitting. *Energy & Environmental Science* **2015**, *8* (10), 2811-2824.
6. Schmidt-Mende, L.; Weickert, J., *Organic and hybrid solar cells: an introduction*. Walter de Gruyter GmbH & Co KG: 2016.
7. Chiang, C. K.; Fincher Jr, C.; Park, Y. W.; Heeger, A. J.; Shirakawa, H.; Louis, E. J.; Gau, S. C.; MacDiarmid, A. G., Electrical conductivity in doped polyacetylene. *Physical review letters* **1977**, *39* (17), 1098.
8. Meng, L.; Zhang, Y.; Wan, X.; Li, C.; Zhang, X.; Wang, Y.; Ke, X.; Xiao, Z.; Ding, L.; Xia, R., Organic and solution-processed tandem solar cells with 17.3% efficiency. *Science* **2018**, *361* (6407), 1094-1098.

## Chapter 1. Background

9. Gregg, B. A., Excitonic solar cells. ACS Publications: 2003.
10. Dyakonov, V.; Frankevich, E., On the role played by polaron pairs in photophysical processes in semiconducting polymers. *Chemical Physics* **1998**, *227* (1-2), 203-217.
11. Scharber, M.; Schultz, N.; Sariciftci, N.; Brabec, C., Optical-and photocurrent-detected magnetic resonance studies on conjugated polymer/fullerene composites. *Physical Review B* **2003**, *67* (8), 085202.
12. Veldman, D.; Ipek, O.; Meskers, S. C.; Sweelssen, J. r.; Koetse, M. M.; Veenstra, S. C.; Kroon, J. M.; van Bavel, S. S.; Loos, J.; Janssen, R. A., Compositional and electric field dependence of the dissociation of charge transfer excitons in alternating polyfluorene copolymer/fullerene blends. *Journal of the American Chemical Society* **2008**, *130* (24), 7721-7735.
13. Obondi, C. O.; Lim, G. N.; Karr, P. A.; Nesterov, V. N.; D'Souza, F., Photoinduced charge separation in wide-band capturing, multi-modular bis (donor styryl) BODIPY–fullerene systems. *Physical Chemistry Chemical Physics* **2016**, *18* (27), 18187-18200.
14. Morteani, A. C.; Sreearunothai, P.; Herz, L. M.; Friend, R. H.; Silva, C., Exciton regeneration at polymeric semiconductor heterojunctions. *Physical review letters* **2004**, *92* (24), 247402.
15. Westenhoff, S.; Howard, I. A.; Hodgkiss, J. M.; Kirov, K. R.; Bronstein, H. A.; Williams, C. K.; Greenham, N. C.; Friend, R. H., Charge recombination in organic photovoltaic devices with high open-circuit voltages. *Journal of the American Chemical Society* **2008**, *130* (41), 13653-13658.
16. Šesták, Z., Blankenship, RE: Molecular Mechanisms of Photosynthesis. *Photosynthetica* **2002**, *40* (1), 12-12.
17. Satoh, K.; Wydrzynski, T. J., Introduction to photosystem II. In *Photosystem II*, Springer: 2005; pp 11-22.
18. Lubitz, W.; Reijerse, E. J.; Messinger, J., Solar water-splitting into H<sub>2</sub> and O<sub>2</sub>: design principles of photosystem II and hydrogenases. *Energy & Environmental Science* **2008**, *1* (1), 15-31.
19. Barber, J.; Nield, J.; Morris, E. P.; Zheleva, D.; Hankamer, B., The structure, function and dynamics of photosystem two. *Physiologia Plantarum* **1997**, *100* (4), 817-827.
20. Govindjee; Kern, J. F; Messinger, J.; and Whitmarsh, (2010) Photosystem II. In: Encyclopedia of Life Sciences (ELS).
21. Haumann, M.; Liebisch, P.; Müller, C.; Barra, M.; Grabolle, M.; Dau, H., Photosynthetic Formation Tracked by Time-Resolved X-ray Experiments. *Science* **2005**, *310* (5750), 1019-1021.
22. Harriman, A.; Pickering, I. J.; Thomas, J. M.; Christensen, P. A., Metal oxides as heterogeneous catalysts for oxygen evolution under photochemical conditions. *Journal of the Chemical Society, Faraday Transactions 1: Physical Chemistry in Condensed Phases* **1988**, *84* (8), 2795-2806.
23. Puntoriero, F.; La Ganga, G.; Sartorel, A.; Carraro, M.; Scorrano, G.; Bonchio, M.; Campagna, S., Photo-induced water oxidation with tetra-nuclear ruthenium sensitizer and catalyst: A unique 4× 4 ruthenium interplay triggering high efficiency with low-energy visible light. *Chemical Communications* **2010**, *46* (26), 4725-4727.

## Chapter 1. Background

24. Pellegrin, Y.; Odobel, F., Molecular devices featuring sequential photoinduced charge separations for the storage of multiple redox equivalents. *Coordination Chemistry Reviews*. **2011**, 255 (21), 2578-2593.
25. Tamaki, Y.; Ishitani, O., ACS Catal. 2017, 7, 3394. *Crossref, CAS*.
26. Valeur, B.; Berberan-Santos, M., Molecular fluorescence: principles and applications, 2012. John Wiley & Sons.
27. Turro, N. J.; Ramamurthy, V.; Ramamurthy, V.; Scaiano, J. C., *Principles of molecular photochemistry: an introduction*. University science books: 2009.
28. Hudhomme, P.; Williams, R. M., Energy and electron transfer in photo-and electro-active fullerene dyads. In *Handbook of Carbon Nano Materials: (In 2 Volumes) Volume 1: Synthesis and Supramolecular Systems Volume 2: Electron Transfer and Applications*, 2011; pp 545-591.
29. Förster, T., 10th Spiers Memorial Lecture. Transfer mechanisms of electronic excitation. *Discussions of the Faraday Society* **1959**, 27, 7-17.
30. Lakwicz, J., Principles of Fluorescence Spectroscopy, 2006. Springer Science+ Business Media, LLC.
31. Marcus, R. A.; Sutin, N., Electron transfers in chemistry and biology. *Biochimica et Biophysica Acta (BBA) - Biomembranes*. **1985**, 811 (3), 265-322.
32. Marcus, R. A., On the theory of oxidation-reduction reactions involving electron transfer. I. *The Journal of Chemical Physics* **1956**, 24 (5), 966-978.
33. Marcus, R. A., Chemical and electrochemical electron-transfer theory. *Annual review of physical chemistry* **1964**, 15 (1), 155-196.
34. Barbara, P. F.; Meyer, T. J.; Ratner, M. A., Contemporary issues in electron transfer research. *The Journal of Physical Chemistry* **1996**, 100 (31), 13148-13168.
35. Ebeling, W.; Sokolov, I. M., *Statistical thermodynamics and stochastic theory of nonequilibrium systems*. World Scientific: 2005; Vol. 8.
36. Bolton, J. R.; Mataga, N.; McLendon, G., *Electron transfer in inorganic, organic, and biological systems*. ACS Publications: 1991; Vol. 228.
37. Miller, J. R.; Calcaterra, L.; Closs, G., Intramolecular long-distance electron transfer in radical anions. The effects of free energy and solvent on the reaction rates. *Journal of the American Chemical Society* **1984**, 106 (10), 3047-3049.
38. Closs, G. L.; Miller, J. R., *Science* **1988**, 240, 440.
39. Šesták, Z., Ke, B.: Photosynthesis. Photobiochemistry and Photobiophysics. *Photosynthetica* **2002**, 40 (2), 278-278.
40. Krauss, N.; Hinrichs, W.; Witt, I.; Fromme, P.; Pritzkow, W.; Dauter, Z.; Betzel, C.; Wilson, K. S.; Witt, H. T.; Saenger, W., Three-dimensional structure of system I of photosynthesis at 6 Å resolution. *Nature* **1993**, 361 (6410), 326-331.

## Chapter 1. Background

41. Hammarström, L., Accumulative Charge Separation for Solar Fuels Production: Coupling Light-Induced Single Electron Transfer to Multielectron Catalysis. *Accounts of Chemical Research*. **2015**, *48* (3), 840-850.
42. Esswein, A. J.; Nocera, D. G., Hydrogen production by molecular photocatalysis. *Chemical reviews* **2007**, *107* (10), 4022-4047.
43. Huang, P.; Magnuson, A.; Lomoth, R.; Abrahamsson, M.; Tamm, M.; Sun, L.; van Rotterdam, B.; Park, J.; Hammarström, L.; Åkermark, B.; Styring, S., Photo-induced oxidation of a dinuclear Mn<sup>II</sup>,II complex to the Mn<sup>III</sup>,IV state by inter- and intramolecular electron transfer to Ru<sup>III</sup>tris-bipyridine. *Journal of Inorganic Biochemistry* **2002**, *91* (1), 159-172.
44. Konduri, R.; de Tacconi, N. R.; Rajeshwar, K.; MacDonnell, F. M., Multielectron Photoreduction of a Bridged Ruthenium Dimer, [(phen)<sub>2</sub>Ru(tatpp)Ru(phen)<sub>2</sub>][PF<sub>6</sub>]<sub>4</sub>: Aqueous Reactivity and Chemical and Spectroelectrochemical Identification of the Photoproducts. *Journal of the American Chemical Society*. **2004**, *126* (37), 11621-11629.
45. Elvington, M.; Brown, J.; Arachchige, S. M.; Brewer, K. J., Photocatalytic Hydrogen Production from Water Employing A Ru, Rh, Ru Molecular Device for Photoinitiated Electron Collection. *Journal of the American Chemical Society* **2007**, *129* (35), 10644-10645.
46. Concepcion, J. J.; Jurss, J. W.; Brennaman, M. K.; Hoertz, P. G.; Patrocinio, A. O. T.; Murakami Iha, N. Y.; Templeton, J. L.; Meyer, T. J., Making Oxygen with Ruthenium Complexes. *Accounts of Chemical Research*. **2009**, *42* (12), 1954-1965.
47. Brimblecombe, R.; Swiegers, G. F.; Dismukes, G. C.; Spiccia, L., Sustained Water Oxidation Photocatalysis by a Bioinspired Manganese Cluster. *Angewandte Chemie International Edition* **2008**, *47* (38), 7335-7338.
48. Cape, J. L.; Hurst, J. K., Detection and Mechanistic Relevance of Transient Ligand Radicals Formed during [Ru(bpy)<sub>2</sub>(OH<sub>2</sub>)<sub>2</sub>O<sub>4</sub><sup>+</sup>]-Catalyzed Water Oxidation. *Journal of the American Chemical Society* **2008**, *130* (3), 827-829.
49. Geletii, Y. V.; Huang, Z.; Hou, Y.; Musaev, D. G.; Lian, T.; Hill, C. L., Homogeneous light-driven water oxidation catalyzed by a tetraruthenium complex with all inorganic ligands. *Journal of the American Chemical Society* **2009**, *131* (22), 7522-7523.
50. Yamazaki, Y.; Takeda, H.; Ishitani, O., Photocatalytic reduction of CO<sub>2</sub> using metal complexes. *Journal of Photochemistry and Photobiology C: Photochemistry Reviews*. **2015**, *25*, 106-137.
51. Tamaki, Y.; Ishitani, O., Supramolecular photocatalysts for the reduction of CO<sub>2</sub>. *ACS Catalysis* **2017**, *7* (5), 3394-3409.
52. Karlsson, S.; Boixel, J.; Pellegrin, Y.; Blart, E.; Becker, H.-C.; Odobel, F.; Hammarstrom, L., Accumulative electron transfer: Multiple charge separation in artificial photosynthesis. *Faraday Discussions* **2012**, *155* (0), 233-252.
53. Molnar, S. M.; Nallas, G.; Bridgewater, J. S.; Brewer, K. J., Photoinitiated Electron Collection in a Mixed-Metal Trimetallic Complex of the Form {[ (bpy) <sub>2</sub>Ru (dpb) ] <sub>2</sub>IrCl<sub>2</sub>} (PF<sub>6</sub>) <sub>5</sub> (bpy= 2, 2'-

## Chapter 1. Background

Bipyridine and dpb= 2, 3-Bis (2-pyridyl) benzoquinoxaline). *Journal of the American Chemical Society* **1994**, *116* (12), 5206-5210.

54. Evans, D. H., One-electron and two-electron transfers in electrochemistry and homogeneous solution reactions. *Chemical reviews* **2008**, *108* (7), 2113-2144.
55. Lancaster, R.; Parson, W.; Fromme, P.; Setif, P.; Zouni, A.; Messinger, J.; Vermeglio, A.; Peschek, G. A.; Cramer, W.; Junge, W., *Primary Processes of Photosynthesis, Part 2: Principles and Apparatus*. Royal Society of Chemistry: 2007.
56. Elvington, M.; Brewer, K. J., Photoinitiated electron collection at a metal in a rhodium-centered mixed-metal supramolecular complex. *Inorganic chemistry* **2006**, *45* (14), 5242-5244.
57. Sun, L.; Raymond, M. K.; Magnuson, A.; LeGourriérec, D.; Tamm, M.; Abrahamsson, M.; Huang Kenéz, P.; Mårtensson, J.; Stenhagen, G.; Hammarström, L.; Styring, S.; Åkermark, B., Towards an artificial model for Photosystem II: a manganese(II,II) dimer covalently linked to ruthenium(II) tris-bipyridine via a tyrosine derivative | Preliminary accounts of this work have been presented as invited lectures at: EUCHEM Conference, Artificial Photosynthesis, May 1998, Sigtuna, Sweden; Fourth Nordic Congress on Photosynthesis, Nov. 1998, Naantali, Finland; EBEC, July 1998, Göteborg, Sweden. *Journal of Inorganic Biochemistry* **2000**, *78* (1), 15-22.
58. de Tacconi, N. R.; Lezna, R. O.; Konduri, R.; Ongeri, F.; Rajeshwar, K.; MacDonnell, F. M., Influence of pH on the Photochemical and Electrochemical Reduction of the Dinuclear Ruthenium Complex, [(phen)<sub>2</sub>Ru(tatpp)Ru(phen)<sub>2</sub>]Cl<sub>4</sub>, in Water: Proton-Coupled Sequential and Concerted Multi-Electron Reduction. *Chemistry – A European Journal* **2005**, *11* (15), 4327-4339.
59. Elliott, K. J.; Harriman, A.; Le Pleux, L.; Pellegrin, Y.; Blart, E.; Mayer, C. R.; Odobel, F., A porphyrin-polyoxometallate bio-inspired mimic for artificial photosynthesis. *Physical Chemistry Chemical Physics*. **2009**, *11* (39), 8767-8773.
60. Borgström, M.; Ott, S.; Lomoth, R.; Bergquist, J.; Hammarström, L.; Johansson, O., Photoinduced Energy Transfer Coupled to Charge Separation in a Ru(II)–Ru(II)–Acceptor Triad. *Inorganic Chemistry* **2006**, *45* (12), 4820-4829.
61. Herrero, C.; Quaranta, A.; Sircoglou, M.; Senechal-David, K.; Baron, A.; Marin, I. M.; Buron, C.; Baltaze, J.-P.; Leibl, W.; Aukauloo, A.; Banse, F., Successive light-induced two electron transfers in a Ru-Fe supramolecular assembly: from Ru-Fe(II)-OH<sub>2</sub> to Ru-Fe(IV)-oxo. *Chemical science*. **2015**, *6* (4), 2323-2327.
62. Lefebvre, J.-F.; Schindler, J.; Traber, P.; Zhang, Y.; Kupfer, S.; Gräfe, S.; Baussanne, I.; Demeunynck, M.; Mouesca, J.-M.; Gambarelli, S.; Artero, V.; Dietzek, B.; Chavarot-Kerlidou, M., An artificial photosynthetic system for photoaccumulation of two electrons on a fused dipyridophenazine (dppz)–pyridoquinolinone ligand. *Chemical Science* **2018**, *9* (17), 4152-4159.
63. Moonshiram, D.; Picon, A.; Vazquez-Mayagoitia, A.; Zhang, X.; Tu, M.-F.; Garrido-Barros, P.; Mahy, J.-P.; Avenier, F.; Aukauloo, A., Elucidating light-induced charge accumulation in an artificial

## Chapter 1. Background

analogue of methane monooxygenase enzymes using time-resolved X-ray absorption spectroscopy. *Chemical Communications* **2017**, 53 (18), 2725-2728.

64. Skaisgirski, M.; Guo, X.; Wenger, O. S., Electron Accumulation on Naphthalene Diimide Photosensitized by [Ru(2,2'-Bipyridine)<sub>3</sub>]<sup>2+</sup>. *Inorganic Chemistry*. **2017**, 56 (5), 2432-2439.

65. O'Neil, M. P.; Niemczyk, M. P.; Svec, W. A.; Gosztola, D.; Gaines, G. L.; Wasielewski, M. R., Picosecond Optical Switching Based on Biphotonic Excitation of an Electron Donor-Acceptor-Donor Molecule. *Science* **1992**, 257 (5066), 63-65.

66. Zhang, X.-F.; Cui, X.; Liu, Q.; Zhang, F., Multiple-Charge Separation in Nanoscale Artificial Photosynthetic Models. *ChemPhysChem* **2008**, 9 (11), 1514-1518.

67. Zhang, X.-F.; Cui, X.; Liu, Q.; Zhang, F., Photoinduced multi-electron transfer in the Dn-A system consisting of multi-phthalocyanines linked to one carbon nanotube. *Physical Chemistry Chemical Physics* **2009**, 11 (18), 3566-3572.

68. Bonn, A. G.; Yushchenko, O.; Vauthey, E.; Wenger, O. S., Photoinduced Electron Transfer in an Anthraquinone-[Ru(bpy)<sub>3</sub>]<sup>2+</sup>-Oligotriarylamine-[Ru(bpy)<sub>3</sub>]<sup>2+</sup>-Anthraquinone Pentad. *Inorganic Chemistry* **2016**, 55 (6), 2894-2899.

69. Oraziatti, M.; Kuss-Petermann, M.; Hamm, P.; Wenger, O. S., Light-Driven Electron Accumulation in a Molecular Pentad. *Angewandte Chemie International Edition*. **2016**, 55 (32), 9407-9410.

70. Kuss-Petermann, M.; Oraziatti, M.; Neuburger, M.; Hamm, P.; Wenger, O. S., Intramolecular Light-Driven Accumulation of Reduction Equivalents by Proton-Coupled Electron Transfer. *Journal of the American Chemical Society*. **2017**, 139 (14), 5225-5232.

71. Nomrowski, J.; Wenger, O. S., Exploiting Potential Inversion for Photoinduced Multielectron Transfer and Accumulation of Redox Equivalents in a Molecular Heptad. *Journal of the American Chemical Society*. **2018**, 140 (16), 5343-5346.

72. Karlsson, S.; Boixel, J.; Pellegrin, Y.; Blart, E.; Becker, H.-C.; Odobel, F.; Hammarström, L., Accumulative Charge Separation Inspired by Photosynthesis. *Journal of the American Chemical Society*. **2010**, 132 (51), 17977-17979.

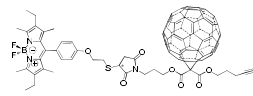
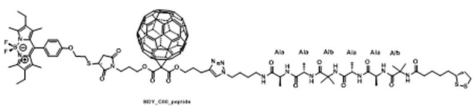
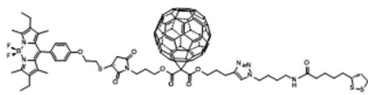
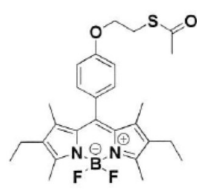
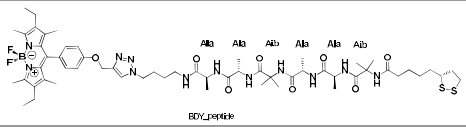
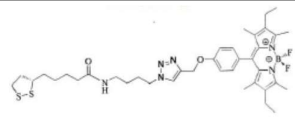
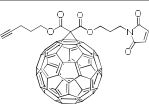
73. Mendes Marinho, S.; Ha-Thi, M.-H.; Pham, V.-T.; Quaranta, A.; Pino, T.; Lefumeux, C.; Chamaille, T.; Leibl, W.; Aukauloo, A., Time-resolved interception of multiple charge accumulation in a sensitizer-acceptor dyad. *Angewandte Chemie International Edition*. **2017**, 56 (50), 15936-15940.

# Chapter 2. Materials and methods

## 2.1 Materials

### 2.1.1 Dyads and their derivatives study in chapter 3

Table 2.1 Molecular structure, chemical formula and molar mass of the dyads and their derivatives under study

Molecule	Chemical Formula	Molecular structure	Molar mass, g/mol
<b>BDP – C<sub>60</sub> Dyad</b>	C <sub>100</sub> H <sub>46</sub> O <sub>7</sub> N <sub>3</sub> BF <sub>2</sub> S		1482.354
<b>BDP-C<sub>60</sub> peptide</b>	C <sub>132</sub> H <sub>102</sub> O <sub>14</sub> N <sub>13</sub> BF <sub>2</sub> S <sub>3</sub>		2239.35
<b>BDP-C<sub>60</sub> alkyl</b>	C <sub>110</sub> H <sub>84</sub> BF <sub>2</sub> N <sub>7</sub> O <sub>8</sub> S <sub>3</sub>		1776.89
<b>Bodipy thioacetate (BDP)</b>	C <sub>27</sub> H <sub>33</sub> BF <sub>2</sub> N <sub>2</sub> O <sub>2</sub> S		498.44
<b>BDP-peptide</b>	C <sub>58</sub> H <sub>85</sub> BF <sub>2</sub> N <sub>12</sub> O <sub>8</sub> S <sub>2</sub>		1191.33
<b>BDP-alkyl</b>	C <sub>38</sub> H <sub>51</sub> BF <sub>2</sub> N <sub>6</sub> O <sub>2</sub> S <sub>2</sub>		736.79
<b>Fullerene (C<sub>60</sub>)</b>	C <sub>75</sub> H <sub>15</sub> NO <sub>6</sub>		1025.92

These are the molecular systems that were studied and reported in the chapter 3. These systems have been synthesized and provided by Dr Allard and his co-workers at Institut Lavoisier de Versailles with the purification of these systems above 85%. Experiments were performed in benzonitrile and dichloromethane which were received from Sigma Aldrich.

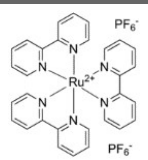
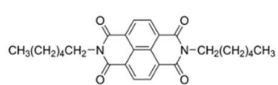
### 2.1.2 Molecular complexes on multicomponent systems study in chapter 4, 5, and 6

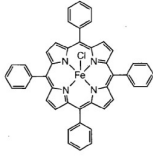
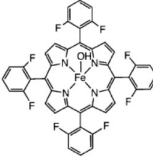
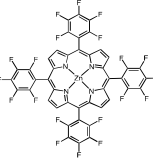
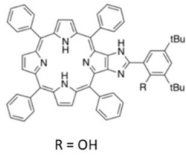
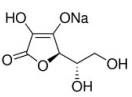
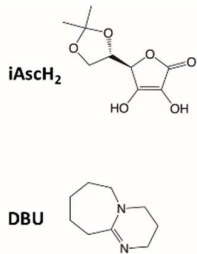
Molecular complexes under study are listed in Table 2. Photosensitizer, acceptor and donor molecules, model for photosystem II, and all photocatalysts have been synthesized and provided by the team of Pr. Aukaaloo at Institut de Chimie Moléculaire et des Matériaux d'Orsay. This close collaboration ignited the photophysical studies for solar conversion at ISMO. Naphthalene diimide (NDI), ascorbate, isoascorbate, DABCO, dry acetonitrile and dry benzonitrile have been purchased from Sigma Aldrich.

For experiments containing photosensitizer, acceptor, and electron donor, ascorbate was used to act as electron donor in argon-deaerated acetonitrile/water (60:40) solvents. Experiments involving (FeTPPCL, FeTPPF8OH, or ZnTPPF20) and electron donor were studied in acetonitrile, with isoascorbated acting as electron donor.

Experiments intended to mimic photosystem II (porphyrin-imidazole-phenol) and MV(PF<sub>6</sub>)<sub>2</sub> in dry acetonitrile were implemented in argon-saturated environment at each step to minimize the role of H<sub>2</sub>O.

*Table 2.2. Molecular structures under studying charge accumulation on multicomponent systems in chapter 4, 5, and 6*

Molecule	Chemical Formula	Molecular structure	Molar mass, g/mol
<b>[Ru(bpy)<sub>3</sub>]<sup>2+</sup></b> <b>(Photosensitizer)</b>	C <sub>30</sub> H <sub>24</sub> F <sub>12</sub> N <sub>6</sub> P <sub>2</sub> Ru		859.55
<b>MV(PF<sub>6</sub>)<sub>2</sub></b> <b>(acceptor molecule)</b>	C <sub>12</sub> H <sub>14</sub> Cl <sub>2</sub> N <sub>2</sub>		257.16
<b>Naphthalene diimide</b> <b>(acceptor molecule)</b>	C <sub>26</sub> H <sub>30</sub> N <sub>2</sub> O <sub>4</sub>		434.53

<b>FeTPPCI</b> <b>(Photocatalyst)</b>	$C_{44}H_{28}ClFeN_4$		704.03
<b>FeTPPF8OH</b> <b>(Photocatalyst)</b>	$C_{44}H_{21}FeN_4O$		829.51
<b>ZnTPPF20</b> <b>(Photocatalyst)</b>	$C_{44}H_{20}F_{20}N_4Zn$		1037.92
<b>Porphyrin-imidazole-phenol</b> <b>(model of photosystem II)</b>	$C_{59}H_{49}N_6O$		858.04
<b>Ascorbate</b> <b>(electron donor)</b>	$C_6H_6NaO_6$		198.11
<b>5,6-iso propylidene-L-ascorbic acid (iAscH<sub>2</sub>) and 1,8-biazabicyclo(5.4.0)undec-7-ene (DBU)on donor)</b>			
<b>DABCO</b> <b>(electron donor)</b>	$N_2(C_2H_4)_3$		112.176

## 2.2 Methods

To probe charge transfer, fast and ultrafast transient absorption (TA) spectroscopies, and nanosecond time-resolved resonance Raman (TR3) spectroscopy are the essential techniques used in this thesis. To solve the first theme of the thesis, studying electron transfer in dyad systems, femtosecond TA and nanosecond pump-probe experiments were implemented. To study the characterization of charge accumulation, the pump-pump probe nanosecond TA

technique has been used. Nanosecond TR3 was utilized to probe changes in vibrational structure following the electron transfer.

### 2.2.1 Nanosecond pump-pump-probe transient experiment

#### *Transient absorption or differential absorption spectroscopy*

The TA technique is based on the measurement of the evolution of absorption according to the time of a solution by a “probe” laser after a (nanosecond) pulse laser excitation. Using this technique it is possible to obtain dynamical and spectral information through the changes of the absorption spectrum, and thus to determine the appearance or disappearance of interesting, transient species. The nanosecond pulse laser which is used to excite is so-called “pump”. Thereby, the involve mechanism can be determined based on the monitoring of the kinetic traces of the transient species.

After shining light by the pulse laser (pump), a part of the molecules is lifted to an electronically excited state. A different absorption spectrum will be measured for those excited molecules. It should be emphasized that the “pump” laser and the “probe” laser are ideally spatially superimposed at an area of the sample, as shown in Figure 2.1.

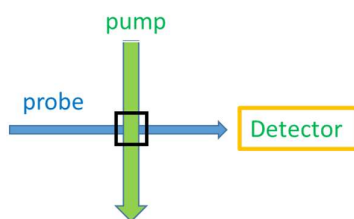


*Figure 2.1. Simplified representation of a pump-probe assembly with the superimposition of the probe and pump lasers.*

The principle of the TA technique is that the spectra results are obtained from the ratio between the signals with and without the pump (equation 1).

$$\Delta A = \log_{10} \left( \frac{S_{ref}^{on}}{S_{ref}^{off}} \times \frac{S_{sample}^{off}}{S_{sample}^{on}} \right) \quad \text{Equation 1}$$

Where  $\Delta A$  is the differential absorption,  $S_{ref}^{on}$  and  $S_{ref}^{off}$  are the intensity of reference spectra of the probe source, with (on) and without (off) pump excitation, respectively; meanwhile,  $S_{sample}^{on}$  and  $S_{sample}^{off}$  are the intensity of sample spectra with and without pump excitation. A differential absorption spectrum can be described as a function of time and

wavelength  $\Delta A(\lambda, t)$ . In general, a spectrum of transient absorption contains contributions from various processes, as shown below:

1. The first process is ground-state bleach. It appears as a negative signal in the wavelength region of ground-state absorption.
2. The second process is stimulated emission. This process contributes as a negative signal when the probe pulse passes through the excited volume, which induces stimulated emission to the ground state. Stimulated emission profile follows the fluorescence spectrum of the excited state; then it is Stokes shifted relative to the ground-state bleaching spectral features.
3. The third process is provided by excited-state absorption. This process contributes as a positive signal due to the transition from the excited state to higher excited states, which can exist in specific wavelength regions, such as charge-separated states, triplet states, and isomer states.
4. A fourth contribution can be given by radiative deactivation, such as fluorescence or phosphorescence appearing as negative signals in  $\Delta A$  profile.

#### ***Double pulse laser flash photolysis setup***

The pump-pump-probe experiment setup established at ISMO (Institut des Sciences Moléculaires d'Orsay). A simplified optical scheme of the setup is shown in Figure 2.2.

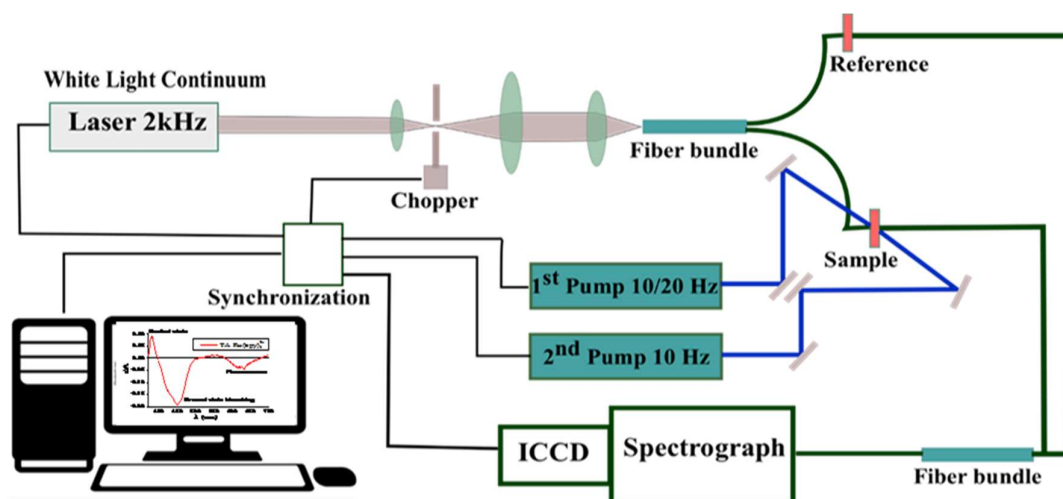


Figure 2.2. Simplified optical setup of the pump-pump-probe system.<sup>1</sup>

The experimental setup shown in Figure 2.2 comprises:

1. A white light continuum laser for probing sample absorption (STM-2-UV Leukos) operates at 2 kHz repetition rate which is then reduced to 20 Hz by an optical chopper. The output power of this laser is about 2.5mW.
2. INDI laser (3<sup>rd</sup> harmonic of a Quanta-Ray INDI-Series pulsed nanosecond Nd:YAG laser head pumping a broadband optical parametric oscillator OPO model BasiScan supplied by GWU) that can operate at either 10 Hz or 20 Hz repetition mode. The excitation wavelength can be tuned from 210-2500 nm with a pulse duration of 4 ns and timing jitter < 2 ns.
3. MOPO laser (3<sup>rd</sup> harmonic of a Quanta-Ray MOPO-730 Nd:YAG laser pumping an OPO) has a fixed repetition rate at 10 Hz. The excitation can be tuned from 440 nm to 1800 nm with a pulse width of about 5 ns.
4. CCD (PIXIS) or ICCD (PI-MAX 4, Princeton Instrument) cameras.
5. Spectrometer (SPEX 270M, Jobin-Yvon)
6. Photodiode (THORLABS DET 10 A/M)
7. Optical Chopper (THORLABS)
8. A cell for the sample and a cell for reference
9. System of lenses and mirrors for the laser beam alignment

Both INDI and MOPO lasers comprise neodymium-doped yttrium aluminum garnet (Nd:YAG), the most widely used and well-understood solid-state laser medium. The cavity is complemented with an electro-optic device (Q-switch), which allows energy to build up. The flash lamp excites Nd ions to build up a large population during the Q-switching operation and generates a laser light that is reflected through the mirrors. When the laser's power reaches its maximum, the laser beam penetrates the semi-permeable mirror and then leads to laser emission. The resulting optical peak energy is tens of megawatts.

Optical parametric oscillator (OPO) is a light source based on optical gain from parametric amplification in a non-linear Beta Barium Borate (BBO) crystal. The output of OPO depends on changing the BBO crystal angle. Thus, the photon maximum will be reached when phase between the pump beam and crystal is matched. Pump photons (355 nm), the third harmonic of the Nd:YAG laser, are decomposed into a signal (410-690 nm) and idler (730-2000 nm) by means of a non-linear optical phenomenon in order to comply with the power conversion rule:

$$h\nu_{\text{pump}} = h\nu_{\text{signal}} + h\nu_{\text{idler}}$$

A charge-couple device (CCD) is an array of photodiodes (light-sensitive pixels) which collect photons. Incident photons on this surface generate charges that can be read by electronics by changing the electrical bias of pixels. This charge can be turned to the voltage by storing the charge on the capacitor. Each voltage presents for a certain amount of charge accumulated on each pixel. Finally, the voltage is transformed to a digital signal (N-bit digital representation). An intensified camera (ICCD) utilizes an image intensifier linked to the CCD chip to enhance sensitivity down to a single photon level. An intensified CCD camera enables image acquisition at very low light level over a broad light spectrum and at comparatively rapid speeds.

The operations and processes in Figure 2 are described as following. The STM-2-UV Leukos laser produces a continuous white light at 2 kHz is chopped to 20 Hz to measure the absorption of the sample when the pump is on and off. The first pump can operate at 10 Hz or 20 Hz, the second pump has a fixed frequency of 10 Hz. A synchronization is responsible for connecting and controlling the pump lasers delay time regard to the probe laser. The fiber bundles that guide the white light probe are a 50/50 splitter with a single core of 900  $\mu\text{m}$ . Recently, the supercontinuum was used in free space without the fiber coupler to optimize the S/N ratio in a new optical configuration.

The system can be operated in both normal mode and online subtraction modes. In normal mode, both pump lasers run at 10 Hz. The transient signal includes signals from molecules that are excited once and from molecules that are excited twice. In online subtraction mode, the transient absorption signals induced by the first excitation is included in the second pump off signal by operating the first pump at 20 Hz, the same as the repetition of the probe and acquisition. Therefore, in fact we receive a relatively pure signal from molecules that are excited twice, as the off signal then includes a singly pumped solution.

### ***Timing control and synchronization***

A master clock trigger signal synchronizes the ICCD detector, pump and probe lasers. A home-built digital pulse generator with various output channels is used to activate lasers, detectors and produce synchronous time scans between the pump laser and probe laser (Figure 2.3). The function generator can produce a minimum delay of 1 ns with jitter < 1 ns. Considering the temporal width of the pump laser pulse (~3-4 ns), that of the probe laser (<1ns) and the inherent jitter, our time resolution is controlled by the width of the pump laser with the width

about 3-4 ns. This value can be estimated approximately from the very fast rise of the excited state of  $[\text{Ru}(\text{bpy})_3]^{2+}$  (Figure 2.4), but to control more precisely we need to do several experiments with small time steps.

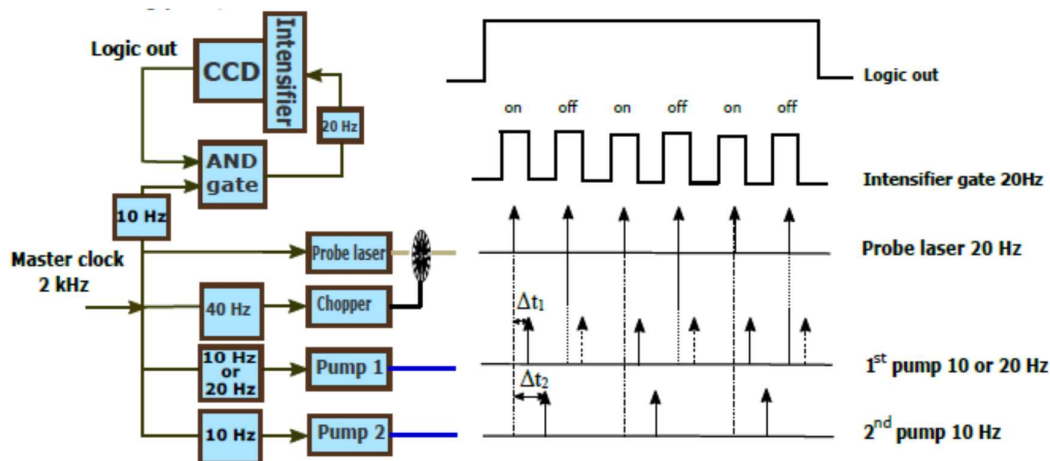


Figure 2.3. Synchronization and timing control. Left side (blue part): shows device block diagrams and how they are synchronized. The right side indicates the approach of timing control and acquisition.

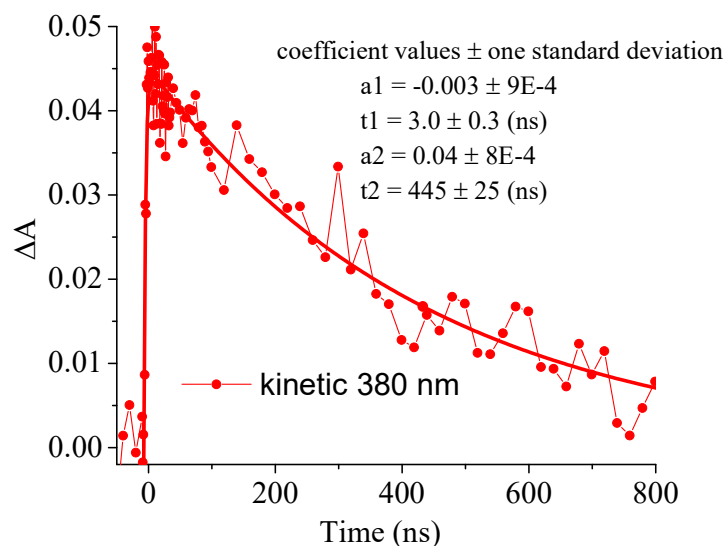


Figure 2.4. Rising time of excited state of  $[\text{Ru}(\text{bpy})_3]^{2+}$  at 380 nm

The master clock operates at 2 kHz. The probe laser output of 2 kHz is cut down to 20 Hz by an optical chopper whose trigger signal is resulted in the master clock. The repetition rates of 10 Hz and 20 Hz are generated to trigger the pump lasers and the intensifier. The time delay of the two laser pumps is governed by the computer via the pulse generator.

### **2.2.2 Femtosecond transient absorption spectroscopy**

Femtosecond transient absorption measurements were implemented at Adam Mickiewicz Univ Poznan, Poland by our collaborator. Femtosecond UV-vis-NIR transient absorption spectra were collected on a commercially available system (Ultrafast Systems, Helios model). The ultrafast laser system consists of a short-pulse titanium-sapphire oscillator (Mai-Tai, Spectra-Physics, 70 fs) followed by a high-energy titanium-sapphire regenerative amplifier (Spitfire Ace, Spectra-Physics, 100 fs). The 800 nm beam was split into two beams to generate: (1) pump ( $\lambda_{\text{exc}} = 527$  nm) in the optical parametric amplifier (Topas Prime with NirUVis frequency mixer) and (2) probe pulses - white light continuum in UV-vis-NIR (330 – 1370 nm) range, using a CaF<sub>2</sub> plate (330 – 660 nm), sapphire (440 – 780 nm) and YAG crystal (830 – 1345 nm). The pump pulse energy was 0.4  $\mu$ J. The absorbance was close to 0.86 at the excitation wavelength in a 2 mm optical path quartz cell. The sample solution was stirred by a Teflon-coated bar; no significant degradation was observed. Before experimentation, the solution was saturated with argon. The entire set of pump-probe delay positions was repeated at least twice, to ensure data reproducibility. The transient absorption data were corrected for the chirp of the white light continuum. The instruments response function (IRF) was about 200 fs (FWHM) in all experiments.

### **2.2.3 Nanosecond time-resolved resonance Raman spectroscopy**

Time-resolved resonance Raman (TR3) spectroscopy is one of the best technique to acquire vibrational structures and dynamics of chemical and biological systems. TR3 spectroscopy experiments can be implemented as single-pulse or pump-probe experiments. A nanosecond pump-probe TR3 which was built up at ISMO consists of a pump and a probe lasers. In this experiment setup, the sample is pumped by the pulsed laser to initiate the photochemical reaction and the probe laser interrogates the sample and the intermediate species generated by the pump laser. The time-delay between the two laser pulses can be varied. The spectra of the probe and the pump-probe lasers are also separate. Separate wavelengths for the pump and probe lasers allow us to optimize experiment conditions for excitation of the sample and in achieving the best resonance enhancement of Raman signal. Experiments are carried out by three separate measurements: (1) The probe measurement; (2) The pump measurement only to obtain background signal; (3) The pump-probe spectrum for each time delay.

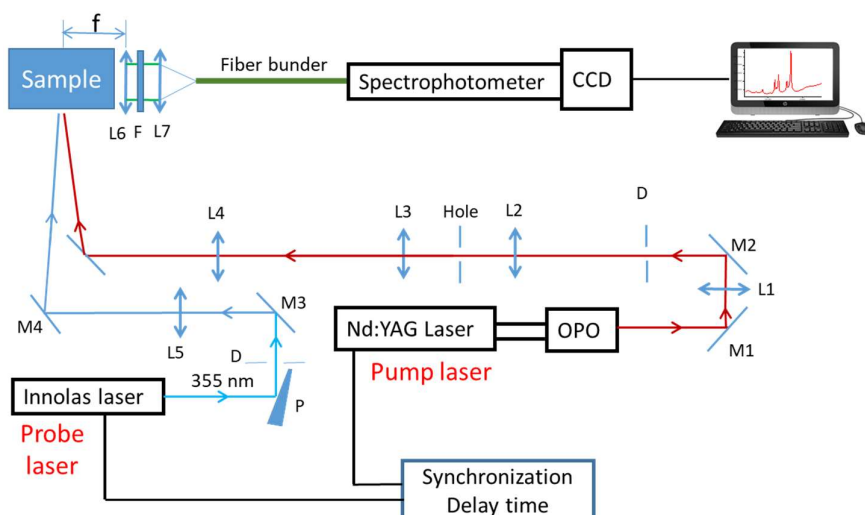


Figure 2.5. Simple schematic diagram of nanosecond pump-probe TR3 system.

Figure 2.5 shows a simple schematic of the nanosecond pump-probe TR3 setup at ISMO. The pump-probe TR3 spectroscopy consists of two pulsed lasers. The pump pulse comprises of neodymium-doped yttrium aluminum garnet (Nd:YAG) pumped optical parametric oscillator (OPO). The pump laser operates at 10 Hz; the excitation wavelength can be tuned in the 210-2500 nm range, pulse duration of  $\sim 4$  ns and timing jitter  $< 2$  ns. The other pulse is the probe laser (SpitLight Standard 600) with a pulse duration of 6-7 ns at 10 Hz of repetition rate. The excitation wavelength can be tuned at five different wavelengths. In our experiment, excitation at 355 nm was employed. The scattered light is detected by a CCD (PIXIS, Princeton Inst.) detector. The time delays between the pumps and the probe laser are electronically controlled.

The operation of the system (Figure 2.5) is depicted as follows. Firstly, the pump laser operated at 10 Hz passes through the mirror (M1) into the lens to create a collimated beam. Then the beam reflects on the mirror (M2) through the diaphragm (D) to enter the lens L2 (10 cm focus distance). Next, the beam passes through the hole with the diameter  $\sim 300 \mu\text{s}$ , placed at the focus point of the lens L2 to obtain a homogenous beam. Then the beam passes through the lenses (L3 and L4, 10 cm focus distance) to enter the sample. The probe laser is operated at 10 Hz, the power output is 7W at 355 nm. The probe laser is reflected on a prismatic window (P), which reflects only 4% of the power of laser into the mirror M3 (M3-maximum reflectance at 355 nm). Then, the beam goes through the lens L5 and reflectance mirror M4 to enter the sample. In this setup, the beams of the pump and the probe are in the same direction and overlap

on the center of the sample. The scattered light is collected and converted into electrical signals via the spectrophotometer.

#### 2.2.4 Time-correlated single-photon counting

Fluorescence decays were recorded on a homemade time-correlated single photo counting (TCSPC) at PPSM laboratory, ENS Paris-Saclay. (Figure 2.6). Excitation is given by an oscillating femtosecond laser Tisa (Tsunami, Spectra Physics) pumped by a double laser Nd:YVO4 (Millenia Xs, Spectra physics). Light pulse are chosen by an acousto-optic crystal and lowered to a repetition frequency of 4 MHz. The excitation wavelengths (300-330 nm and 350-500 nm) are achieved by a second or third harmonic generator. Fluorescence is detected at 90° by a monochromator and a MCP-PMT hybrid detector (R3809U-50, Hamamatsu) connected to a TCSPC module from Becker & Hickl (SPC 630). The instrumental response is recorded with a Ludox suspension and has a typical full width at half-maximum of ~25 ps. Data are evaluated using the Global software package (Laboratory for fluorescence dynamics at the University of Illinois at Urbana-Champaign), which involves a deconvolution analysis and global non-linear least-squares minimization method.

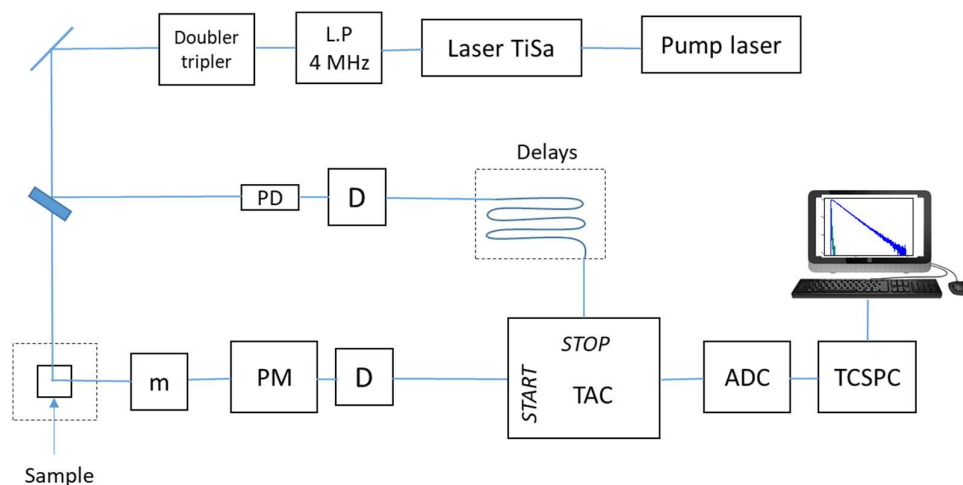


*Figure 2.6. Schematic presentation of the TCSPC experimental setup. Abbreviation: Light pulses are collected; PD: photodiode; D: discriminator; m: monochromator; PM: photomultiplier; TAC: time-amplitude converter; ADC: analogic-digital converter; TCSPC: TCSPC module.*

#### 2.2.5 Steady-state spectroscopy

Ground-state absorption measurements were performed using a UV-2600 UV-Vis spectrophotometer Shimadzu, which is a double channel spectrophotometer (two cell holders;

one for the reference and one for the sample). Another system was also utilized is a SPECORD 600 (Analytic Jena) which is a single-channel spectrophotometer, using 1 cm quartz cell.

HORIBA Scientific Fluoromax PLUS that utilizes xenon arc lamp to illuminate recorded emission spectra. FluorEssence ver.3.8.0 software was used to visualize the emission. The fluorescence quantum yields were measured relatively to Rhodamine 590 in ethanol  $\Phi_F = 0.95$  as reference.

### **2.2.6 Cyclic voltammetry measurements**

Cyclic voltammetry (CV) of the BDP-C<sub>60</sub> dyad were measured by Emmanuel Allard, our collaborator at Institut Lavoisier de Versailles. BDP thioacetate **4**, fullerene **2**, and **BDP-C<sub>60</sub>** Dyad were dissolved in anhydrous DCM or benzonitrile containing 0,1 M of n-Bu<sub>4</sub>NPF<sub>6</sub> into a standard three-electrode cell under a nitrogen atmosphere. CV measurements were then undertaken with a potentiostat using a platinum disc electrode and a large platinum counter-electrode to obtain the potentials versus an Ag wire pseudo-reference electrode. The latter was separated from the bulk solution using a capillary with frit. Potentials were calibrated versus ferrocene/ferrocenium.

CVs of porphyrin molecules were performed by Zakaria Halime, our collaborators at ICMMO (Institute de Chimie Moléculaire et des Matériaux d'Orsay). CV measurements were carried out in an electrochemical cell composed of a glassy carbon (3 mm diameter) working electrode, a saturated calomel electrode (SCE) as a reference electrode and a platinum mesh counter electrode. Acetonitrile (VWR Chemicals HPLC grad) was distilled over CaH<sub>2</sub> and *tetra-N*-butylammonium hexafluorophosphate ([Bu<sub>4</sub>N]PF<sub>6</sub>, Aldrich 99%) was recrystallized in ethanol. Solutions of the complex were prepared at a concentration of 1 mM and [Bu<sub>4</sub>N]PF<sub>6</sub> was used as supporting electrolyte and its concentration was maintained at a hundred-fold excess compared to the sample. The solutions were purged with inert argon gas and the cyclic voltammograms were measured at a scan rate of 100 mV/s.

### **2.2.7 Spectroelectrochemical absorption measurements**

Spectroelectrochemical absorption measurements were implemented in PPSM, CNRS-ENS Paris-Saclay in collaboration with Pr. Fabien Miomandre. Spectra are recorded in a Horiba Cary 5000 spectrophotometer using an OTTLE cell<sup>2</sup> composed of a Pt minigrad working electrode, a Pt wire counter-electrode and an Ag wire pseudo-reference electrode connected to a potentiostat (CHI Instruments 600). The sample is a 0.2 mM solution of BDP4 in 0.1 M

hexafluorophosphate tetraethylammonium in dichloromethane. The background is made on the cell filled with the electrolyte solution only.

## REFERENCES

1. Mendes Marinho, S.; Ha-Thi, M.-H.; Pham, V.-T.; Quaranta, A.; Pino, T.; Lefumeux, C.; Chamaille, T.; Leibl, W.; Aukauloo, A., Time-resolved interception of multiple charge accumulation in a sensitizer-acceptor dyad. *Angewandte Chemie International Edition* **2017**, *56* (50), 15936-15940
2. Krejčík, M.; Daněk, M.; Hartl, F., Simple construction of an infrared optically transparent thin-layer electrochemical cell: Applications to the redox reactions of ferrocene, Mn<sub>2</sub>(CO)<sub>10</sub> and Mn(CO)<sub>3</sub>(3, 5-di-*t*-butyl-catecholate)<sup>-</sup>. *Journal of electroanalytical chemistry and interfacial electrochemistry* **1991**, *317* (1-2), 179-187.

# Chapter 3. Energy transfer and electron transfer in BODIPY-C<sub>60</sub> Dyad systems

## 3.1 Introduction

Global energy demand is continuously increasing. One of the best renewable energy sources to meet this demand is solar power, which has attracted much attention to replace exhausted fossil fuels. A well-studied approach is creating photoelectrochemical devices and cells in which solar energy is converted into electrical energy. Among all of the available options, organic solar cells have certain advantages; for example, they are low cost, lightweight, versatile materials<sup>1-5</sup>.

Consequently, a wide variety of donor-acceptor Dyad systems has been developed to build organic solar cells.<sup>6-10</sup> Specifications for a Dyad system to be used in organic solar cells should involve strong light absorbance, efficient charge separation, and slow charge recombination. Among vast numbers of donors – acceptor candidates, Boron-dipyrromethene (commonly abbreviated as BODIPY, referred to hereafter as BDP) donors, and fullerene acceptors show many advantages. BDP and its derivatives play a dual function: as efficient light-harvesting molecule, and electron donors upon photoexcitation.<sup>11-12</sup> Additionally, they possess numerous useful properties such as a relatively broad spectral range both in absorption and emission, and an intense molar extinction coefficient in the visible region. The system also requires an acceptor candidate, and fullerene (C<sub>60</sub>) has recently emerged as one of the most promising electron acceptors due to its small reorganization energies and its high degree of charge delocalization.<sup>13-14</sup> The donor-acceptor Dyad systems have been immobilized on a wide variety of surfaces for the construction of photoelectrochemical devices.<sup>15-16</sup> In our case, the BDP-C<sub>60</sub> Dyad system will be immobilized on a gold surface through association with a helical peptide.<sup>17</sup> The rigid helical conformation adopted by the peptide keeps the chromophore away from the surface. Therefore, it helps to prevent or limit quenching of the excited state of the chromophore. Additionally, it is also a good electron mediator in comparison to an alkyl chain.

Taking advantage of all these properties, the new BDP -C<sub>60</sub> Dyad systems including BDP-C<sub>60</sub>, BDP-C<sub>60</sub>-peptide assembly, and BDP-C<sub>60</sub>-alkyl assembly have been synthesized and studied photophysically. In the framework of this thesis, the main objectives are focused on studying photophysical properties of those Dyad systems as the first steps for completing the goal of self-assembled monolayers (SAMs) on gold surfaces. Figure 3.1, Figure 3.2, and figure 3.3 present the structures of the BDP-C<sub>60</sub> Dyad systems and their donor/acceptor derivatives which were investigated. This work is done in strong collaboration with Dr Allard and his co-workers at Institut Lavoisier de Versailles, in the frame of Labex Charmmat.

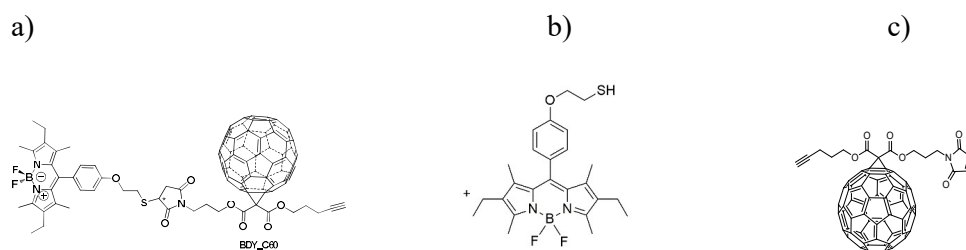


Figure 3.1. The molecular structures of a) BDP-C<sub>60</sub> Dyad, b) BDP, and c) C<sub>60</sub>

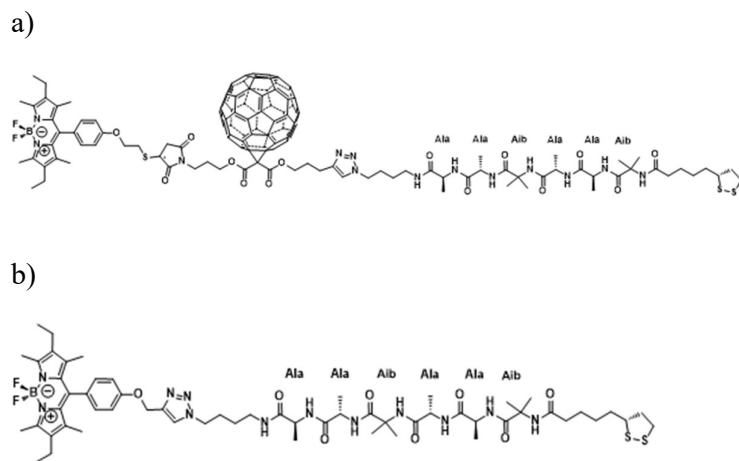


Figure 3.2. The molecular structures of a) BDP-C<sub>60</sub>-peptide assembly Dyad and b) BDP-peptide derivative

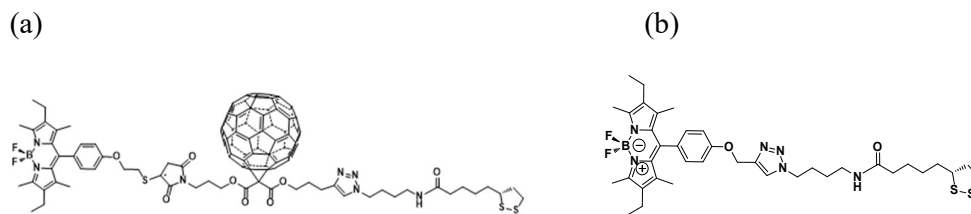


Figure 3.3. The molecular structures of a) BDP-C<sub>60</sub>-alkyl assembly Dyad and b) BDP-alkyl derivative

In these molecules, both donor and acceptor can be excited to study charge transfer and energy transfer. The study of the photophysical properties under excitation at 527 nm to excite the BDP moiety in the BDP-C<sub>60</sub> Dyad system was completed by both experimental techniques and theoretical calculations. These results are in preparation to submit in an international journal.

The paper represents a significant part of this chapter. The photophysical investigation results of the BDP-C<sub>60</sub> Dyad system under excitation at 380nm will be presented in this chapter. Additionally, this chapter will discuss the elementary results of the photophysical properties of the BDP-C<sub>60</sub>-peptide and BDP-C<sub>60</sub>-alkyl assembly systems.

### **3.2 Light-induced electron transfer and energy transfer processes in a new BODIPY-C<sub>60</sub> Dyad (manuscript prepared)**

*Thu-Trang Tran,<sup>†,§</sup> Jad Rabah,<sup>‡</sup> Minh-Huong Ha-Thi,<sup>†\*</sup> Emmanuel Allard,<sup>‡\*</sup> Stanislaw Nizinski,<sup>#</sup> Gotard Burdzinski,<sup>#</sup> Stéphane Aloïse,<sup>§</sup> Hélène Fensterbank,<sup>‡</sup> Krystyna Baczko,<sup>‡</sup> Gilles Clavier,<sup>⊥</sup> Fabien Miomandre,<sup>⊥</sup> Thomas Pino,<sup>†</sup> and Rachel Méallet-Renault<sup>†\*</sup>*

<sup>†</sup>Institut des Sciences Moléculaires d'Orsay, CNRS, Univ. Paris-Sud, Université Paris-Saclay, 91405 Orsay Cedex, France

<sup>‡</sup>Institut Lavoisier de Versailles, UMR 8180, Université de Versailles Saint-Quentin-en-Yvelines, Université Paris-Saclay, 78035 Versailles Cedex, France

<sup>#</sup>Adam Mickiewicz Univ in Poznan, Fac Phys, Quantum Elect Lab, PL-61614 Poznan, Poland

<sup>⊥</sup>PPSM, CNRS-ENS Paris Saclay, 61 Avenue Président Wilson, 94235 CACHAN, France

<sup>§</sup>Univ Lille, CNRS, UMR 8516, LASIR, Lab Spectrochim Infrarouge & Raman, F-59000 Lille, France

<sup>§</sup> Faculty of Physics and Technology, Thai Nguyen University of Sciences, Thai Nguyen, Vietnam

KEYWORDS: Electron transfer, energy transfer, BODIPY, fullerene, dyad, transient absorption.

ABSTRACT: A new donor–acceptor dyad comprised of a BODIPY (BDP) donor and a fullerene (C<sub>60</sub>) acceptor has been synthesized. Thanks to the combination of semi-empirical and

density functional theory (DFT) calculations, spectroelectrochemical experiments, steady-state and time-resolved spectroscopy (from ns to fs), the photophysical properties of the new BDP-C<sub>60</sub> Dyad were thoroughly studied. By using semi-empirical calculations, the simultaneous existence of three conformations of the BDP-C<sub>60</sub> Dyad has been deduced, and their molecular orbital structures have been analysed using DFT. Two short fluorescence lifetimes were attributed to two conformers, with variable donor-acceptor distances (17.5 and 20.5 Å, denoted as conformer 2 and conformer 3, respectively). The efficiency of Förster resonance energy transfer (FRET) was estimated for these two conformations. Additionally, the driving force for photoinduced electron transfer (PET) from the singlet excited state of the BDP to the C<sub>60</sub> moiety was calculated using redox potentials determined with electrochemical studies. Spectroelectrochemical measurements were carried out to investigate the absorption profiles of radicals in the BDP-C<sub>60</sub> Dyad, in order to assign the transient species in pump-probe experiments. Under selective excitation of the BDP moiety, ultrafast transient absorption (TA) spectroscopy demonstrates two ultrafast PET mechanisms for an additional conformer with donor-acceptor distance of 8.8 Å (denoted as conformer 1). The charge-separated state persisted for several ns and the charge recombination process populated the C<sub>60</sub> triplet state before returning to the ground state.

### 1. Introduction

The association of donor and acceptor in dyads (and polyads) has significantly contributed to the development of many light-harvesting materials for organic electronics.<sup>13, 18-33</sup> These systems are able to undergo electron transfer and/or energy transfer due to photo-excitation of either the donor or acceptor moiety. Studies on these light-induced processes, and more specifically electron transfer, are of prime importance not only from a fundamental point of view but also for practical applications.<sup>19-33</sup> Indeed, conversion of solar light energy to electricity in photovoltaics or to chemical energy (solar fuel) through photocatalytic processes invariably starts with photoinduced electron transfer (PET).<sup>34</sup> Consequently, a huge number of donor-acceptor conjugates have been designed and light-induced electron transfer and/or energy transfer events in solution have been probed.<sup>18-33</sup> Among the different acceptors, fullerene C<sub>60</sub> is probably the most attractive due to its outstanding properties including good electron acceptor capability, a high degree of charge delocalization within the  $\pi$ -extended conjugation and small reorganization energies in electron transfer processes.<sup>13-14</sup> Among the chromophores used both as light-harvester and electron donor, BDPs have recently gained more attention in the design of donor-C<sub>60</sub> conjugates.<sup>12, 35-47</sup> Indeed, BDPs are interesting

chromophores; they are chemically stable and display remarkable photophysical properties, including high absorption coefficients and emission quantum yields. Another remarkable feature relies on the ease of functionalization of the BDP core, allowing to tune its spectral and electrochemical properties.<sup>40</sup> In many examples, it was shown that the PET in these BDP-C<sub>60</sub> assemblies was the main pathway leading to charge separated states,<sup>36-37, 48, 38-44, 46</sup> whereas energy transfer appeared as a competitive process in a few cases.<sup>35, 49</sup>

The occurrence of this PET in these BDP-fullerene systems observed in solution could also be exploited in the construction of photocurrent generating photoelectrochemical cells. These molecular photovoltaic devices have already been prepared from self-assembled monolayers (SAMs) of donor-fullerene systems on gold surfaces, mainly with porphyrin-fullerene conjugates.<sup>16, 50</sup> However, the existence of energy transfer of the excited state of the chromophores by the metallic surface has appeared as a limiting factor for the photocurrent generation.<sup>19, 50</sup> In this context, it was recently proposed that helical peptide could be used as a spacer between the chromophore and the gold surface. The rigid helical conformation adopted by the peptide keeps the chromophore away from the surface and thus prevents (or limits) the quenching of the chromophore excited state.<sup>51-52</sup> Another remarkable feature of the helical peptide is related to its good electron mediator ability compared to an alkyl chain.<sup>51-52</sup> Thus, promising results were recently obtained with peptide-based SAMs functionalized with electroactive and/or photoactive probes in the construction of devices for photo-energy conversion applications.<sup>52-53</sup>

Consequently, we are interested in the synthesis of a BDP-C<sub>60</sub> dyad that could be associated with a helical peptide. The resulting BDP-C<sub>60</sub>-peptide assembly could then be immobilized on surfaces to develop photoelectrochemical devices. To accomplish this goal, we have to firstly address the synthesis and the photophysical characterization of a BDP-C<sub>60</sub> dyad that could be used as a building block in the design of dyad-terminated helical peptides.

Herein, we present the synthesis of a BDP-C<sub>60</sub> Dyad obtained from a “clickable fullerene” and BDP-thiol derivative. What makes our system different from most of the previous BDP-C<sub>60</sub> dyads which were prepared by direct functionalization of C<sub>60</sub> in the final step,<sup>36-37, 41-45, 47-49, 54</sup> is the use of the “clickable” fullerene building block to prepare the dyad. This “clickable” fullerene bears two different reactive centers: an alkyne moiety on one side and a maleimide unit on the other side. This derivative can be easily functionalized using sequential orthogonal transformations based on copper(I)-catalyzed alkyne-azide cycloaddition (CuAAC) “click” and thiol-maleimide reactions as we have previously demonstrated.<sup>55-56</sup> In the present study, the

fullerene building block is functionalized by a BDP thiol leaving the alkyne moiety available for the further functional arrangement with a peptide azide through the use of a CuAAC reaction.<sup>17</sup> Finally, the photoinduced processes in the BDP-C<sub>60</sub> Dyad have been investigated thanks to the combination of computational studies, spectroelectrochemical experiments, steady-state and time-resolved spectroscopy techniques.

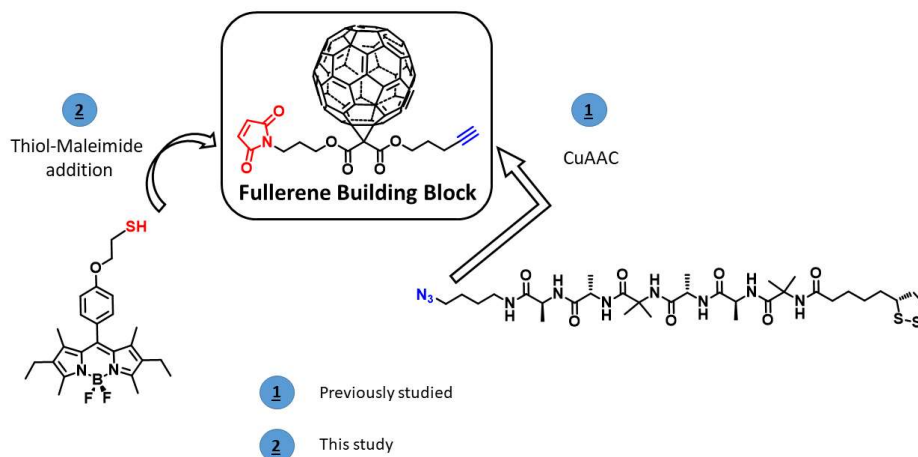
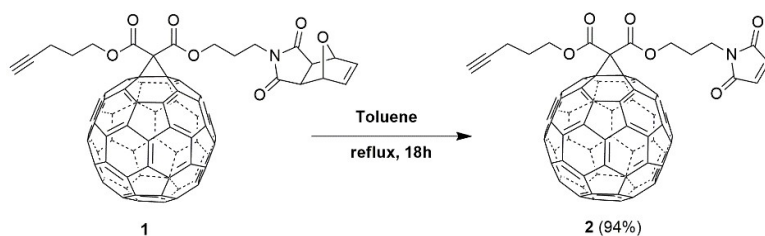


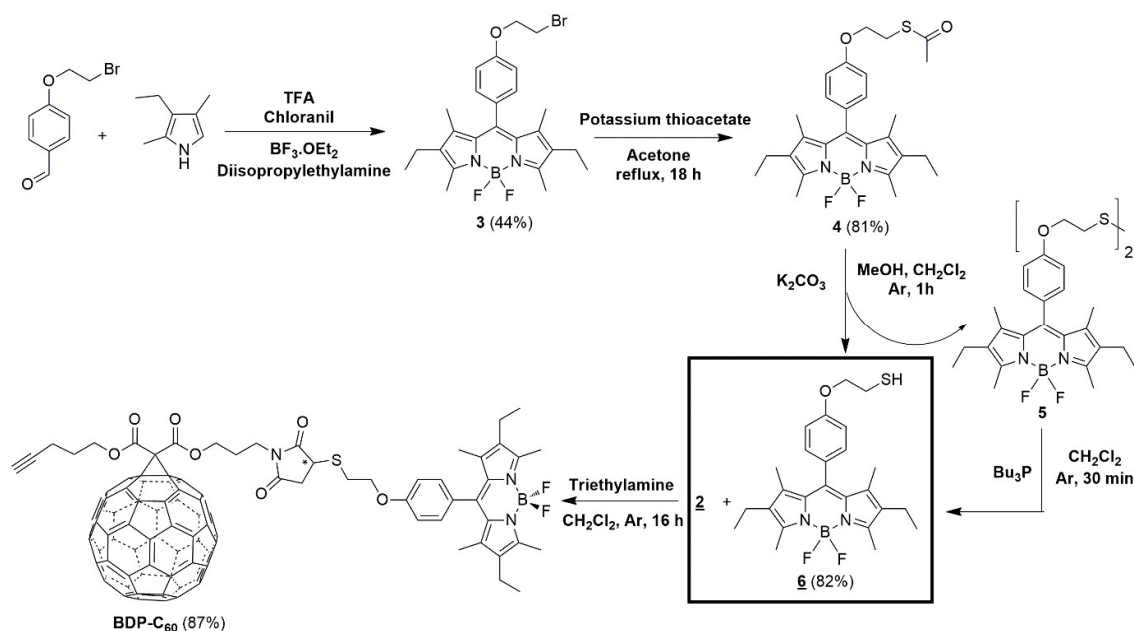
**Figure 1.** Scheme of “clickable” fullerene with two different reactive centers: an alkyne moiety (in blue) and a maleimide unit (in red). Steps 1 and 2 indicate the sequential orthogonal transformations based on copper(I)-catalyzed alkyne-azide cycloaddition (CuAAC) “click” and thiol-maleimide reactions.

## 2. Results and discussion

### 2.1 Synthesis and characterization

**Scheme 1.** Synthetic pathway for the preparation of the BDP-C<sub>60</sub> Dyad.





**Synthesis.** The synthesis of the BDP-C<sub>60</sub> Dyad from the fullerene and the BDP building blocks (**2** and **6**) is outlined in scheme 1. Briefly, the fullerene derivative **1** was prepared in five steps according to a previously published procedure.<sup>17</sup> The desired fullerene building block **2** (C<sub>60</sub> **2**), functionalized by a maleimide moiety, was then prepared from **1** by performing a retro Diels-Alder reaction. For the preparation of the second building block (**6**), the synthesis starts with the preparation of the BDP derivative **3** (BDP **3**). This latter was obtained using a three-step one-pot approach. The kryptopyrrole was reacted with 4-(2-bromoethoxy) benzaldehyde in dry dichloromethane (DCM) and trifluoroacetic acid followed by *p*-chloranil oxidation and finally treatment with boron trifluoride etherate in the presence of diisopropylethylamine. The BDP **3** was then reacted with potassium thioacetate in acetone to give the BDP **4**. The desired BDP building block **6**, functionalized by a thiol moiety, was thus prepared by reacting BDP **4** with potassium carbonate in a mixture of DCM and methanol under argon. The crude mixture was composed of desired thiol derivative **6** along with the disulfide **5**. This by-product can be easily reduced by reacting the crude mixture with tributylphosphine in DCM under argon to give exclusively the BDP-thiol **6** in 82% yield. This derivative was purified by column chromatography and was used directly in the final step. Finally, the synthesis of the BDP-C<sub>60</sub> Dyad was realized by performing a Michael addition from the fullerene-maleimide **2** and the BDP-thiol **6** in DCM in the presence of triethylamine. The BDP-C<sub>60</sub> Dyad was isolated after chromatographic purification on silica gel in high yield (87%).

**NMR analysis.** All the new compounds were fully characterized by NMR spectroscopy and by electrospray mass spectrometry; the data were in accordance with the depicted structures. Examination of the <sup>1</sup>H NMR spectrum of the **BDP-C<sub>60</sub>** Dyad shows the signals corresponding to the <sup>1</sup>H of the fullerene (<sup>1</sup>H in blue) and BDP (<sup>1</sup>H in red) building blocks (Figure 2). Importantly, the formation of the thiol-maleimide adduct is confirmed by the disappearance of the maleimide protons at 6.75ppm and the presence of a set of new signals in the 2.55-4.1ppm region. These signals are attributed to the protons of the imide ring. The <sup>1</sup>H belonging to the chiral center (**H<sub>n</sub>**) appears as a doublet of doublets at 4.04ppm while the methylenic protons (**H<sub>m</sub>**) near this chiral center are diastereotopic and display an AB pattern. Furthermore, the methylenic protons of the BDP moiety (**H<sub>H</sub>**) close to this chiral center are also diastereotopic leading to an AB pattern.

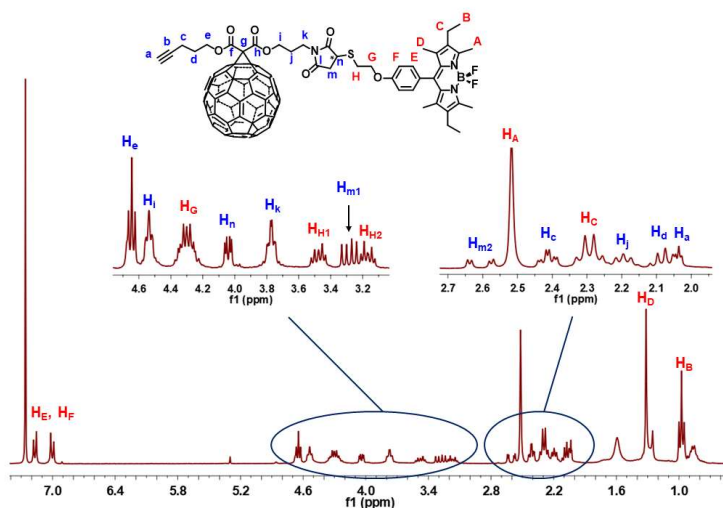


**Figure 2.** <sup>1</sup>H NMR spectrum recorded (300MHz, CDCl<sub>3</sub>, 25°C) for the **BDP-C<sub>60</sub>** Dyad.

## 2.2 Computational studies – Conformations of the **BDP-C<sub>60</sub>** Dyad

The conformational search of the **BDP-C<sub>60</sub>** Dyad was carried out by theoretical calculations at the semi-empirical PM3 level. We firstly considered a set of two conformers for each enantiomer in which the fullerene moiety and the thiol-maleimide bond are located on the same or opposite side with respect to the imide ring. The geometries of these conformers denoted S-(I, IV) and R-(II, III) were optimized at the PM3 level and the most stable conformers (Figure 3) were used as initial points for further conformational study.

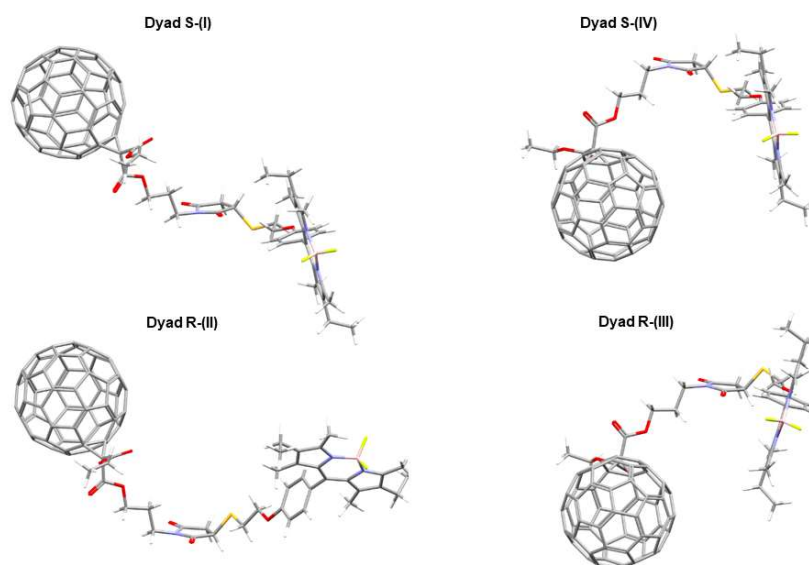


**Figure 3.** Conformers of the **BDP-C<sub>60</sub>** optimized by semi-empirical calculations (PM3) used as initial point for further geometrical optimization. Alkynyl propyl group was substituted with ethyl group for the computational study.

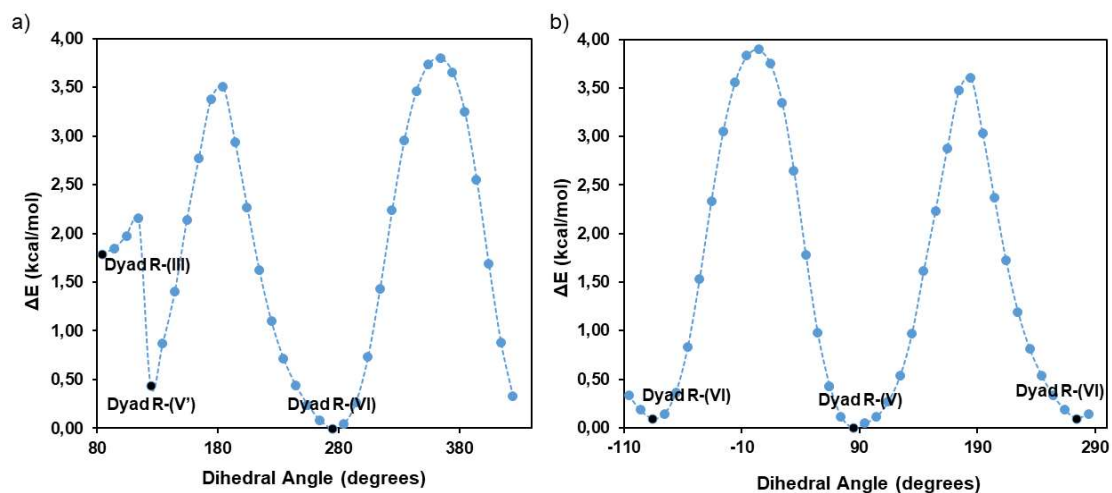


**Figure 4.** a) and b) Calculated energy profiles obtained by a relaxed scan around the OCN-CH<sub>2</sub>CH<sub>2</sub> dihedral angle for the (R) configuration. Energies are given relative to the minimum energy conformation. c) Theoretical structures of the different conformers, starting from the R-(III) conformer, including the two global minima R-(V) and R-(VI).

Then, the potential energy surfaces (PESs) were scanned as a function of the OCN-CH<sub>2</sub>CH<sub>2</sub> dihedral angle starting from R-(III) and S-(I) enantiomers to find out remarkable

conformers when rotating the C<sub>60</sub> moiety. Figures 4 and S9-S10 show the energy profiles of the dyad for both enantiomers. The R-(III) dyad gave two global minima, namely R-(V) and R-(VI) which are close in energy and more stable in comparison to the starting conformer R-(III). These conformers R-(V) and R-(VI) are characterized by a folded and a stretched linear geometry, respectively. The rotational energy barrier between these two conformational minima is close to 3.7 kcal.mol<sup>-1</sup>. The S-(I) dyad gave the same trend with new minima, namely S-(VII) and S-(VIII) which are also characterized by a folded and a stretched linear geometry, and a rotational energy barrier of 3.6 kcal.mol<sup>-1</sup> (Figures S9-S10). The results of the semi-empirical calculations show that there are at least two stable conformations for the dyad in the R and S configurations. For both enantiomers, the rotational energy barrier between the two conformational minima is low. Hence, the dyad can easily adopt either a folded or a stretched linear geometry through the motion of the fullerene part like a windshield wiper (Figure 5). In addition, we have determined from the most stable conformation, the center-to-center distances between the BDP and the C<sub>60</sub>. These distances are the same in the folded conformation for the (R) and (S) configurations, with a BDP-C<sub>60</sub> distance of 8.8Å while in the stretched linear conformation, there are minor discrepancies in the BDP-C<sub>60</sub> distances with 20.0 Å and 17.5 Å for the (R) and (S) configurations, respectively (Figure 5).

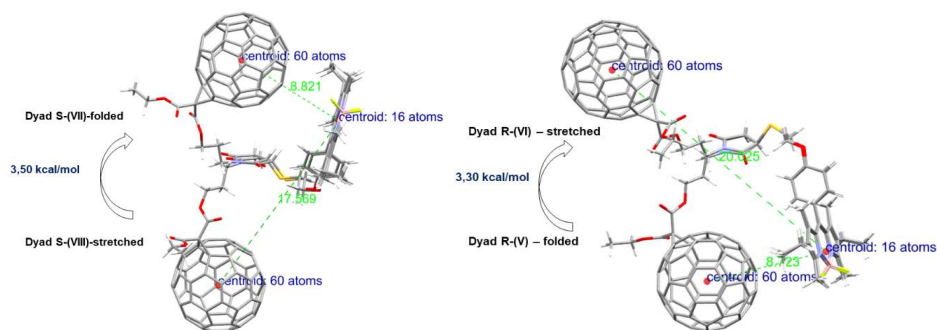


**Figure 5.** Rotational energy barrier between the folded and stretched linear geometry for both enantiomers along with the distances for each minimum-energy conformer.

Finally, we also ran a single point energy calculation using the long ranged corrected cam-B3LYP hybrid functional and 6-311+g(d,p) basis set on the previously optimized conformations (S-(VII, VIII) and R-(V, VI), see Figure 5) of the **BDP-C<sub>60</sub>** Dyad to get a picture of the molecular orbitals (MO). As expected for the stretched linear geometry and whatever the configuration, MO are exclusively localized on the C<sub>60</sub> or BODIPY moieties without delocalization (Figures S12-S14). It is noteworthy that the LUMO is localized on the C<sub>60</sub> electron acceptor while the HOMO is localized on the BDP electron donor unit (Figures S12-

S14). We have similar trend for the folded geometry (Figures S11-S13) except in the case of HOMO which is mainly localized on the BDP unit with some contribution on fullerene C<sub>60</sub> (Figure 6).

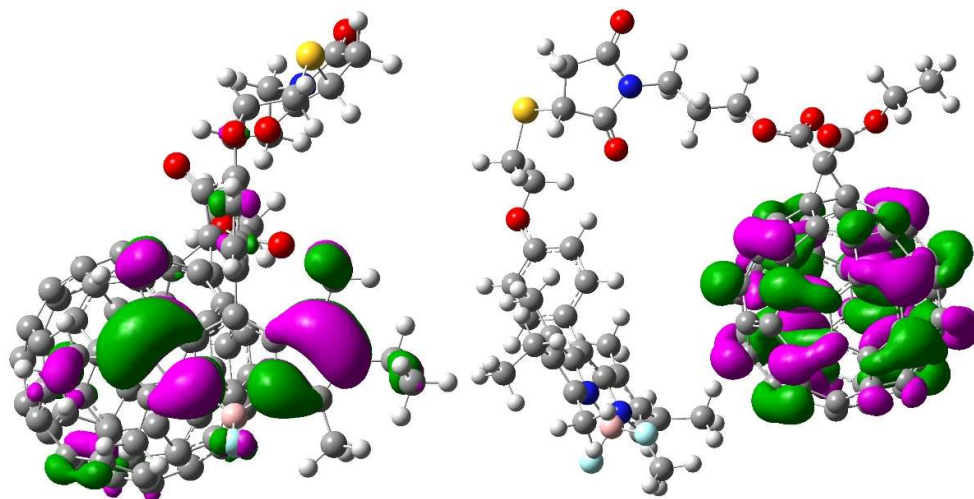


**Figure 6.** HOMO (left) and LUMO (right) for the folded R-(V) conformer.

### 2.3 Absorption and fluorescence

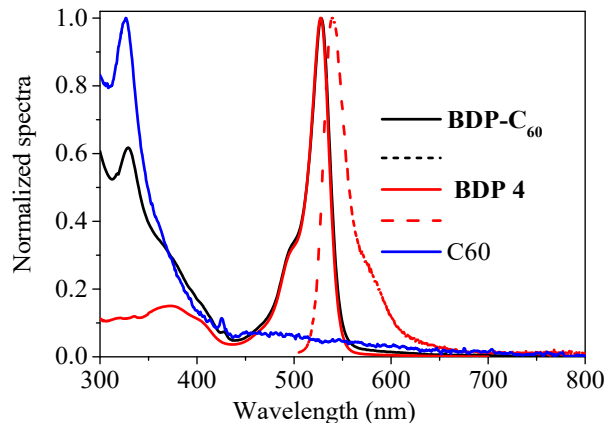


**Figure 7.** Normalized absorption (solid line) and fluorescence (dashed line) spectra in benzonitrile of the **BDP 4** ( $1.3 \times 10^{-6}$  M), **BDP-C<sub>60</sub>** Dyad ( $1.3 \times 10^{-6}$  M) and **C<sub>60</sub>** ( $0.2 \times 10^{-3}$  M),  $\lambda_{\text{exc}} = 510$  nm. The normalized fluorescence spectra are almost identical for the two compounds.

The normalized absorption and fluorescence of the **BDP-C<sub>60</sub>** Dyad and **BDP 4** in benzonitrile are compared in figure 7. The absorption of the **BDP 4** shows the expected strong  $S_0$ - $S_1$  transition band at 527 nm and a higher energy  $S_0$ - $S_2$  transition band at 380 nm.<sup>57</sup> The main absorption band of the **BDP-C<sub>60</sub>** Dyad is characteristic of the BDP fragment. It indicates that

the C<sub>60</sub> moiety does not affect the absorption spectra of the BDP moiety in the **BDP-C<sub>60</sub>** Dyad (for wavelengths longer than 440 nm). Moreover, the absorption spectrum of the **BDP-C<sub>60</sub>** Dyad shows the expected contribution of the methanofullerene moiety with a sharp band at 330 nm and a small band at 427 nm (Figure S8).<sup>58</sup> The absorption features suggest a negligible ground state interaction between BDP and C<sub>60</sub> entities. Upon excitation at 510 nm, the fluorescence spectrum of the **BDP 4** in benzonitrile showed an expected emission band at 537 nm. The normalized fluorescence spectra are almost identical for the **BDP 4** and the **BDP-C<sub>60</sub>** Dyad, indicating that the BDP moiety is responsible for the Dyad emission.

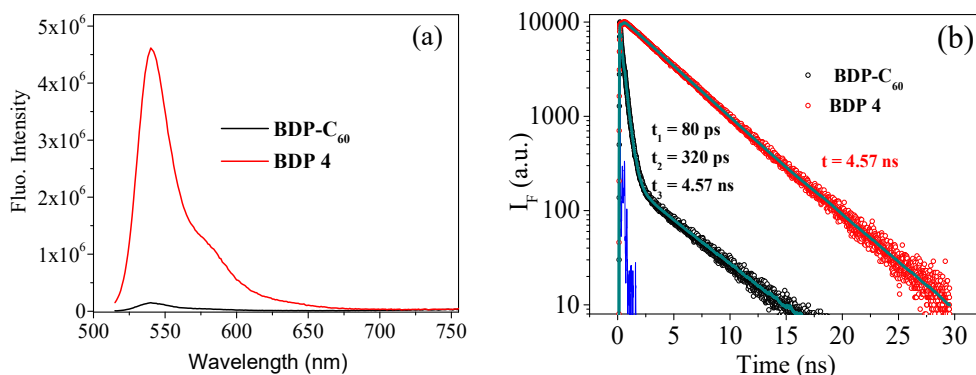


**Figure 8.** Emission spectra (a) and fluorescence decay (b) of the **BDP-C<sub>60</sub>** Dyad and the **BDP 4** excited at 510 nm in benzonitrile ( $1.3 \times 10^{-6}$  M). Blue line: Instrument response function.

Table 1. Photophysical parameters of the **BDP 4**, **C<sub>60</sub> 2**, and **BDP-C<sub>60</sub>** Dyad in Benzonitrile. Absorption band  $\lambda_{\text{abs}}$  (nm) and emission band  $\lambda_{\text{em}}$  (nm) maximum wavelengths, molar absorption coefficient  $\epsilon$  ( $\text{M}^{-1} \text{cm}^{-1}$ ), fluorescence quantum yield  $\Phi_{\text{F}}$ , fluorescence lifetime  $\tau$  (ns), radiative  $k_{\text{r}}$  ( $\text{s}^{-1}$ ) and nonradiative rate  $k_{\text{nr}}$  ( $\text{s}^{-1}$ ) constants.

	$\lambda_{\text{abs}}$ (nm)	$\lambda_{\text{em}}$ (nm)	$\epsilon_{\text{max}}$ ( $\text{M}^{-1} \text{cm}^{-1}$ )	$\Phi_{\text{F}}$	$\tau$ (ns)	$k_{\text{r}}$ ( $\text{s}^{-1}$ )	$k_{\text{nr}}$ ( $\text{s}^{-1}$ )
<b>BDP 4</b>	380, 527	537	74 500 (527nm)	0.73	4.57 ( $\pm 0.01$ )	$1.6(\pm 0.1) \times 10^8$	$5.9(\pm 0.1) \times 10^7$
<b>C<sub>60</sub> 2</b>	330, 428	697 <sup>59</sup>	3000 <sup>59</sup> (428nm)	0.005 <sup>60</sup>	1.50 <sup>59</sup>	-	-
<b>BDP-C<sub>60</sub> Dyad</b>	380, 527	537	77 500 (527nm)	0.04	0.32( $\pm 0.01$ ) (58%); 0.08( $\pm 0.01$ ) (41%); 4.57 ( $\pm 0.01$ ) (1.1%)	$1.5(\pm 0.1) \times 10^8$	$3.6(\pm 0.1) \times 10^9$

The comparison of fluorescence spectra of the **BDP 4** and **BDP-C<sub>60</sub>** Dyad recorded in the same condition is shown in Figure 8a. Photophysical parameters of these compounds are summarized in Table 1. The fluorescence of the BDP moiety in **BDP-C<sub>60</sub>** Dyad is strongly quenched (90%) as compared to the fluorescence of the **BDP 4** (high fluorescence quantum yield  $\Phi_F = 0.73$ ). Time-resolved fluorescence measurements were performed by the time-correlated single-photon counting (TCSPC), and the decays are shown in Figure 8b. The fluorescence decay of **BDP 4** can be fitted with a single exponential function with a lifetime of 4.57 ns, which is characteristic of the BDP singlet excited state ( $^1\text{BDP}^*$ ). However, the fluorescence of the **BDP-C<sub>60</sub>** Dyad can only be fitted with three exponentials. Two short lifetimes (80 ps and 320 ps) have major contributions (respectively 41% and 58%). A long-lived decay time (4.57 ns) has a minor 1.1% amplitude contribution. The two short fluorescence lifetimes observed in the **BDP-C<sub>60</sub>** dyad could be associated with the presence of conformers with different donor-acceptor distances in the dyad (see paragraph above).<sup>61-62</sup> The longest lifetime component (4.57 ns) in the **BDP-C<sub>60</sub>** dyad which is similar to the lifetime of the **BDP 4** could be attributed to the presence of "free BDP" because of the breaking of the thiol-maleimide bond as already described in the literature.<sup>63</sup>

The radiative and non-radiative rate constants are related to the corresponding fluorescence quantum yield and decay by  $k_r = \Phi_F/\tau$  and  $k_{nr} = 1/\tau - k_r$ . Using the average lifetime obtained for the **BDP-C<sub>60</sub>** Dyad, we can notice that the radiative constant is very similar between the **BDP-C<sub>60</sub>** Dyad and the **BDP 4**, but significant enhancement of the non-radiative constant is observed for the **BDP-C<sub>60</sub>** Dyad. All these results strongly suggest that an interaction between the  $^1\text{BDP}^*$  and C<sub>60</sub> moiety in the **BDP-C<sub>60</sub>** Dyad exists through an electron transfer and/or energy transfer from the  $^1\text{BDP}^*$  to C<sub>60</sub>.

The ability of Förster resonance energy transfer (FRET) in the **BDP-C<sub>60</sub>** Dyad molecule can be estimated by using Förster theory. The Förster radius  $R_0$  was estimated to be 30 Å according to equation (1):<sup>64</sup>

$$R_0 = 0.2108 * [n^{-4} * \Phi_d * k^2 * \int_0^\infty I_D(\lambda) \varepsilon_A(\lambda) \lambda^4 d\lambda]^{1/6} \text{ (in \AA)} \quad (1)$$

Where  $n$  is the refractive index of the solvent ( $n_{\text{benzonitrile}} = 1.528$ ).  $\Phi_d$  is the emission quantum yield of the donor chromophore in the absence of the acceptor ( $\Phi_d = 0.73$  was used).  $k$  is the orientation factor. For a random distribution of dipole-dipole interaction,  $k^2$  is a constant equal to 2/3.  $I_D(\lambda)$  is the entire emission intensity normalized to unity.  $\varepsilon_A(\lambda)$  is the extinction coefficient of the acceptor.

Using the 30 Å R<sub>0</sub> value and the center-to-center distances of the **BDP-C<sub>60</sub>** Dyad determined from semi-empirical calculations. The rate of FRET for the different conformations could be estimated from equation (2), in which τ<sub>D</sub><sup>0</sup> is the excited state lifetime of the donor in the absence of the acceptor:

$$k_{FRET} = \frac{1}{\tau_D^0} \left[ \frac{R_0}{R} \right]^6 \quad (2)$$

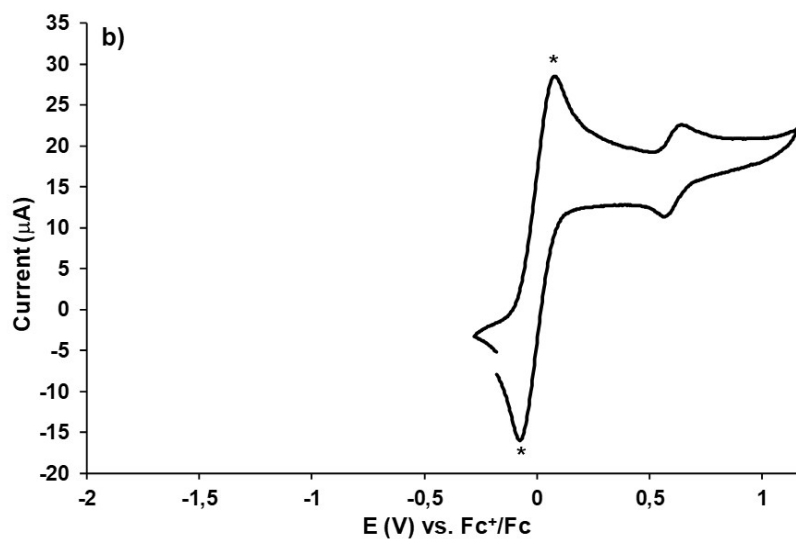
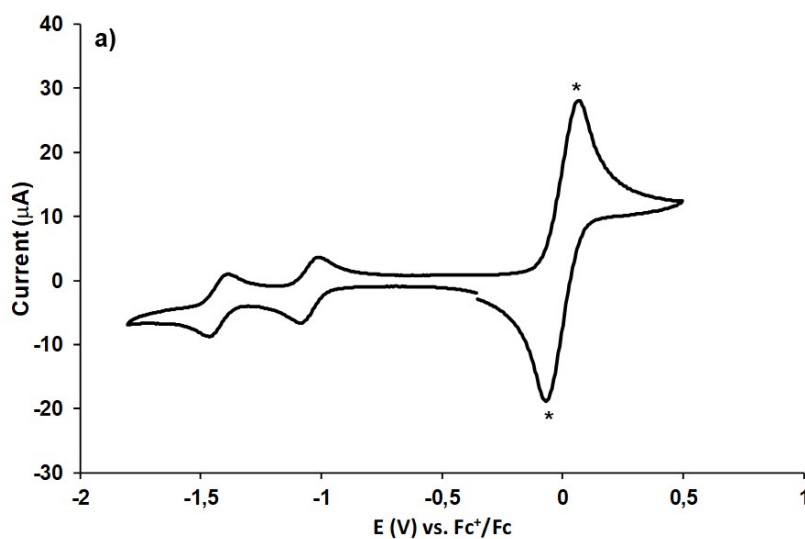
Among the different geometries, we decided to ignore the contribution of FRET for the folded conformers due to the short distance center-to-center in the **BDP-C<sub>60</sub>** Dyad molecule (8.8 Å). Indeed, the main relaxation pathways of the excited state is likely to be the ultrafast electron transfer (see 2.6 section). Thus, we have considered the two stretched linear geometry conformers with the donor-acceptor long distances (17.5 and 20.0 Å). Two approximate rate constants of excitation energy transfer k<sub>en1</sub> = 5.5×10<sup>9</sup> s<sup>-1</sup> and k<sub>en2</sub> = 2.1×10<sup>9</sup> s<sup>-1</sup> have been found, which correlate with 2 time-constants 180 and 460 ps, respectively. These results show a relevance with two short fluorescence lifetimes (80 and 320 ps), which were measured in TCSPC.

#### 2.4 Electrochemical and spectroelectrochemical studies

**Electrochemical Studies.** To estimate the energies of charge separated states formed by PET, the oxidation and reduction potentials of the **BDP 4**, **C<sub>60</sub> 2**, and **BDP-C<sub>60</sub>** Dyad were determined by cyclic voltammetry (CV). All experiments were performed at room temperature in DCM and in benzonitrile containing tetra *n*-butylammonium hexafluorophosphate (0.1M) as supporting electrolyte. A platinum disc electrode was used as a working electrode while a large platinum electrode was employed as the counter-electrode, Ag wire was used as a pseudoreference. Ferrocene (Fc) was added as an internal reference, and all the potentials were referenced relative to the Fc/Fc<sup>+</sup> couple. The half-wave potentials for the **BDP-C<sub>60</sub>** Dyad along with those of the **C<sub>60</sub> 2** and **BDP 4** derivatives are reported in table 2. The cyclic voltammograms of these compounds performed in DCM are presented in figure 9. In the cathodic region, the **BDP-C<sub>60</sub>** Dyad displays two reversible reduction waves (Figure 9c). By comparison with the reduction potentials of those of the **C<sub>60</sub> 2** (Figure 9a), these two waves are undoubtedly assigned to the two first reduction waves of the C<sub>60</sub>. In the anodic region, the **BDP-C<sub>60</sub>** Dyad gives a reversible oxidation wave that is assigned to the oxidation of the BDP moiety by comparison with the oxidation potential of the pristine **BDP 4** (Figure 9b). The cyclic voltammograms (Figure S15) were also recorded in benzonitrile to get the redox potentials which will be used for the driving force calculations. The cyclic voltammograms are broader

and less defined than in DCM. However, the **BDP-C<sub>60</sub>** Dyad displays in the cathodic region, the two first reversible reduction waves corresponding to the fullerene core while, in the anodic region, the oxidation wave is partially reversible and attributed to the BDP moiety.

Since that the values of the half-wave potentials of the **BDP-C<sub>60</sub>** dyad and the parents **BDP** and **C<sub>60</sub>** are identical (Table 2), we can conclude that no significant electronic interactions are found for the **BDP-C<sub>60</sub>** Dyad in the ground state.



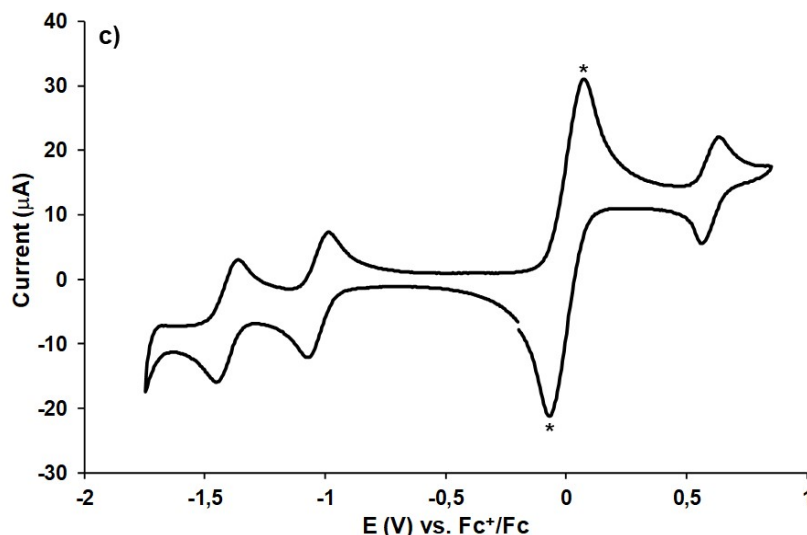


**Figure 9.** Cyclic voltammograms of a) C<sub>60</sub> **2**, b) BDP **4**, and c) BDP-C<sub>60</sub> Dyad in DCM. Oxidation and reduction waves of ferrocene, used as an internal standard, are denoted with an asterisk.

**Table 2.** Half-Wave Potentials (V) of C<sub>60</sub> **2**, BDP **4**, and BDP-C<sub>60</sub><sup>a</sup> Dyad.

Compound	DCM			Benzonitrile		
	E <sup>1/2</sup> <sub>1</sub>	E <sup>1/2</sup> <sub>2</sub>	E <sup>1/2</sup> <sub>3</sub>	E <sup>1/2</sup> <sub>1<sup>b,c</sup></sub>	E <sup>1/2</sup> <sub>2<sup>c</sup></sub>	E <sup>1/2</sup> <sub>3<sup>c</sup></sub>
fullerene <b>2</b>	-	-1.05	-1.43	-	-0.97	-1.37
BDP <b>4</b>	0.60	-	-	0.59	-	-
BDP-C <sub>60</sub> Dyad	0.60	-1.03	-1.41	0.59	-0.95	-1.38

<sup>a</sup> Versus ferrocene/ferrocenium. Experimental conditions: Compounds dissolved in anhydrous and oxygen-free DCM or benzonitrile solutions, 0,1M of *n*-Bu<sub>4</sub>NPF<sub>6</sub>, pseudo-reference electrode: Ag wire, working electrode: Pt, auxiliary electrode: Pt, scanning rate: 100mV·s<sup>-1</sup>. <sup>b</sup> partially reversible. <sup>c</sup> broader and less defined redox waves.

**Driving force calculation (free energy changes).** Driving forces for the electron transfer were estimated based on redox potential measurements. The free energy change of charge separated state ( $\Delta G_{CS}$ ) and charge recombination ( $\Delta G_{CR}$ ) in the BDP-C<sub>60</sub> Dyad system were estimated by using the Rehm-Weller approach,<sup>65</sup> according to equations (3-4):

$$-\Delta G_{CR} = e [E_{ox}^{1/2} - E_{red}^{1/2}] - \Delta G_S \quad (3)$$

$$-\Delta G_{CS} = E_{0,0} - (-\Delta G_{CR}) \quad (4)$$

$$\text{In which: } \Delta G_s = \frac{e^2}{4\pi\epsilon_0} \left[ \left( \frac{1}{2R_+} + \frac{1}{2R_-} \right) \Delta \left( \frac{1}{\epsilon_R} \right) - \frac{1}{R_{CC}\epsilon_R} \right]$$

Where  $\Delta G_s$  is the solvation energy,  $E_{ox}$  is the half-wave potential for one-electron oxidation of the electron-donor unit,  $E_{red}$  is the half-wave potential for one-electron reduction of the electron acceptor unit,  $E_{0,0}$  is the energy associated with the 0,0 optical transition (the corresponding midpoint of absorption and emission). The symbols  $\epsilon_0$  and  $\epsilon_R$  refer to vacuum permittivity and dielectric constant of the employed solvent, respectively. The symbols  $R_+$  and  $R_-$  refer to radii of the radical cation and radical anion species, respectively.  $R_{CC}$  is the center-to-center distance.

**Table 3.** Free energy change of charge separation ( $\Delta G_{CS}$ ) and charge recombination ( $\Delta G_{CR}$ ) of the **BDP-C<sub>60</sub>** Dyad in DCM and benzonitrile solvents.

	- $\Delta G_{CS}$ (eV)			- $\Delta G_{CR}$ (eV)		
	8.8	17.5	20.0	8.8	17.5	20.0
<b>R<sub>CC</sub> (Å)</b>	8.8	17.5	20.0	8.8	17.5	20.0
<b>Benzonitrile</b>	1.55	1.56	1.56	0.78	0.77	0.77
<b>DCM</b>	1.61	1.62	1.63	0.72	0.70	0.70

The calculated free energy changes for the most stable conformations are given in table 3. The values of  $\Delta G_{CS}$  and  $\Delta G_{CR}$  are negative in both DCM and benzonitrile solvents. These results show that electron transfer is thermodynamically favorable in both solvents.

According to the Förster and the driving force calculations, both the energy and electron transfers are likely to occur within the **BDP-C<sub>60</sub>** Dyad molecule and might be both responsible for the BDP donor quenching.

**UV-vis-NIR Spectroelectrochemistry studying for oxidized states of the BDP 4 and C<sub>60</sub> 2.** In order to assign the absorption spectra of the charge-separated state in the Dyad, spectroelectrochemistry experiments were carried out. The **BDP-C<sub>60</sub>** Dyad, pristine **BDP 4** and **C<sub>60</sub> 2** in DCM, display entirely reversible oxidation and reduction processes. Thus spectroelectrochemical absorptions were conducted in this solvent to locate the bands corresponding to the oxidized state of the **BDP 4** and reduced state of the **C<sub>60</sub> 2**.

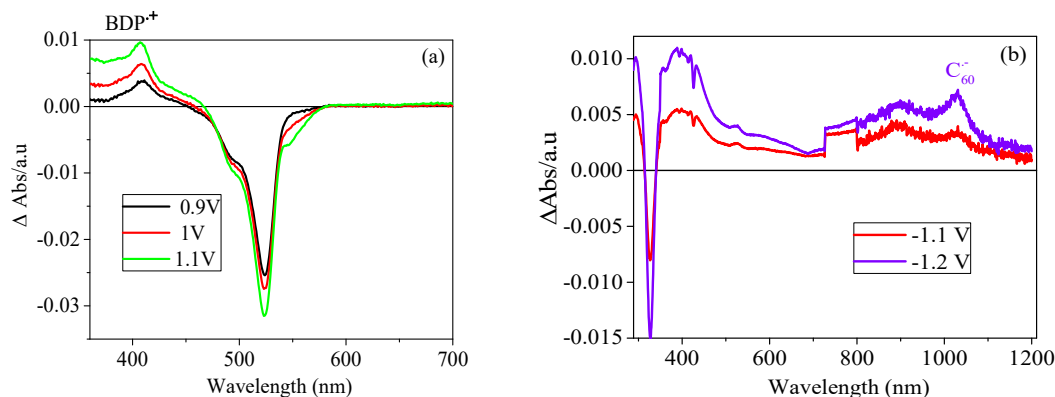


**Figure 10.** Differential absorption spectra relative to the neutral state of (a) the oxidized state of the **BDP 4** fragment (0.2 mM) and (b) the reduced state of the  $C_{60}$  **2** fragment (0.3 mM) in DCM under different potentials.

The spectroelectrochemical absorption spectra of the oxidized and reduced states of the pristine **BDP 4** and  $C_{60}$  **2** are shown in figure 10. As the applied voltage gradually increases from 0.9 V to 1.1 V, an increasing positive band at 407 nm is observed (Figure 10(a)). This band is characteristic of the oxidized state of the **BDP 4**.<sup>42</sup>

Figure 10(b) shows the NIR characteristic absorption bands of the reduced state of the  $C_{60}$  **2** pristine under voltage applied (-1.2 V). The first reduced state of  $C_{60}$  ( $C_{60}^{\bullet-}$ ) has a sharp absorption band at 1035 nm.<sup>14</sup> The characteristic wavelength and profile of the reduced  $C_{60}$  band is an ideal guide to support the distinction between energy transfer and electron transfer processes in femtosecond transient absorption experiments (see next section).

### 2.5. Femtosecond and nanosecond transient absorption studies

Transient absorption measurements were then conducted in order to decipher the overall excited state mechanisms in the **BDP- $C_{60}$**  dyad

First, 527 nm selective excitation of the BDP moiety in the **BDP- $C_{60}$**  Dyad was realized in argon-saturated benzonitrile in the femtosecond and nanosecond regimes (figure 10 and figure 11, respectively). The spectral range of the femtosecond TA data is [330-1400 nm] (see details in the experiment section 4.4) for delay times up to 2.7 ns. For comparison, the TA spectra of the **BDP 4** (femtosecond regime) and  $C_{60}$  **2** (nanosecond regime) fragments in argon-saturated benzonitrile are presented in figure S16 and S17.

**Identifying transient species spectro-kinetic signatures.** As seen in figure S16, the singlet excited state of the **BDP 4** is characterized by positive signatures at 340, 450 nm, and

broadband band in the infrared region with the maximum at 1278 nm. The appearance of a negative band at 540 nm corresponds to the ground state bleaching accompanied by some contributions from stimulated emission. Additionally, the singlet excited state of the C<sub>60</sub> **2** in the visible region shows broadband absorption band from 400 to 700 nm with the interference of a characteristic dip at 427 nm related to the ground state bleaching. The triplet-excited state of the C<sub>60</sub> **2** (<sup>3</sup>C<sub>60</sub><sup>\*</sup>) in argon-deaerated benzonitrile was found at 700 nm in nanosecond TA with the lifetime 6.6 μs (Figure S17).

**Deactivation processes for the BDP-C<sub>60</sub> Dyad.** In figure 11, for the sake of simplicity, the TA spectra of BDP-C<sub>60</sub> Dyad are divided into four temporal windows distinguishing UV-Vis [330-600 nm] and NIR regions [600 -1400 nm] (eight panels in total). In parallel, we performed a robust global fitting analysis choosing eight characteristic wavelengths with all the details given in figure S18, S19 and table S1. The choice of the wavelength has been made for following reasons: the kinetic traces at 344, 427 and 1278 nm correspond to the <sup>1</sup>BDP<sup>\*</sup>; the triplet excited state of C<sub>60</sub> (<sup>3</sup>C<sub>60</sub><sup>\*</sup>) has an absorption band at 700 nm (see above) and the singlet excited state of C<sub>60</sub> (<sup>1</sup>C<sub>60</sub><sup>\*</sup>) can be probed at about 910 nm in the NIR region.<sup>14, 35, 41</sup> Negative absorption bands at 495 and 555 nm are assigned to the ground state bleaching and stimulated emission, respectively. And, finally kinetics of charge transfer state can be followed at 1045 nm corresponding to the first reduced state of C<sub>60</sub> (C<sub>60</sub><sup>•-</sup>) as shown in the spectroelectrochemical measurements. The global fitting procedure converged with five characteristic times (with acceptable error bars) 100 fs, 4 ps, 50 ps, 230 ps and 1600 ps (See Table S1). These times are assigned here to the different conformers reported from the previous section.

As seen in the first panels ([-0.3;0.5 ps]), in parallel to the rise of the <sup>1</sup>BDP<sup>\*</sup>, the clear rise of C<sub>60</sub><sup>•-</sup> is observed, providing evidence for an ultrafast charge transfer process from the Franck-Condon (FC) region. This ultrafast charge transfer process, with a probable rising time of 100 fs, may correspond to conformer 1, with the shorter donor-acceptor distance of 8.8 Å as illustrated in figure 12.

In the second temporal window ([0.5-100ps]), a concomitant decrease is observed of the <sup>1</sup>BDP<sup>\*</sup> with an additional rise of the C<sub>60</sub><sup>•-</sup> band with a characteristic time of 4 ps. This process is assigned for an additional charge transfer process from <sup>1</sup>BDP<sup>\*</sup> to C<sub>60</sub>. Furthermore, the decay of <sup>1</sup>BDP<sup>\*</sup> is also concomitant with a rise of both <sup>1</sup>C<sub>60</sub><sup>\*</sup> (right panel) and a bleaching band recovery (left panel) with a characteristic time of 50 ps. Note that this time is close to the 80 ps characteristic time found from the TCSPC experiment. We can safely assign this process as energy transfer from <sup>1</sup>BDP<sup>\*</sup> to C<sub>60</sub>, that may occur with the conformer 2. Similarly, the third

panel [100-300 ps], shows similar decays of <sup>1</sup>BDP\* with ground state recovery, with the characteristic time of 230 ps (related with 320 ps TCSPC) assigned as energy transfer for conformer 3.

For the final temporal window [300-2700 ps], the decay of the <sup>1</sup>C<sub>60</sub>\* band formed simultaneously with the ground state recovery and a clear rise of <sup>3</sup>C<sub>60</sub>\* giving evidence for the intersystem crossing (ISC) of <sup>1</sup>C<sub>60</sub>\* to <sup>3</sup>C<sub>60</sub>\* with a characteristic time of 1.6 ns, which is exactly the same time reported by Palit et al. However, as seen on the 2.7 ns trace, the C<sub>60</sub>\* is still present, indicating a longer back charge transfer recombination.

Nanosecond TA of the **BDP-C<sub>60</sub>** Dyad in figure 12 (a) presents a longer rising time of <sup>3</sup>C<sub>60</sub>\* at 700 nm (approximately 8.5 ns) simultaneously with the decay trace at 400 nm corresponding to the BDP\*+ state which is confirmed by the kinetic trace global fitting (see figure 12b). Therefore, it should be thought that the charge transfer state populated on the <sup>3</sup>C<sub>60</sub>\* state with the lifetime of the order of a few nanoseconds. The second time constant of 5.1 μs obtained for all traces in figure 12 (b) shows the relaxation of <sup>3</sup>C<sub>60</sub>\* to the ground state. The population on the triplet excited state of C<sub>60</sub> from the charge separated state has already been described in the literature.<sup>35, 43</sup>

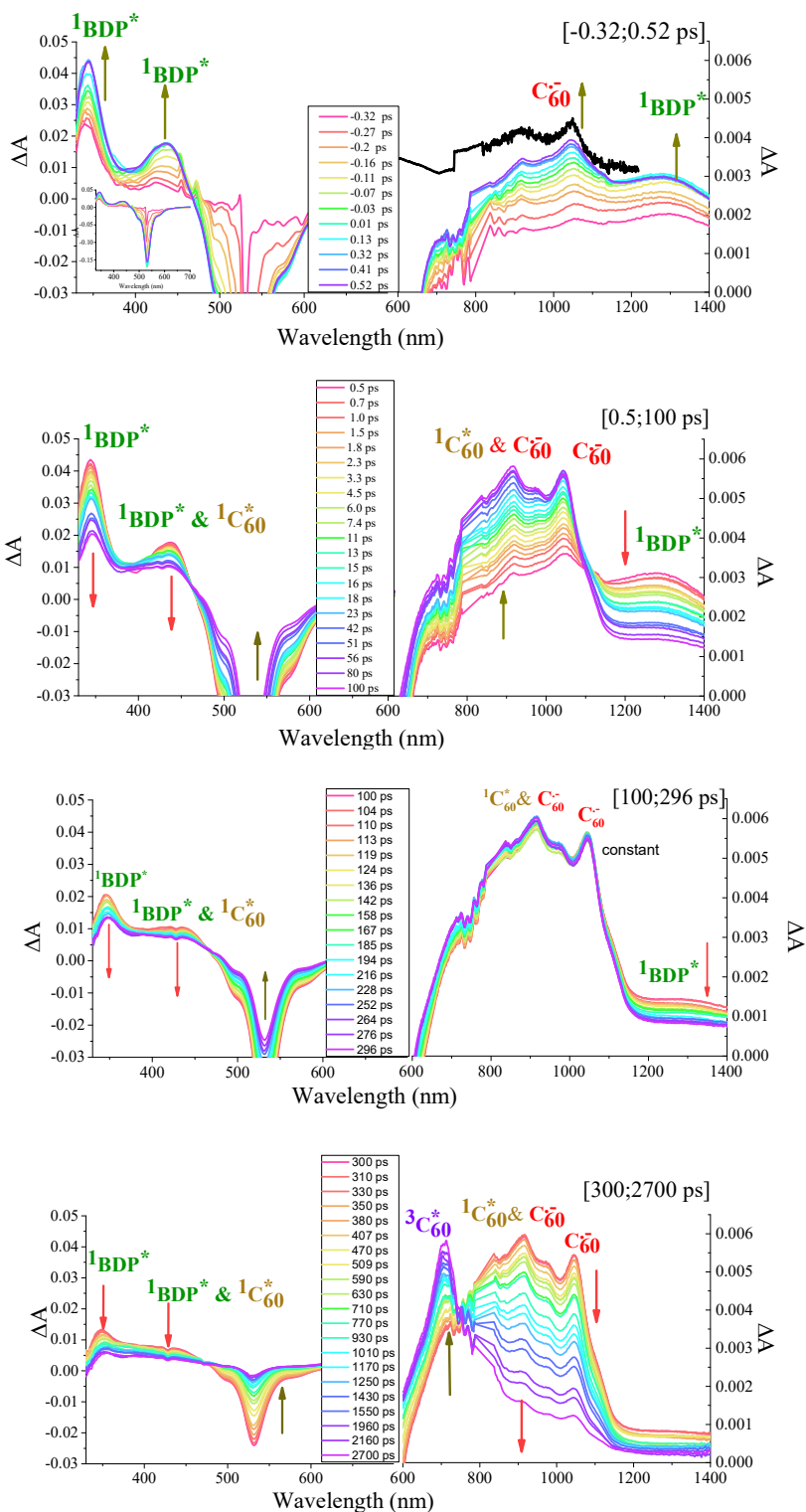


**Figure 11.** Femtosecond TA spectra at the indicated delay times and kinetic traces of the BDP- $C_{60}$  Dyad ( $5.5 \times 10^{-5}$  M) in argon saturated benzonitrile,  $\lambda_{\text{exc}} = 527$  nm. A difference spectrum after reduction of the BDP- $C_{60}$  Dyad by spectroelectrochemistry is also presented

(black curve) for comparison. Abbreviations: Singlet excited state of the BDP (<sup>1</sup>BDP\*); singlet excited state of the C<sub>60</sub> (<sup>1</sup>C<sub>60</sub>\*); triplet excited state of C<sub>60</sub> (<sup>3</sup>C<sub>60</sub>\*); charge transfer state of C<sub>60</sub> (C<sub>60</sub><sup>•-</sup>);

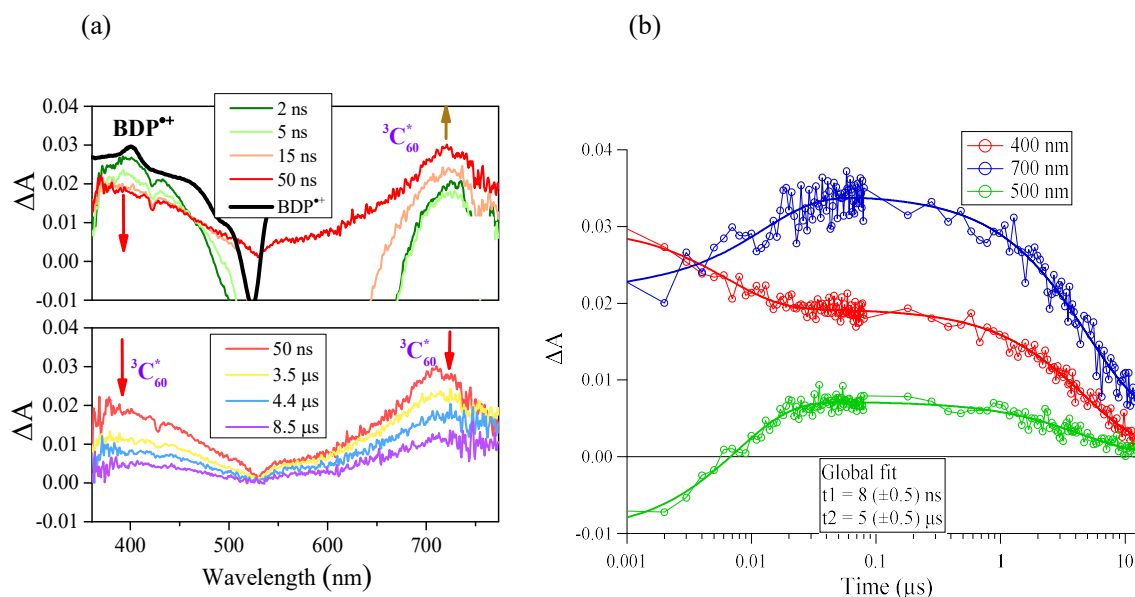


**Figure 12.** (a) Nanosecond TA spectra of the **BDP-C<sub>60</sub>** Dyad ( $5 \times 10^{-6}$  M) in argon saturated benzonitrile at the indicated delay times. (b) Kinetic traces fitting 700 nm, 400 nm, and 500 nm,  $\lambda_{\text{exc}}$  527 nm

The different photoinduced events of the **BDP-C<sub>60</sub>** Dyad in benzonitrile are then summarized in figure 12. The energy levels of the **BDP-C<sub>60</sub>** Dyad intermediates in benzonitrile are obtained from the excited state energies and the redox potentials of the donor and acceptor units. In this diagram, the donor BDP moiety is mainly excited. The energy of the radical ion pairs and the <sup>1</sup>C<sub>60</sub>\* are higher than that of the <sup>3</sup>C<sub>60</sub>\* state. Thus it matches with the results in femtosecond TA that both C<sub>60</sub><sup>•-</sup> and <sup>1</sup>C<sub>60</sub>\* populate on the <sup>3</sup>C<sub>60</sub>\* state before returning to the ground state.

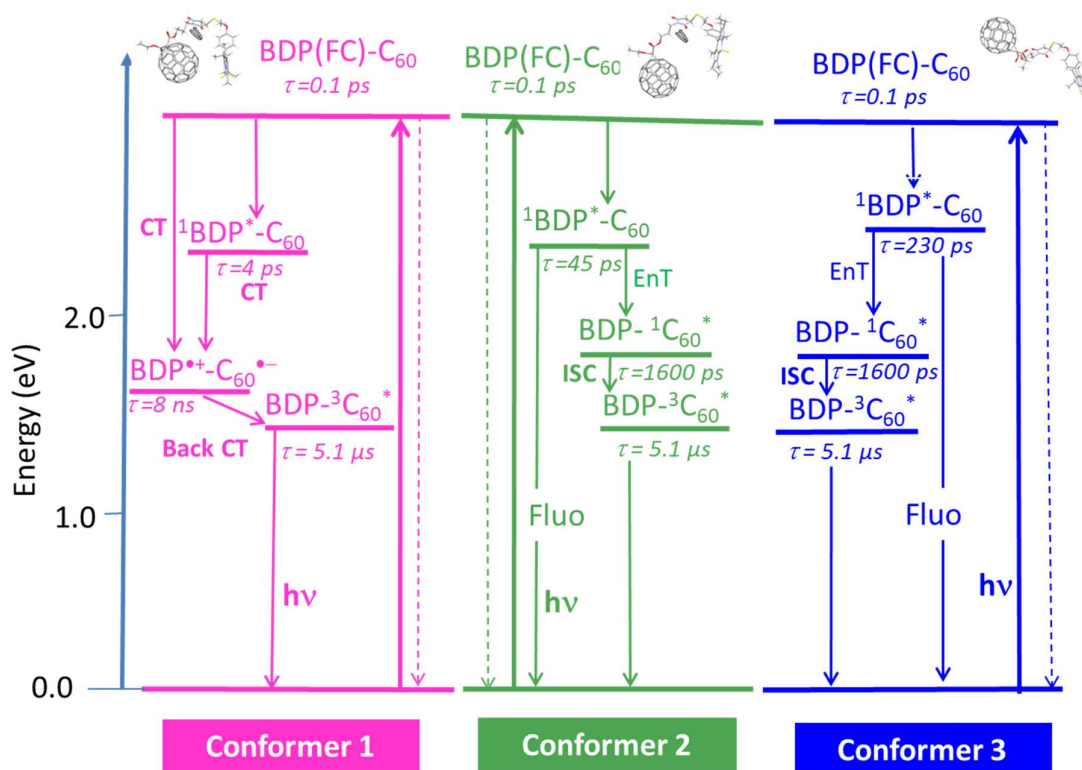


**Figure 13.** Energy level diagram presenting the photoinduced processes obtained following laser excitation ( $\lambda_{\text{exc}} = 527 \text{ nm}$ ) of the three conformers of **BDP-C<sub>60</sub>** Dyad in benzonitrile. Abbreviations: FC = Frank-Condon,  $\tau$  = lifetime, EnT= Energy transfer, CT = charge transfer, Back CT = back charge transfer, ISC = intersystem crossing, Fluo = fluorescence; Energies:  $^1\text{BDP}^* = 2.33\text{eV}$ ,  $^1\text{C}_{60}^* = 1.75\text{eV}^{51, 59}$ ,  $^3\text{C}_{60}^* = 1.55\text{eV}^{59, 66}$

### 3. Conclusions

We have presented herein, the synthesis and complete characterization, including semi-empirical and DFT calculations, electrochemical and photophysical studies, of a new molecular **BDP-C<sub>60</sub>** Dyad containing a BDP chromophore covalently linked to a fullerene acceptor. The geometries of at least three conformations of the **BDP-C<sub>60</sub>** Dyad is deduced from semi-empirical calculations. Electrochemical studies allow the estimation of the energy of intermediate states, whereas spectroelectrochemistry measurements in the UV-vis-NIR region give the spectral signature of the acceptor in a reduced state, allowing assignment of the photoinduced charge-separated state. The strong fluorescence quenching and the decrease of the fluorescence lifetime in the **BDP-C<sub>60</sub>** Dyad are evidence of an interaction between  $^1\text{BDP}^*$  and C<sub>60</sub> moieties. The two short fluorescence lifetimes were associated with two conformers with donor-acceptor distances of 17.5 and 20.0 Å. These lifetimes are in good agreement with

the two-time constants of energy transfer in femtosecond TA experiments, as well as in FRET calculations.

Ultrafast charge transfer from the Franck-Condon and <sup>1</sup>BDP\* states to the C<sub>60</sub> moiety was evidenced for the folded conformer with the BDP-C<sub>60</sub> distance of 8.8 Å. The charge-separated state resulting from photoinduced electron transfer persists with a relatively long lifetime of several nanoseconds. The spectroscopic and electrochemical results have allowed a better understanding of all relaxation pathways of the **BDP-C<sub>60</sub>** Dyad, which is an important step toward the improvement of supramolecular systems and development for energy conversion.

#### 4. Experimental section

##### 4.1 Synthesis

**General Methods.** All reagents were used directly without further purification. The purity of fullerene C<sub>60</sub> was 99.5+%. DCM was dried on CaCl<sub>2</sub> and distilled over CaH<sub>2</sub> prior to use. Toluene was distilled over NaH prior to use. All other solvents were used as received. Column chromatography was performed using silica gel 60 (0.040-0.063mm). Thin layer chromatography (TLC) was performed on aluminium sheets coated with silica gel 60 F254. NMR spectra were performed in CDCl<sub>3</sub>, chemical shifts were referenced to this internal solvent (7.26 for <sup>1</sup>H and 77.16 ppm for <sup>13</sup>C). High-Resolution ESI-MS mass spectra were obtained with a Qtof analyser type.

*Synthesis of 1.* Fullerene-maleimide **1** was prepared in five steps according to a previously published procedure.<sup>48</sup>

*Synthesis of 2.* In a round bottomed flask, 50mg of protected fullerene-maleimide **1** was introduced with 3 mL of dried toluene. The reaction mixture was stirred overnight at 110°C and evaporated to dryness. Purification of the black residue by column chromatography (SiO<sub>2</sub>, DCM) gave 44mg of a black solid in 94% yield. <sup>1</sup>H NMR (300MHz, CDCl<sub>3</sub>) δ 2.03 (t, 1H, J = 2.6 Hz, H<sub>a</sub>), 2.05-2.13 (m, 2H, H<sub>d</sub>), 2.13-2.21 (m, 2H, H<sub>j</sub>), 2.42 (dt, 2H, J = 6.9 Hz, J = 2.6 Hz, H<sub>c</sub>), 3.75 (t, 2H, J = 6.8 Hz, H<sub>k</sub>), 4.52 (t, 2H, J = 6.2 Hz, H<sub>i</sub>), 4.65 (t, 2H, J = 6.2 Hz, H<sub>e</sub>), 6.75 (s, 2H, H<sub>m</sub>); <sup>13</sup>C NMR (75 MHz, CDCl<sub>3</sub>) δ 15.4 (C<sub>c</sub>), 27.5 (C<sub>d</sub>), 27.9 (C<sub>j</sub>), 35.0 (C<sub>k</sub>), 64.9 (C<sub>i</sub>), 66.0 (C<sub>e</sub>), 69.8 (C<sub>a</sub>), 71.6 (C<sub>sp3</sub> C<sub>60</sub>), 82.7 (C<sub>b</sub>), 134.4 (C<sub>m</sub>), [139.0, 139.3, 141.2, 142.1, 142.4, 143.1, 143.2, 143.22, 144.0, 144.76, 144.79, 144.81, 144.84, 145.1, 145.2, 145.22, 145.3, 145.4, 145.42 (C<sub>sp2</sub> C<sub>60</sub>)], 163.6 (C<sub>f</sub>, C<sub>h</sub>), 170.8 (C<sub>l</sub>); HRMS (ESI+) m/z calcd for C<sub>75</sub>H<sub>15</sub>NO<sub>6</sub>Na : 1048.0797 [M + Na<sup>+</sup>], found 1048.0863.

*Synthesis of 3.* In a three-necked flask, 4-(2-bromoethoxy) benzaldehyde (0.66g, 2.87mmol) was dissolved in anhydrous DCM (50 mL), argon was bubbled through the solution for 10 min. To this oxygen-free solution were added successively kryptopyrrole (0.9ml, 6.60mmol) and trifluoroacetic acid (0.6mL). The reaction mixture was stirred for 2 hours and chloranil (0.71g, 2.87mmol) was then added, the reaction was further stirred for 5 minutes. N,N-Diisopropylethylamine (DIPEA, 3.5mL, 20.1mmol) was then added to the mixture that was left to stir for 15 minutes. Boron trifluoride etherate (3.9mL, 31.6mmol) was finally introduced to the reaction. The resulting solution was stirred at room temperature for 2 hours and evaporated to dryness. Purification of the black-red residue by column chromatography (SiO<sub>2</sub>, EP/DCM 1:2) gave 625mg of a red solid in 44% yield. <sup>1</sup>H NMR (300MHz, CDCl<sub>3</sub>) δ 0.98 (t, 6H, J = 7.6 Hz, H<sub>B</sub>), 1.32 (s, 6H, H<sub>D</sub>), 2.30 (q, 4H, J = 7.6 Hz, H<sub>C</sub>); 2.52 (s, 6H, H<sub>A</sub>), 3.70 (t, 2H, J = 6.2 Hz, H<sub>H</sub>), 4.36 (t, 2H, J = 6.2 Hz, H<sub>G</sub>), 7.02 (d, 2H, J = 8.7 Hz, H<sub>F</sub> or H<sub>E</sub>), 7.19 (d, 2H, J = 8.6 Hz, H<sub>F</sub> or H<sub>E</sub>); <sup>13</sup>C NMR (75 MHz, CDCl<sub>3</sub>) δ 12.0 (C<sub>D</sub>), 12.6 (C<sub>A</sub>), 14.8 (C<sub>B</sub>), 17.2 (C<sub>C</sub>), 29.1 (C<sub>H</sub>), 68.1 (C<sub>G</sub>), 115.4 (C<sub>E</sub> or C<sub>F</sub>), 128.9, 129.8 (C<sub>E</sub> or C<sub>F</sub>), 131.1, 132.9, 138.5, 153.8, 158.7; <sup>19</sup>F NMR (188 MHz, CDCl<sub>3</sub>) δ -145.81 (q, J = 33.2 Hz); <sup>11</sup>B RMN (96 MHz, CDCl<sub>3</sub>) δ 2.25 (t, J = 33.5 Hz); HRMS (ESI+) m/z calcd for C<sub>25</sub>H<sub>31</sub>BBrF<sub>2</sub>N<sub>2</sub>O : 505.1660 [M+H]<sup>+</sup>, found 505.1665.

*Synthesis of 4.* To a two-necked flask was added BDP-bromide **3** (590mg, 1.18mmol) and potassium thioacetate (280mg, 2.47mmol) in anhydrous acetone (25mL). The reaction mixture was stirred overnight under reflux at 60°C. The crude product was taken up in DCM and washed with water and finally dried over MgSO<sub>4</sub>. Purification of the crude product by column chromatography (SiO<sub>2</sub>, DCM/EP 1:1.3 then 1:1) gave 475mg of a red solid in 81% yield. <sup>1</sup>H NMR (300 MHz, CDCl<sub>3</sub>) δ 0.98 (t, 6H, J = 7.5 Hz, H<sub>B</sub>), 1.32 (s, 6H, H<sub>D</sub>), 2.30 (q, 4H, J = 7.5 Hz, H<sub>C</sub>), 2.40 (s, 3H, H<sub>I</sub>); 2.52 (s, 6H, H<sub>A</sub>), 3.32 (t, 2H, J = 6.5 Hz, H<sub>H</sub>), 4.15 (t, 2H, J = 6.2 Hz, H<sub>G</sub>), 7.01 (d, 2H, J = 8.6 Hz, H<sub>F</sub> or H<sub>E</sub>); 7.17 (d, 2H, J = 8.6 Hz, H<sub>F</sub> or H<sub>E</sub>); <sup>13</sup>C NMR (75 MHz, CDCl<sub>3</sub>) δ 12.0 (C<sub>D</sub>), 12.6 (C<sub>A</sub>), 14.8 (C<sub>B</sub>), 17.2 (C<sub>C</sub>), 28.5 (C<sub>H</sub>), 30.8 (C<sub>I</sub>), 66.7 (C<sub>G</sub>), 115.2 (C<sub>F</sub>), 128.5, 129.7 (C<sub>E</sub>), 131.3, 132.8, 138.5, 140.2, 153.7, 158.9, 195.5 (C=O); <sup>19</sup>F NMR (188 MHz, CDCl<sub>3</sub>) δ -145.76 (q, J = 35.0 Hz); <sup>11</sup>B RMN (96 MHz, CDCl<sub>3</sub>) δ 2.24 (t, J = 35.0 Hz); HRMS (ESI+) m/z calcd for C<sub>27</sub>H<sub>33</sub>BF<sub>2</sub>N<sub>2</sub>O<sub>2</sub>S : 497.2360 [M<sup>+</sup>], found 497.2361.

**Synthesis of 6.** In a round bottomed flask, a BDP-thioacetate **4** (80mg, 0.16 mmol) was dissolved in a mixture of dried MeOH/DCM (10mL:6 mL), argon was bubbled through the solution for 20 min. Potassium carbonate (22mg, 0.16mmol) was then added to this oxygen-free solution, and the resulting reaction mixture was stirred for 1 hour. Potassium carbonate

was filtered and the solvent was evaporated under reduced pressure. Dried DCM (5mL) was then added to the solid, and argon was bubbled through the solution for 10 min. To this oxygen-free solution was added tributylphosphine (0.04mL, 0.16mmol). The resulting reaction mixture was stirred for 30 minutes at room temperature and evaporated to dryness. Purification of the crude product by column chromatography (SiO<sub>2</sub>, DCM/EP: 3/1) gave 60mg of a red solid in 82% yield. <sup>1</sup>H NMR (300 MHz, CDCl<sub>3</sub>) δ 0.98 (t, 6H, J = 7.5 Hz, H<sub>B</sub>), 1.33 (s, 6H, H<sub>D</sub>), 1.74 (t, 1H, J = 8.5 Hz, H<sub>I</sub>), 2.30 (q, 4H, J = 7.5 Hz, H<sub>C</sub>), 2.53 (s, 6H, H<sub>A</sub>), 2.96 (dt, 2H, J = 8.4Hz, J = 6.4Hz, H<sub>H</sub>), 4.18 (t, 2H, J = 6.4Hz, H<sub>G</sub>), 7.01 (d, 2H, J = 8.6Hz, H<sub>E</sub> or H<sub>F</sub>), 7.18 (d, 2H, J = 8.5Hz, H<sub>E</sub> or H<sub>F</sub>); <sup>19</sup>F NMR (282MHz, CDCl<sub>3</sub>) δ -145.73 (q, J = 34.8Hz); <sup>11</sup>B RMN (96 MHz, CDCl<sub>3</sub>) δ 2.25 (t, J = 35.1 Hz); HRMS (ESI+) m/z calcd for C<sub>25</sub>H<sub>31</sub>BF<sub>2</sub>N<sub>2</sub>OS :456.2218 [M + Na<sup>+</sup>], found 456.2229.

*Synthesis of the BDP-C<sub>60</sub> Dyad.* In a round bottomed flask, a BDP-thiol **6** (60mg, 0.13mmol) was dissolved in 10mL of dried DCM, argon was bubbled through the solution for 30 min. To this oxygen-free solution were added successively the fullerene-maleimide **2** (67mg, 0.065mmol) and 0.03mL (0.22mmol) of triethylamine. The reaction mixture was stirred overnight at room temperature under argon and evaporated to dryness. Purification of the crude product by column chromatography (SiO<sub>2</sub>, DCM/Et<sub>2</sub>O: 96/2) gave 83mg of a black solid in 87% yield. <sup>1</sup>H NMR (300 MHz, CDCl<sub>3</sub>) δ 0.98 (t, 6H, J = 7.5 Hz, H<sub>B</sub>), 1.32 (s, 6H, H<sub>D</sub>), 2.04 (t, 1H, J = 2.6 Hz, H<sub>a</sub>), 2.05 – 2.12 (m, 2H, H<sub>d</sub>), 2.15-2.22 (m, 2H, H<sub>j</sub>), 2.30 (q, 4H, J = 7.4 Hz, H<sub>C</sub>), 2.42 (dt, 2H, J = 6.9 Hz, J = 2.6 Hz, H<sub>c</sub>), 2.52 (s, 6H, H<sub>A</sub>), 2.61 (dd, 1H, J = 18.8 Hz, J = 3.5 Hz, H<sub>m2</sub>), 3.12-3.21 (m, 1H, H<sub>H2</sub>), 3.29 (dd, 1H, J = 18.7Hz, J = 9.0Hz, H<sub>m1</sub>), 3.43-3.50 (m, 1H, H<sub>H1</sub>), 3.78 (dt, 2H, J = 6.7Hz, J = 2.4Hz, H<sub>k</sub>), 4.04 (dd, 1H, J = 9.0Hz, J = 3.5Hz, H<sub>n</sub>), 4.23-4.37 (m, 2H, H<sub>G</sub>), 4.54 (m, 2H, H<sub>i</sub>), 4.64 (t, 2H, J = 6.2Hz, H<sub>e</sub>), 7.01 (d, 2H, J = 8.6 Hz, H<sub>E</sub> or H<sub>F</sub>), 7.17 (d, 2H, J = 8.6 Hz, H<sub>E</sub> or H<sub>F</sub>); <sup>13</sup>C NMR (75 MHz, CDCl<sub>3</sub>): δ 12.1 (C<sub>D</sub>), 12.6 (C<sub>A</sub>), 14.8 (C<sub>B</sub>), 15.4 (C<sub>d</sub>), 17.2 (C<sub>C</sub>), 27.1, 27.5, 31.3, 36.2, 36.5, 39.5 (C<sub>n</sub>), 52.1 (C<sub>g</sub>), 65.0 (C<sub>i</sub>), 66.0 (C<sub>e</sub>), 67.7, 69.9 (C<sub>a</sub>), 71.6 (C<sub>sp3</sub> C<sub>60</sub>), 82.6 (C<sub>b</sub>), 115.2 (C<sub>E</sub> or C<sub>F</sub>), 128.7 (C<sub>sp2</sub> BDY), 129.8 (C<sub>E</sub> or C<sub>F</sub>); 131.3, 132.8 (C<sub>sp2</sub> BDY), 138.5 (C<sub>sp2</sub> C<sub>60</sub>), 138.81 (C<sub>sp2</sub> BDY), 138.83 (C<sub>sp2</sub> C<sub>60</sub>), 139.5 (C<sub>sp2</sub> C<sub>60</sub>), 140.1 (C<sub>sp2</sub> BDY); [141.2, 142.0, 142.1, 142.4, 143.1, 143.19, 143.23, 143.25, 144.02, 144.04, 144.81, 144.84, 144.86, 145.0, 145.1, 145.2, 145.32, 145.34, 145.37, 145.42 (C<sub>sp2</sub> C<sub>60</sub>)]; 153.8, 158.9 (C<sub>sp2</sub> BDY); 163.5, 163.7 (C<sub>f</sub>, C<sub>h</sub>); 174.6, 176.9 (C<sub>l</sub>). <sup>19</sup>F NMR (282 MHz, CDCl<sub>3</sub>) δ -145.69 (q, J = 34.7 Hz); <sup>11</sup>B RMN (96 MHz, CDCl<sub>3</sub>) δ 2.23 (t, J = 35.9 Hz); HRMS (ESI+) m/z calcd for C<sub>100</sub>H<sub>46</sub>BF<sub>2</sub>N<sub>3</sub>O<sub>7</sub>S: 1482.3196 [M+H<sup>+</sup>], found 1482.3147.

## 4.2 Spectra measurements

The UV/vis absorption spectra were implemented on a Varian Cary5000 spectrophotometer and corrected emission spectra were carried out on a Horiba FluoroMax+ in a right-angle configuration. The fluorescence quantum yields were measured relatively to Rhodamine 590 in ethanol  $\Phi_F = 0.95$  as a reference. Fluorescence intensity decays were measured by the TCSPC method with femtosecond laser excitation using a Spectra-Physics setup composed of a Titanium Sapphire laser (Tsunami, Spectra-Physics) pumped by a doubled Nd:YVO<sub>4</sub> laser (Millennia Xs, Spectra-Physics). Light pulses at 1000nm were selected by optoacoustic crystals at a repetition rate of 4MHz, and a doubling crystal is used to reach the excitation wavelength of 500 nm. Fluorescence photons were detected (at 90°) through a monochromator using a Hamamatsu MCP R3809U photomultiplier, connected to a SPC-630 TCSPC module from Becker & Hickl. The fluorescence data were analyzed by a nonlinear least-squares method with the aid of Globals software package developed at the Laboratory of Fluorescence Dynamics at the University of Illinois, Urbana-Champaign.

#### 4.3 Electrochemistry, Spectroelectrochemical absorption

**Cyclic Voltammetry.** BDP thioacetate **4**, fullerene **2**, and **BDP-C<sub>60</sub>** Dyad were dissolved in anhydrous DCM or benzonitrile containing 0,1 M of n-Bu<sub>4</sub>NPF<sub>6</sub> into a standard three-electrode cell under a nitrogen atmosphere. CV measurements were then undertaken with a potentiostat using a platinum disc electrode and a large platinum counter-electrode to obtain the potentials versus an Ag wire pseudo-reference electrode. The latter was separated from the bulk solution using a capillary with frit. Potentials were calibrated versus ferrocene/ferrocenium.

**Spectroelectrochemical absorption.** Spectra are recorded in a Horiba Cary 5000 spectrophotometer using an OTTLE cell<sup>67</sup> composed of a Pt minigrid working electrode, a Pt wire counter-electrode and an Ag wire pseudo-reference electrode connected to a potentiostat (CHInstruments 600). The sample is a x mM solution of BDP4 in 0.1 M hexafluorophosphate tetraethylammonium in dichloromethane. Background is made on the cell filled with the electrolyte solution only.

#### 4.4 Transient absorption measurement

- Femtosecond transient absorption:

Femtosecond UV-vis-NIR transient absorption spectra were collected on a commercially available system (Ultrafast Systems, Helios). The ultrafast laser system consists of a short-pulse titanium-sapphire oscillator (Mai-Tai, Spectra-Physics, 70 fs) followed by a high-energy

titanium-sapphire regenerative amplifier (Spitfire Ace, Spectra-Physics, 100 fs). The 800 nm beam was split into two beams to generate: (1) pump ( $\lambda_{exc} = 527$  nm) in the optical parametric amplifier (Topas Prime with NirUVis frequency mixer) and (2) probe pulses - white light continuum in UV-vis-NIR (330 – 1370 nm) range, using a CaF<sub>2</sub> plate (330 – 660 nm), sapphire (440 – 780 nm) and YAG crystal (830 – 1345 nm). The pump pulse energy was 0.4  $\mu$ J. The absorbance was close to 0.86 at the excitation wavelength in a 2 mm optical path quartz cell. The sample solution was stirred by a Teflon-coated bar; no significant degradation was observed. Before experimentation, the solution was saturated with argon. The entire set of pump-probe delay positions was repeated at least twice, to ensure data reproducibility. The transient absorption data were corrected for the chirp of the white light continuum. The instruments response function (IRF) was about 200 fs (FWHM) in all experiments.

- Nanosecond transient absorption

Nanosecond transient absorption measurements were measured on a home-built setup which has been described previously.<sup>68</sup> Briefly, the Nd:YAG pumped optical parametric oscillator (OPO) laser is used for sample excitation at 527nm with the energy of  $\sim$ 5mJ per pulse. The pump operates at 10Hz. After excitation, the sample is probed with a pulsed nanosecond white light continuum laser (LEUKOS) at a repetition rate of 20Hz. The probe beam is split into two arms, one for probing the sample and the other for reference in order to compensate for the pulse to pulse energy fluctuation. The probing arm after passing through the sample is coupled to a round to linear optical fibre bundle before being analyzed with a spectrograph SPEX 270 M (Jobin–Yvon). The detection of the dispersed white light is performed with an intensified CCD (ICCD) detector PIMAX 4 (Princeton Instrument). The transient absorption spectra can be calculated using the following formula:

$$\Delta OD = \log_{10} \left( \frac{S_{ref}^{on}}{S_{ref}^{off}} \times \frac{S_{prob}^{off}}{S_{prob}^{on}} \right) \quad (4)$$

Where  $S_{ref}^{on}$  and  $S_{ref}^{off}$  are reference spectra when the pump laser is on and off relatively,  $S_{prob}^{off}$  and  $S_{prob}^{on}$  are probe spectra when the pump laser is on and off relatively.

ASSOCIATED CONTENT

**Supporting Information.** The normalized absorption spectrum of the fullerene **2** in benzonitrile; the cyclic voltammograms the fullerene **2**, BDP **4**, and **BDP-C<sub>60</sub>** Dyad in benzonitrile; Femtosecond transient absorption spectra of the BDP **4** and fullerene **2** pristine in

benzonitrile at the indicated delay times; Nanosecond transient absorption spectra of the fullerene **2** in Ar-saturated benzonitrile at the indicated delay times; Kinetic traces (scattered points) of the fullerene **2** at 710nm in the comparison between Ar-saturated and air in benzonitrile. The supporting information is available free of charge via the internet at <http://pubs.asc.org>

#### AUTHOR INFORMATION

##### **Corresponding Author**

\*E-mail: [minh-huong.ha-thi@u-psud.fr](mailto:minh-huong.ha-thi@u-psud.fr).

\*E-mail: [emmanuel.allard@uvsq.fr](mailto:emmanuel.allard@uvsq.fr)

\*E-mail: [rachel.meallet-renault@u-psud.fr](mailto:rachel.meallet-renault@u-psud.fr).

##### **Present Addresses**

##### **Author Contributions**

##### **Funding Sources**

##### **Notes**

#### ACKNOWLEDGMENT

This work was supported by the CNRS (PICS project n° 08198), the LabEx PALM ANR-10LABX-0039-PALM and CHARMMMAT ANR-11-LABX-0039. T.-T.T is grateful to the Vietnamese government for the scholarship (2016-2019)

#### ABBREVIATIONS

BDP, BODIPY; C<sub>60</sub>, Fullerene; DFT, density functional theory; PET, photoinduced electron transfer; CV, cyclic voltammetry; DCM, dichloromethane; FRET, Förster energy transfer; NMR, Nuclear Magnetic Resonance; TCSPC, time-correlated single-photon counting; ET, electron transfer; EnT, energy transfer; CT, charge transfer; CR, charge recombination; ISC, intersystem crossing, k<sub>T</sub>, rate constant for deactivation of triplet excited state of the C<sub>60</sub>; TLC, thin layer chromatography.

#### SUPPORTING INFORMATION

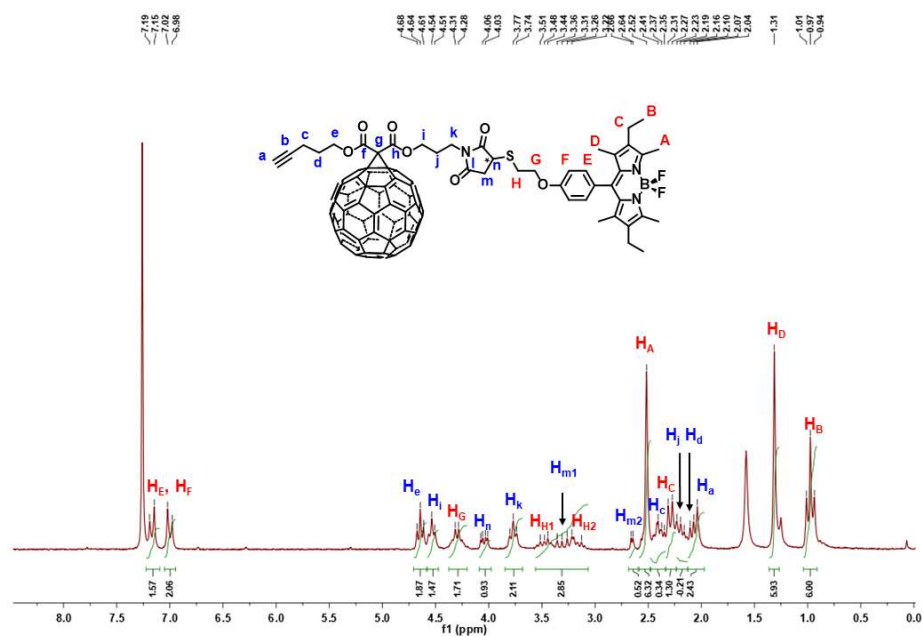


Figure S1.  $^1\text{H}$  NMR ( $\text{CDCl}_3$ ) of the **BDP- $C_{60}$**  dyad.

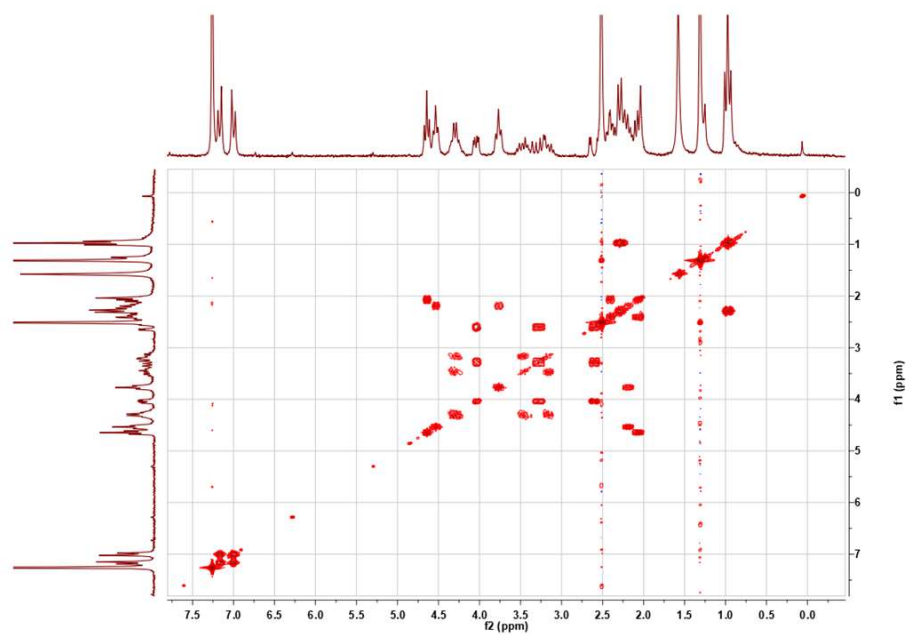


Figure S2. COSY NMR ( $\text{CDCl}_3$ ) of the **BDP- $C_{60}$**  dyad.

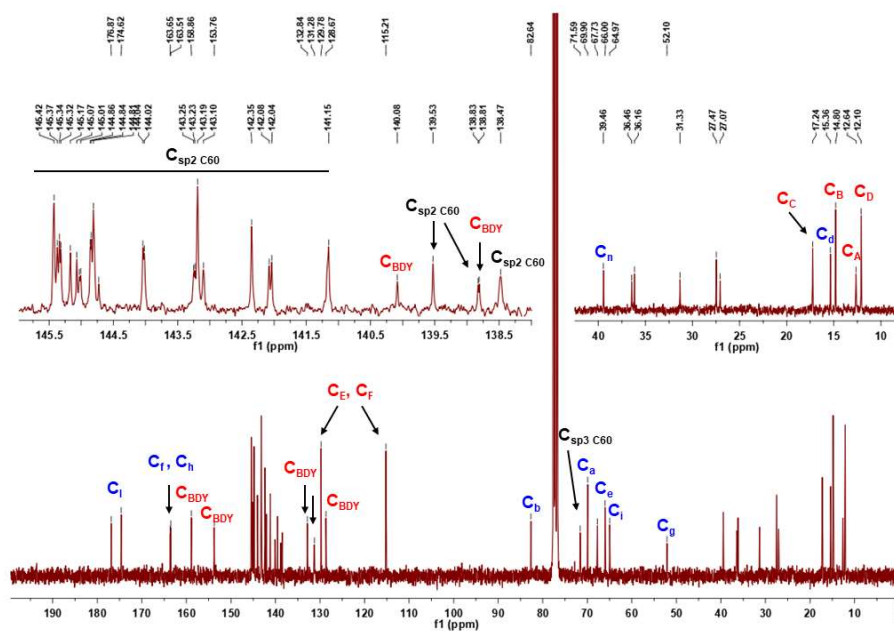


Figure S3. <sup>13</sup>C NMR (CDCl<sub>3</sub>) of the BDP-C<sub>60</sub> dyad.

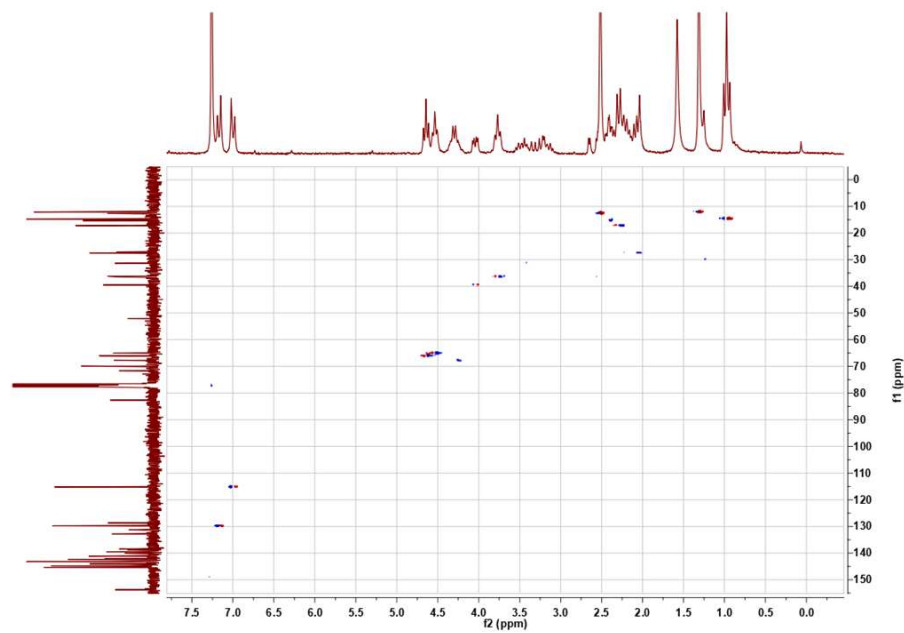


Figure S4. HSQC NMR (CDCl<sub>3</sub>) of the BDP-C<sub>60</sub> dyad.

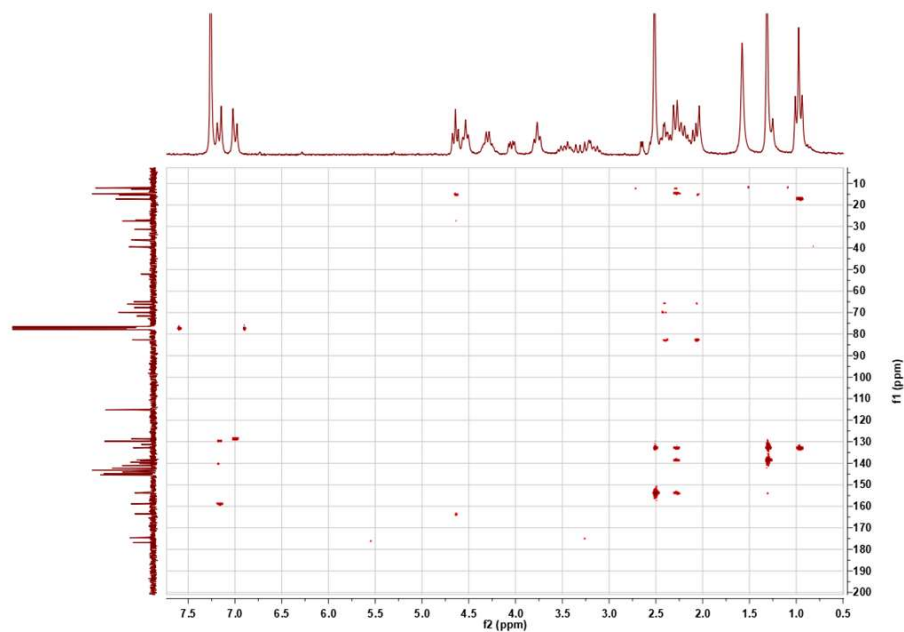


Figure S5. HMBC NMR (CDCl<sub>3</sub>) of the BDP-C<sub>60</sub> dyad.

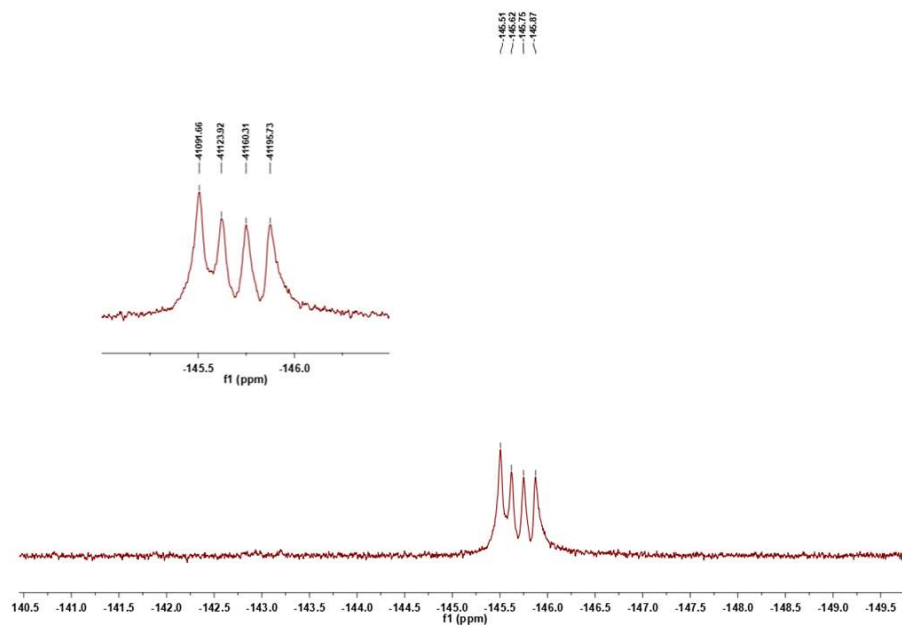


Figure S6. <sup>19</sup>F NMR (CDCl<sub>3</sub>) of the BDP-C<sub>60</sub> dyad.

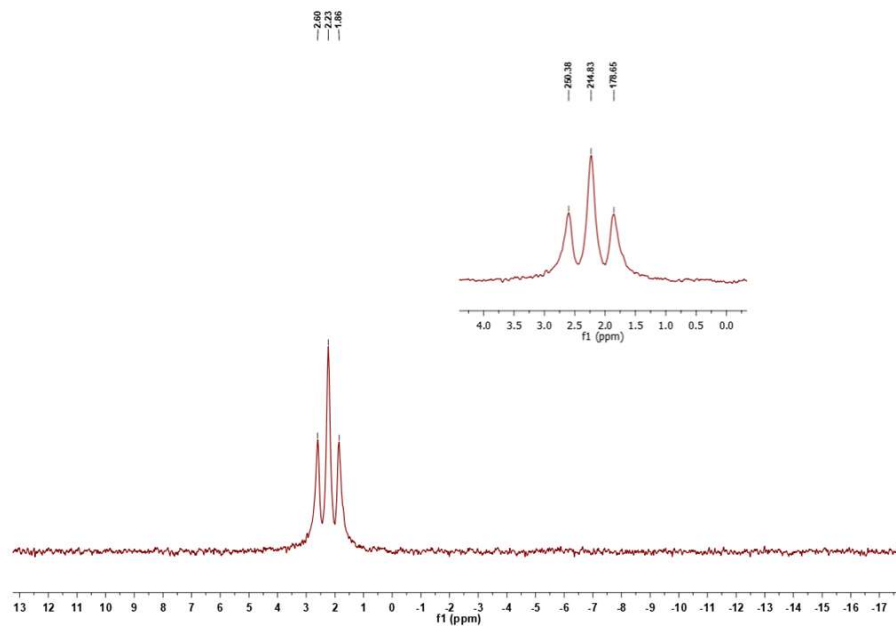


Figure S7. <sup>11</sup>B NMR (CDCl<sub>3</sub>) of the BDP-C<sub>60</sub> dyad.

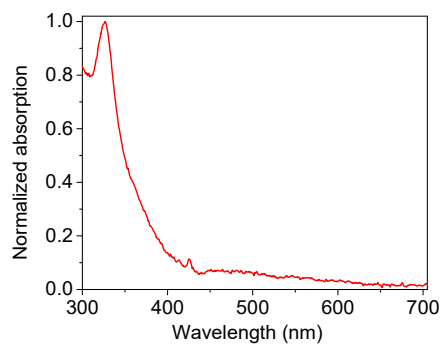
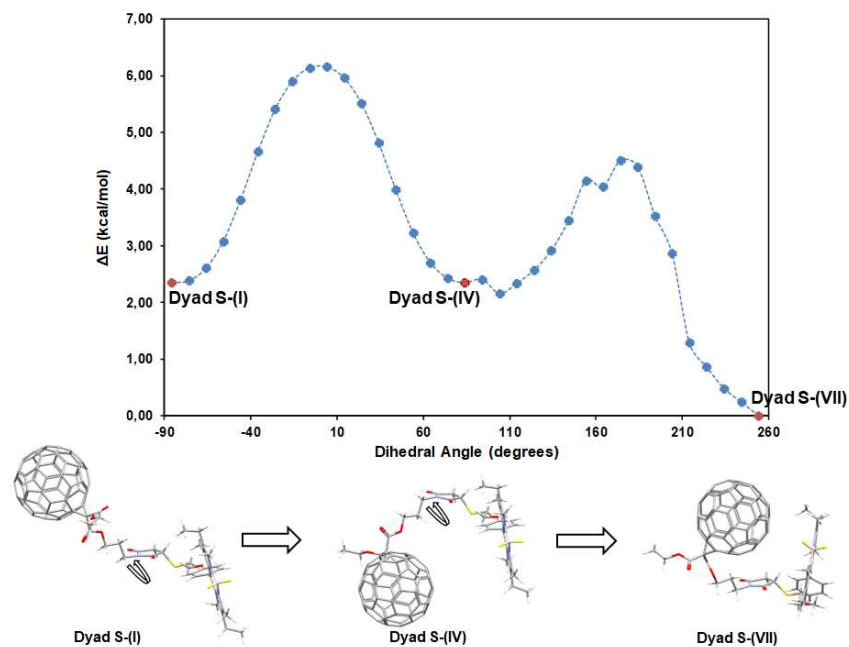
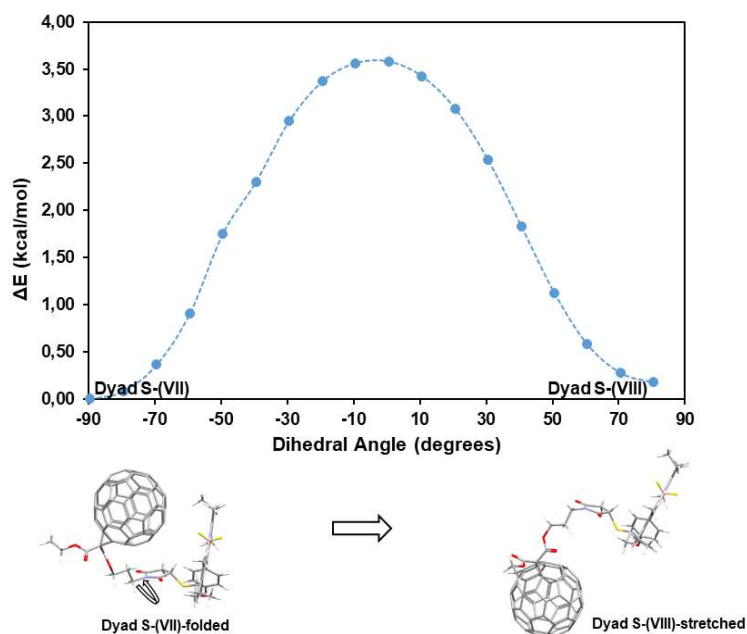


Figure S8. The normalized absorption spectrum of the C<sub>60</sub> building block 2 in benzonitrile.



**Figure S9.** Top: Calculated energy profile obtained by a relaxed scan around the OCN- $\underline{\text{C}}\text{H}_2\text{CH}_2$  dihedral angle for the (S) configuration. Energies are given relative to the minimum energy conformation. Bottom: Theoretical structures of the S-(I) and S-(IV) conformers along with a new minimum conformer S-(VII).



**Figure S10.** Top: Calculated energy profile obtained by a relaxed scan around the OCN- $\underline{\text{C}}\text{H}_2\text{CH}_2$  dihedral angle for the (S) configuration. Energies are given relative to the minimum

energy conformation. Bottom: Theoretical structures of the two conformers corresponding to the two minima (S-(VII) and S-(VIII)) for the (S) configuration.

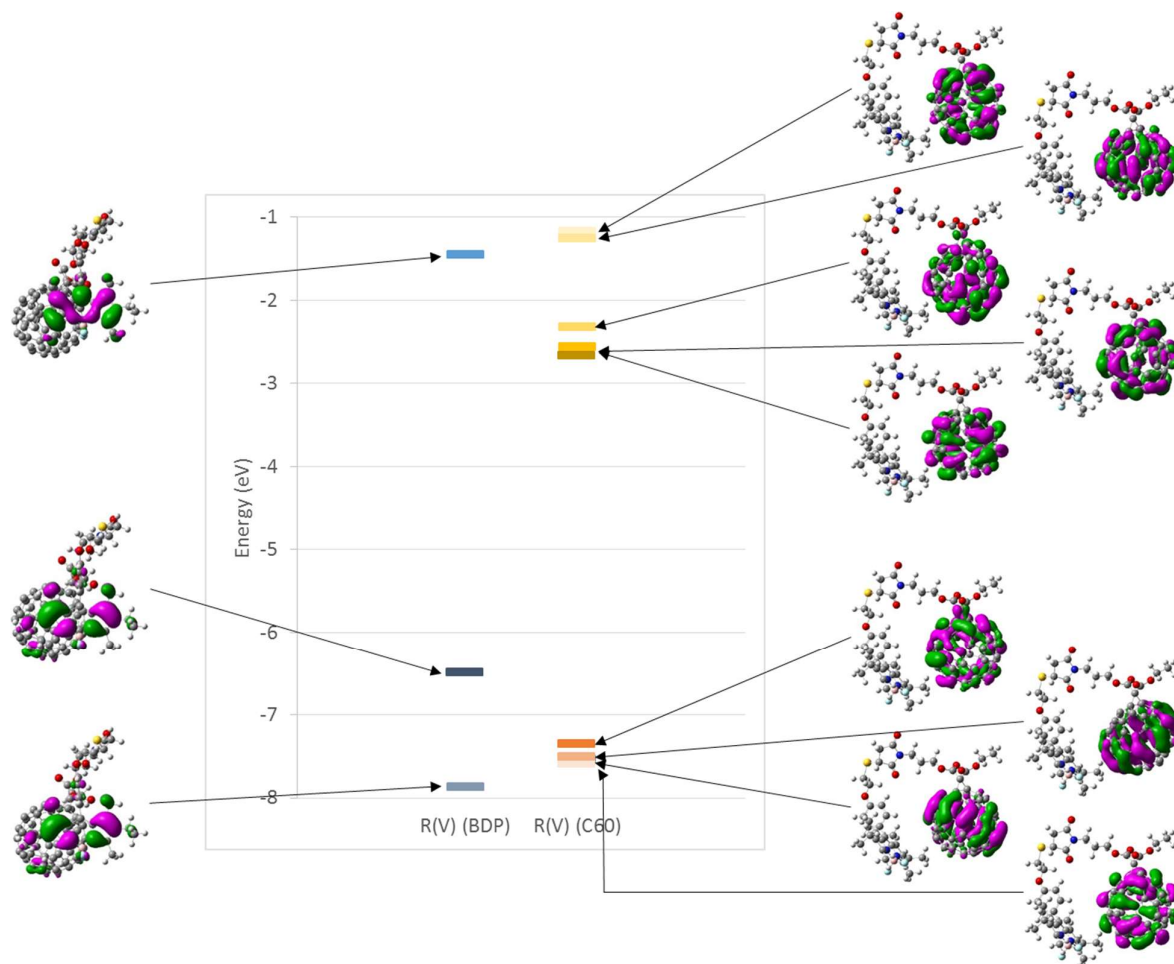


**Figure S11.** Main molecular orbitals of folded conformer R-(V).

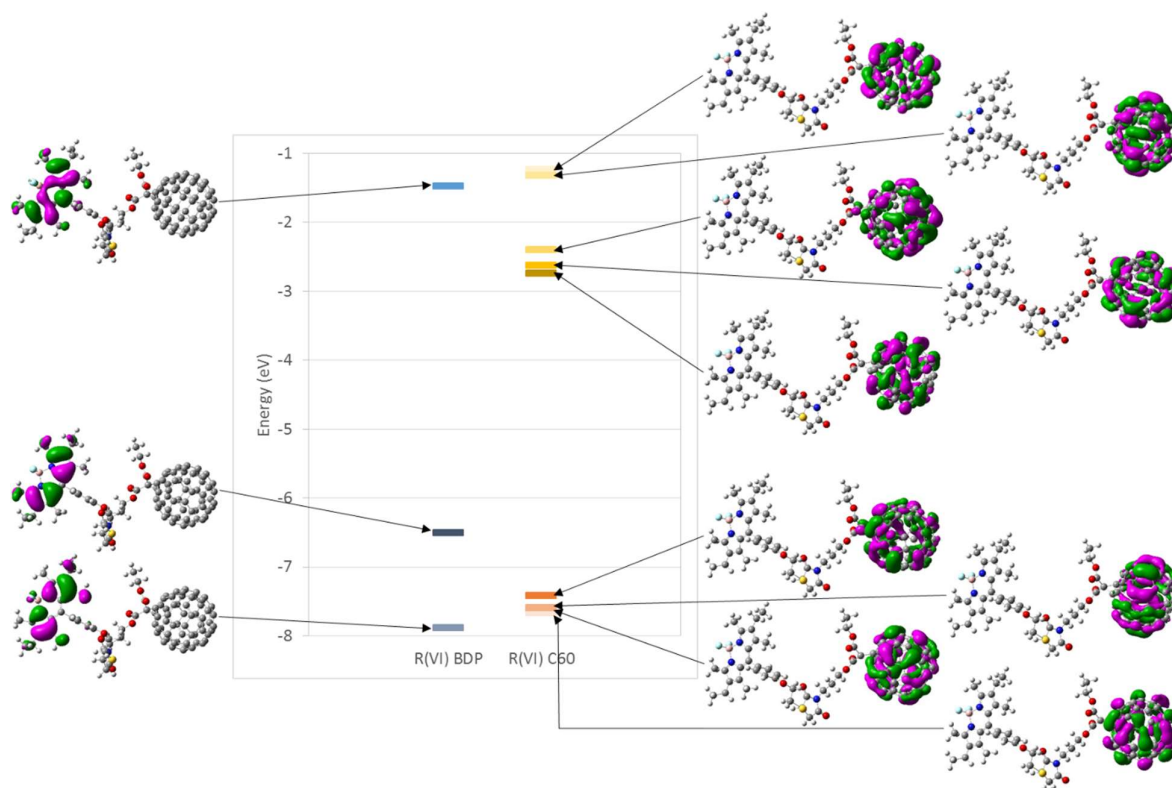


Figure S12. Main molecular orbitals of extended conformer R-(VI).

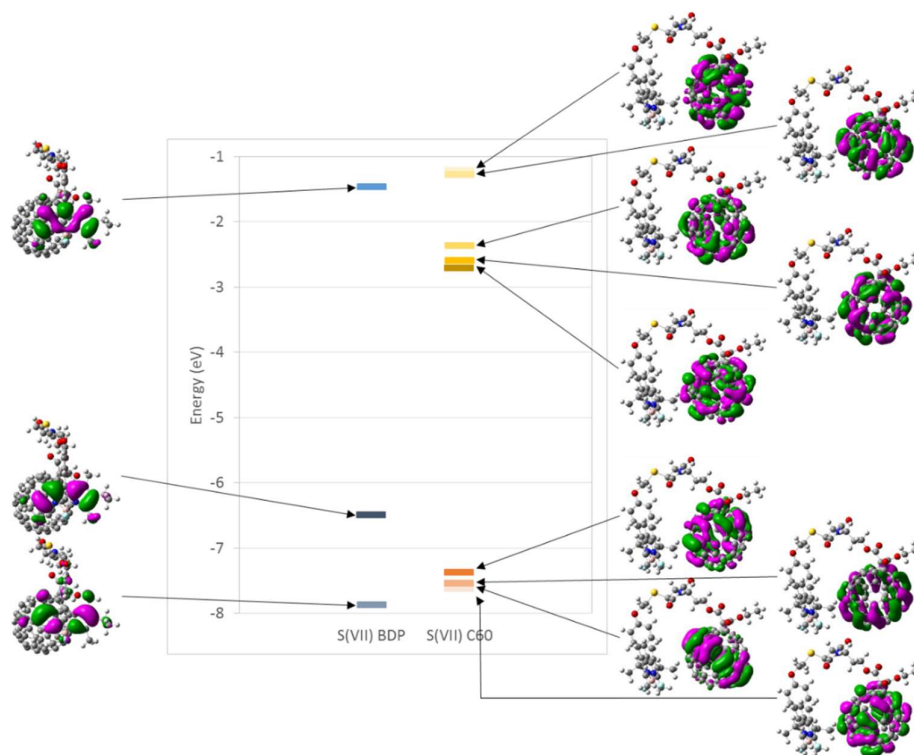
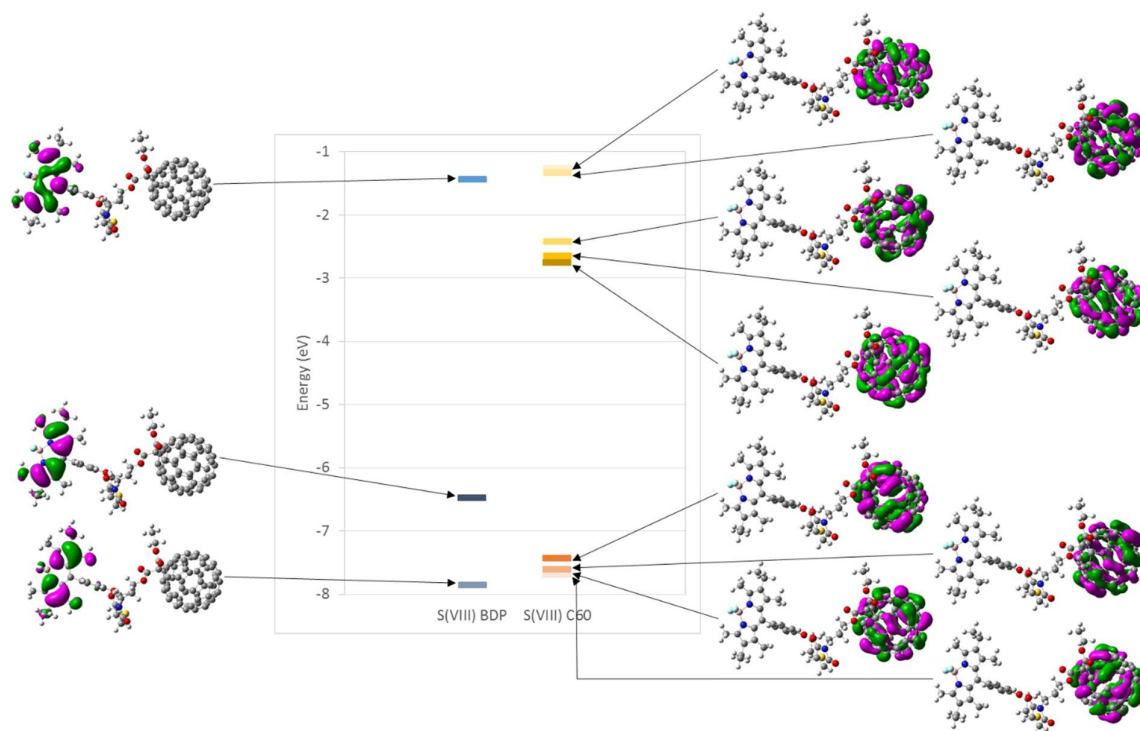
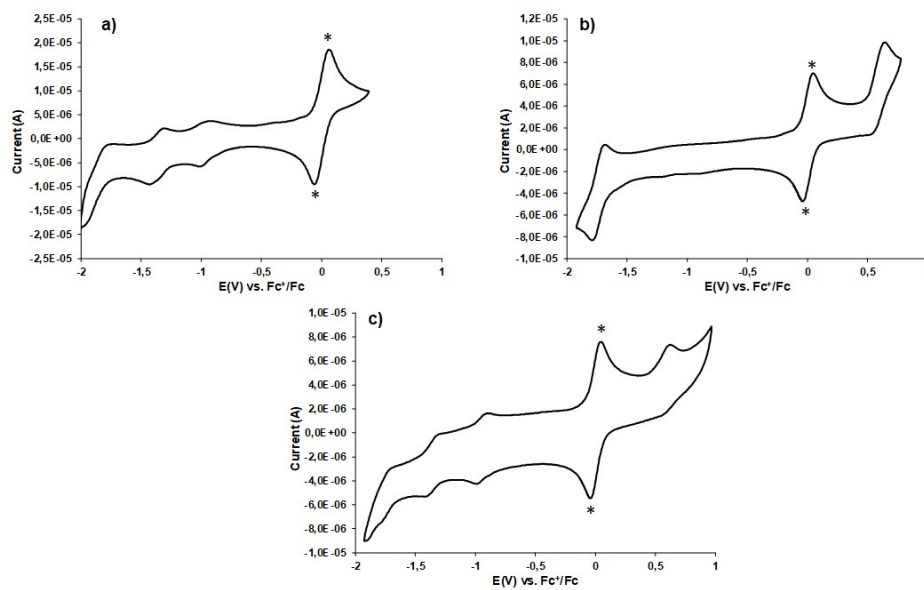


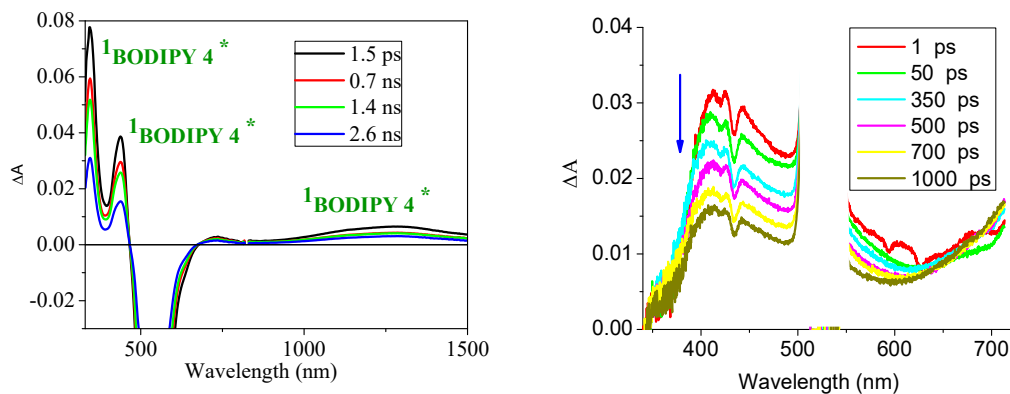
Figure S13. Main molecular orbitals of folded conformer S-(VII).



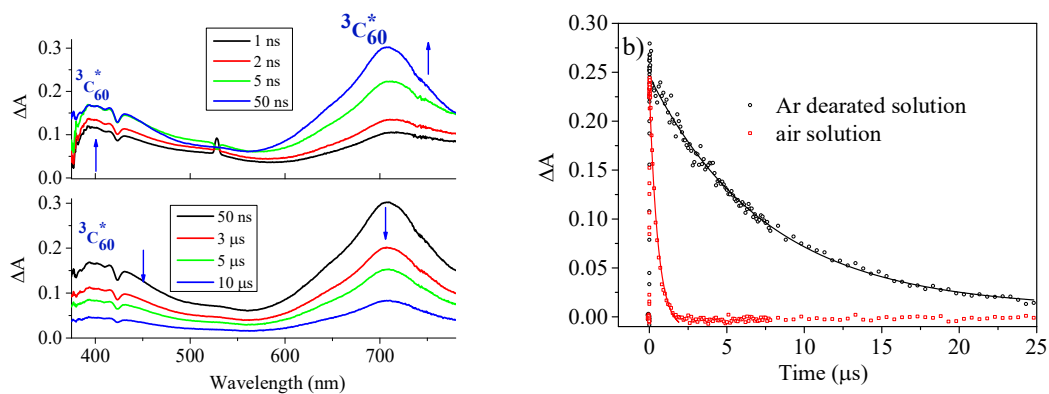
**Figure S14.** Main molecular orbitals of extended conformer S-(VIII).



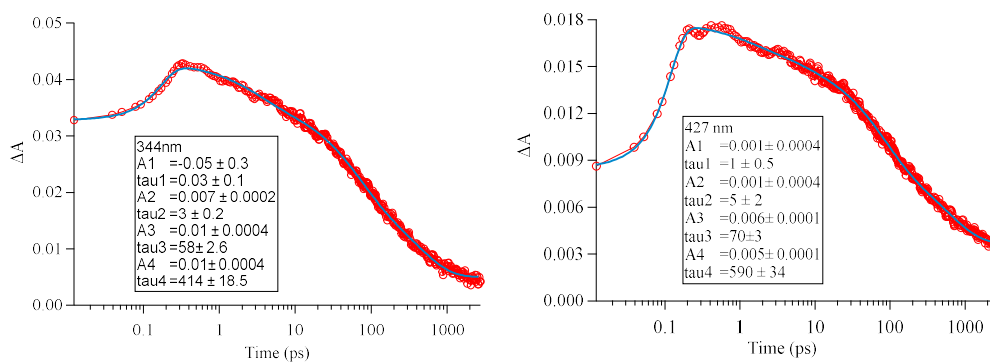
**Figure S15.** Cyclic voltammograms of a)  $C_{60}$  building block **2**, b) **BDP 4** and c) **BDP- $C_{60}$**  dyad in PhCN. The “\*” correspond to the oxidation and reduction waves of the ferrocene used as an internal standard.



**Figure S16.** Femtosecond transient absorption spectra of the **BDP 4** and  $C_{60}$  building block **2** pristine in benzonitrile at the indicated delay times.



**Figure S17.** a) Nanosecond transient absorption spectra of the  $C_{60}$  building block **2** in Ar-saturated benzonitrile at the indicated delay times; b) Kinetic traces (scattered points) of the  $C_{60}$  building block **2** at 710nm in the comparison between Ar-saturated and air in benzonitrile.



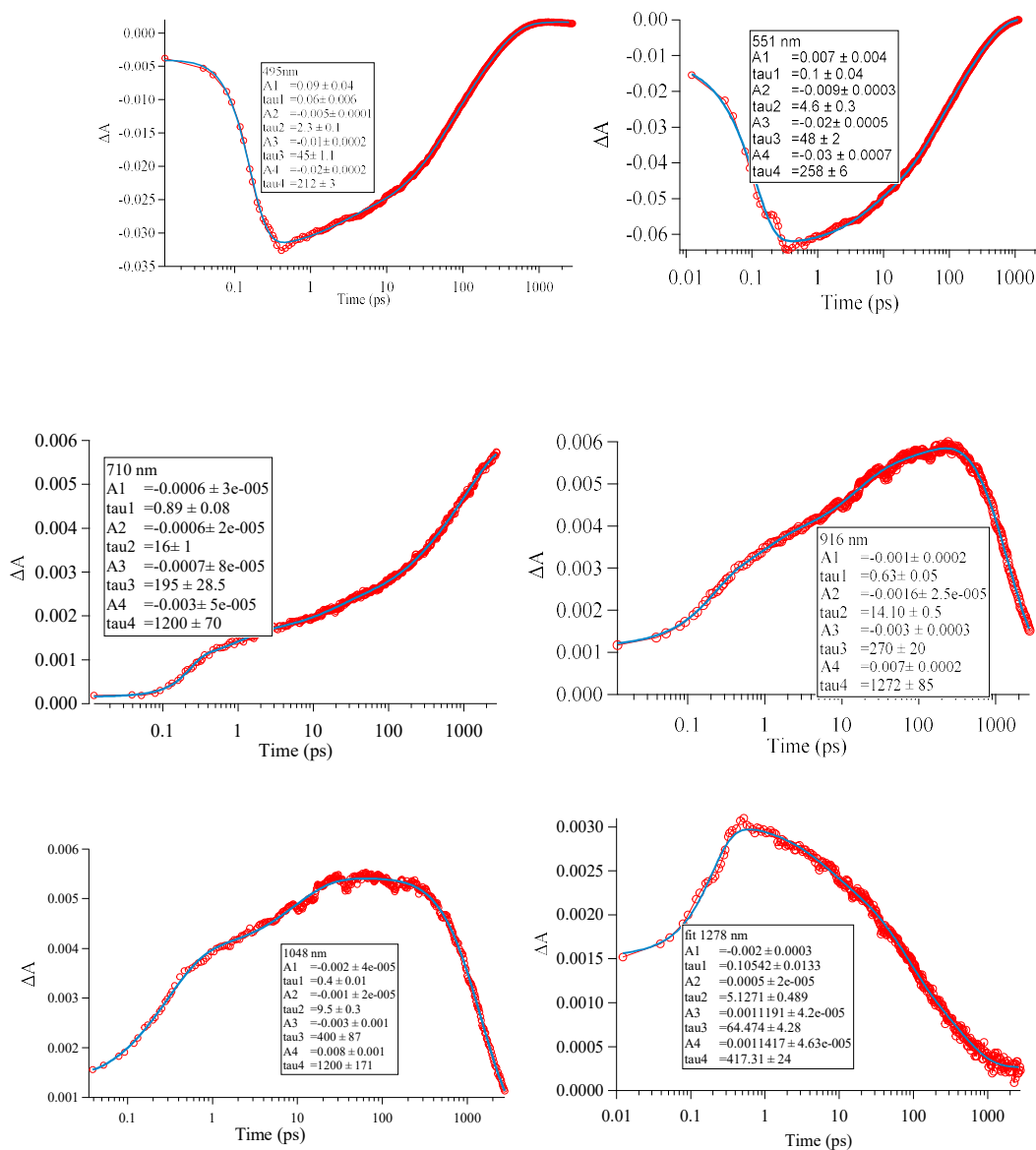


**Figure S18.** Femtosecond transient absorptions kinetic traces and their kinetic fittings at specific characteristic bands of the BDP- $C_{60}$  Dyad ( $5.5 \times 10^{-5}$  M) in argon saturated benzonitrile,  $\lambda_{exc}$  527 nm.

	<b>t<sub>1</sub>(ps)</b>	<b>t<sub>2</sub>(ps)</b>	<b>t<sub>3</sub>(ps)</b>	<b>t<sub>4</sub>(ps)</b>
<b>344 nm</b> <b><sup>1</sup>BDP*</b>	(r) 0.4	(d) 3	(d) 60	(d) 420
<b>427nm</b> <b><sup>1</sup>C<sub>60</sub>* + <sup>1</sup>BDP*</b>	(d) 0.75	(d) 5	(d) 70	(d) 590
<b>495 nm</b> <b>(bleaching)</b>	(r) 0.06	(d) 2.3	(d) 45	(d) 212
<b>551 nm</b> <b>(bleaching)</b>	(r) 0.1	(d) 4.6	(d) 48	(d) 258
<b>710 nm</b> <b><sup>3</sup>C<sub>60</sub>*</b>	(r) 0.89	(r) 16	(r) 195	(r) 1200
<b>916 nm</b> <b><sup>1</sup>C<sub>60</sub>*</b>	(r) 0.6	(r) 14	(r) 270	(d) 1200
<b>1045 nm</b> <b>C<sub>60</sub><sup>•-</sup></b>	(r) 0.4	(r) 9.5	(r) 400	(d) 1200
<b>1278 nm</b> <b><sup>1</sup>BDP*</b>	(r) 0.1	(d) 5	(d) 65	(d) 420

**Table S1.** Compilation of the various fitting time-constants of the femtosecond transient kinetic traces at specific bands of the **BDP-C<sub>60</sub>** Dyad ( $5.5 \times 10^{-5}$  M) in argon-saturated benzonitrile,  $\lambda_{exc}$  527 nm. Abbreviations: Rising time (r); decay time (d); singlet excited state of the BDP (<sup>1</sup>BDP\*); singlet excited state of the C<sub>60</sub> (<sup>1</sup>C<sub>60</sub>\*); triplet excited state of C<sub>60</sub> (<sup>3</sup>C<sub>60</sub>\*); charge transfer state of C<sub>60</sub> (C<sub>60</sub><sup>•-</sup>).

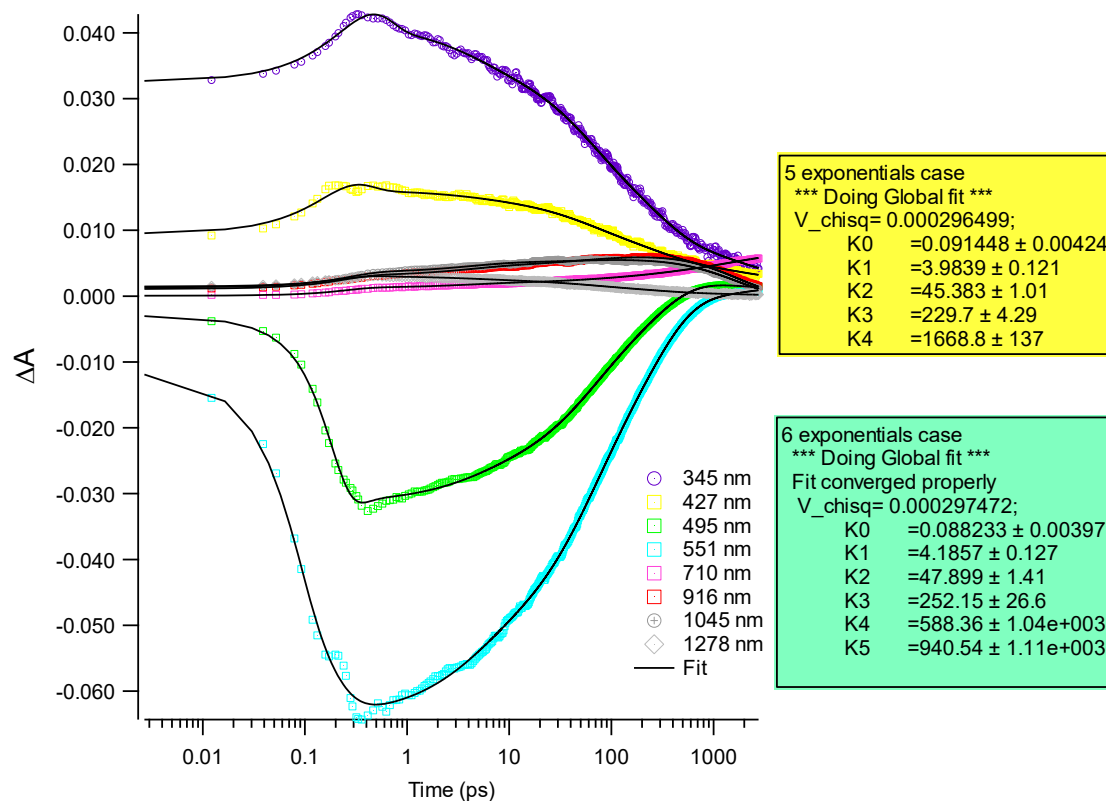


**Figure S19.** Femtosecond transient absorption global fit kinetic traces of the BDP-C<sub>60</sub> Dyad ( $5.5 \times 10^{-5}$  M) in argon saturated benzonitrile,  $\lambda_{exc}$  527 nm

### 3.3 Results and discussion in studying photophysical properties of the BDP-C<sub>60</sub> Dyad system

**Identifying spectro-kinetic signatures of transient species.** As seen in Figure 3.4, the singlet-excited state of the **BDP** is characterized by positive signatures at 340, 450 nm, and a broad band in the infrared region with the center at 1278 nm. The appearance of a negative band at 500 - 540 nm corresponds to the ground state bleaching accompanied by some contributions from stimulated emission. Additionally, the singlet excited state of the **C<sub>60</sub>** in the visible region shows a broadband absorption from 400 to 700 nm with the interference of a characteristic dip at 427 nm related to the ground state bleaching.

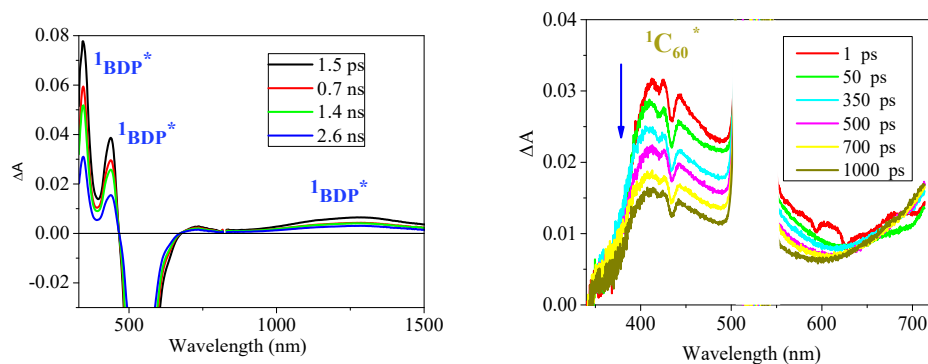


Figure 3.4. Femtosecond transient absorption spectra of the **BDP** and  **$C_{60}$**  pristine in benzonitrile at the indicated delay times.

**Deactivation processes for the BDP- $C_{60}$  Dyad.** To examine and compare the ability of charge transfer of acceptor and donor in the BDP- $C_{60}$  Dyad, the excitation wavelength at 380 nm was chosen that excite the  $C_{60}$  and BDP moieties in the femtosecond transient absorption (TA) measurement. This section will discuss briefly the results of the BDP- $C_{60}$  Dyad system in benzonitrile under excitation at 380 nm. Because of the significant contribution of the signal from benzonitrile solvent before 0.6 ps in the 350-450 nm region, the spectra and kinetic traces in this visible region will be presented from 0.6 ps, and consequently the rise of the singlet excited state of the BDP ( $^1\text{BDP}^*$ ) and  $C_{60}$  ( $^1\text{C}_{60}^*$ ) could not be observed.

Figure 3.6 shows the femtosecond TA spectra of the BDP- $C_{60}$  Dyad in argon saturated benzonitrile at indicated delay times. The spectral range of the femtosecond TA data is 330-1500 nm. In Figure 3.6, to simplify, the TA spectra of the BDP- $C_{60}$  Dyad are divided into three temporal windows distinguishing UV-Vis [330-750 nm] and NIR-infrared regions [600-1500 nm]. In parallel, the six basic kinetic traces, which are representative of specific characteristic states were chosen and fitted. The detail information is indicated in Figure 3.7 and Table 1. The time fitting converged in five characteristic times of (0.15-0.4) ps, (2-6) ps, (50-97) ps, (470-590) ps, and approximately 1200 ps. As mentioned in the paper, the computational studies have deduced the existence of at least three conformers with the donor-acceptor distances of 8.8 Å (conformer 1), 17.5 Å (conformer 2), and 20.5 Å (conformer 3); therefore, those times above have to be assigned to the different conformers (Figure 3.5).

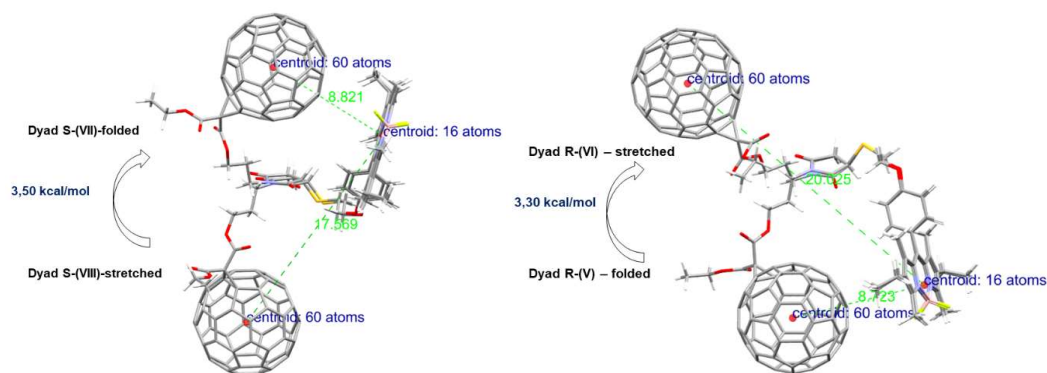


Figure 3.5. Three conformers with the distance of 8.8 Å corresponding to the folded conformer and two distances of 17.5 and 20.5 Å for stretched conformers.

Under 380 nm wavelength excitation, the immediately formed  $^1C_{60}^*$  with the broadband at 900 nm was observed simultaneously with the formation of the singlet excited state of BDP ( $^1BDP^*$ ) at 1278 nm (Figure 3.6a). Unexpectedly, Figure 3.6a also indicates the fast formation of the charge-separated state from the Frank-Condon (FC) region of BDP with the specific band at 1045 nm of the first reduced state of C<sub>60</sub> (C<sub>60</sub><sup>•-</sup>). These ultrafast processes with a rising time of  $\sim 0.4$  ps (taken as an approximate value 0.15-0.4 ps from tau1 kinetic fits) are presented in Figure 3.8 as the initial stage, in which charge transfer has to occur for conformer 1 that has the shortest donor-acceptor distance of 8.8 Å.

In the second temporal window [0.6-20 ps], one notices first that a simultaneous decrease of the  $^1BDP^*$  with an additional rise of C<sub>60</sub><sup>•-</sup> with a characteristic time of 6 ps. This process is assigned for a second charge transfer process from  $^1BDP^*$  to C<sub>60</sub>. Thereby, the two rates of two mechanism charge transfer due to conformer 1 are  $2.5 (\pm 0.3) \times 10^{12}$  and  $1.7 (\pm 0.6) \times 10^{11} \text{ s}^{-1}$ . It is noteworthy that these rates indicate better efficiency of charge transfer in comparison with the same class molecules.<sup>18-20</sup> Furthermore, the decay of the  $^1BDP^*$  is also concomitant with the first time constant of bleaching band recovery (Figure 3.6b). The second decay of  $^1BDP^*$  (50 ps) can be attributed to the process of energy transfer from  $^1BDP^*$  to C<sub>60</sub> that occurred for conformer 2 with the donor-acceptor distance of 17.5 Å. Similarly, the last decay time of the  $^1BDP^*$  state could be attributed to energy transfer to C<sub>60</sub> for conformer 3 with the donor-acceptor distance of 20.5 Å. In comparison with the case of 527 nm excitation, the formation of  $^1C_{60}^*$  could not be observed by monitoring the rise at 916 nm for 380 nm excitation. This could potentially be explained by a very low energy transfer from  $^1BDP^*$  compared with direct excitation, which prevents  $^1C_{60}^*$  from being detected.

The decays of both  $^1C_{60}^*$  and  $C_{60}^{\bullet-}$  show the simultaneous appearance of a new band at 700 nm corresponding to the triplet excited state of  $C_{60}$  ( $^3C_{60}^*$ ) (Figure 3.6e). The rate constants of charge recombination and intersystem crossing were found similarly to be  $8.3 \times 10^8 \text{ s}^{-1}$ . This value is also of the same order of magnitude as the rise of the  $^3C_{60}^*$ . Hence, these results indicate that both  $^1C_{60}^*$  and  $C_{60}^{\bullet-}$  relax to the  $^3C_{60}^*$  state before returning to the ground state.

The different photoinduced events of the BDP-C<sub>60</sub> Dyad in benzonitrile are summarized in Figure 3.8. The energy diagram shows various photophysical processes of the BDP-C<sub>60</sub> Dyad in benzonitrile built up using excited state energies of the donor and acceptor units and the free energy calculated data. In the diagram, both the donor BDP and C<sub>60</sub> moieties are excited. Under 380 nm excitation, the direct electronic excitation of the C<sub>60</sub> moiety can also induce some vibrational excitation and corresponding structures,<sup>14,21</sup> (noted as  $^nC_{60}^*$  in Figure 3.8). The energies of the radical ion pairs and the singlet excited state of the C<sub>60</sub> are higher than that of the  $^3C_{60}^*$  state. Thus it matches with the results in femtosecond TA: both  $C_{60}^{\bullet-}$  and  $^1C_{60}^*$  populate the  $^3C_{60}^*$  state before returning to the ground state.

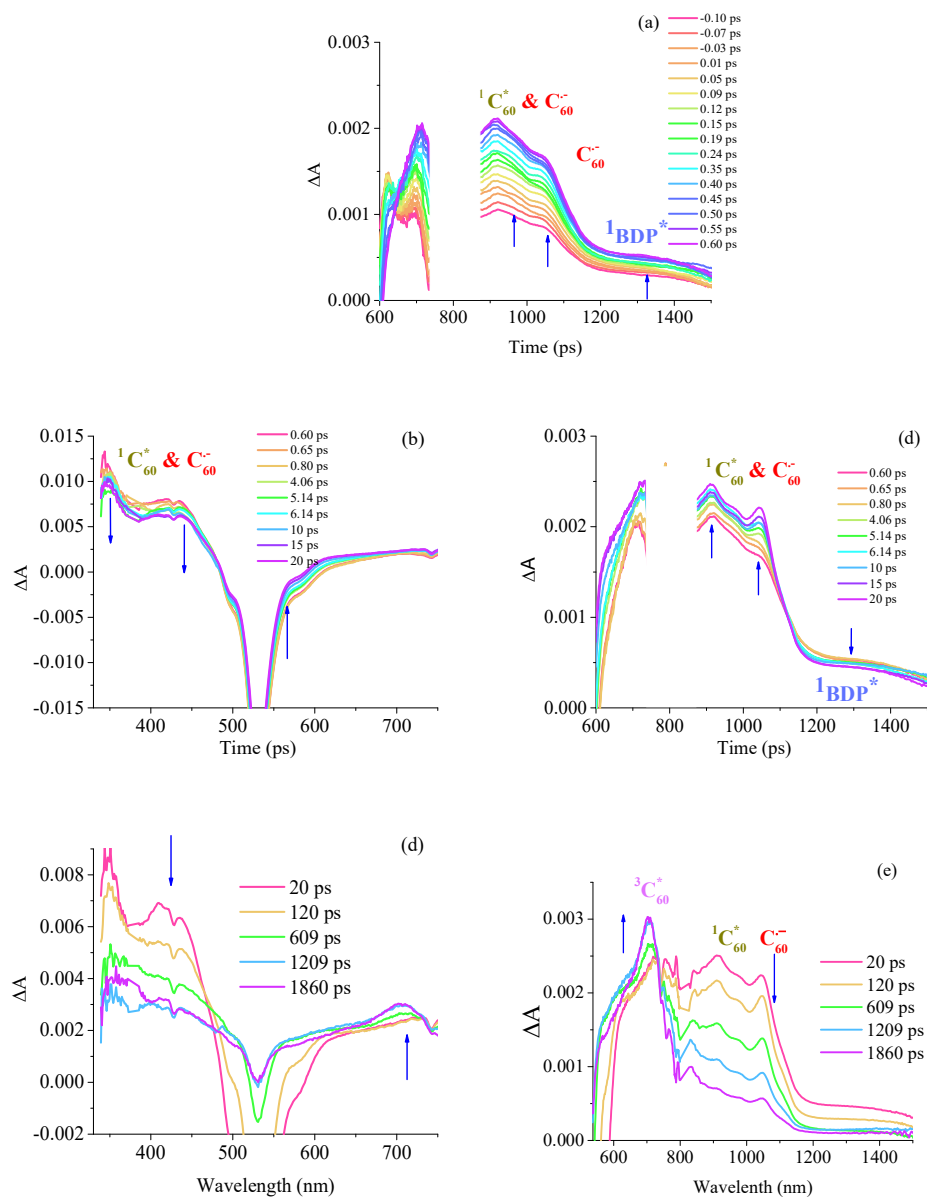


Figure 3.6. Femtosecond transient absorption spectra of the BDP-C<sub>60</sub> Dyad ( $5.5 \times 10^{-5}$  M) in argon-saturated benzonitrile at the indicated delay times,  $\lambda_{exc}$  380 nm.

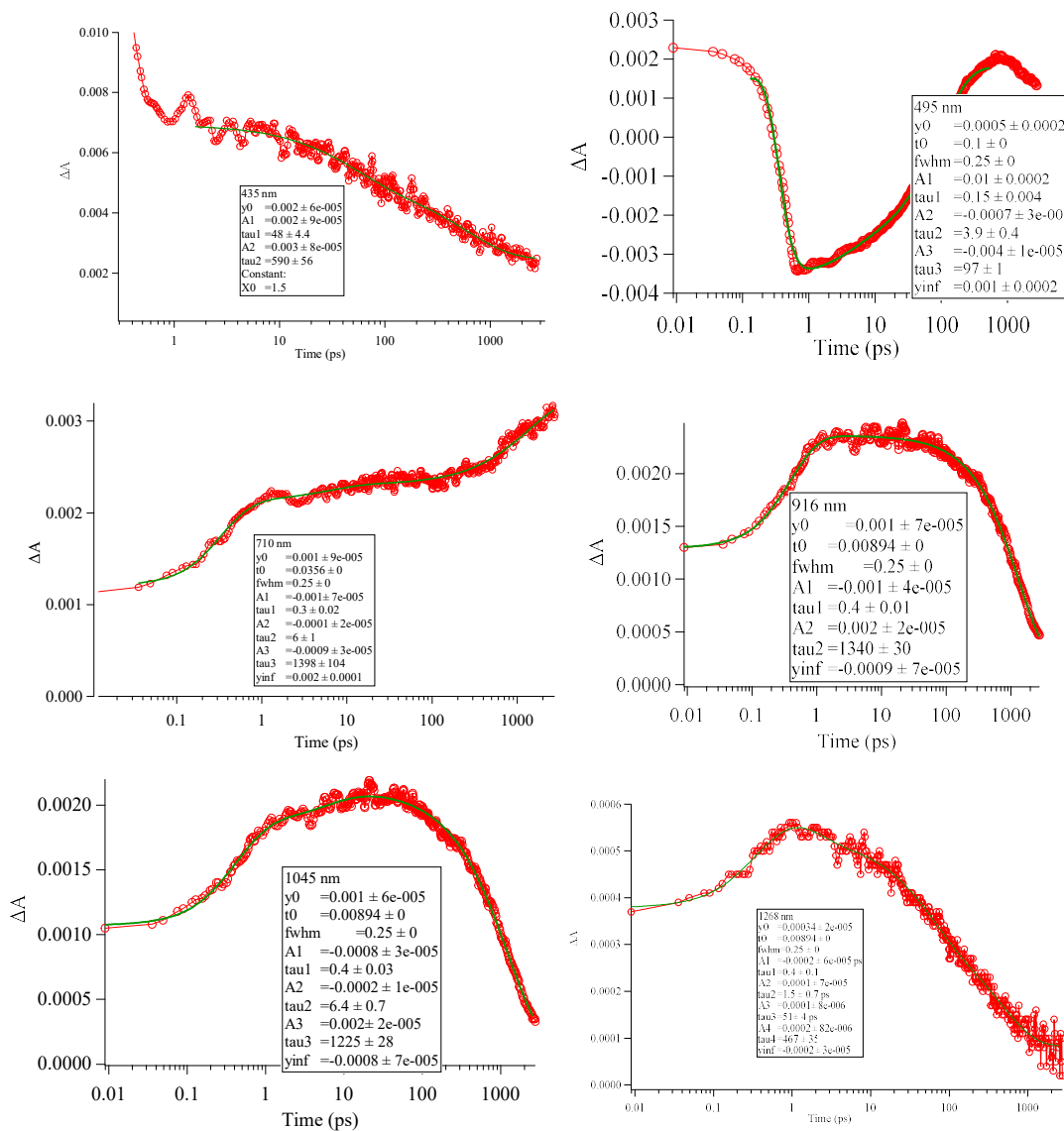


Figure 3.7. Basic kinetic fits at specific characterization bands.

Table 3.1. Basic kinetic traces were fitting at the specific bands. The singlet excited state of C<sub>60</sub> (<sup>1</sup>C<sub>60</sub><sup>\*</sup>), singlet excited state of BDP (<sup>1</sup>BDP<sup>\*</sup>), triplet excited state of C<sub>60</sub> (<sup>3</sup>C<sub>60</sub><sup>\*</sup>), the first reduced-state of C<sub>60</sub> (C<sub>60</sub><sup>•-</sup>), decay time (d), rising time (r).

	t <sub>1</sub> (ps)	t <sub>2</sub> (ps)	t <sub>3</sub> (ps)	t <sub>4</sub> (ps)
<b>435nm</b> ( <sup>1</sup> C <sub>60</sub> <sup>*</sup> + <sup>1</sup> BDP <sup>*</sup> )	-	(d) 48±4.4	(d) 590±56	-
<b>500 nm (Bleaching band BDP)</b>	(d) 0.15±0.004	(r) 3.9±0.4	(r) 97 ±1	-
<b>710 nm (<sup>3</sup>C<sub>60</sub><sup>*</sup>)</b>	(r) 0.30 ±0.02	(r) 6.0 ±1	(d) 1398 ±104	-
<b>916 nm</b> ( <sup>1</sup> C <sub>60</sub> <sup>*</sup> + C <sub>60</sub> <sup>•-</sup> )	(r) 0.4 ± 0.01	(d) 1340 ± 30	-	-
<b>1045 nm (C<sub>60</sub><sup>•-</sup>)</b>	(r) 0.4 ±0.03	(r) 6.4 ± 0.7	(d) 1225± 28	-
<b>1268 nm (<sup>1</sup>BDP<sup>*</sup>)</b>	(r) 0.4 ±0.1	(d) 1.5± 0.7	(d) 51 ± 4	(d) 467 ± 35

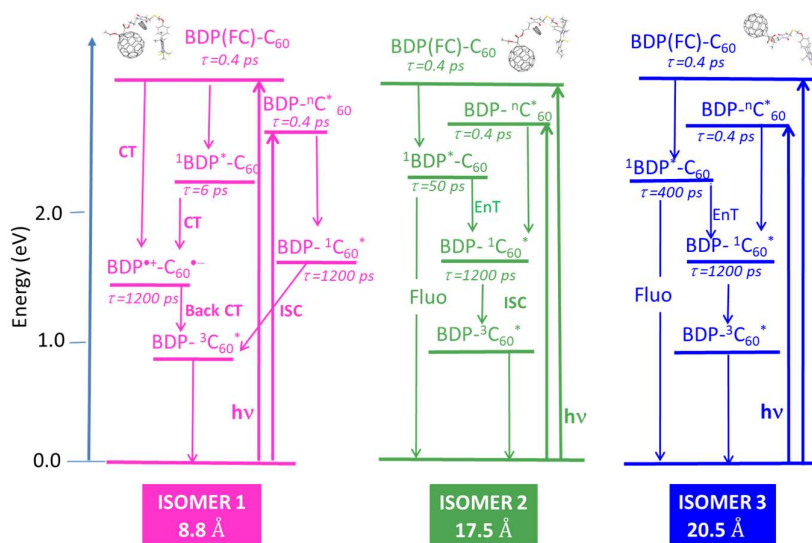


Figure 3.8. Energy level diagram presents the photoinduced processes obtained following laser excitation ( $\lambda_{exc}$  380 nm) in the two conformations of the BDP-C<sub>60</sub> Dyad in benzonitrile. Abbreviations: EnT= Energy transfer, CT = charge transfer, Back CT = back charge transfer, ISC = intersystem crossing, energies: <sup>1</sup>BDP<sup>\*</sup> = 2.33 eV, <sup>1</sup>C<sub>60</sub><sup>\*</sup> = 1.75 eV, <sup>3</sup>C<sub>60</sub><sup>\*</sup> = 1.55 eV<sup>59,66</sup>.

In conclusion, under excitation at 380 nm, both BDP and C<sub>60</sub> moieties in the BDP-C<sub>60</sub> Dyad were excited. However, the excited state of the C<sub>60</sub> seems to show no charge transfer to the BDP moiety. In contrast, the ultrafast charge transfer from the FC and <sup>1</sup>BDP<sup>\*</sup> states of the

BDP to the C<sub>60</sub> were observed for conformer 1, which possesses the shortest donor-acceptor distance. It should be emphasized that our results indicate a high efficiency of charge transfer with the rate constants of  $2.5 (\pm 0.3) \times 10^{12}$  and  $1.7 (\pm 0.6) \times 10^{11} \text{ s}^{-1}$ . Finally, the excited state and charge separated state of the C<sub>60</sub> populated the triplet excited state of the C<sub>60</sub>.

### 3.4 Results and discussion in studying photophysical properties of Dyad peptide and Dyad alkyl systems

This section will discuss the results of the photophysical study of the BDP-C<sub>60</sub>-Peptide and BDP-C<sub>60</sub>-alkyl dyad systems (denoted as Dyad-peptide and Dyad-alkyl – Figure 3.2a and 3.3a) and their BDP donor derivatives (BDP-peptide and BDP-alkyl – Figure 3.2b and 3.3b).

#### 3.4.1 Absorption and fluorescence measurements

The absorption and fluorescence spectra of two Dyad systems and its BDP derivatives have been studied in benzonitrile. The spectra show the identical absorption and fluorescence characteristics between Dyad-peptide and Dyad-alkyl, as well as its BDP derivatives. Thus, only the spectra of Dyad-peptide and BDP-peptide will be presented. The photophysical properties of the Dyad-peptide, Dyad-alkyl, and its BDP derivatives are summarized in Table 2.

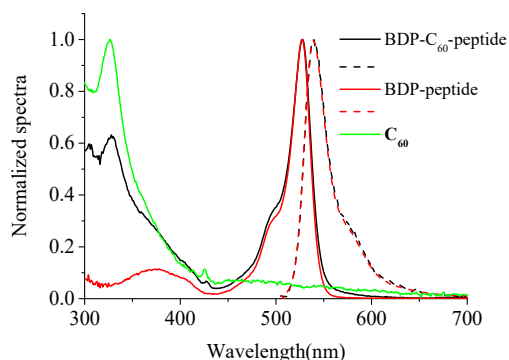


*Figure 3.9. Red and black lines: Normalized absorption (solid line) and fluorescence (dash line) spectra in benzonitrile of the BDP-peptide and Dyad-peptide ( $1.4 \times 10^{-6} \text{ M}$ ),  $\lambda_{exc} = 510 \text{ nm}$ . Green line: the normalized absorption spectrum of the C<sub>60</sub> fragment in benzonitrile.*

Figure 3.9 presents the normalized absorption and fluorescence spectra of the Dyad-peptide and BDP-peptide in benzonitrile. The active absorption band in the visible region (527 nm) of the Dyad-peptide is characteristic of the BDP-peptide fragment, and the higher energy

band at 326 nm corresponds to the contribution of the C<sub>60</sub> moiety. Upon excitation at 510 nm, the fluorescence spectra of the Dyad-peptide and BDP-peptide show a similar band at 539 nm. It indicates that the BDP-peptide moiety is responsible for the emission in the Dyad-peptide. The comparison of fluorescence intensities of the Dyad-peptide and BDP-peptide in the same conditions is shown in Figure 3.10a. The fluorescence of the BDP moiety in the Dyad-peptide is strongly quenched as compared to the fluorescence of the BDP-peptide. Time-resolved fluorescence measurements were performed by time-correlated single-photon counting (TCSPC), and the decays are shown in Figure 3.10b for the Dyad-peptide and BDP-peptide.

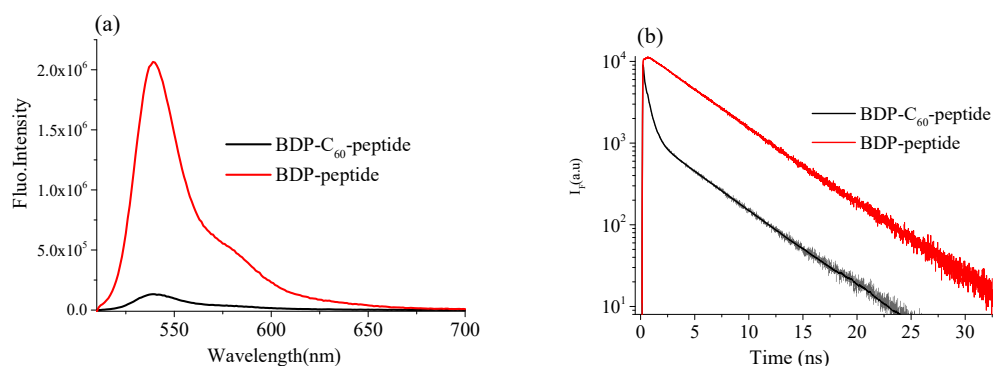


*Figure 3.10. Fluorescence spectra (a) and fluorescence decays (b) of the Dyad-peptide and BDP-peptide ( $1.4 \times 10^{-6}$  M) excited at 490 nm in benzonitrile,  $\lambda_{exc}$  527 nm.*

The fluorescence decays of the BDP-peptide and BDP-alkyl can be fitted by a single exponential function with the lifetimes of 4.50 and 4.57 ns, respectively. These lifetimes are characteristic of the singlet excited state of the BDP-peptide and BDP-alkyl. However, the fluorescence of the Dyad-peptide and Dyad-alkyl can only be fitted with three exponentials. For both Dyad systems, two short lifetimes have significant contributions (approximately 40% and 50%) and a long-lived decay time as a minor contribution. These results are evidence of an interaction between the singlet excited state of the BDP moiety and the C<sub>60</sub> moiety in the Dyad assembly system through electron transfer and/or energy transfer. The longest lifetime components in the Dyad assembly systems are similar to the lifetime of their free BDP moiety fragments.

Table 3.2. Photophysical properties of the BDP-C<sub>60</sub>-peptide, BDP-C<sub>60</sub>-alkyl Dyad assembly, BDP-peptide and BDP-alkyl in Benzonitrile. Absorption band  $\lambda_{abs}$  (nm) and emission band  $\lambda_{em}$  (nm), fluorescence quantum yield  $\Phi_F$ , fluorescence lifetime  $\tau$  (ns), radiative  $k_r$  (s<sup>-1</sup>) and nonradiative rate  $k_{nr}$  (s<sup>-1</sup>) constants.

	$\lambda_{abs}$ (nm)	$\lambda_{em}$ (nm)	$\Phi(F)$	$\tau$ (ns)	$k_r$ (s <sup>-1</sup> )	$k_{nr}$ (s <sup>-1</sup> )
BDP-peptide	380, 527	539	0.79	4.5	1.73×10 <sup>8</sup>	4.60×10 <sup>7</sup>
Dyad-peptide	327, 527	539	0.05	4.5(9.5%); 0.10 (41.5%); 0.44 (49.0%) $\tau_s = 0.68$	7.33×10 <sup>7</sup>	1.39×10 <sup>9</sup>
BDP-alkyl	380, 527	539	0.68	4.57	1.48×10 <sup>8</sup>	7.00×10 <sup>7</sup>
Dyad -alkyl	327, 527	539	0.025	4.50(8.4%); 0.07 (40.6%); 0.36 (51.0%); $\tau_s = 0.59$	4.24×10 <sup>7</sup>	1.66×10 <sup>9</sup>

### 3.4.2 Femtosecond and nanosecond TA studies

#### 3.4.2.1 Femtosecond TA spectra

To shed light on the photoinduced processes, TA spectra have been implemented for these Dyad systems and their donor derivatives. Unfortunately, TA experiments were only performed in the visible range, which cannot probe the reduced state of the C<sub>60</sub>. However, the dynamic trace of the oxidized state of BDP (BDP<sup>•+</sup>) can be obtained in the visible region at 400 nm.

Firstly, the femtosecond TA was measured for the BDP fragment in argon-saturated benzonitrile to give an overview of its excited states.

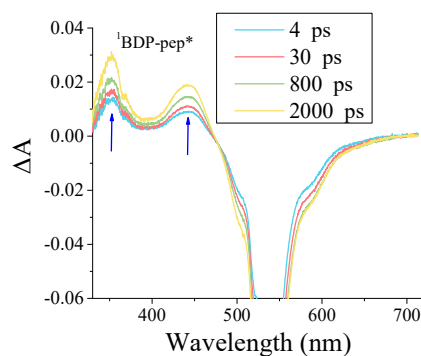


Figure 3.11. Femtosecond transient absorption spectra of the BDP-peptide ( $4.6 \times 10^{-5}$  M) in benzonitrile at the indicated delay times ( $\lambda_{exc}$  527 nm).

Figure 3.11 presents the transient spectra of the BDP-peptide under excitation at 527 nm. Because the experiment results indicated identical spectra between the BDP-peptide and BDP-alkyl fragments, only spectra of the BDP-peptide are shown. The singlet-excited states of the BDP-peptide and BDP-alkyl were observed at 352 and 440 nm, while the appearance of a negative band at 527 nm corresponds to the ground state bleaching.

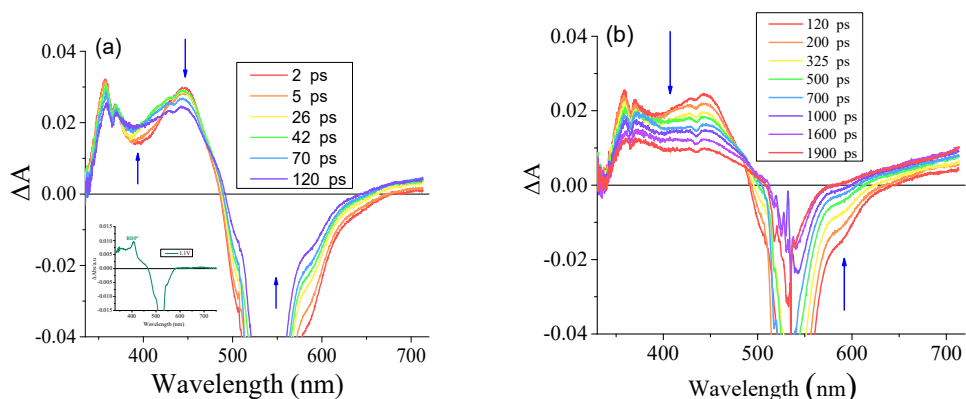


Figure 3.12. Femtosecond transient absorption spectra of the BDP- $C_{60}$ -peptide assembly Dyad ( $4.6 \times 10^{-5}$  M) in benzonitrile at the indicated delay times,  $\lambda_{exc}$  527 nm; inset: Spectrum of BDP after oxidization by spectroelectrochemistry, presented for comparison.

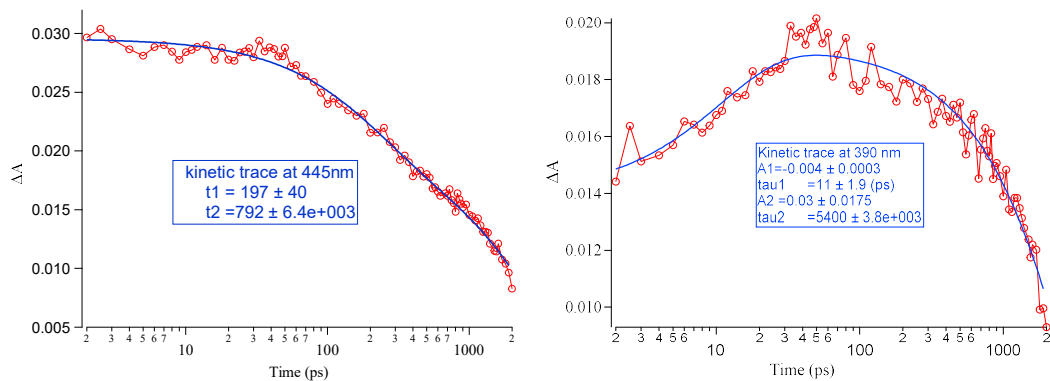
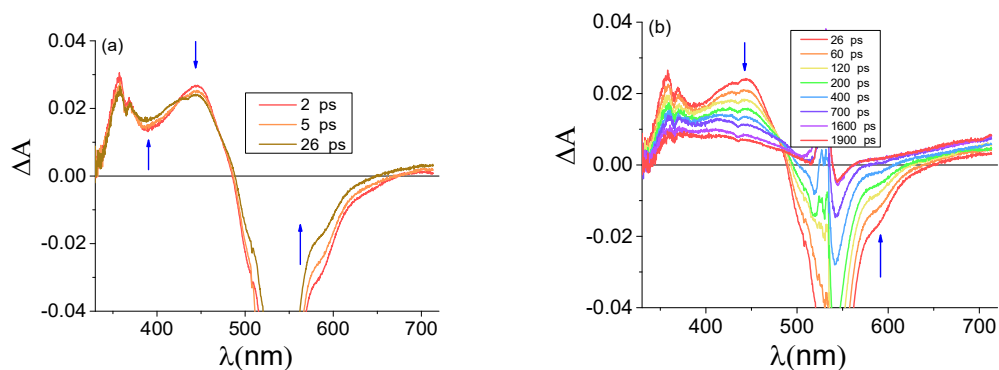


Figure 3.13. The kinetic traces of the peaks at 445 and 390 nm of the Dyad-peptide in benzonitrile,  $\lambda_{exc}$  527 nm.

The Dyad-peptide solution in benzonitrile was excited at 527 nm to primarily excite the BDP moiety. The femtosecond TA spectra of the Dyad-peptide have been presented in Figure 3.12 at the indicated delay times. The immediately formed singlet excited state of the BDP moiety at 352 and 440 nm on the short timescale ( $\sim 2$  ps) decayed simultaneously with the

growth of the region at 390 nm (Figure 3.12a). The rising feature at 390 nm is quite well fitted with the position of the BDP<sup>•+</sup> state in spectroelectrochemical studies. Additionally, the decay spectra of the <sup>1</sup>BDP\* show the characteristic changes associated with the singlet excited state of C<sub>60</sub> (Figure 3.12b). Therefore, under excitation of the BDP moiety in the Dyad-peptide, it appears that both electron transfer and energy transfer occur. Because of the overlapping bands between many states in the visible region (<sup>1</sup>BDP\*, <sup>1</sup>C<sub>60</sub>\*, and BDP<sup>•+</sup>), a clear band of the BDP<sup>•+</sup> was difficult to obtain, for the same reason, it was highly difficult to estimate precisely the rate constant of charge separation and energy transfer using femtosecond TA in the visible region. Figure 3.13 shows the kinetic traces at 445 and 390 nm of the Dyad-peptide that are the most representative of the bands of <sup>1</sup>C<sub>60</sub>\* and BDP<sup>•+</sup>, respectively. It follows that the rate constant of the charge-separated state, which was determined by the growth kinetic trace at 390 nm, is  $9.1 \times 10^{10} \text{ s}^{-1}$ . The lifetime of charge separated-states may be estimated more than 6 ns from the decay of the BDP<sup>•+</sup> at 400 nm. Whereas, the kinetic trace at 445 nm shows overlapping bands between the singlet-excited state of the BDP and C<sub>60</sub>. Therefore, the rate constant of energy transfer cannot be evaluated with only the data in the visible region. The femtosecond TA of Dyad-alkyl also indicates the similarity with the spectra of the Dyad-peptide (Figure 3.14)



*Figure 3.14. Femtosecond transient absorption spectra of the Dyad-alkyl assembly Dyad ( $5.9 \times 10^{-5} \text{ M}$ ) in benzonitrile at the indicated delay times,  $\lambda_{exc} 527 \text{ nm}$ .*

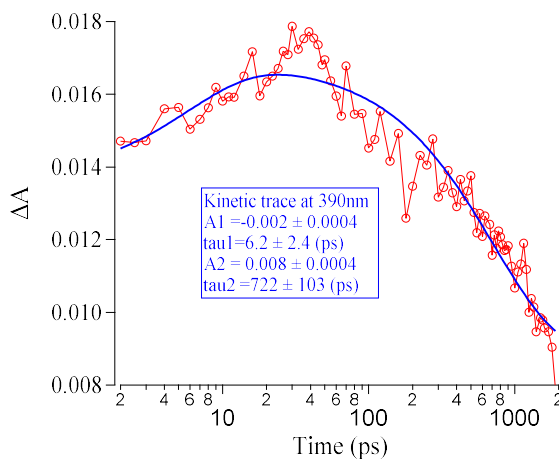


Figure 3.15. Kinetic trace at 390 nm corresponding the singlet-excited state of the BDP.

The photophysical processes occur identically in the case of the Dyad-peptide, except for the rate constant of the processes. The kinetic trace at 390 nm of the Dyad-alkyl assembly, corresponding to the band of the  $BDP^{*+}$ , was fitted with a rising time 6.2 ps and a decay time 722 ps (Figure 3.15). These times indicate the faster rate of charge-separated state formation ( $1.6 \times 10^{11} \text{ s}^{-1}$ ) in comparison to the Dyad-peptide assembly. However, the Dyad-peptide assembly showed a charge separated state with a much longer lifetime. It can be related to the helical peptide in Dyad-peptide, which is an excellent electron mediator in comparison with an alkyl chain in Dyad-alkyl.<sup>17</sup>

#### 3.4.2.2 Nanosecond TA spectra

Nanosecond TA has been performed to unravel all the processes in the Dyad-assembly systems. First, the nanosecond TA of the  $C_{60}$  fragment was measured to support data analysis in measurements of the Dyad assembly systems. Figure 3.16a illustrates the nanosecond transient spectra of the  $C_{60}$  fragment in argon-saturated benzonitrile under excitation at 527 nm. The spectra show the triplet excited state of the  $C_{60}$  ( ${}^3C_{60}^*$ ) at 710 nm with decay times of 7.2 and 0.36  $\mu\text{s}$  in benzonitrile saturated with argon and in air, respectively (Figure 3.16b). These triplet excited state bands of the  $C_{60}$  fragment were similar to the bands that were obtained in experiments for Dyad-peptide and Dyad-alkyl. Figure 3.17a presents the spectra of Dyad-peptide with the central band of the  ${}^3C_{60}^*$  at 700 nm. The decay time at 700 nm of the Dyad-peptide was found to be 6.16  $\mu\text{s}$  (Figure 3.17b), corresponding to a rate constant of  $1.6 \times 10^6 \text{ s}^{-1}$ . For the Dyad-alkyl assembly, the rate constant of the triplet-excited state was found to be smaller ( $2.3 \times 10^5 \text{ s}^{-1}$ ) (Figure 3.18).

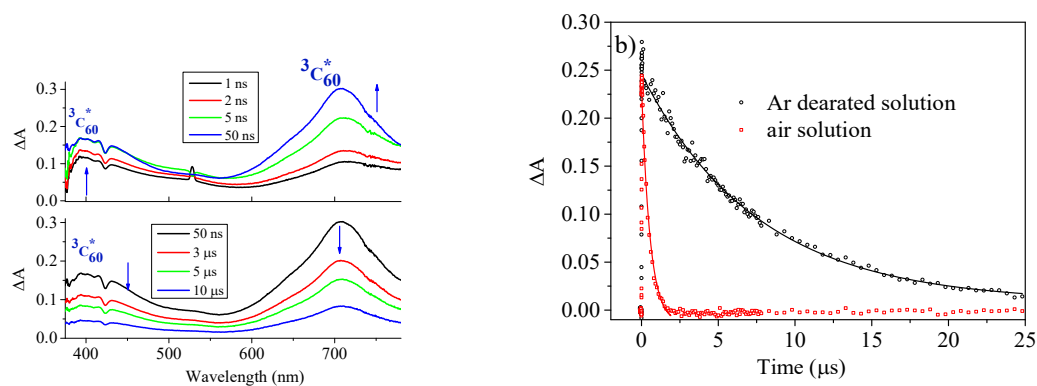


Figure 3.16. a) Nanosecond transient absorption spectra of the  $C_{60}$  in Argon-saturated benzonitrile at the indicated delay times; b) Kinetic traces (scattered points) of the  $C_{60}$  at 710 nm in the comparison between argon-saturated and air in benzonitrile.

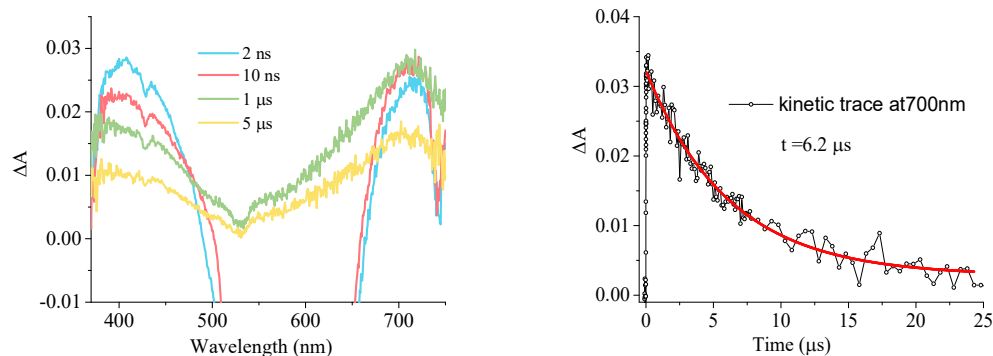


Figure 3.17. (a) Nanosecond transient absorption spectra of the Dyad-peptide ( $5.1 \times 10^{-6} M$ ) in argon-saturated benzonitrile at the indicated delay times. (b) Kinetic traces of the Dyad-peptide assembly at 700 nm corresponding to the  ${}^3C_{60}^*$ ,  $\lambda_{exc}$  527 nm.

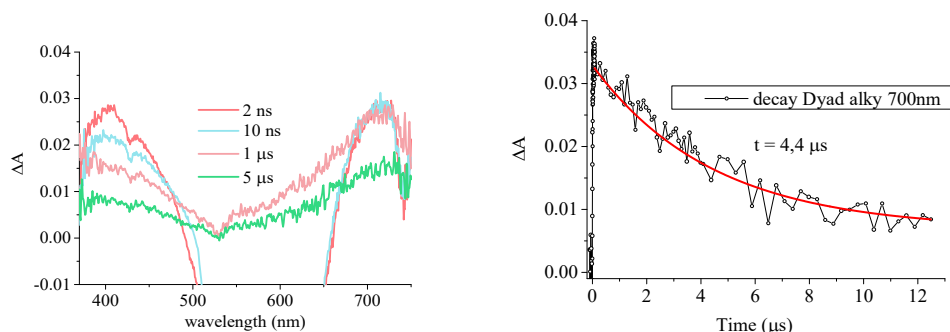


Figure 3.18. (a) Nanosecond transient absorption spectra of the Dyad-alkyl assembly ( $5 \times 10^{-6} M$ ) in argon-saturated benzonitrile at the indicated delay times. (b) Kinetic traces of the Dyad-alkyl assembly at 700 nm corresponding to the  ${}^3C_{60}^*$ ,  $\lambda_{exc}$  527 nm.

In general, both the Dyad-peptide and Dyad-alkyl assemblies show similar photoinduced processes, in which both electron transfer and energy transfer are likely to be favorable. The final step observed in nanosecond transient absorption shows the population of the triplet excited state of C<sub>60</sub> before returning to the ground state. The population of the triplet excited state of the C<sub>60</sub> as a final excited state has also been indicated in some literature.<sup>35</sup>

### **3.5 Perspective**

This chapter, we investigated photophysical properties dyad systems which constructed by fullerene and different derivatives of BODIPY. Fullerene was proved that it is a good electron acceptor in reaction with BODIPY donor under light excitation. The most important part of this chapter is given in appendices to provide supplementary discussion.<sup>16</sup> Besides, studying photophysical properties of the BDP-C<sub>60</sub> Dyad and BDP-C<sub>60</sub> assembly systems is an essential step for the construction of photocurrent photoelectrochemical cells using these compounds. These results above clearly indicated that electron transfer from BDP to C<sub>60</sub> upon excitation of the BDP moiety in solution of all these Dyad systems is possible. The BDP-C<sub>60</sub> peptide and BDP-C<sub>60</sub> alkyl with their helical peptide and alkyl chains can be prepared for self-assembled monolayers on gold surfaces, which facilitates the study of molecular photovoltaic devices. However, the helical peptide is a good electron mediator in comparison with an alkyl chain, thus it might be a better choice in the construction of devices for photo-energy conversion applications.

Electron transfer in the BDP-C<sub>60</sub>-peptide Dyad gives a promising future for self-assembled monolayers on gold surfaces because of its long lived charge-separated state. The molecular photovoltaic devices have been mainly developed for porphyrin-fullerene systems.<sup>43, 50</sup> Our results encourage us to continue the development by immobilizing the BDP-C<sub>60</sub>-peptide assembly on the gold surface for efficient molecular photovoltaic devices.

## **REFERENCES**

1. Sun, S.-S.; Sariciftci, N. S., *Organic photovoltaics: mechanisms, materials, and devices*. CRC press: 2017.
2. Hiramoto, M.; Fujiwara, H.; Yokoyama, M., p-i-n like behavior in three-layered organic solar cells having a co-deposited interlayer of pigments. *Journal of applied physics* **1992**, 72 (8), 3781-3787.
3. Peumans, P.; Uchida, S.; Forrest, S. R., Efficient bulk heterojunction photovoltaic cells using small-molecular-weight organic thin films. In *Materials for Sustainable Energy: A Collection of Peer-*

*Reviewed Research and Review Articles from Nature Publishing Group*, World Scientific: 2011; pp 94-98.

4. O'regan, B.; Grätzel, M., A low-cost, high-efficiency solar cell based on dye-sensitized colloidal TiO<sub>2</sub> films. *nature* **1991**, *353* (6346), 737.
5. Grätzel, M., Photoelectrochemical cells. *nature* **2001**, *414* (6861), 338.
6. Xue, J.; Rand, B. P.; Uchida, S.; Forrest, S. R., Mixed donor-acceptor molecular heterojunctions for photovoltaic applications. II. Device performance. *Journal of Applied Physics* **2005**, *98* (12), 124903.
7. Izawa, S.; Hashimoto, K.; Tajima, K., Efficient charge generation and collection in organic solar cells based on low band gap dyad molecules. *Chemical Communications* **2011**, *47* (22), 6365-6367.
8. Nishizawa, T.; Tajima, K.; Hashimoto, K., Supramolecular formation of fibrous nanostructure in donor-acceptor dyad film. *Journal of Materials Chemistry* **2007**, *17* (23), 2440-2445.
9. Nishizawa, T.; Lim, H. K.; Tajima, K.; Hashimoto, K., Efficient dyad-based organic solar cells with a highly crystalline donor group. *Chemical Communications* **2009**, (18), 2469-2471.
10. Rousseau, T.; Cravino, A.; Bura, T.; Ulrich, G.; Ziessel, R.; Roncali, J., BODIPY derivatives as donor materials for bulk heterojunction solar cells. *Chemical Communications* **2009**, (13), 1673-1675.
11. Ulrich, G.; Ziessel, R.; Harriman, A., The Chemistry of Fluorescent Bodipy Dyes: Versatility Unsurpassed. *Angewandte Chemie International Edition* **2008**, *47* (7), 1184-1201.
12. El-Khouly, M. E.; Fukuzumi, S.; D'Souza, F., Photosynthetic antenna-reaction center mimicry by using boron dipyrromethene sensitizers. *ChemPhysChem* **2014**, *15* (1), 30-47.
13. Rudolf, M.; Kirner, S. V.; Guldi, D. M., A multicomponent molecular approach to artificial photosynthesis - the role of fullerenes and endohedral metallofullerenes. *Chemical Society Reviews*. **2016**, *45* (3), 612-630.
14. Guldi, D. M.; Prato, M., Excited-State Properties of C<sub>60</sub> Fullerene Derivatives. *Accounts of Chemical Research*. **2000**, *33* (10), 695-703.
15. Kim, K.-S.; Kang, M.-S.; Ma, H.; Jen, A. K.-Y., Highly efficient photocurrent generation from a self-assembled monolayer film of a novel c<sub>60</sub>-tethered 2, 5-dithienylpyrrole triad. *Chemistry of materials* **2004**, *16* (24), 5058-5062.
16. Imahori, H.; Fukuzumi, S., Porphyrin-and fullerene-based molecular photovoltaic devices. *Advanced functional materials* **2004**, *14* (6), 525-536.
17. Nasrallah, H.; Rabah, J.; Bui-Thi-Tuyet, V.; Baczko, K.; Fensterbank, H.; Bourdreux, F.; Goncalves, A.-M.; Declerck, V.; Boujday, S.; Humblot, V., A fullerene helical peptide: synthesis, characterization and formation of self-assembled monolayers on gold surfaces. *New Journal of Chemistry* **2018**, *42* (24), 19423-19432.
18. D'Souza, F.; Ito, O., Photoinduced electron transfer in supramolecular systems of fullerenes functionalized with ligands capable of binding to zinc porphyrins and zinc phthalocyanines. *Coordination chemistry reviews* **2005**, *249* (13-14), 1410-1422.

19. Guldi, D. M.; Rahman, G. A.; Sgobba, V.; Ehli, C., Multifunctional molecular carbon materials—from fullerenes to carbon nanotubes. *Chemical Society Reviews* **2006**, *35* (5), 471-487.
20. Martin, N.; Sanchez, L.; Herranz, M. A.; Illescas, B.; Guldi, D. M., Electronic communication in tetrathiafulvalene (TTF)/C<sub>60</sub> systems: toward molecular solar energy conversion materials? *Accounts of chemical research* **2007**, *40* (10), 1015-1024.
21. Fukuzumi, S., Development of bioinspired artificial photosynthetic systems. *Physical Chemistry Chemical Physics* **2008**, *10* (17), 2283-2297.
22. Fukuzumi, S.; Kojima, T., Photofunctional nanomaterials composed of multiporphyrins and carbon-based  $\pi$ -electron acceptors. *Journal of Materials Chemistry* **2008**, *18* (13), 1427-1439.
23. Balzani, V.; Credi, A.; Venturi, M., Photochemical conversion of solar energy. *ChemSuschem* **2008**, *1* (1-2), 26-58.
24. Gust, D.; Moore, T. A.; Moore, A. L., Solar Fuels via Artificial Photosynthesis. *Accounts of Chemical Research* **2009**, *42* (12), 1890-1898.
25. Wasielewski, M. R., Self-assembly strategies for integrating light harvesting and charge separation in artificial photosynthetic systems. *Accounts of chemical research* **2009**, *42* (12), 1910-1921.
26. González-Rodríguez, D.; Carbonell, E.; Guldi, D. M.; Torres, T., Modulating Electronic Interactions between Closely Spaced Complementary  $\pi$  Surfaces with Different Outcomes: Regio- and Diastereomerically Pure Subphthalocyanine-C<sub>60</sub> Tris Adducts. *Angewandte Chemie International Edition* **2009**, *48* (43), 8032-8036.
27. Fukuzumi, S.; Honda, T.; Ohkubo, K.; Kojima, T., Charge separation in metallomacrocyclic complexes linked with electron acceptors by axial coordination. *Dalton Transactions* **2009**, (20), 3880-3889.
28. D'Souza, F.; Ito, O., Supramolecular donor-acceptor hybrids of porphyrins/phthalocyanines with fullerenes/carbon nanotubes: electron transfer, sensing, switching, and catalytic applications. *Chemical Communications* **2009**, (33), 4913-4928.
29. Guldi, D. M.; Illescas, B. M.; Atienza, C. M.; Wielopolski, M.; Martín, N., Fullerene for organic electronics. *Chemical Society Reviews* **2009**, *38* (6), 1587-1597.
30. D'Souza, F.; Ito, O., Photosensitized electron transfer processes of nanocarbons applicable to solar cells. *Chemical Society Reviews* **2012**, *41* (1), 86-96.
31. Dirian, K.; Herranz, M. A.; Katsukis, G.; Malig, J.; Rodríguez-Pérez, L.; Romero-Nieto, C.; Strauss, V.; Martin, N.; Guldi, D. M., Low dimensional nanocarbons—chemistry and energy/electron transfer reactions. *Chemical Science* **2013**, *4* (12), 4335-4353.
32. Espíldora, E.; Delgado, J. L.; Martín, N., Donor-Acceptor Hybrids for Organic Electronics. *Israel Journal of Chemistry* **2014**, *54* (5-6), 429-439.
33. Zieleniewska, A.; Lodermeier, F.; Roth, A.; Guldi, D., Fullerenes—how 25 years of charge transfer chemistry have shaped our understanding of (interfacial) interactions. *Chemical Society Reviews* **2018**, *47* (3), 702-714.

34. Ponceca, C. S.; Chábera, P.; Uhlig, J.; Persson, P.; Sundström, V., Ultrafast Electron Dynamics in Solar Energy Conversion. *Chemical Reviews* **2017**, *117* (16), 10940-11024.
35. Ziessel, R.; Retailleau, P.; Elliott, K. J.; Harriman, A., Boron Dipyrin Dyes Exhibiting "Push-Pull-Pull" Electronic Signatures. *Chemistry-a European Journal* **2009**, *15* (40), 10369-10374.
36. Wijesinghe, C. A.; El-Khouly, M. E.; Blakemore, J. D.; Zandler, M. E.; Fukuzumi, S.; D'Souza, F., Charge stabilization in a closely spaced ferrocene–boron dipyrin–fullerene triad. *Chemical Communications* **2010**, *46* (19), 3301-3303.
37. Liu, J.-Y.; El-Khouly, M. E.; Fukuzumi, S.; Ng, D. K.; P, Photoinduced Electron Transfer in a Distyryl BODIPY–Fullerene Dyad. *Chemistry – An Asian Journal* **2011**, *6* (1), 174-179.
38. Bandi, V.; Das, S. K.; Awuah, S. G.; You, Y.; D'Souza, F., Thieno-Pyrrole-Fused 4, 4-Difluoro-4-bora-3a, 4a-diaza-s-indacene–Fullerene Dyads: Utilization of Near-Infrared Sensitizers for Ultrafast Charge Separation in Donor–Acceptor Systems. *Journal of the American Chemical Society* **2014**, *136* (21), 7571-7574.
39. Bandi, V.; Gobeze, H. B.; D'Souza, F., Ultrafast Photoinduced Electron Transfer and Charge Stabilization in Donor–Acceptor Dyads Capable of Harvesting Near-Infrared Light. *Chemistry–A European Journal* **2015**, *21* (32), 11483-11494.
40. Shao, S.; Gobeze, H. B.; Karr, P. A.; D'Souza, F., Ultrafast Photoinduced Charge Separation in Wide-Band-Capturing Self-Assembled Supramolecular Bis (donor styryl) BODIPY–Fullerene Conjugates. *Chemistry–A European Journal* **2015**, *21* (45), 16005-16016.
41. Bandi, V.; Gobeze, H. B.; Lakshmi, V.; Ravikanth, M.; D'Souza, F., Vectorial Charge Separation and Selective Triplet-State Formation during Charge Recombination in a Pyrrolyl-Bridged BODIPY–Fullerene Dyad. *The Journal of Physical Chemistry C* **2015**, *119* (15), 8095-8102.
42. Iagatti, A.; Cupellini, L.; Biagiotti, G.; Caprasecca, S.; Fedeli, S.; Lapini, A.; Ussano, E.; Cicchi, S.; Foggi, P.; Marcaccio, M.; Mennucci, B.; Di Donato, M., Efficient Photoinduced Charge Separation in a BODIPY–C<sub>60</sub> Dyad. *The Journal of Physical Chemistry C* **2016**, *120* (30), 16526-16536.
43. Obondi, C. O.; Lim, G. N.; Karr, P. A.; Nesterov, V. N.; D'Souza, F., Photoinduced charge separation in wide-band capturing, multi-modular bis (donor styryl) BODIPY–fullerene systems. *Physical Chemistry Chemical Physics* **2016**, *18* (27), 18187-18200.
44. Liu, J.-Y.; Hou, X.-N.; Tian, Y.; Jiang, L.; Deng, S.; Röder, B.; Ermilov, E. A., Photoinduced energy and charge transfer in a bis (triphenylamine)–BODIPY–C<sub>60</sub> artificial photosynthetic system. *RSC Advances* **2016**, *6* (62), 57293-57305.
45. Ünlü, H.; Okutan, E., Preparation of BODIPY-fullerene and monostyryl BODIPY-fullerene dyads as heavy atom free singlet oxygen generators. *Dyes and Pigments* **2017**, *142*, 340-349.
46. Shao, S.; Thomas, M. B.; Park, K. H.; Mahaffey, Z.; Kim, D.; D'Souza, F., Sequential energy transfer followed by electron transfer in a BODIPY–bisstyrylBODIPY bound to C<sub>60</sub> triad via a 'two-point' binding strategy. *Chemical communications* **2018**, *54* (1), 54-57.

47. Cabrera-Espinoza, A.; Insuasty, B.; Ortiz, A., Novel BODIPY-C<sub>60</sub> derivatives with tuned photophysical and electron-acceptor properties: Isoxazolino [60] fullerene and pyrrolidino [60] fullerene. *Journal of Luminescence* **2018**, *194*, 729-738.
48. Liu, J.-Y.; El-Khouly, M. E.; Fukuzumi, S.; Ng, D. K. P., Photoinduced Electron Transfer in a Ferrocene–Distyryl BODIPY Dyad and a Ferrocene–Distyryl BODIPY–C<sub>60</sub> Triad. *ChemPhysChem* **2012**, *13* (8), 2030-2036.
49. Yang, P.; Wu, W.; Zhao, J.; Huang, D.; Yi, X., Using C<sub>60</sub>-bodipy dyads that show strong absorption of visible light and long-lived triplet excited states as organic triplet photosensitizers for triplet–triplet annihilation upconversion. *Journal of Materials Chemistry* **2012**, *22* (38), 20273-20283.
50. Yamada, H.; Imahori, H.; Nishimura, Y.; Yamazaki, I.; Ahn, T. K.; Kim, S. K.; Kim, D.; Fukuzumi, S., Photovoltaic properties of self-assembled monolayers of porphyrins and porphyrin–fullerene dyads on ITO and gold surfaces. *Journal of the American Chemical Society* **2003**, *125* (30), 9129-9139.
51. Amdursky, N., Electron transfer across helical peptides. *ChemPlusChem* **2015**, *80* (7), 1075-1095.
52. Venanzi, M.; Gatto, E.; Formaggio, F.; Toniolo, C., The importance of being Aib. Aggregation and self-assembly studies on conformationally constrained oligopeptides. *Journal of Peptide Science* **2017**, *23* (2), 104-116.
53. Gatto, E.; Venanzi, M., The Impervious Route to Peptide-Based Dye-Sensitized Solar Cells. *Israel Journal of Chemistry* **2015**, *55* (6-7), 671-681.
54. Jian-Yong, L.; E., E.-K. M.; Shunichi, F.; P., N. D. K., Photoinduced Electron Transfer in a Ferrocene–Distyryl BODIPY Dyad and a Ferrocene–Distyryl BODIPY–C<sub>60</sub> Triad. *ChemPhysChem* **2012**, *13* (8), 2030-2036.
55. Constant, C.; Albert, S.; Zivic, N.; Baczko, K.; Fensterbank, H.; Allard, E., Orthogonal functionalization of a fullerene building block through copper-catalyzed alkyne–azide and thiol–maleimide click reactions. *Tetrahedron* **2014**, *70* (18), 3023-3029.
56. Fensterbank, H.; Baczko, K.; Constant, C.; Idttalbe, N.; Bourdreux, F.; Vallée, A.; Goncalves, A.-M.; Méallet-Renault, R.; Clavier, G.; Wright, K.; Allard, E., Sequential Copper-Catalyzed Alkyne–Azide Cycloaddition and Thiol-Maleimide Addition for the Synthesis of Photo- and/or Electroactive Fullerodendrimers and Cysteine-Functionalized Fullerene Derivatives. *Journal of Organic Chemistry* **2016**, *81* (18), 8222-8233.
57. Chaudhuri, T.; Mula, S.; Chattopadhyay, S.; Banerjee, M., Photophysical properties of the 8-phenyl analogue of PM567: a theoretical rationalization. *Spectrochimica Acta Part A: Molecular and Biomolecular Spectroscopy* **2010**, *75* (2), 739-744.
58. Guldi, D. M.; Hungerbühler, H.; Carmichael, I.; Asmus, K.-D.; Maggini, M., [6-6]-Closed versus [6-5]-Open Isomers of Imino-and Methanofullerenes: A Comparison with Pristine C<sub>60</sub> and (C<sub>59</sub>N)<sup>•</sup>. *The Journal of Physical Chemistry A* **2000**, *104* (38), 8601-8608.

59. Baffreau, J.; Leroy-Lhez, S.; Van Anh, N.; Williams, R. M.; Hudhomme, P., Fullerene C<sub>60</sub>–Perylene-3,4:9,10-bis(dicarboximide) Light-Harvesting Dyads: Spacer-Length and Bay-Substituent Effects on Intramolecular Singlet and Triplet Energy Transfer. *Chemistry – A European Journal* **2008**, *14* (16), 4974-4992.
60. D’Souza, F.; Sandanayaka, A. S. D.; Ito, O., SWNT-Based Supramolecular Nanoarchitectures with Photosensitizing Donor and Acceptor Molecules. *The Journal of Physical Chemistry Letters* **2010**, *1* (17), 2586-2593.
61. Guldi, D. M.; Giacalone, F.; de la Torre, G.; Segura, J. L.; Martın, N., Topological Effects of a Rigid Chiral Spacer on the Electronic Interactions in Donor–Acceptor Ensembles. *Chemistry–A European Journal* **2005**, *11* (24), 7199-7210.
62. Bell, T. D. M.; Ghiggino, K. P.; Haynes, A.; Langford, S. J.; Woodward, C. P., Charge separation in a conformationally-flexible porphyrin-fullerene dyad synthesised using cross-metathesis. *Journal of Porphyrins and Phthalocyanines* **2007**, *11* (06), 455-462.
63. Ravasco, J. M.; Faustino, H.; Trindade, A.; Gois, P. M., Bioconjugation with Maleimides: A Useful Tool for Chemical Biology. *Chemistry–A European Journal* **2019**, *25* (1), 43-59.
64. Forster, T., 10th Spiers Memorial Lecture. Transfer mechanisms of electronic excitation. *Discussions of the Faraday Society* **1959**, *27*, 7-17.
65. Rehm, D.; Weller, A., *Isr. J. Chem.* **1970**, *8*, 259.
66. Wijesinghe, C. A.; El-Khouly, M. E.; Subbaiyan, N. K.; Supur, M.; Zandler, M. E.; Ohkubo, K.; Fukuzumi, S.; D’Souza, F., Photochemical Charge Separation in Closely Positioned Donor–Boron Dipyrin–Fullerene Triads. *Chemistry – A European Journal* **2011**, *17* (11), 3147-3156.
67. Krejcık, M.; Danek, M.; Hartl, F., Simple construction of an infrared optically transparent thin-layer electrochemical cell: Applications to the redox reactions of ferrocene, Mn<sub>2</sub>(CO)<sub>10</sub> and Mn(CO)<sub>3</sub>(3,5-di-t-butyl-catecholate)<sup>–</sup>. *Journal of electroanalytical chemistry and interfacial electrochemistry* **1991**, *317* (1-2), 179-187.
68. Mendes Marinho, S.; Ha-Thi, M.-H.; Pham, V.-T.; Quaranta, A.; Pino, T.; Lefumeux, C.; Chamaille, T.; Leibl, W.; Aukauloo, A., Time-resolved interception of multiple charge accumulation in a sensitizer-acceptor dyad. *Angewandte Chemie International Edition* **2017**, *56* (50), 15936-15940.

# Chapter 4. Charge accumulation on multicomponent systems

## 4.1 Introduction

Multiple electron transfers play a key role in natural processes, such as photosynthesis, respiration and photocatalysis of small molecules. Mimicking these processes by using artificial photosynthesis to capture, store and convert solar energy into chemical energy has emerged as a challenge for current research,<sup>1,2</sup> with photocatalytic CO<sub>2</sub> reduction being an attractive possibility. To reduce CO<sub>2</sub> via chemical reactions, multi-electron reactions are required. CO<sub>2</sub> reduction reactions are shown in Table 4.1.

Reaction	E <sup>0</sup> <sub>app</sub> (V)
CO <sub>2</sub> + 2H <sup>+</sup> + 2e <sup>-</sup> → HCOOH	-0.61
CO <sub>2</sub> + 2H <sup>+</sup> + 2e <sup>-</sup> → CO + H <sub>2</sub> O	-0.53
CO <sub>2</sub> + 4H <sup>+</sup> + 4e <sup>-</sup> → HCHO + H <sub>2</sub> O	-0.48
CO <sub>2</sub> + 6H <sup>+</sup> + 6e <sup>-</sup> → CH <sub>3</sub> OH + H <sub>2</sub> O	-0.38
CO <sub>2</sub> + 8H <sup>+</sup> + 8e <sup>-</sup> → CH <sub>4</sub> + 2H <sub>2</sub> O	-0.24
E <sup>0</sup> <sub>app</sub> potentials are in an aqueous solution at pH 7	

*Table 4.1. CO<sub>2</sub> reduction potentials vs. NHE<sup>3</sup>*

In principle, each absorbed photon can only induce a one-electron transfer. Therefore, an artificial system has to be built to complete the catalytic reaction by sequential absorption of several photons leading to accumulation of electrons and holes. In general, most of the photocatalytic reactions use transition metal complexes that can act as redox photosensitizers causing initiation of photochemical electron transfer from a reductant to a catalyst. The second component is a catalyst which accepts and accumulates the electrons from the photosensitizer and gives them to the CO<sub>2</sub> molecule to complete photocatalytic CO<sub>2</sub> reduction.<sup>4</sup> In the photocatalytic reaction of CO<sub>2</sub>, a reductant is usually used to provide the complementary redox equivalents, as a so-called “sacrificial electron donor”.<sup>1,4</sup> Various photocatalytic systems based

on metal complexes have been developed.<sup>5</sup> For example, multiple metal complexes can be combined via bridging ligands, forming supramolecular photocatalysts such as  $[\text{Ru}(\text{bpy})_3]^{2+}$ - $[\text{Ni}]$ ,  $[\text{Ru}(\text{bpy})_3]^{2+}$ -Co,  $[\text{Ru}(\text{bpy})_3]^{2+}$ - $[\text{Re}]$ .<sup>5-6</sup> These systems give rapid electron transfer between components, which helps to improve the performance of the photocatalytic system.<sup>7</sup> However, these covalently linked systems also frequently suffer from rapid charge recombination.<sup>1</sup>

A multicomponent photocatalytic system is a simple approach, which has attracted much research, for example, to perform water splitting, hydrogen evolution, and  $\text{CO}_2$  reduction. In a multicomponent photocatalytic system, the photosensitizer works with the catalyst as unbound molecules in the same solution. Intermolecular charge transfer gives a long-lived charge-separated state. The diffusion of components limits the speed of the process, resulting in slow charge recombination.

To date, there are many successful reported photocatalytic reactions using multicomponent systems to reduce  $\text{CO}_2$  to CO.<sup>4-5</sup> It is noteworthy that the reduction of  $\text{CO}_2$  to form CO requires two electrons. However, to understand how charge accumulates on catalyst molecules and is passed on to  $\text{CO}_2$  for the reduction reaction requires further spectroscopic observation. Therefore, efforts to interpret charge accumulation in the model catalyst molecules are required to improve the efficiency of the photocatalytic reaction.

## **4.2 Components for constructing charge accumulation systems – a model photocatalytic system**

### **4.2.1 Photosensitizer (PS) and reductant**

Electron transfer in photocatalytic reactions has been implemented via photosensitizers. The initiating photosensitizer reaction can be either reductive quenching when the excited state of the photosensitizer ( $\text{PS}^*$ ) is quenched by reductant, forming a one-electron-reduced species (OERS), or oxidative quenching when  $\text{PS}^*$  is quenched by a catalyst or a mediator. However, in most reported cases of the photocatalytic reaction of  $\text{CO}_2$ ,  $\text{PS}^*$  is frequently used as a OERS. Reasons for this include: the OERS of PS ( $\text{PS}^{\bullet-}$ ) has a strong reductive power which makes reduction of the catalyst easier to achieve, and reduction of  $\text{CO}_2$  by the one-electron-oxidized species (OEOS) of the photosensitizer ( $\text{PS}^{\bullet+}$ ) is an unfavourable process.

The criteria for a good photosensitizer should include the following photophysical and electrochemical properties:

(1) Stronger absorption than other components, such as donor and catalyst. Particularly, it should strongly absorb in the visible region to apply in the utilization of solar energy.

(2) The long excited-state lifetime (on the order of microseconds) helps for efficient reductive quenching processes.

(3) Oxidative power of the excited state is strong enough to capture an electron from the reductant.

(4) Sufficiently long lifetime (on the order of microseconds) of the  $PS^{\bullet-}$  to favor sequential electron transfer reactions.

### **Ruthenium [Ru(bpy)<sub>3</sub>]<sup>2+</sup>**

In this thesis, [Ru(bpy)<sub>3</sub>]<sup>2+</sup> was used as the main photosensitizer to study charge accumulation in model catalytic systems. [Ru(bpy)<sub>3</sub>]<sup>2+</sup> has become one of the most widely used PS in photocatalytic CO<sub>2</sub> reduction systems. It shows strong absorption in the visible region ( $\epsilon_{450\text{nm}} = 11300 \text{ M}^{-1}\text{cm}^{-1}$ ) due to the singlet metal-to-ligand charge transfer (<sup>1</sup>MLCT), which undergoes an intersystem crossing with  $\tau = 100 \text{ fs}$ , forming a long-lived triplet state in deaerated water<sup>8</sup> (<sup>3</sup>MLCT). This relatively long-lived state has a remarkable property of being both more oxidized and reductive than the ground state. Therefore, it can undergoes rapid redox reactions in the excited state. It is also photochemically stable in many solutions. In this works, We used [Ru(bpy)<sub>3</sub>]<sup>2+</sup> as a photosensitizer to study charge accumulation on MV<sup>2+</sup> and NDI systems.

### **Reductant: ascorbate**

The photocatalytic reduction of CO<sub>2</sub> by using H<sub>2</sub>O as a reductant is a final target. Because the oxidative power of the photosensitizer is not enough to capture electrons from water, most photocatalytic systems require a sacrificial electron donor to supply the complementary redox equivalents. In this chapter, doubly reduced model molecules by using ascorbate reductant are described. For electron transfer to proceed from reductant to the excited state of photosensitizer, a reductant should have the following properties:<sup>9</sup>

- (1) Strong reducing power to reduce the excited state of photosensitizer.
- (2) Short lifetime of the OEOS of the reductant is necessary, in order to maximize reaction efficiency.
- (3) The OEOS of the reductant has no effect on the photocatalytic reaction.

Therefore, choosing a proper reductant is very important for photocatalytic reactions and charge accumulation as well. In this work, ascorbate, with a redox potential  $\text{ascorbate}^+/\text{ascorbate} = -0.164 \text{ V vs SCE}$  in comparison with  $[\text{Ru}(\text{bpy})_3]^{2+}/[\text{Ru}(\text{bpy})_3]^+ = 0.92 \text{ V vs SCE}$ , is chosen to act as an electron donor in mixed aqueous-acetonitrile solution.

#### **4.2.2 Model complexes for studying charge accumulation**

To date, there have been important developments of successful photocatalytic systems using metal complexes. However, studies to monitor charge accumulation on those molecular systems have not been performed yet. Therefore, studying charge accumulation on model molecules is worthwhile to elucidate and optimize fundamental processes in photocatalytic reactions.

##### **Methyl viologen ( $\text{MV}^{2+}$ )**

Methyl viologen has been used to study fundamental photoinduced electron transfer<sup>10</sup> and solar energy conversion<sup>11</sup> as well. Methyl viologen is a well-studied compound possessing two reversible redox potentials ( $\text{MV}^{2+}/\text{MV}^+ = -0.42 \text{ V vs SCE}$  and  $\text{MV}^+/\text{MV}^0 = -0.81 \text{ vs SCE}$ )<sup>12</sup>, and is widely used in photochemical electron transfer reactions. With distinguishable electronic absorption of the singly and doubly reduced states,<sup>12</sup> studying charge accumulation on Methyl viologen using pump-pump excitation transient absorption spectroscopy seems particularly well-suited.

##### **Naphthalene Diimide (NDI)**

Aromatic diimides have been known as electron acceptors to study photoinduced electron transfer in a wide variety of molecular systems designed for photosynthesis,<sup>13</sup> and solar energy conversion.<sup>14</sup> Diimides are widely used in electron transfer reactions because of the following reasons:

- (1) Diimides can be reduced stepwise in two phases with modest potentials ( $\text{NDI}/\text{NDI}^{\bullet-} = -0.48 \text{ V vs SCE}$  and  $\text{NDI}^{\bullet-}/\text{NDI}^{2-} = -0.99 \text{ V vs SCE}$ )<sup>15</sup>
- (2) The electronic absorption spectra of the radical anions and the doubly reduced dianions are distinguishable in visible and near-infrared region (Figure 4.1)<sup>15</sup>

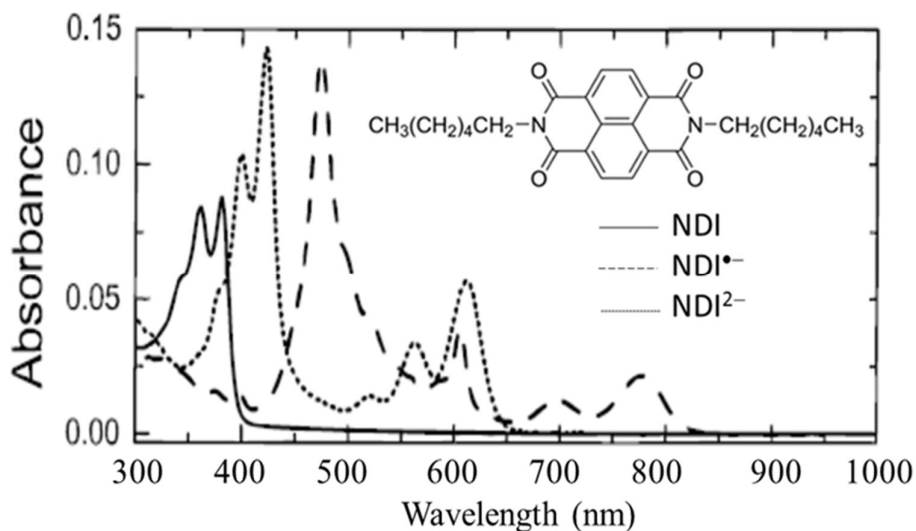


Figure 4.1. Ground-state absorption spectra of neutral (NDI), first reduced ( $\text{NDI}^{\bullet-}$ ) and second reduced state of NDI ( $\text{NDI}^{2-}$ )<sup>15</sup>. Inset: structure of NDI.

(3) The electrochemical and photophysical properties have been well studied and reported in the literature.<sup>15-16</sup>

In light of the above properties, we have chosen NDI as a model molecule to study charge accumulation by using nanosecond transient absorption to monitor the formation of NDI dianion.

### 4.3 Snapshots of light-induced accumulation of two charges on Methylviologen using a sequential nanosecond pump- pump photoexcitation (The Journal of physical chemistry letters)

## Snapshots of Light Induced Accumulation of Two Charges on Methylviologen using a Sequential Nanosecond Pump-Pump Photoexcitation<sup>17</sup>

Thu-Trang Tran,<sup>†</sup> Minh-Huong Ha-Thi,<sup>\* †</sup> Thomas Pino,<sup>†</sup> Annamaria Quaranta,<sup>‡</sup> Christophe Lefumeux,<sup>†</sup> Winfried Leibl<sup>‡</sup> and Ally Aukauloo<sup>\*§‡</sup>

†Institut des Sciences Moléculaire d'Orsay (ISMO), CNRS, Univ. Paris-Sud, Université Paris-Saclay, F-91405 Orsay, France.

‡ Institute for integrative Biology of the Cell (I2BC), CEA, CNRS, UMR 9198, F-91191, Gif-sur-Yvette, France.

§ Institut de Chimie Moléculaire et des Matériaux d'Orsay (ICMMO), Université Paris Sud, CNRS, F-91405 Orsay Cedex, France

#### AUTHOR INFORMATION

#### Corresponding Authors

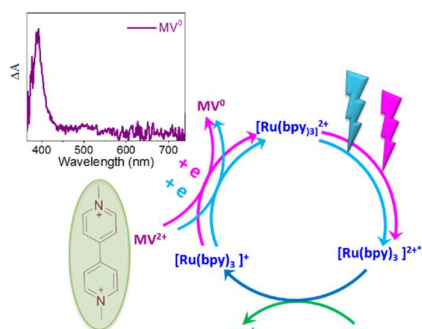
\* E-mail: minh-huong.ha-thi@u-psud.fr

\* E-mail: ally.aukaouo@u-psud.fr

#### ABSTRACT:

Methylviologen ( $MV^{2+}$ ) is perhaps the most used component as a reversible electron acceptor in photophysical studies. While  $MV^{2+}$  is most commonly implicated as a reversible one-electron mediator, its electrochemical properties clearly evidence two successive one-electron reduction processes. In this report, we have investigated on the light driven two-charge accumulation on  $MV^{2+}$  using a multicomponent system composed of the prototypical molecular photosensitizer  $[Ru(bpy)_3]^{2+}$  and  $MV^{2+}$  in the presence of ascorbate as reversible electron donor. The sequential addition of two electrons on the methylviologen was tracked upon sequential excitation of the  $[Ru(bpy)_3]^{2+}$  at optimized concentration of the electron acceptor. The charge accumulated state carries an energy of 0.9 eV above the ground state and has a lifetime of ca. 50  $\mu s$ . We have reached a fairly good global yield of approximately 9% for the two-charge accumulation. This result clearly demonstrates the potential of this simple approach for applications in artificial photosynthesis.

#### TOC GRAPHICS



**KEYWORDS.** Methylviologen, electron transfer, accumulative charge separation, time-resolved spectroscopy, double excitation, photosynthesis.

Multiple electron transfers are at the basis of the functioning of natural processes such as energy transduction pathways in photosynthesis and respiration, and also in the catalytic chemical transformations of small molecules.<sup>2, 18</sup> In the actual quest of finding new ways to produce a sustainable solar-based fuel, scientists are focusing on the storage of sunlight in a chemical form.<sup>19</sup> Such a strategy will demand to optimize the capture of sunlight to perform multiple charge accumulation and realizing multielectronic bond making and breaking catalysis. In recent years, we have seen an enormous number of reports on photocatalytic molecular systems to drive water oxidation, production of H<sub>2</sub> or reduction of CO<sub>2</sub>.<sup>20-23</sup> However, very little is known in these multielectronic light-induced catalytic processes on the productive and deleterious pathways taking place under excitation.<sup>1, 24-29</sup> There is therefore an urgent need to address these fundamental issues on the way towards optimization.

Photocatalytic systems are generally composed of a chromophore, a catalyst and a sacrificial electron donor (or acceptor).<sup>20, 30-33</sup> Upon absorption of light, the chromophore excited state is quenched by a sacrificial electron donor (acceptor) to give its reduced (oxidized) state. These highly reactive species can then transfer an electron (hole) to activate the catalytic module. Sequential photoinduced charge accumulation is crucial for driving multielectronic chemical transformations. In such approach, usually sacrificial (irreversible) electron donors (acceptors) are used to prevent unproductive charge-recombination processes.<sup>30, 33</sup> In more realistic situations (in the presence of reversible electron donors or acceptors), one bottleneck reaction in these systems is the accumulation of more than one charge on the catalyst, since in the absence of further charge-stabilization processes, the process of charge accumulation is thermodynamically less favorable than the charge recombination reaction. Therefore successful charge accumulation has to rely on kinetic out competition of back reactions.

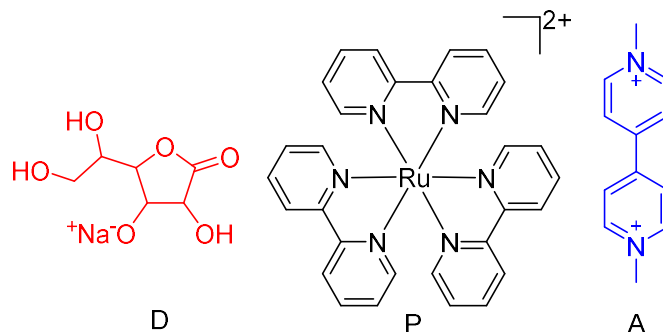
The scarcity of reports on the study of stepwise charge accumulation is a telling fact of this challenging but nonetheless crucial task. In Photosystem II, the enzyme that performs the light-driven oxidation of water, all the first photophysical events that ultimately lead to charge accumulation at the Oxygen Evolving Complex are reversible in nature. Our recent effort in this field was based on the charge accumulation process within a molecular dyad containing a [Ru(bpy)<sub>3</sub>]<sup>2+</sup> chromophore and a naphthalenediimide (NDI), unveiling the operating processes in competition with charge accumulation on the NDI moiety.<sup>34</sup> Like in most of the above mentioned works, the charge accumulating unit was covalently tethered to the sensitizer. In

doing so, chemists aim to control the distance and electronic communication between the constitutive units allowing faster charge transfer reactions compared to diffusion limited processes in multicomponent systems. However, strong coupling also favors the back charge transfer, especially in the excited state.<sup>1, 35</sup> This process is, on the contrary, disfavored in multicomponent systems with diffusion-limited kinetics, due to small concentrations of photoactivated species. Another drawback in linked systems might be the presence of efficient quenching of the chromophore excited state by energy transfer, for example to the catalyst.

Viologens, of general formula N,N'-disubstituted-4,4'-bipyridinium dication, are well-established class of compounds exhibiting two stable, reversible cathodic waves at quite negative potentials.<sup>36</sup> Studied since the 70s, they have recently received attention for potential applications in organic electronics, molecular machines and organic storage systems, as recently reviewed by Striepe and Baumgartner.<sup>37</sup> Methylviologen, the archetypal compound, has been extensively used as a reversible one-electron acceptor and transporter in many photochemical reactions. Recently, storage of electrons on methylviologen acceptor sites has been achieved by tethering a chromophore  $[\text{Ru}(\text{bpy})_3]^{2+}$  to multiple viologen units whereby electrons could be stored upon single-electron transfer processes.<sup>38-39</sup> Using this strategy, photodriven Pt-catalysed  $\text{H}_2$  evolution could be observed. It is to be noted that the doubly reduced form of methylviologen, which is a highly reducing species and that can act as a potential two-electron mediator in chemical and photochemical transformations has received only little attention.<sup>12, 40</sup> Of note, the photo-catalytic system developed by Willner and co-workers where the doubly reduced form  $\text{MV}^0$ , created by disproportionation of  $\text{MV}^{+}$  in a water-organic two-phase system, was able to reduce dibromides to the corresponding alkenes.<sup>41-42</sup>

We have been interested in investigating the sequential two-charge accumulation on methylviologen dication. We have used for this study a multicomponent system, containing  $[\text{Ru}(\text{bpy})_3]^{2+}$  and methylviologen (N,N'-dimethyl-4,4'-bipyridinium dication,  $\text{MV}^{2+}$ ) and ascorbate as electron donor. It is noteworthy that in our condition, both the methylviologen and ascorbate are reversible electron acceptor and donor respectively. As such these features confer a more biomimetic aspect to this present study. Interestingly, we have reached a global efficiency of around 9% for the double charge accumulation. Structures of the compounds in this study are presented in Scheme 1. Our choice for monitoring the accumulation of charges on methylviologen was also guided by the distinguishable electronic absorption features of the mono and doubly reduced species.<sup>12</sup> The accumulative charge separation in this multicomponent system was probed using nanosecond pump-pump-probe transient absorption

spectroscopy. We report herein the kinetics of the different reaction steps for the formation of the charge accumulation state as well as those of competitive reaction pathways.



**Scheme 1.** Molecular structure of ascorbate (D), [Ru(bpy)<sub>3</sub>]<sup>2+</sup> (P) and MV(PF<sub>6</sub>)<sub>2</sub> (A)

To investigate the formation of the first charge separated state (CSS1), samples containing 43  $\mu\text{M}$  of [Ru(bpy)<sub>3</sub>]<sup>2+</sup>, 13.4  $\mu\text{M}$  of MV<sup>2+</sup> and 100 mM of ascorbate in a acetonitrile/water (60:40) mixture were studied by transient absorption by irradiating with 460 nm nanosecond laser pulses ( $\sim 5$  mJ/pulse). The experimental setup is described in the SI. In order to study different routes of electron transfer in this triptych mixture, experiments were also carried out in the same conditions on samples containing i) [Ru(bpy)<sub>3</sub>]<sup>2+</sup> alone, ii) [Ru(bpy)<sub>3</sub>]<sup>2+</sup> in the presence of ascorbate, and iii) [Ru(bpy)<sub>3</sub>]<sup>2+</sup> with MV<sup>2+</sup>. A ground state bleach at 450 nm after excitation of [Ru(bpy)<sub>3</sub>]<sup>2+</sup> alone indicates the formation of 20.4  $\mu\text{M}$  of [Ru(bpy)<sub>3</sub>]<sup>2+\*</sup> ( $\Delta A_{450} = -0.23$ , using a  $\Delta \epsilon_{450} = -11300 \text{ M}^{-1}\text{cm}^{-1}$ ),<sup>43</sup> corresponding to 47 ( $\pm 2$ ) % of the ground state population (Fig. S1). Decay of the absorption bleach was found to be mono-exponential with  $\tau = 0.77 \pm 0.02 \mu\text{s}$  corresponding to the excited state lifetime of [Ru(bpy)<sub>3</sub>]<sup>2+\*</sup>.<sup>8</sup> In the presence of 13.4  $\mu\text{M}$  of MV<sup>2+</sup>, no change was observed for the emission spectra and for the lifetime of [Ru(bpy)<sub>3</sub>]<sup>2+\*</sup>, indicating a negligible interaction between MV<sup>2+</sup> and [Ru(bpy)<sub>3</sub>]<sup>2+\*</sup> due to the low concentration of the quencher. In the sample containing the same concentration of [Ru(bpy)<sub>3</sub>]<sup>2+</sup> and 100 mM of ascorbate, a new absorption feature centered at 500-510 nm was observed (Fig. S2). This band was assigned to the formation of [Ru(bpy)<sub>3</sub>]<sup>+</sup>, which is formed following reductive electron transfer from ascorbate to the excited state of [Ru(bpy)<sub>3</sub>]<sup>2+\*</sup>. Kinetic decay traces were measured around 510 nm and the rate constant of the formation of [Ru(bpy)<sub>3</sub>]<sup>+</sup> was found as  $k_q = 2.9 (\pm 0.5) \times 10^8 \text{ M}^{-1}\text{s}^{-1}$ , corresponding to a rise time of  $34 \pm 5 \text{ ns}$  (Fig. S2). The differential absorption spectrum indicates the formation of 15  $\mu\text{M}$  of [Ru(bpy)<sub>3</sub>]<sup>+</sup> ( $\Delta A_{500} = 0.18$ , using a  $\Delta \epsilon_{500} = 12000 \text{ M}^{-1}\text{cm}^{-1}$ )<sup>33</sup>, which is 73 ( $\pm 4$ ) % of [Ru(bpy)<sub>3</sub>]<sup>2+\*</sup> population. Charge recombination between the [Ru(bpy)<sub>3</sub>]<sup>+</sup> and oxidized ascorbate occurs with a second-order rate constant,  $k_{\text{rec1}} = 3 (\pm 0.5) \times 10^9 \text{ M}^{-1}\text{s}^{-1}$  (Fig. S3).

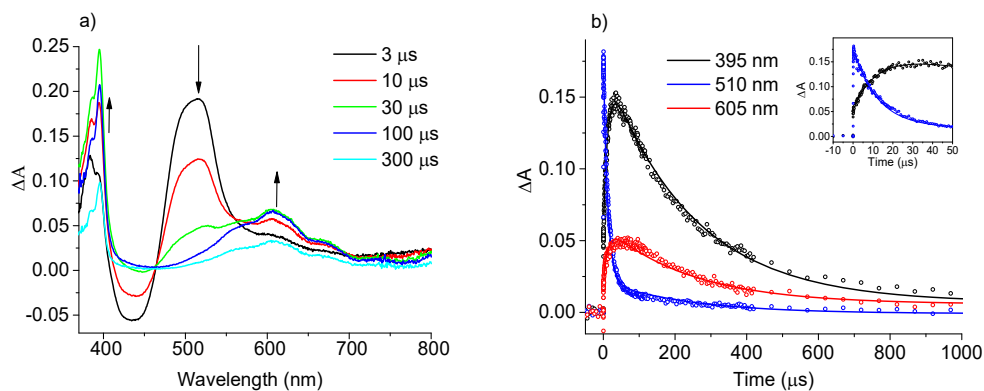


**Figure 1.** (a) Transient absorption spectra and (b) selected kinetics measured at the indicated delay times after excitation at 460 nm of  $[\text{Ru}(\text{bpy})_3]^{2+}$  ( $43 \mu\text{M}$ ) in de-aerated  $\text{CH}_3\text{CN}/\text{H}_2\text{O}$  (60:40) in the presence of 100 mM ascorbate,  $13.4 \mu\text{M MV}^{2+}$ . Inset: kinetics at 395 and 510 nm at short delay times.

The same experiment was then performed in the sample containing  $[\text{Ru}(\text{bpy})_3]^{2+}$ ,  $\text{MV}^{2+}$  and ascorbate. Figure 1a shows the transient absorption spectra and the transient kinetic traces of  $\text{asc}/\text{Ru}^{2+}/\text{MV}^{2+}$  system with 100 mM ascorbate,  $13.4 \mu\text{M MV}^{2+}$  at the indicated delay times. The electronic absorption of the singly reduced species  $\text{MV}^{\bullet+}$  is characterized by two positive absorption bands at 395 ( $\epsilon \sim 39000 \text{ M}^{-1} \text{ cm}^{-1}$ ) and 605 nm ( $\epsilon \sim 13000 \text{ M}^{-1} \text{ cm}^{-1}$ ) whereas only one absorption band centered at 395 nm ( $\epsilon \sim 39000 \text{ M}^{-1} \text{ cm}^{-1}$ ) is observed for the doubly reduced species  $\text{MV}^0$ .<sup>12, 44</sup> The spectra show a decrease of absorption band of  $[\text{Ru}(\text{bpy})_3]^+$  at 510 nm concomitantly to the formation of  $\text{MV}^{\bullet+}$  which is evidenced by the absorption bands at 395 and 605 nm. The initial  $\Delta A_{605}$  corresponds to  $3.8 \mu\text{M}$  of the  $\text{MV}^{\bullet+}$  (CSS1) that is  $28 (\pm 2) \%$  of the initial  $\text{MV}^{2+}$ . The transient kinetic traces were fitted globally and satisfactory fits were obtained using biexponential decay functions with time constants of  $12 (\pm 1)$  and  $250 (\pm 20) \mu\text{s}$ . The kinetic traces in Fig. 1b show the disappearance of  $[\text{Ru}(\text{bpy})_3]^+$  absorption around 510 nm together with a growth of absorption at 395 and 605 nm, characteristics of the  $\text{MV}^{\bullet+}$ , with the same kinetics of  $12 \mu\text{s}$ . The pre-exponential factors associated with this lifetime also indicate the loss of  $[\text{Ru}(\text{bpy})_3]^+$  (positive values at 510 nm) and the formation of  $\text{MV}^{\bullet+}$  (negative values at 395 and 605 nm; Fig. S4). The formation of the CSS1 occurs with an apparent rate constant of  $k_{\text{app}1} = 8.3 (\pm 0.7) \times 10^4 \text{ s}^{-1}$  (Scheme 2). Thus, an electron transfer rate constant  $k_{\text{et}1}$  close to the diffusion limit could be estimated ( $\sim 6 (\pm 3) \times 10^9 \text{ M}^{-1}\text{s}^{-1}$ ). This CSS1 state decays with a second-order rate constant,  $k_{\text{rec}2} \sim 1.1 (\pm 0.5) \times 10^9 \text{ M}^{-1}\text{s}^{-1}$ , approximately calculated using the decay time of  $250 \mu\text{s}$  and  $\text{MV}^{\bullet+}$  concentration of  $3.8 \mu\text{M}$  (Scheme 2). The results after the single excitation show an efficient conversion of  $28 (\pm 2) \%$  of the  $\text{MV}^{2+}$  molecules uplifted in the

CSS1  $MV^{*+}$  in our experimental conditions. No change was observed in the ground state absorption spectrum of the sample before and after the transient absorption experiment, indicating complete reversibility of the electron transfer.

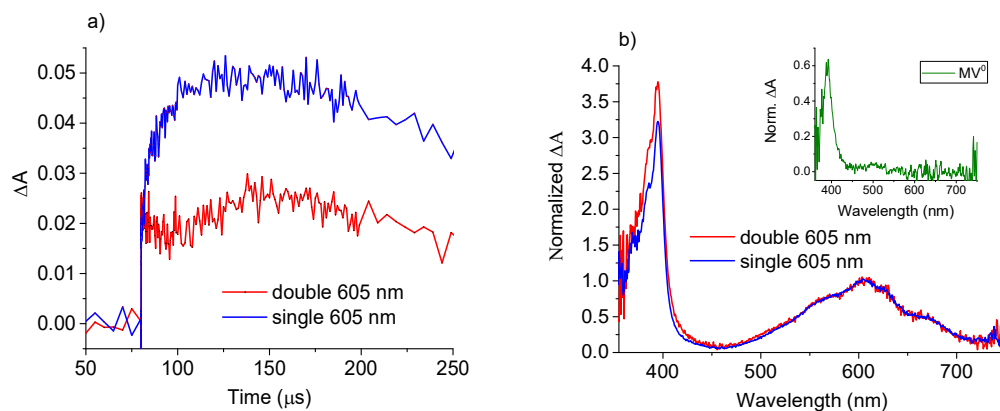


**Figure 2.** (a) Transient absorption kinetics and (b) transient absorption spectra normalized at 605 nm of  $[Ru(bpy)_3]^{2+}$  ( $43 \mu M$ ) in de-aerated  $CH_3CN/H_2O$  (60:40) in the presence of 100 mM ascorbate and  $13.4 \mu M MV^{2+}$ , obtained 80  $\mu s$  after a single-pulse excitation (blue line) and 80  $\mu s$  after the second pulse of a two-pulse excitation (red line). The two nanosecond pulses were delayed by 80  $\mu s$ . Inset: the difference between single and double excitation spectra corresponding to the spectroelectrochemical absorption spectra of  $MV^0$ .<sup>12</sup>

The possibility to create the doubly reduced  $MV^0$  species in this multicomponent system was then investigated by transient absorption using double-pulse sequential excitation with two nanosecond laser pulses at 460 nm separated by 80  $\mu s$ , duration by which the first charge separation state is completely achieved. Figure 2a presents the comparison of transient absorption data of the sample after excitation of  $[Ru(bpy)_3]^{2+}$  at 460 nm after single and double-pulse excitation. The kinetic trace at 605 nm, probe for  $MV^{*+}$  population shows a loss of intensity at short delay time ( $\sim 50 \mu s$ ) after the second excitation. This can be assigned to another process leading to the consumption of the CSS1  $MV^{*+}$ . The normalized transient spectra at 605 nm also indicate a difference in the intensity of the absorption band centered at 395 nm (Fig. 2b). The doubly excited sample clearly shows a higher intensity at this wavelength originating from the absorption spectra of the second charge-separated state (CSS2),  $MV^0$  with two electrons on the methyl viologen molecule. The difference between the normalized spectra of double-pulse and single-pulse excitation is presented in the inset of Fig. 2b, that undoubtedly confirm the formation of the doubly reduced  $MV^0$  species.<sup>12</sup>

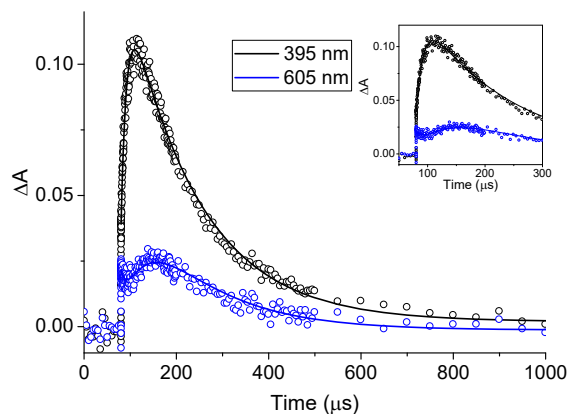


**Figure 3.** Selected transient absorption traces of  $[\text{Ru}(\text{bpy})_3]^{2+}$  ( $43 \mu\text{M}$ ) in de-aerated  $\text{CH}_3\text{CN}/\text{H}_2\text{O}$  (60:40) in the presence of 100 mM ascorbate and  $13.4 \mu\text{M}$   $\text{MV}^{2+}$  after a double-pulse excitation by two nanosecond pulses delayed by  $80 \mu\text{s}$ . Inset: kinetics at short delay time.

The absorption transients monitored at different wavelengths are presented in Fig.3. Kinetic traces at 605 nm and 395 nm correspond to the maximum absorption of  $\text{MV}^{\bullet+}$  and near the maximum absorption of  $\text{MV}^0$ , respectively. All the transients were fitted globally (Fig. S5) using a triexponential function yielding time constants of  $12 (\pm 1)$ ,  $50 (\pm 5)$  and  $155 (\pm 15) \mu\text{s}$ . Due to the overlap of absorption spectra of  $\text{MV}^{\bullet+}$  and  $\text{MV}^0$  at 395 nm, the signal at this wavelength is dominated by the kinetic of the CSS1 formed after the second excitation. A decay time of  $12 \mu\text{s}$  was observed at the absorptions of  $\text{MV}^{\bullet+}$  at 605 nm, which can be attributed to the depopulation of the CSS1 to create the doubly reduced state CSS2 of  $\text{MV}^0$ . An apparent rate constant of  $k_{\text{app}2} = 8.3 (\pm 0.7) \times 10^4 \text{ s}^{-1}$  was found for the formation of this CSS2 (Scheme 2). This indicates a near diffusion-limited rate constant of the second electron transfer  $k_{\text{et}2}$  as previously observed for  $k_{\text{et}1}$ . This charge accumulative state,  $\text{MV}^0$ , then decays with a time constant of  $50 \mu\text{s}$  to repopulate the single charge separated state  $\text{MV}^{\bullet+}$ . As can be seen in the Fig S5, the pre-exponential factor associated with this time constant clearly indicates the repopulation of  $\text{MV}^{\bullet+}$  (negative signal around 605 nm) and the formation of  $\text{MV}^{\bullet+}$  accompanied with the loss of  $\text{MV}^0$  at the 395 nm band. This mixture of transient signals of  $\text{MV}^{\bullet+}$  and  $\text{MV}^0$  in this region is similar to what was observed in the study of bimolecular reaction between electrochemical reduced  $\text{MV}^0$  and  $[\text{Ru}(\text{bpy})_3]^{2+}$  by Hammarström et coll.<sup>12</sup> The recombination time of  $\text{MV}^0$  is shorter than that of the singly reduced state ( $50 \mu\text{s}$  vs  $250 \mu\text{s}$ ). This can be associated with (i) the higher driving force for the recombination reaction of  $\text{MV}^0$  with oxidized ascorbate ( $\Delta G = -0.65 \text{ eV}$ ) as compared to that of  $\text{MV}^{\bullet+}$  ( $\Delta G = -0.26 \text{ eV}$ ), which is similar to what we observed for the recombination of a molecular dyad system with ascorbate<sup>34</sup> and (ii) a

possible additional relaxation pathway by a comproportionation reaction from  $MV^{2+}$  and  $MV^0$  to generate  $2MV^{\bullet+}$  ( $\Delta G = -0.39$  eV) which is diffusion limited in one-phase system.<sup>42, 45-46</sup> Moreover,  $MV^{2+}$  being in excess with respect to the oxidized ascorbate, this reaction might be favored over (i). Kinetics associated to the CSS2  $MV^0$  can be deduced from its absorption band at 395 nm. In order to remove the contribution of CSS1  $MV^{\bullet+}$  signals and examine directly the dynamics of the CSS2, a correction was applied to extract the pure CSS2 kinetic signal. Keeping in mind that there is no contribution of CSS2 in the band centered at 605 nm, the contribution of CSS1 at 395 nm can be calculated from the ratio of signal between 605 and 395 nm observed in the single flash experiment. The subtraction of this contribution from the signal centered at 395 nm in the double flash experiment then gave the pure dynamics of the CSS2  $MV^0$ . The temporal evolution of  $MV^0$  at 395 nm is presented in Fig. 4. The transient trace can be adequately simulated with a rise time of 12  $\mu$ s and a decay time of 50  $\mu$ s. The kinetic rate constant for the charge recombination of the  $MV^0$  is then estimated approximatively as  $k_{rec3} \sim 3 (\pm 2) \times 10^9$   $M^{-1}s^{-1}$ .

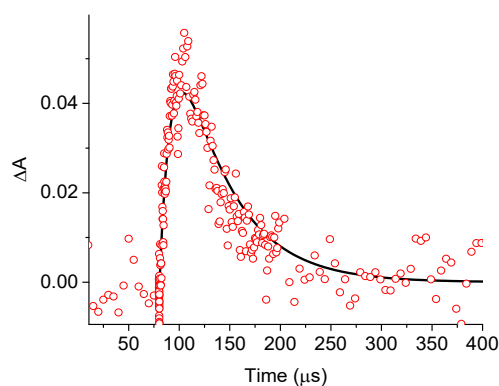
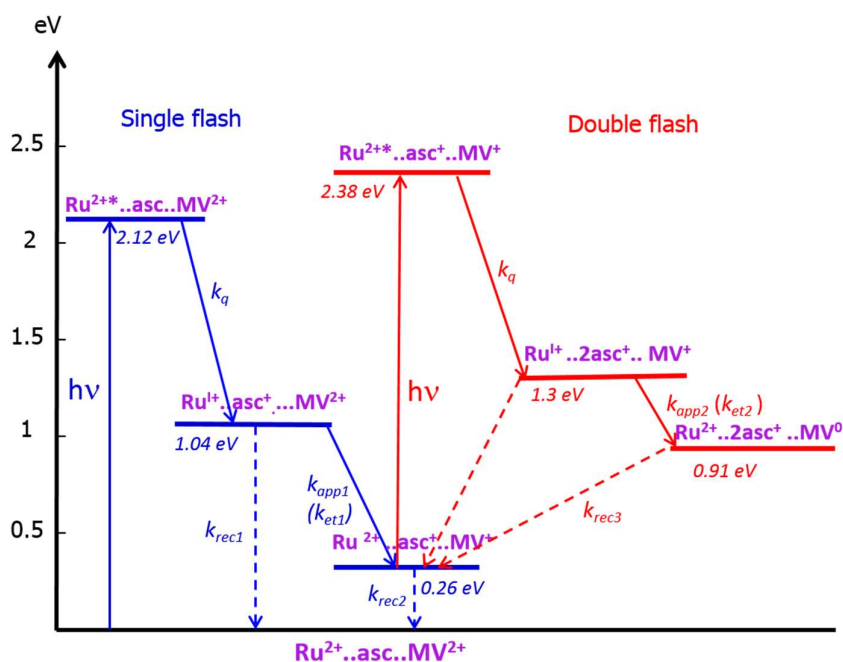


**Figure 4.** Corrected transient at 395 nm (red dots) showing formation and decay of  $MV^0$ . The signal can be adequately simulated with a rise time of 12  $\mu$ s and a decay time of 50  $\mu$ s (black trace)

From the corrected signal, the concentration of the doubly reduced state  $MV^0$  is estimated to be 1.2  $\mu$ M, that is 31 ( $\pm 3$ ) % of the CSS1  $MV^{\bullet+}$  created after the first excitation and 9 ( $\pm 1$ ) % of total population of  $MV^{2+}$ . This efficiency of the accumulative charge transfer process is similar or even higher than that previously observed for intramolecular systems.<sup>1, 25, 29</sup> This result clearly indicates the advantages of multicomponent systems in terms of simplicity and efficiency. In contrast to linked systems, the charge separation processes in multicomponent systems cannot be generated very fast since it is effectively limited by diffusion. However, the

charge recombination is also in general slower due to the low concentration of the photoactivated molecules and accordingly small bimolecular rate. In covalently bound systems, additional unproductive reactions can enter in competition with the formation of the CSS2, like the back electron transfer from the excited sensitizer of CSS1 to the oxidized electron donor or from the reduced electron acceptor to the excited sensitizer. These reactions are largely suppressed in multicomponent systems due to the increased distance. It is to be noted that the  $MV^{•+}$  product does not absorb at the excitation wavelength used in this study, avoiding possible reverse electron transfer reactions as observed by Wenger *et al.*<sup>47</sup> On the other hand, this would no longer be the case for white (solar) light excitation and therefore it would be useful to investigate on potential detrimental effects due to excitation of this strongly absorbing intermediate, in particular under continuous illumination.



**Scheme 2.** Energy level diagram and reaction pathways for photoinduced sequential charge transfer in the asc/Ru<sup>2+</sup>/MV<sup>2+</sup> system. Blue part: First charge separated state CSS1, Red part: second charge separated state CSS2. Solid line: productive processes. Dashed line: unproductive reactions and deactivation pathways, approximate rate constants are  $k_q = 2.9 (\pm 0.5) \times 10^8 \text{ M}^{-1}\text{s}^{-1}$ ,  $k_{rec1} = 3 (\pm 0.5) \times 10^9 \text{ M}^{-1}\text{s}^{-1}$ ,  $k_{app1} = 8.3 (\pm 0.5) \times 10^4 \text{ s}^{-1}$  ( $k_{et1} \sim 6 (\pm 3) \times 10^9 \text{ M}^{-1}\text{s}^{-1}$ ),  $k_{rec2} = 1.1 (\pm 0.5) \times 10^9 \text{ M}^{-1}\text{s}^{-1}$ ,  $k_{app2} = 8.3 (\pm 0.5) \times 10^4 \text{ s}^{-1}$  ( $k_{et2} \sim 6 (\pm 3) \times 10^9 \text{ M}^{-1}\text{s}^{-1}$ ),  $k_{rec3} = 3 (\pm 2) \times 10^9 \text{ M}^{-1}\text{s}^{-1}$ .

In summary, we have examined in this work the photo-accumulation of two electrons on methylviologen, a well-recognized and widely used reversible one electron acceptor and carrier in photochemical studies. Nanosecond pump-pump-probe spectroscopy was used to investigate a simple multicomponent system consisting of  $[\text{Ru}(\text{bpy})_3]^{2+}$  as photosensitizer, ascorbate as reversible electron donor, and methylviologen as reversible electron acceptor. The formation of the neutral doubly reduced species  $\text{MV}^0$  where two electrons are accumulated was demonstrated. A global quantum yield of ca. 9% was reached to deliver the doubly reduced methylviologen carrying an accumulated energy of 0.9 eV with a lifetime of  $\sim 50 \mu\text{s}$ . So far, it is the first time that two sequential charge accumulation is evidenced in a multicomponent system in the presence of a reversible electron donor and electron acceptor. Our results therefore pave the way to interrogate more sophisticated multielectronic photocatalytic processes, a hot and contemporary research theme within the realm of solar energy to fuel conversion.

#### ASSOCIATED CONTENT

##### **Supporting Information.**

Nanosecond pump-pump-probe set-up, TA spectra and kinetics of  $[\text{Ru}(\text{bpy})_3]^{2+}$ ,  $[\text{Ru}(\text{bpy})_3]^{2+}$  and ascorbate in short and long delay times, DADS spectra of the system after single-pulse excitation, TA and DADS spectra after double-pulse excitation.

#### AUTHOR INFORMATION

##### **Corresponding Authors**

\* E-mail: [minh-huong.ha-thi@u-psud.fr](mailto:minh-huong.ha-thi@u-psud.fr) (M.-H.H.-T.)

\* E-mail: [ally.aukaaloo@u-psud.fr](mailto:ally.aukaaloo@u-psud.fr) (A.A.)

##### **Notes**

The authors declare no competing financial interests.

#### ACKNOWLEDGMENT

This work was supported by the LabEx PALM (*ANR-10-LABX-0039-PALM*). T.-T. Tran is grateful to the Vietnamese government for the scholarship (2017-2020).

#### SUPPORTING INFORMATION

##### **Nanosecond pump-pump-probe experiment**

Single pump and double pump nanosecond transient absorption measurements were performed on a home-built setup which has been described previously.<sup>34</sup> Briefly, one or two

Nd:YAG pumped optical parametric oscillator (OPO) lasers are used for sample excitation at 460 nm with an energy of  $\sim 5$  mJ/pulse. The first pump operates at 20 Hz, and the second one has a repetition rate at 10 Hz. After excitation the sample is probed by a white light continuum laser (LEUKOS) in a repetition rate of 20 Hz. The probe beam is split into two arms, one for probing sample and the other for reference in order to compensate for energy fluctuation. The probing arm after passing the sample is coupled into a round to linear optical fiber bundle before being analyzed by a spectrograph SPEX 270M (Jobin-Yvon). Detection of the dispersed white light is performed by an intensified CCD (ICCD) detector PIMAX 4 (Princeton Instrument). Transient absorption spectra can be calculated using the following formula:

$$\Delta OD = \log_{10} \left( \frac{S_{ref}^{on}}{S_{ref}^{off}} \times \frac{S_{prob}^{off}}{S_{prob}^{on}} \right) \quad (1)$$

where  $S_{ref}^{on}$  and  $S_{ref}^{off}$  are reference spectra when pump laser is on and off respectively,  $S_{prob}^{on}$  and  $S_{prob}^{off}$  are probe spectra when pump laser is on and off respectively. The setup is operated in online subtraction mode in which the transient absorption after the first excitation is inherently removed by running the first pump at 20 Hz which is the same as the repetition rate of the probe. Therefore, in principle we obtain a relatively pure signal from molecules that are excited twice, as the *off* signal then contains contributions from the singly pumped solution. It is noteworthy that the double-pumped transient signal actually contains contributions from singly and doubly-excited molecules because excitation efficiency by the first pump laser cannot reach 100%.

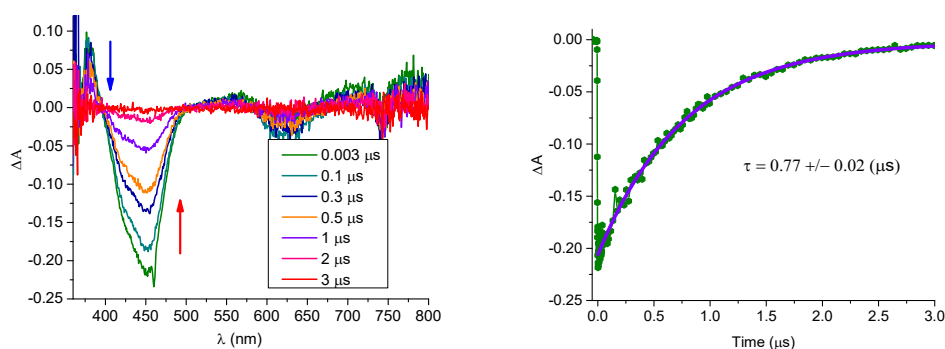


**Figure S1:** Differential absorption spectra and kinetics at 450 nm after single pulse at 460 nm of a solution containing  $[\text{Ru}(\text{bpy})_3]^{2+}$  43  $\mu\text{M}$  in  $\text{CH}_3\text{CN}/\text{H}_2\text{O}$  60:40.

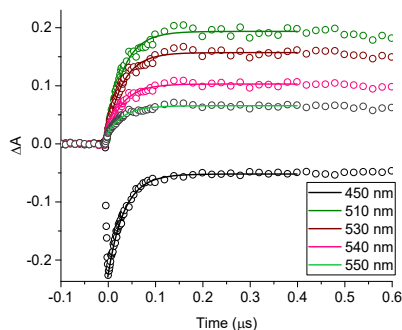


**Figure S2:** Differential absorption spectra and kinetics at selected wavelengths at short delay time obtained after single pulse excitation of a solution containing  $[\text{Ru}(\text{bpy})_3]^{2+}$  in the presence of 100 mM ascorbate in  $\text{CH}_3\text{CN}/\text{H}_2\text{O}$  60:40. Solid lines: global fit of kinetics.

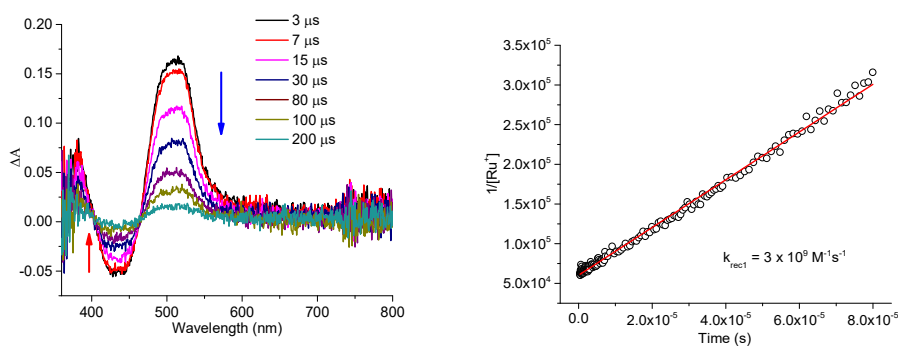


**Figure S3:** Differential absorption spectra and kinetic trace of the sample at 510 nm plotted as  $1/[\text{Ru}^+]$  vs. time obtained after single pulse excitation of a solution containing  $[\text{Ru}(\text{bpy})_3]^{2+}$  in the presence of 100 mM ascorbate in  $\text{CH}_3\text{CN}/\text{H}_2\text{O}$  6/4. Solid lines: global fit decays.

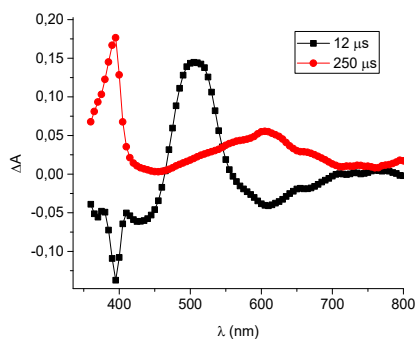


**Figure S4:** Decay Associated Difference Spectra obtained from global analysis of transient decays of  $[\text{Ru}(\text{bpy})_3]^{2+}$  (43  $\mu\text{M}$ ) in de-aerated  $\text{CH}_3\text{CN}/\text{H}_2\text{O}$  4/6 in the presence of 100mM ascorbate, 13.4  $\mu\text{M}$   $\text{MV}^{2+}$ ,  $\lambda_{\text{exc}} = 460$  nm.

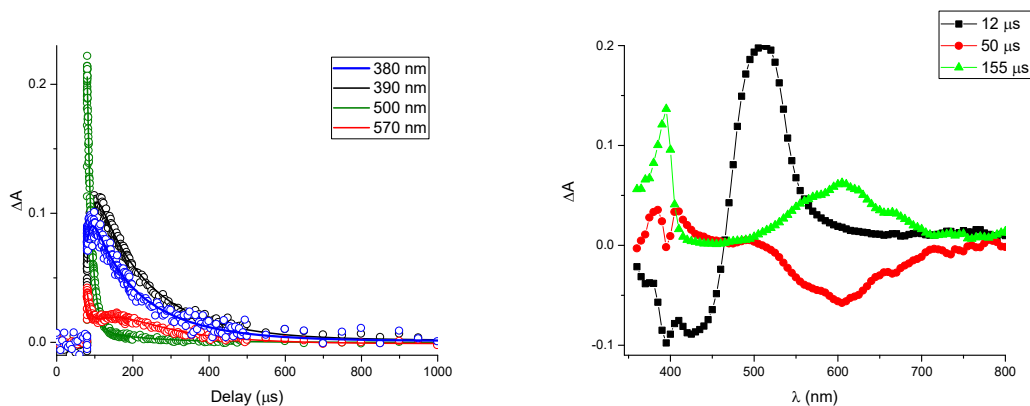


**Figure S5:** Transient absorption decays at selected wavelengths of  $[\text{Ru}(\text{bpy})_3]^{2+}$  (43  $\mu\text{M}$ ) in de-aerated  $\text{CH}_3\text{CN}/\text{H}_2\text{O}$  60:40 in the presence of 100mM ascorbate, 13.4  $\mu\text{M}$   $\text{MV}^{2+}$ , after a pump-pump excitation by two nanosecond pulses at 460 nm delayed by 80  $\mu\text{s}$ . All the decays was fitted with 3 decay times (12, 50 and 155 $\mu\text{s}$ ) by global fits and Decay Associated Difference Spectra obtained from global analysis.

#### 4.4 Watching intermolecular light-induced charge accumulation on Naphthalene diimide by Tris(bipyridyl) ruthenium (II) photosensitizer (Manuscript in preparation)

## Watching Intermolecular Light-induced Charge Accumulation on Naphthalene Diimide by Tris(bipyridyl)ruthenium(II) Photosensitizer

Thu-Trang Tran,<sup>†#</sup> Thomas Pino,<sup>\*†</sup> and Minh-Huong Ha-Thi,<sup>\*†</sup>

†Institut des Sciences Moléculaire d'Orsay (ISMO), CNRS, Univ. Paris-Sud, Université Paris-Saclay, F-91405 Orsay, France.

# Faculty of Physics and Technology, Thai Nguyen University of Science, Thai Nguyen, Vietnam.

#### AUTHOR INFORMATION

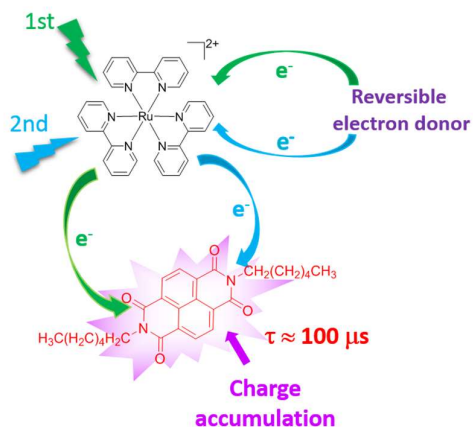
##### **Corresponding Author**

\* E-mail: [minh-huong.ha-thi@u-psud.fr](mailto:minh-huong.ha-thi@u-psud.fr)

\* E-mail: [thomas.pino@u-psud.fr](mailto:thomas.pino@u-psud.fr)

ABSTRACT. Performing photocatalytic reactions to produce solar fuels requires the coupling of multiple photoinduced one-electron transfer steps on multielectronic catalysis. Understanding the light-driven charge accumulation in photocatalytic systems is of pivotal importance in the optimization process. Herein, we investigated the elementary steps of light-induced two-electron accumulation on a triptych mixture constituted of three archetypal molecular system commonly used in photophysical studies ( $[\text{Ru}(\text{bpy})_3]^{2+}$ , ascorbate as a reversible electron donor and naphthalene diimide as a two-electron acceptor). Remarkably, accumulative charge separation was observed both in single-pulse and double-pulse experiments in a reversible manner, indicating a very high efficiency of charge transfer reactions. The doubly reduced state of  $\sim 100 \mu\text{s}$  lifetime was obtained with a formation yield of 4.2 %. Rate constants of all elementary steps in the formation and the relaxation of the doubly reduced state were determined with the aid of a newly developed numerical simulation method for this photosystem.

#### **TOC GRAPHICS**



**KEYWORDS.** Charge transfer, accumulative charge separation, energy conversion, pump-pump-probe spectroscopy, photochemistry.

Light-driven charge separation and charge accumulation are the key steps in the conversion of sunlight into organic molecules in photosynthetic organisms.<sup>2, 48-49</sup> Mimicking these processes by using artificial photosynthesis to capture, store, and convert solar energy into chemical energy has emerged as a challenge for current research, with the goal of duplicating the functional characteristics of natural photosynthesis.<sup>1, 19-20, 50-53</sup> To implement this strategy, an artificial system has to be built to complete the catalytic reactions by sequential absorption of several photons leading to accumulation of electrons and holes.

Various photocatalytic systems have been explored for CO<sub>2</sub> reduction, water oxidation, and hydrogen evolution, in which catalysts and photosensitizers might either be attached covalently to each other, as dyads, triads, or pentads (known as integrated systems),<sup>4, 23, 50, 53-58</sup> or might be present as unlinked multicomponent systems.<sup>4, 31, 59</sup> In general, most studies have paid attention to product formation, with less focus on understanding the essential fundamentals of the charge accumulation reactions that occur at the catalyst. However, the study of light-driven charge accumulation at the catalytic site is the pivotal task on the way to realize solar fuels.

Probing multiple-electron transfers in artificial systems is challenging in comparison with single electron transfer because many additional reaction pathways can counteract the stepwise charge accumulation as recently discussed in the reviews of Odobel, Hammarström, and Wenger.<sup>1, 60-61</sup> Therefore, monitoring charge accumulation is difficult to accomplish effectively because the efficiency is usually low. To date, few reports have been published regarding light-driven electron accumulation in the presence of sacrificial reagents<sup>35, 62-69</sup> or a reversible manner.<sup>24-27, 29, 34, 39, 70-73</sup> These reports have focused on integrated systems to take advantage of

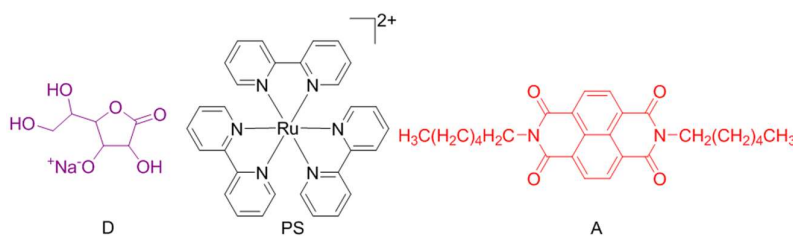
the fast intramolecular electron transfer reactions. However, these systems commonly suffer from rapid back transfer due to strong coupling. Alternatively, a multicomponent system in which photosensitizer and catalyst are unbound molecules generally gives longer intermolecular charge transfer and charge recombination due to diffusion-limited processes. Our recent success in studying charge accumulation has been achieved with a multicomponent system composed of  $[\text{Ru}(\text{bpy})_3]^{2+}$ , methylviologen ( $\text{MV}^{2+}$ ), and ascorbate.<sup>17</sup> Until now, this study stands as the first example where two sequential charge accumulation was evidenced in a multicomponent system in a reversible manner. This success opens a simple approach for the construction of artificial photosynthesis systems and, consequently, we are interested in prolonging our studies on these multicomponent systems, utilizing photosensitizer, catalyst, and electron donor (or acceptor).

Aromatic diimides have been known as electron acceptors to study photoinduced electron transfer in a wide variety of molecular systems designed for photosynthesis<sup>13, 74</sup> and solar energy conversion.<sup>14</sup> Naphthalene diimide (NDI) has received attention in investigation of multiple charge accumulations since (i) it can be reduced stepwise in two phases with modest potentials; (ii) the electronic absorption spectra of the radical anions and the doubly reduced dianions are distinguishable in the visible and near-infrared region.<sup>15-16</sup> A number of integrated systems have been developed to study double electron accumulation on NDI moieties. This has been demonstrated for a  $[\text{Ru}\text{-NDI}]$  dyad by our group, using nanosecond pump-pump-probe spectroscopy.<sup>34</sup> We succeeded in monitoring double electron accumulation on the NDI moiety in this dyad system with an exceptional lifetime of accumulative charge separated state (200  $\mu\text{s}$ ). However, the dyad system manifested a disadvantage, which is the low efficiency of double charge accumulation. Additionally, charge accumulation was detected in a molecular triad containing  $[\text{Ru}(\text{bpy})_3]^{2+}$  and NDI in the presence of trimethylamine as a sacrificial electron donor by the group of Wenger.<sup>35</sup> However, for the same triad in the presence of reversible electron donor (ascorbate) or in a multicomponent system including NDI,  $[\text{Ru}(\text{bpy})_3]^{2+}$ , and trimethylamine, the authors only obtained the signal of the first reduced state of NDI due to a low cage escape yield.

In this work, we present a successful investigation of light-driven charge accumulation on NDI in a multicomponent system containing  $[\text{Ru}(\text{bpy})_3]^{2+}$  as photosensitizer (PS) and ascorbate as a reversible electron donor (D) (Scheme 1). The charge accumulation in this system was investigated using nanosecond transient pump-pump-probe experiment.<sup>34</sup> Unexpectedly and remarkably, double charge accumulation was observed with only a single pump laser excitation of  $[\text{Ru}(\text{bpy})_3]^{2+}$ . However, the sequential double pulse excitation induced a much higher

efficiency of the accumulated charge separation. Herein, the kinetics of the different relaxation pathways for the formation of the charge accumulation state as well as those of undesired competitive reactions was reported.

**Scheme 1.** Molecular structure of ascorbate (D – reversible electron donor),  $[\text{Ru}(\text{bpy})_3]^{2+}$  (PS – photosensitizer) and NDI (A – reversible two-electron acceptor).



To control the initial charge separation, firstly, two samples containing (i)  $[\text{Ru}(\text{bpy})_3]^{2+}$  (13  $\mu\text{M}$ ) alone (ii)  $[\text{Ru}(\text{bpy})_3]^{2+}$  (13  $\mu\text{M}$ ) with ascorbate (100 mM) in deaerated  $\text{CH}_3\text{CN}/\text{H}_2\text{O}$  (60:40) were studied in the same conditions as the multicomponent system with nanosecond transient absorption (TA) under single laser excitation at 460 nm at 1 mJ/pulse. Similar photophysical properties were observed for those systems as compared with our previous work<sup>17</sup> (see SI for more detail). Secondly, the single pump TA measurements were investigated in the multicomponent system containing  $[\text{Ru}(\text{bpy})_3]^{2+}$  (13  $\mu\text{M}$ ), ascorbate (100 mM), and NDI (31  $\mu\text{M}$ ). It is noteworthy that the electronic absorption spectra of the first reduced and second reduced states of the NDI (denoted as  $\text{NDI}^{\bullet-}$  and  $\text{NDI}^{2-}$  respectively) have been carefully studied by Gosztola *et al.*<sup>15</sup> The apparently distinguishable absorption spectra between  $\text{NDI}^{\bullet-}$  and  $\text{NDI}^{2-}$  are indicated at  $\sim 480$  nm ( $\epsilon \approx 23000 \text{ M}^{-1}\text{cm}^{-1}$ ) as a central band of  $\text{NDI}^{\bullet-}$ , and at 520 nm as a shoulder band; whereas  $\text{NDI}^{2-}$  is characterized by a main band approximately at 400 nm ( $\epsilon \approx 28400 \text{ M}^{-1}\text{cm}^{-1}$ ).<sup>15</sup> The multicomponent system was studied by TA by irradiating at 460 nm to excite the  $[\text{Ru}(\text{bpy})_3]^{2+}$  photosensitizer, and the TA spectra and kinetic traces of the multicomponent system are shown in Fig. 1 and Fig. S3. For the initial reaction, the formation of  $[\text{Ru}(\text{bpy})_3]^+$  (denoted as  $\text{Ru}^+$ ) showed similar behavior to the solution containing  $[\text{Ru}(\text{bpy})_3]^{2+}$  and ascorbate. Fig. 1(a1) indicates the decay of  $\text{Ru}^+$  simultaneously with the rising of the  $\text{NDI}^{\bullet-}$  state at 480 nm as a significant process with contribution from an  $\text{NDI}^{2-}$  state with a corresponding band at 400 nm as a minor process. Due to the spectral overlap of intermediate species formed upon photoexcitation ( $\text{Ru}^+$ ,  $\text{NDI}^{\bullet-}$  and  $\text{NDI}^{2-}$ ), transient spectra at each delay time were decomposed to extract the proportion of each species using their pure absorption

spectra (Fig. S4). The obtained kinetic traces related to the concentrations of each species  $\text{Ru}^+$ ,  $\text{NDI}^{\bullet-}$ , and  $\text{NDI}^{2-}$  are presented in Fig. 1(a2) and (b2).

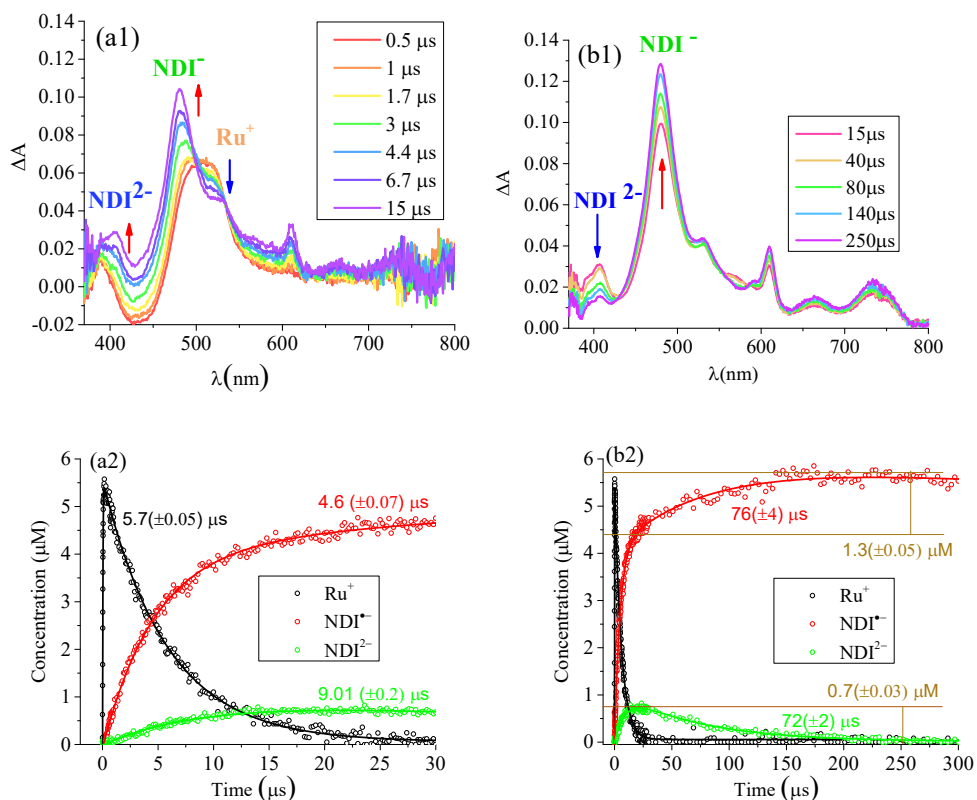


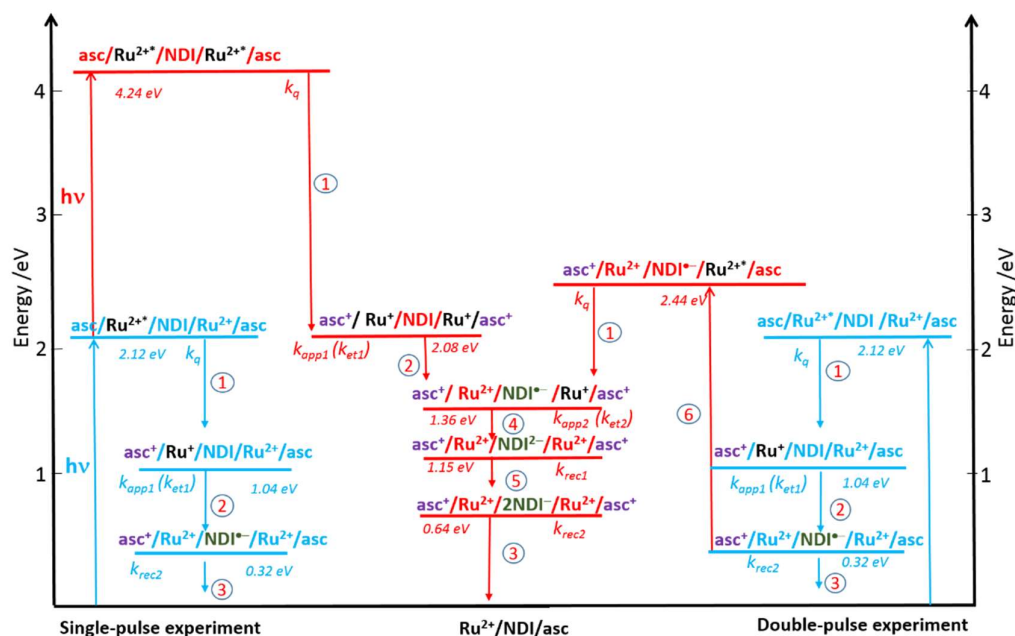
**Figure 1.** TA spectra (a1) and (b1), and kinetic traces (a2) and (b2) of concentration of  $\text{Ru}^+$ ,  $\text{NDI}^{\bullet-}$ , and  $\text{NDI}^{2-}$  states at the indicated delay times of the solution  $[\text{Ru}(\text{bpy})_3]^{2+}$  (13  $\mu\text{M}$ ), ascorbate (100 mM), and NDI (31  $\mu\text{M}$ ) in deaerated  $\text{CH}_3\text{CN}/\text{H}_2\text{O}$  (60:40); Single pump excitation at 460 nm.

The formation of the first charge separated state  $\text{NDI}^{\bullet-}$  can be described by two rising steps. The first rising step (red curve Fig. 1 (a2)) in 0-30  $\mu\text{s}$  time intervals corresponds to the relaxation of  $\text{Ru}^+$  (black curve), indicating the formation of  $\text{NDI}^{\bullet-}$  from the reaction of  $\text{Ru}^+$  and NDI. This first rising curve of  $\text{NDI}^{\bullet-}$  can be fitted with an apparent rate constant of  $k_{\text{app}1} = 2.2(\pm 0.1) \times 10^5 \text{ s}^{-1}$ , which was calculated by using the rising time  $4.6(\pm 0.1) \mu\text{s}$ , forming a  $\text{NDI}^{\bullet-}$  concentration of about  $4.3(\pm 0.2) \mu\text{M}$ . Thus, the rate constant of the first charge separated state ( $k_{\text{et}1}$ ) is approximately estimated to be  $7(\pm 2) \times 10^9 \text{ M}^{-1}\text{s}^{-1}$ , which is limited by the diffusion rate (process 2 in Scheme 2). In parallel, one additional consecutive reaction to form the second charge separated state of NDI (green curve) shows  $0.70(\pm 0.05) \mu\text{M}$  of  $\text{NDI}^{2-}$ , with an apparent rate constant of  $k_{\text{app}2} = 1.1(\pm 0.1) \times 10^5 \text{ s}^{-1}$  (step 4 in Scheme 2). To extract the rate constant for the different processes, numerical simulation of the kinetic equations of different transient species

was performed (see SI for more detail). The rate constant of formation of  $\text{NDI}^{2-}$  was found as  $k_{\text{et}2} = 8 (\pm 2) \times 10^9 \text{ M}^{-1}\text{s}^{-1}$ , which is closed to the diffusion-limited rate as observed for  $k_{\text{et}1}$ .

The second rising step of  $\text{NDI}^{\bullet-}$  can be observed in the 30-300  $\mu\text{s}$  time intervals (red curve, Fig. 1 (b2)). The kinetic traces show the disappearance of  $\text{NDI}^{2-}$  together with the second growth of  $\text{NDI}^{\bullet-}$ , indicating the depopulation of the doubly reduced state  $\text{NDI}^{2-}$  to recreate the singly reduced state  $\text{NDI}^{\bullet-}$ . Two possible relaxation pathways of  $\text{NDI}^{2-}$  to repopulate  $\text{NDI}^{\bullet-}$  are (i) the recombination with oxidized ascorbate ( $\Delta G = -0.82 \text{ eV}$ )<sup>15</sup> or (ii) the comproportionation reaction from NDI and  $\text{NDI}^{2-}$  to generate 2  $\text{NDI}^{\bullet-}$  ( $\Delta G = -0.51 \text{ eV}$ ).<sup>75</sup> Even if a more favorable driving force is obtained for the first pathway, it seems that the relaxation of the doubly reduced state follows the second pathway, since the concentration of  $\text{NDI}^{\bullet-}$  formed in the second growth is twice the concentration of  $\text{NDI}^{2-}$  ( $0.70 (\pm 0.05) \mu\text{M}$  for  $\text{NDI}^{2-}$  versus  $1.30 (\pm 0.05)$  for  $\text{NDI}^{\bullet-}$  as shown in Fig. 1 (b2). Effectively, the value of rate constant obtained for the numerical simulation for the recombination with ascorbate is close to 0, indicating a negligible relaxation pathway of  $\text{NDI}^{2-}$  by ascorbate. For the comproportionation reaction (step 5 in Scheme 2), the same rate constant for the charge recombination  $k_{\text{rec}1} = 5 (\pm 1) \times 10^8 \text{ M}^{-1} \text{ s}^{-1}$ , was obtained from both the estimation using the decay time of  $72 (\pm 2) \mu\text{s}$  and the residual concentration of NDI of  $\sim 25.3 (\pm 0.3) \mu\text{M}$  and the numerical simulation. Then, the first charge separated state relaxes with a second-order rate constant,  $k_{\text{rec}2} = 4.5 (\pm 0.3) \times 10^7 \text{ M}^{-1} \text{ s}^{-1}$  (process 3 in Scheme 2).

The first pump laser excitation led to a remarkable efficient charge transfer, with almost 100% electron transfer from  $[\text{Ru}(\text{bpy})_3]^+$  to form the reduced states of NDI. We estimated that about 24%  $[\text{Ru}(\text{bpy})_3]^+$  underwent double charge transfer to form  $\text{NDI}^{2-}$  and the 76% left exhibited only single charge transfer to create  $\text{NDI}^{\bullet-}$ . The formation yield of the  $\text{NDI}^{2-}$  from the total NDI is estimated to be  $2.2 (\pm 0.1) \%$  ( $0.7 \mu\text{M}$   $\text{NDI}^{2-}$  from a total of  $31 \mu\text{M}$  NDI).



Scheme 2. The energy levels and relaxation pathways for photoinduced processes in the  $[\text{Ru}(\text{bpy})_3]^{2+}$  (denoted as  $\text{Ru}^{2+}$ ), ascorbate (denoted as  $\text{asc}$ ), and NDI system for single pulse excitation (left) and double pulse excitation (right). First photon absorption is shown in blue, second photon absorption is shown in red. Approximate rate constants are:  $k_q = 2.8 (\pm 0.3) \times 10^8 \text{ M}^{-1} \text{ s}^{-1}$ ,  $k_{\text{app}1} = 2.2 (\pm 0.1) \times 10^5 \text{ s}^{-1}$ ,  $k_{\text{et}1} = 7 (\pm 2) \times 10^9 \text{ M}^{-1} \text{ s}^{-1}$ ,  $k_{\text{app}2} = 1.1 (\pm 0.1) \times 10^5 \text{ s}^{-1}$ ,  $k_{\text{et}2} = 8 (\pm 2) \times 10^9 \text{ M}^{-1} \text{ s}^{-1}$ ,  $k_{\text{rec}1} = 5 (\pm 1) \times 10^8 \text{ M}^{-1} \text{ s}^{-1}$ ,  $k_{\text{rec}2} = 4.5 (\pm 0.3) \times 10^7 \text{ M}^{-1} \text{ s}^{-1}$ .

The mechanism of formation of  $\text{NDI}^{2-}$  follows the reaction  $[\text{Ru}(\text{bpy})_3]^+ + \text{NDI}^{\bullet-} \rightarrow \text{NDI}^{2-} + [\text{Ru}(\text{bpy})_3]^{2+}$  with a driving force  $\Delta G = -0.21 \text{ eV}$ . Consequently, the formation mechanism of  $\text{NDI}^{2-}$  significantly depends on the kinetic and concentration of  $[\text{Ru}(\text{bpy})_3]^+$ , resulting from the reaction between  $[\text{Ru}(\text{bpy})_3]^{2+\bullet}$  and ascorbate. To verify the dependence of  $\text{NDI}^{2-}$  formation on the characteristics of  $[\text{Ru}(\text{bpy})_3]^+$ , similar TA experiments for different concentrations of  $[\text{Ru}(\text{bpy})_3]^{2+}$  were investigated (Table S1). The time constant seems to be independent on the concentration of  $[\text{Ru}(\text{bpy})_3]^{2+}$ , whereas the concentration of  $\text{NDI}^{2-}$  formed is proportional to that of  $[\text{Ru}(\text{bpy})_3]^+$  which also increases with the concentration of  $[\text{Ru}(\text{bpy})_3]^{2+}$ . Considering higher concentration of NDI as compared to that of  $[\text{Ru}(\text{bpy})_3]^{2+}$ , this can be explained by the fact that the generation of  $\text{NDI}^{2-}$  only depends on the concentration of  $[\text{Ru}(\text{bpy})_3]^{2+}$ . Furthermore, TA experiments were studied by changing the laser power (Fig. S5). The formation of the  $\text{NDI}^{2-}$  was shown to increase more rapidly with laser power than that of  $\text{NDI}^{\bullet-}$ . Indeed, the formation of the doubly reduced state  $\text{NDI}^{2-}$  requires the sequential reaction with

two  $[\text{Ru}(\text{bpy})_3]^+$  (thus a square dependence to the laser intensity as a result of the dependence to the square of  $[\text{Ru}(\text{bpy})_3]^+$  concentration) whereas the singly reduced species  $\text{NDI}^{\bullet-}$  formation needs only one  $[\text{Ru}(\text{bpy})_3]^+$ . This observation is very similar to what Fox *et al.* reported in their system of dendrimers containing viologen and naphthalene groups.<sup>70</sup> Singly and doubly reduced viologens were observed upon photoexcitation of these systems, and the production of doubly reduced viologen was shown to be more sensitive to laser power than that of singly reduced species. Charge accumulation induced by two absorbed photons was also observed in different covalently linked systems in a reversible way<sup>24-25, 27, 35, 71</sup>, but our observation here stands as one of the first observations in multicomponent photosystem.

To investigate the ability of charge accumulation induced by sequential single-photon absorption, the multicomponent system was studied by a double-pulse excitation at 460 nm. The second laser was applied 300  $\mu\text{s}$  after the first laser pulse, when the second reduced state of  $\text{NDI}^{2-}$  relaxed completely and  $\text{NDI}^{\bullet-}$  reaches its highest concentration (process 6 in Scheme 2). In order to compare the difference between single-pulse and double-pulse excitation, the TA spectra and normalized TA spectra are shown in Fig. 2. The TA spectra were taken at 15  $\mu\text{s}$  after excitation where the contribution of the  $\text{NDI}^{2-}$  was highest for both single-pulse and double-pulse experiments. Thus, the discrepancy is clearly observed for the formation of  $\text{NDI}^{2-}$  in the two TA spectra, with a much more higher efficiency for  $\text{NDI}^{2-}$  in the double-pulse excitation. The difference between the normalized spectra of the single-pulse and double-pulse excitation, which indicates the pure signal of the  $\text{NDI}^{2-}$  induced by the effect of the second pump is presented in the inset of Fig. 2. This different spectrum shows a perfect match with the doubly reduced state of NDI, as obtained in previous reports.<sup>15</sup>

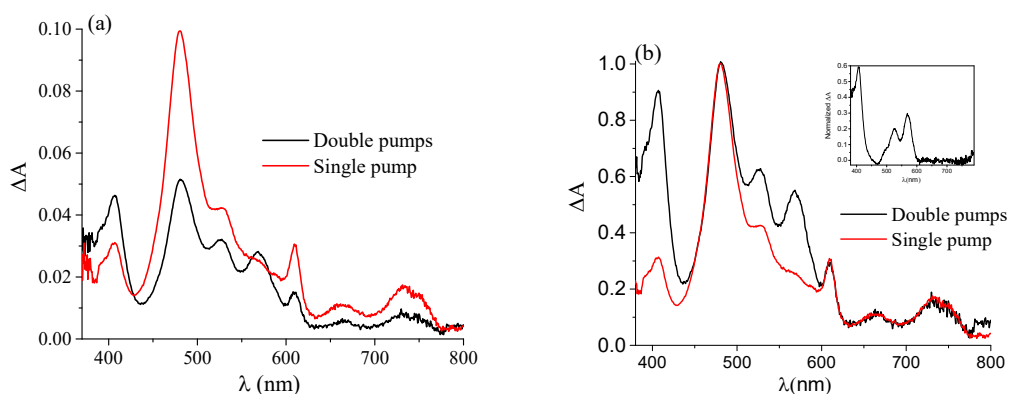


**Figure 2.** TA spectra (a) and normalized TA spectra at 480 nm (b) of the solution  $[\text{Ru}(\text{bpy})_3]^{2+}$  (13  $\mu\text{M}$ ), ascorbate (100 mM), and NDI (31  $\mu\text{M}$ ) in deaerated  $\text{CH}_3\text{CN}/\text{H}_2\text{O}$  (60:40). Red line was obtained 15  $\mu\text{s}$  after single-pulse excitation. Black line was obtained 15  $\mu\text{s}$  after the second

pulse in double-pump excitation (first pump at 20 Hz, second pump at 10 Hz); the delay time between two pulses was 300  $\mu$ s. Inset: the difference between single and double pulse excitation spectra of the  $\text{NDI}^{2-}$ .

To distinguish the mechanisms of formation of the  $\text{NDI}^{2-}$  between single-pulse and double-pulse excitations, the relative intensities of  $\Delta A_{\text{NDI}^{\bullet-}}/\Delta A_{\text{NDI}^{2-}}$  was plotted in the function of the power of laser for the two cases (Fig. 3). For single-pulse excitation, the formation of the  $\text{NDI}^{2-}$  is expected to be proportional to the square of the laser intensity as a result of the dependence to the square of  $[\text{Ru}(\text{bpy})_3]^+$  concentration, while the  $\text{NDI}^{\bullet-}$  formation is directly proportional to the intensity, unless saturation occurs.<sup>76</sup> Consequently,  $\Delta A_{\text{NDI}^{\bullet-}}/\Delta A_{\text{NDI}^{2-}}$  is inversely proportional to the laser intensity, as depicted by the red curve in Fig. 3, until saturation is reached above 1mJ. For the double-pulse excitation, with  $\text{NDI}^{\bullet-}$  being already formed from the first excitation, the formation of the  $\text{NDI}^{2-}$  linearly depends on  $[\text{Ru}(\text{bpy})_3]^+$  concentration and thus linearly to the second laser pulse intensity. Therefore, the ratio  $\Delta A_{\text{NDI}^{\bullet-}}/\Delta A_{\text{NDI}^{2-}}$  in the case of double-pulse excitation is proportional to the ratio  $[\text{Ru}(\text{bpy})_3]^+ / [\text{Ru}(\text{bpy})_3]^+$ , and thus is independent of laser intensity (black curve in Fig. 3).

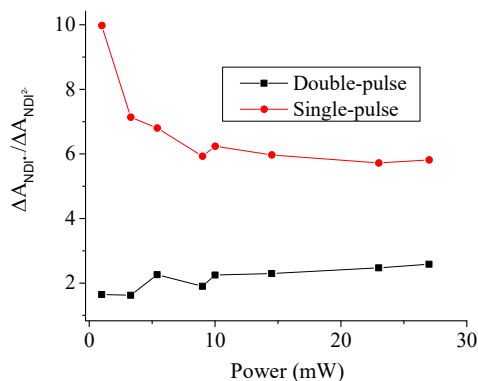


**Figure 3.** The plot of  $\Delta A_{\text{NDI}^{\bullet-}}/\Delta A_{\text{NDI}^{2-}}$  within single-pulse (red curve) and double-pulse (black curve) excitation versus power excitation (power of the second laser for double-pulse excitation). The intensity was taken at the delay time 15  $\mu$ s for both single-pulse and double-pulse excitations, the delay time between two pulses was 300  $\mu$ s for the case of double-pulse excitation. The intensities of  $\text{NDI}^{2-}$  were obtained by subtracting the contribution of  $\text{NDI}^{\bullet-}$  and  $\text{NDI}^{2-}$  created by single pulse excitation to quantify that formed from only the second pulse at 400 nm. The correction was done thanks to the formula:  $\Delta A_{400\text{nm\_corr}} = \Delta A_{400\text{nm\_double}} - \Delta A_{480\text{nm\_double}} / r$  with  $r$  being the ratio of  $\Delta A_{480\text{nm\_single}} / \Delta A_{400\text{nm\_single}}$  at 15  $\mu$ s.

The spectral decomposition method was also implemented for the treatment of double-pulse TA measurements to obtain the temporal evolutions of intermediate concentrations (Fig. 4). To extract the rate constants of the photoinduced reactions, the similar numerical simulation used in the single-pulse experiment was fitted with these experimental evolutions. We noticed that the only differences are the initial conditions for the concentration of  $\text{NDI}^{\bullet-}$  and oxidized ascorbate that were generated by the first excitation. The values are reported in Scheme 2. Unsurprisingly, similar rate constants were obtained for the single-pulse and double-pulse experiments since the doubly reduced  $\text{NDI}^{2-}$  was formed by similar reaction pathways. The shorter rising time of  $\text{NDI}^{2-}$  of  $6.5 (\pm 0.08) \mu\text{s}$  in the case of double-pulsed resulted from the reaction of available  $\text{NDI}^{\bullet-}$  created by the first-pulse excitation with  $[\text{Ru}(\text{bpy})_3]^+$  generated by the second-pulse excitation.

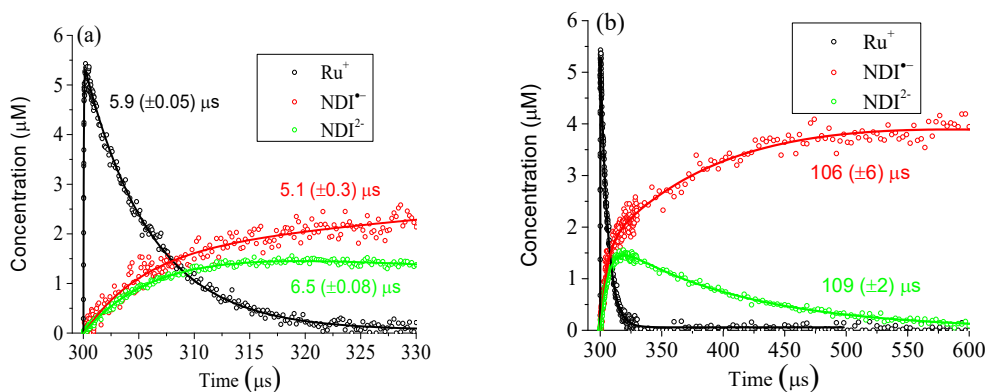


**Figure 4.** Kinetic traces at selected species states ( $\text{Ru}^+$ ,  $\text{NDI}^{\bullet-}$ , and  $\text{NDI}^{2-}$ ) as a function of concentration obtained from TA experiments with the solution containing  $[\text{Ru}(\text{bpy})_3]^{2+}$  (13  $\mu\text{M}$ ), ascorbate (100 mM), and NDI (31  $\mu\text{M}$ ) in deaerated  $\text{CH}_3\text{CN}/\text{H}_2\text{O}$  (60:40), upon double-pulse excitation (460 nm, separated by 300  $\mu\text{s}$ , first pump at 20 Hz, second pump at 10 Hz). (a) at short and (b) long time scales, solid lines are fit curves.

In order to estimate precisely the total quantity of formed  $\text{NDI}^{2-}$ , the double-pulse excitation with the first pulse and the second pulse both operated at 10 Hz, with a 300  $\mu\text{s}$  delay, was studied as well (Fig. S6 and S7). Fig. S6 presents the TA kinetic traces at 400 nm of the pure signal of  $\text{NDI}^{2-}$  after removing the contribution of  $\text{NDI}^{\bullet-}$ . It is clear that the formation of  $\text{NDI}^{2-}$  in double-pulse excitation is about twice times higher than that obtained by single-pulse excitation. Therefore, we can conclude that the formation of  $\text{NDI}^{2-}$  under double-pulse excitation involves the contribution of that due to the second pulse only (green curve, Fig. S6)

and that due to the two sequential single-photon absorption processes. Thereby, the total concentration of  $\text{NDI}^{2-}$  is estimated to be  $1.30 (\pm 0.07) \mu\text{M}$  ( $\Delta A_{400 \text{ nm}} = 0.039$ , with  $\Delta \epsilon_{400 \text{ nm}} \approx 28400 \text{ M}^{-1}\text{cm}^{-1}$ ), corresponding to about 49% of  $[\text{Ru}(\text{bpy})_3]^+$  participating to the formation of  $\text{NDI}^{2-}$  and a formation yield of  $4.2 (\pm 0.2)\%$  ( $1.3 \mu\text{M} \text{NDI}^{2-}$  from a total of  $31 \mu\text{M} \text{NDI}$ ).

A multicomponent system, such as the one we describe here, shows an advantage in term of simpler construction in comparison with covalently-linked systems.<sup>24-25, 27, 29, 34-35, 71</sup> As compared to our previous study of charge accumulation on a Ru-NDI dyad, the formation of the first charge separated state (CSS1) in the dyad is evidently more efficient ( $k_{\text{app}1} = 3.8 (\pm 0.7) \times 10^7 \text{ s}^{-1}$  for the dyad<sup>34</sup> vs.  $k_{\text{app}1} = 2.2 (\pm 0.1) \times 10^5 \text{ s}^{-1}$  vs. for the multicomponent system), thanks to the close distance of the photosensitizer and the NDI unit. Thus, once the PS is reduced to form  $\text{Ru}^{\text{I}}\text{-NDI}$ , the only efficient pathway is to form the singly reduced state  $\text{Ru-NDI}^{\bullet-}$ , the doubly reduced  $\text{Ru-NDI}^{2-}$  (CSS2) was thus not be observed in the single-pulse experiments. In the case of multicomponent systems, the formation of the accumulative charge separation state was shown be more efficient since the reduced PS  $\text{Ru}^{\text{I}}$  formed after excitation can react immediately with the CSS1 to form the CSS2 without any reaction with the ground state of NDI, in particular when the CSS1 is already generated by the first pump excitation. Furthermore, counter-productive reaction such as reverse electron transfer from the reduced electron acceptor to the excited sensitizer is largely suppressed in the multicomponent system due to the increased distance. Using double-pulse excitation, we improve the efficiency of charge accumulation on the NDI moiety in comparison with that of the single-pulse experiment (4.2% versus 2.2%, respectively). The main cause, which leads to this result, is the higher concentration of the CSS1 already created by the first pump. It is worth noting that despite being a multicomponent system, our results show a higher efficiency of second charge accumulation (4.2%) in comparison with  $\sim 1\%$  in the case of Ru-NDI dyad system.<sup>34</sup> This result can be explained thanks to the higher distance between molecules in the multicomponent system which helps to limit unproductive reactions.<sup>47, 77</sup>

In summary, we have reported here the light driven two-electron accumulation on NDI in a multicomponent system in a reversible manner. The charge accumulation was observed with only single-pulse excitation, indicating a high efficiency of photoinduced charge transfer in this three archetypal molecular system. Furthermore, pump-pump-probe TA indicated the formation of  $\text{NDI}^{2-}$  from the sequential single-photon absorption with higher efficiency. The doubly reduced species was observed with the formation yield of 4.2% and exhibited a lifetime of about  $100 \mu\text{s}$ . For the first time, the use of numerical simulation of the kinetic equations allows the

determination of the rate constants of all the reactions involved in the formation of the charge-accumulated state. This solution can be applied systematically to analyze experimental data of similar photosystems. This fundamental work indicates the great advantages of using multicomponent systems to elucidate multi-electronic photocatalytic processes. The lessons learned from these studies on accumulative charge separation are of particular importance on the way towards the development of more efficient catalytic systems for artificial photosynthesis.

#### ASSOCIATED CONTENT

**Supporting Information.** Nanosecond pump-pump-probe set-up, TA spectra and kinetics of  $[\text{Ru}(\text{bpy})_3]^{2+}$ ,  $[\text{Ru}(\text{bpy})_3]^{2+}$  and ascorbate and the multicomponent system, TA spectra of different intermediate species used for decomposition analysis, the dependence of the formation of doubly reduced species on the concentration and laser power, TA decay of double flash experiment using two pumps laser at 10 Hz of repetition rate, procedure for spectral decomposition of TA spectra and numerical solution and fitting of TA decay.

#### AUTHOR INFORMATION

##### Corresponding Authors

\* E-mail: [minh-huong.ha-thi@u-psud.fr](mailto:minh-huong.ha-thi@u-psud.fr) (M.-H.H-T)

\* E-mail: [thomas.pino@u-psud.fr](mailto:thomas.pino@u-psud.fr) (T.P)

##### Notes

The authors declare no competing financial interests.

#### ACKNOWLEDGMENT

This work was supported by the LabEx PALM (ANR-10LABX-0039-PALM). T.-T.T. is grateful to the Vietnamese government for the scholarship (2016-2019). We thank Prof. A. Aukauloo, Dr. W. Liebl and Dr. A. Quaranta for fruitful discussion and C. Lefumeux for experimental support.

## Supporting Information

# Watching Intermolecular Light-induced Charge accumulation on Naphthalene diimide (NDI) by Tris(bipyridyl)ruthenium(II) Photosensitizer

*Thu-Trang Tran,<sup>†#</sup> Thomas Pino,<sup>\*†</sup> and Minh-Huong Ha-Thi,<sup>\*†</sup>*

<sup>†</sup>Institut des Sciences Moléculaire d'Orsay (ISMO), CNRS, Univ. Paris-Sud, Université Paris-Saclay, F-91405 Orsay, France.

<sup>#</sup>Faculty of Physics and Technology, Thai Nguyen University of Science, Thai Nguyen, Vietnam.

### Nanosecond pump-pump-probe experiment

Single pump and double pump nanosecond transient absorption measurements were performed on a home-built setup which has been described previously.<sup>34</sup> Briefly, one or two Nd:YAG pumped optical parametric oscillator (OPO) lasers are used for sample excitation at 460 nm with an energy of  $\sim 5$  mJ/pulse. The first pump operates at 10 or 20 Hz, and the second one has a repetition rate at 10 Hz. After excitation the sample is probed by a white light continuum laser (LEUKOS) in a repetition rate of 20 Hz. The probe beam is split into two arms, one for probing sample and the other for reference in order to compensate for energy fluctuation. The probing arm after passing the sample is coupled into a round to linear optical fiber bundle before being analyzed by a spectrograph SPEX 270M (Jobin-Yvon). Detection of the dispersed white light is performed by an intensified CCD (ICCD) detector PIMAX 4 (Princeton Instrument). Transient absorption spectra can be calculated using the following formula:

$$\Delta OD = \log_{10} \left( \frac{S_{ref}^{on}}{S_{ref}^{off}} \times \frac{S_{prob}^{off}}{S_{prob}^{on}} \right) \quad (1)$$

where  $S_{ref}^{on}$  and  $S_{ref}^{off}$  are reference spectra when pump laser is on and off respectively,  $S_{prob}^{off}$  and  $S_{prob}^{on}$  are probe spectra when pump laser is on and off respectively. The setup is operated both in normal mode in which the two pumps run at 10Hz and in online subtraction mode in which the transient absorption after the first excitation is inherently removed by running the first pump at 20 Hz which is the same as the repetition rate of the probe. Therefore,

in principle we obtain a relatively pure signal from molecules that are excited twice, as the *off* signal then contains contributions from the singly pumped solution. It is noteworthy that the double-pumped transient signal actually contains contributions from singly and doubly-excited molecules because excitation efficiency by the first pump laser cannot reach 100%.

**Charge separation studies of (i)  $[\text{Ru}(\text{bpy})_3]^{2+}$  (13  $\mu\text{M}$ ) and (ii)  $[\text{Ru}(\text{bpy})_3]^{2+}$  (13  $\mu\text{M}$ ) with ascorbate (100 mM) in deaerated  $\text{CH}_3\text{CN}/\text{H}_2\text{O}$  (60:40)**

The  $[\text{Ru}(\text{bpy})_3]^{2+}$  alone shows a bleaching band at 450 nm corresponding to the formation of 6.2 ( $\pm 0.3$ )  $\mu\text{M}$  of  $[\text{Ru}(\text{bpy})_3]^{2+*}$  ( $\Delta A_{450 \text{ nm}} = -0.07$ , with  $\Delta \epsilon_{450 \text{ nm}} = -11300 \text{ M}^{-1}\text{cm}^{-1}$ ), corresponding to 48 ( $\pm 2$ ) % of the ground state of  $[\text{Ru}(\text{bpy})_3]^{2+}$  (Fig. S1). The excited state lifetime of  $[\text{Ru}(\text{bpy})_3]^{2+}$  is 0.80 ( $\pm 0.02$ )  $\mu\text{s}$  corresponding to the monoexponential fit of the decay of the absorption bleach. In the solution composed of  $[\text{Ru}(\text{bpy})_3]^{2+}$  and ascorbate, a band appearing at 510 nm is characteristic of reduced  $[\text{Ru}(\text{bpy})_3]^+$  (Fig. S2a). The TA measurement also indicates that approximately 94% of  $[\text{Ru}(\text{bpy})_3]^{2+*}$  reacted with the ascorbate to create the  $[\text{Ru}(\text{bpy})_3]^+$  ( $\Delta A_{500\text{nm}} = 0.07$ , with  $\Delta \epsilon_{500 \text{ nm}} = 12000 \text{ M}^{-1} \text{ cm}^{-1}$ ; 5.8 ( $\pm 0.3$ )  $\mu\text{M}$  of  $[\text{Ru}(\text{bpy})_3]^+$  formed). The rate constant of the formation of  $[\text{Ru}(\text{bpy})_3]^+$  was found as  $k_q = 2.9 (\pm 0.3) \times 10^8 \text{ M}^{-1} \text{ s}^{-1}$ , corresponding to a rise time of  $34 \pm 5 \text{ ns}$ . The second-order rate constant for this charge recombination process was found to be  $k_{\text{rec}} = 2.8 (\pm 0.3) \times 10^9 \text{ M}^{-1}\text{s}^{-1}$  (Fig. S2b).

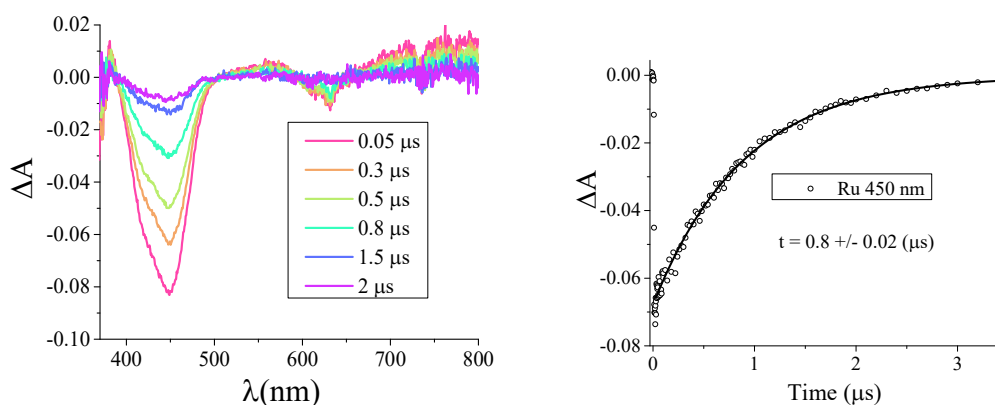


Figure S1. TA spectra at indicated delay times and kinetic trace at 450 nm of  $[\text{Ru}(\text{bpy})_3]^{2+}$   $13 \times 10^{-6} \text{ M}$  in deaerated  $\text{CH}_3\text{CN}/\text{H}_2\text{O}$  (60:40),  $\lambda_{\text{exc}} = 460 \text{ nm}$ .

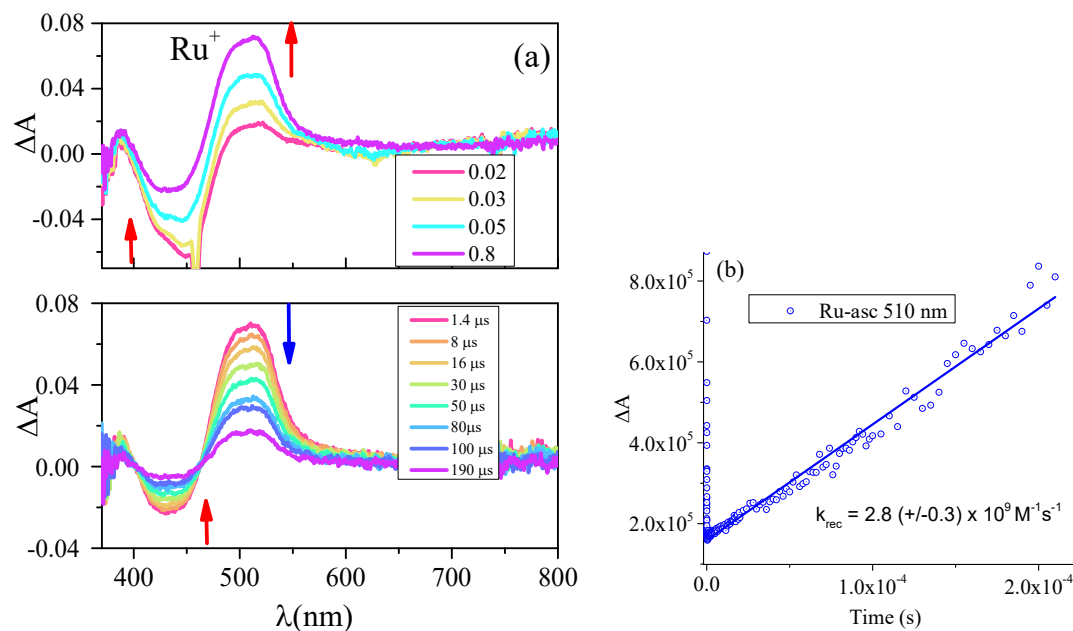


Figure S2. (a) TA spectra at indicated delay times and (b) second-order rate plotted for  $1/[\text{Ru}^+]$  vs. time at 510 nm of a solution involving  $[\text{Ru}(\text{bpy})_3]^{2+}$   $13 \times 10^{-6}$  M, ascorbate 100 mM in deaerated  $\text{CH}_3\text{CN}/\text{H}_2\text{O}$  (60:40),  $\lambda_{\text{exc}} = 460 \text{ nm}$ .

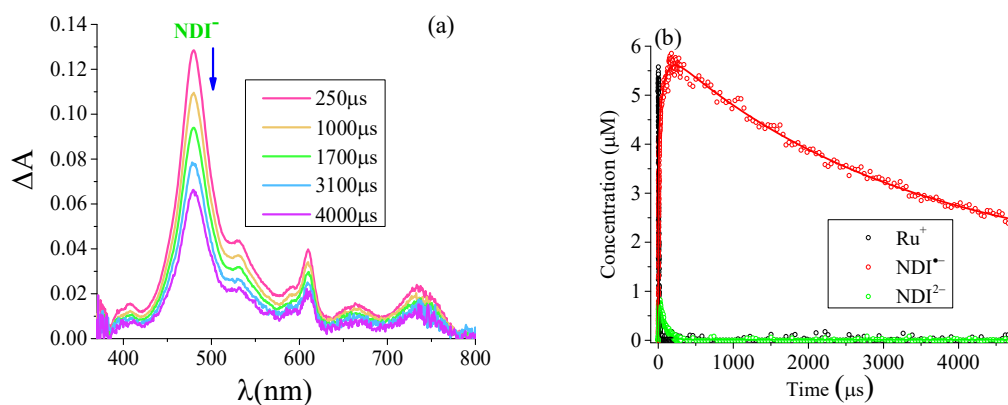


Figure S3. TA spectra (a), and temporal evolution (b) of  $\text{Ru}^+$ ,  $\text{NDI}^{\square-}$ , and  $\text{NDI}^{2-}$  states at the indicated delay times of the solution  $[\text{Ru}(\text{bpy})_3]^{2+}$  (13 μM), ascorbate (100 mM), and NDI (31 μM) in deaerated  $\text{CH}_3\text{CN}/\text{H}_2\text{O}$  (60:40); Single pump excitation at 460 nm.

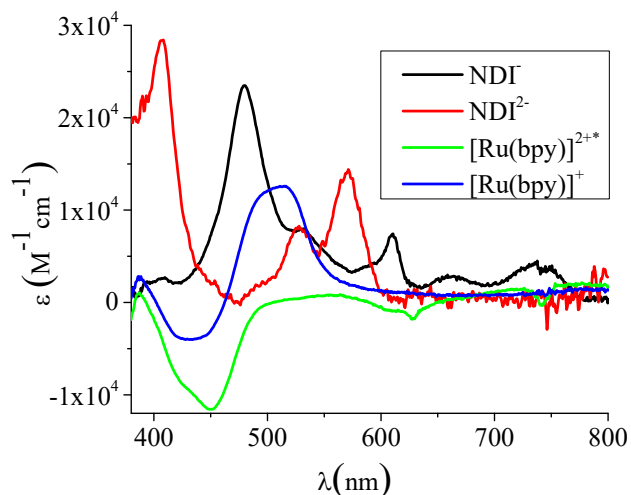


Figure S4. The pure absorption spectra of  $\text{NDI}^{\bullet-}$ ,  $\text{NDI}^{2-}$ , and TA spectra of  $[\text{Ru}(\text{bpy})_3]^{2+*}$  and  $[\text{Ru}(\text{bpy})_3]^+$  obtained from TA measurement, in which  $\text{NDI}^{\bullet-}$  got in the last process of the charge recombination in the multicomponent system;  $\text{NDI}^{2-}$  obtained from subtracted the contribution of  $\text{NDI}^{\bullet-}$  in TA spectra at the delay time that shows the predominant contribution of  $\text{NDI}^{2-}$ ;  $[\text{Ru}(\text{bpy})_3]^{2+*}$  took from TA measurement of  $[\text{Ru}(\text{bpy})_3]^{2+}$ ;  $[\text{Ru}(\text{bpy})_3]^+$  obtained from TA measurement of  $[\text{Ru}(\text{bpy})_3]^{2+*}$  and ascorbate. All the TA experiments were measured in the same condition.

#### Dependence of double charge transfer on the concentration of $[\text{Ru}(\text{bpy})_3]^{2+}$ under single laser excitation

The series TA experiments were performed for different concentrations of  $[\text{Ru}(\text{bpy})_3]^{2+}$  in the same conditions of NDI and ascorbate to clarify the dependence of the formation  $\text{NDI}^{2-}$  on  $[\text{Ru}(\text{bpy})_3]^+$ . Table S1 presents the characteristic times and concentrations of the component species, which were obtained by decomposition analyzing treatment.

Time ( $\mu\text{s}$ )	$t_{\text{decay}} \text{Ru}^+$	$t_{\text{rise}} \text{NDI}^{\bullet-}$	$t_{\text{rise}} \text{NDI}^{\bullet-}$	$t_{\text{decay}} \text{NDI}^{\bullet-}$	$t_{\text{rise}} \text{NDI}^{2-}$	$t_{\text{decay}} \text{NDI}^{2-}$
Concentration	$[\text{Ru}]^+ (\mu\text{M})$	$[\text{NDI}^{\bullet-}] (\mu\text{M})$			$[\text{NDI}^{2-}] (\mu\text{M})$	
<b>Ru12.8 <math>\mu\text{M}</math></b>	5.7( $\pm 0.05$ )	4.6( $\pm 0.07$ )	76( $\pm 4$ )	3266( $\pm 158$ )	9.01( $\pm 0.2$ )	71.5( $\pm 2$ )
<b>NDI – asc</b>	5.5( $\pm 0.2$ )	4.3( $\pm 0.2$ )			0.67( $\pm 0.06$ )	

<b>Ru 28 <math>\mu\text{M}</math></b>	5.1 $\pm$ 0.09	3.2 $\pm$ 0.05	89 $\pm$ 2	2218 $\pm$ 31	9.1 $\pm$ 0.3	92.8 $\pm$ 3.5
<b>NDI-asc</b>	11.7 ( $\pm$ 0.3)	7.5( $\pm$ 0.3)			2( $\pm$ 0.2)	
<b>Ru 42 <math>\mu\text{M}</math></b>	5.2 $\pm$ 0.1	2.4 $\pm$ 0.03	121 $\pm$ 2	2118 $\pm$ 24	9.1 $\pm$ 0.2	127 $\pm$ 5
<b>NDI-asc</b>	16( $\pm$ 1)	7.8( $\pm$ 0.2)			4( $\pm$ 0.2)	

Table S1. The characteristic times and concentrations of the component species involving  $[\text{Ru}(\text{bpy})_3]^+$  (denoted as  $\text{Ru}^+$ ),  $\text{NDI}^{\bullet-}$ , and  $\text{NDI}^{2-}$ , in which the concentration of  $\text{NDI}^{\bullet-}$  refers to the initial single electron transfer. The solution  $[\text{Ru}(\text{bpy})_3]^{2+}$ , ascorbate (100 mM), and NDI (31  $\mu\text{M}$ ) in deaerated  $\text{CH}_3\text{CN}/\text{H}_2\text{O}$  (60:40); Single pump excitation at 460 nm.

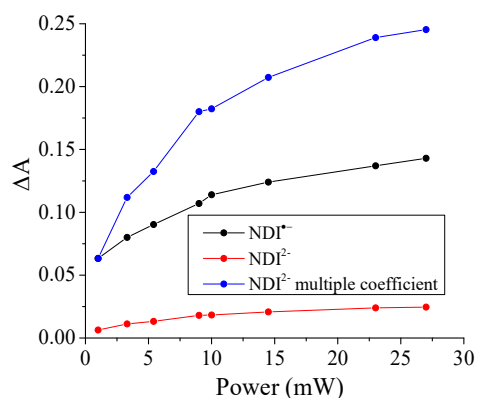


Figure S5. Plot of  $\Delta A$  of  $\text{NDI}^{\bullet-}$  at 480 nm (black curve) and  $\text{NDI}^{2-}$  corrected in subtracting the contribution of  $\text{NDI}^{\bullet-}$  at 400 nm (blue curve) versus power intensity of single-pulse excitation after 15  $\mu\text{s}$ . The blue curve is the normalized curve of  $\text{NDI}^{2-}$  to be clearer in comparison with  $\text{NDI}^{\bullet-}$ .

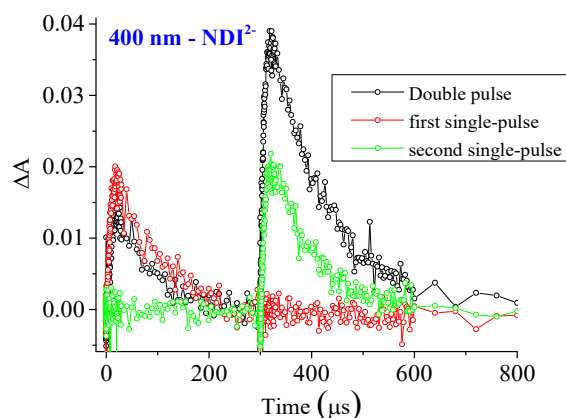


Figure S6. TA kinetic traces at 400 nm (corresponding to the absorption of  $\text{NDI}^{2-}$ ), were corrected by removing the contribution of the  $\text{NDI}^{\bullet-}$  of the solution  $[\text{Ru}(\text{bpy})_3]^{2+}$  (13  $\mu\text{M}$ ), ascorbate (100 mM), and NDI (31  $\mu\text{M}$ ) in deaerated  $\text{CH}_3\text{CN}/\text{H}_2\text{O}$  (60:40), upon double-pulse excitation (460 nm, separated by 300  $\mu\text{s}$ , first pump at 10 Hz, second pump at 10 Hz). The corrected kinetic traces were calculated using the method indicated in Figure 3. The red and the green curves show the time traces of the two single pulse excitations with each laser and the black curve presents the kinetic of double pulse excitation.

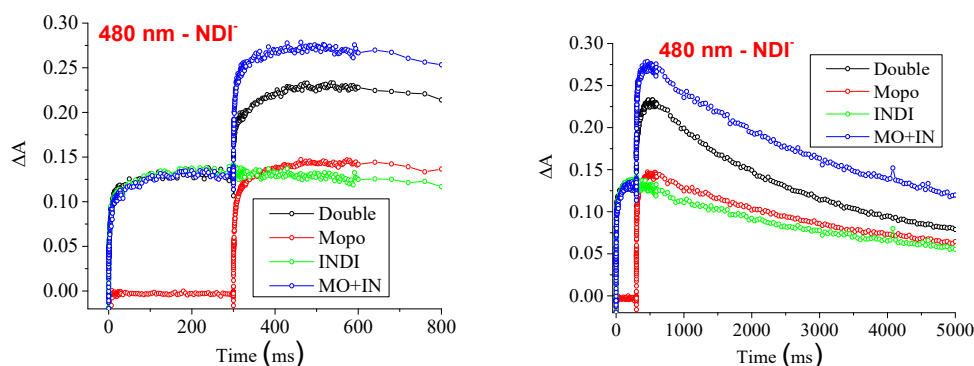


Figure S7. TA kinetic traces at 480 nm of the  $\text{NDI}^{\bullet-}$  of the solution  $[\text{Ru}(\text{bpy})_3]^{2+}$  (13  $\mu\text{M}$ ), ascorbate (100 mM), and NDI (31  $\mu\text{M}$ ) in deaerated  $\text{CH}_3\text{CN}/\text{H}_2\text{O}$  (60:40), upon double-pulse excitation (460 nm, separated by 300  $\mu\text{s}$ , first pump at 10 Hz, second pump at 10 Hz). The different intensity between the black curve (kinetic of double pulse excitation) and the blue curve (kinetic of the total two single pulse together). The final  $\Delta A = 0.22 (\pm 0.02)$  of the  $\text{NDI}^{\bullet-}$  in double pulse laser excitation indicates the concentration of 9.5 ( $\pm 0.5$ )  $\mu\text{M}$  (using a  $\Delta\epsilon_{480} = 23000 \text{ M}^{-1} \cdot \text{cm}^{-1}$ ).

### Procedure for spectral decomposition

In this paragraph, we describe the process to decompose the measured spectra as a combination of the reference spectra characterizing the four intermediate species  $\text{Ru}^*$ ,  $\text{Ru}^{\text{I}}$ ,  $\text{NDI}^{\bullet-}$ ,  $\text{NDI}^{2-}$ . For each delayed time  $t$ , we expressed the transient spectrum as a linear combination of the above basis:

$$\Delta A(t, \lambda) = [\text{Ru}^*]_t \times \epsilon_{\text{Ru}^*}(\lambda) + [\text{Ru}^{\text{I}}]_t \times \epsilon_{\text{Ru}^{\text{I}}}(\lambda) + [\text{NDI}^{\bullet-}]_t \times \epsilon_{\text{NDI}^{\bullet-}}(\lambda) + [\text{NDI}^{2-}]_t \times \epsilon_{\text{NDI}^{2-}}(\lambda),$$

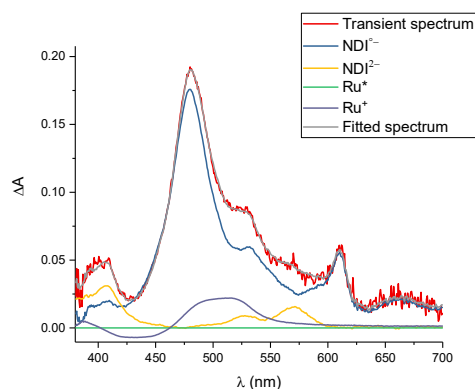
where  $[Ru^*]_t, [Ru^I]_t, [NDI^{\bullet-}]_t, [NDI^{2-}]_t$  are the set of concentration at time  $t$  and  $\varepsilon_{Ru^*}(\lambda), \varepsilon_{Ru^I}(\lambda), \varepsilon_{NDI^{\bullet-}}(\lambda), \varepsilon_{NDI^{2-}}(\lambda)$  are the reference absorption spectra of the intermediate species.

In order to determine the set of concentrations, we performed a least square optimization to fit this linear combination with the experimental data.

$$\min_{[Ru^*]_t, [Ru^I]_t, [NDI^{\bullet-}]_t, [NDI^{2-}]_t} [\Delta A^{exp}(t, \lambda) - \Delta A(t, \lambda)]^2$$

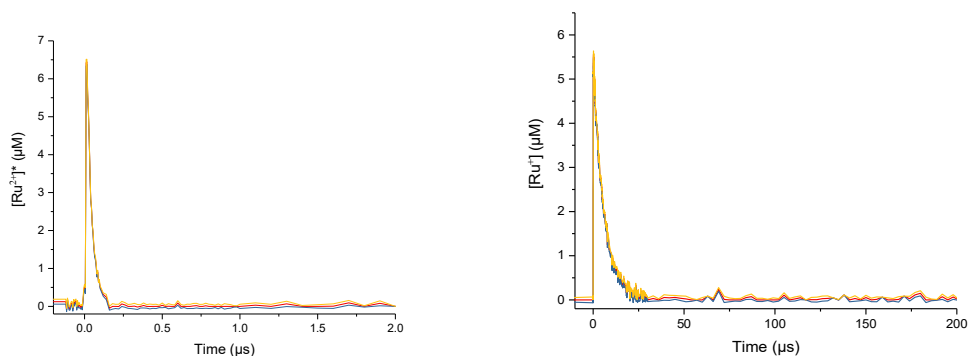
Here,  $\Delta A^{exp}(t, \lambda)$  is the experimental spectrum and  $\Delta A(t, \lambda)$  is the linear model of the transient spectrum at time  $t$ .

In the Figure S8, we show how a single spectrum is decomposed on the given basis ( $\varepsilon_{Ru^*}(\lambda), \varepsilon_{Ru^I}(\lambda), \varepsilon_{NDI^{\bullet-}}(\lambda), \varepsilon_{NDI^{2-}}(\lambda)$ ).



**Figure S.** Decomposition of a single transient spectrum at 7  $\mu$ s delay time.

Repeating this process for all delayed times, we were able to characterize the dynamics of the different processes occurring in the multi-component photosystem. In the below figure, we present the temporal evolution of the concentrations  $[Ru^*]_t, [Ru^I]_t, [NDI^{\bullet-}]_t, [NDI^{2-}]_t$  fitted over all our experimental data.



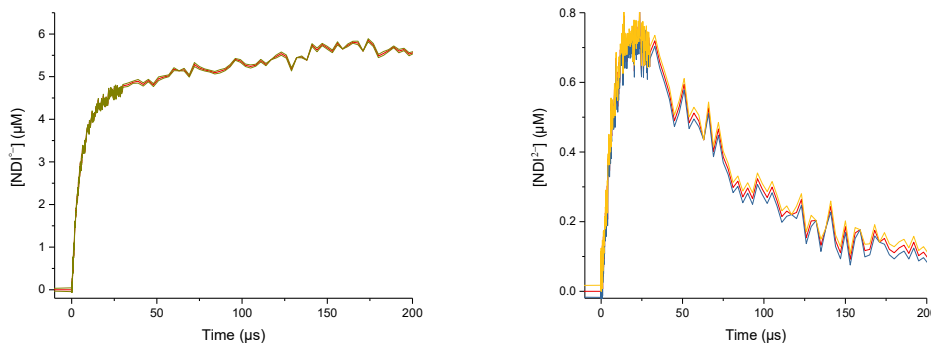


**Figure S9.** Temporal evolution of the concentration of different intermediate species obtained from spectral decomposition at all delay times.

Numerical solution and data fitting of the Ru-NDI experiment

### Numerical solution and data fitting of the Ru-NDI experiment

In this session, we present the details of our numerical simulation of the kinetic equations and the fitting procedure of the concentrations in order to obtain the rate constants characterizing the different reactions.

Let us first write down the different light-driven reactions:

- (1)  $Ru^* \rightarrow Ru^{II} + h\nu$  (with rate constant  $k_0$ )
- (2)  $Ru^* + asc \rightarrow Ru^I + asc^+$  (with rate constant  $k_q$ )
- (3)  $Ru^I + asc^+ \rightarrow Ru^{II} + asc$  (with rate constant  $k_{rec}$ )
- (4)  $Ru^I + NDI \rightarrow Ru^{II} + NDI^{\bullet-}$  (with rate constant  $k_{et1}$ )
- (5)  $Ru^I + NDI^{\bullet-} \rightarrow Ru^{II} + NDI^{2-}$  (with rate constant  $k_{et2}$ )
- (6)  $NDI^{2-} + NDI \rightarrow 2NDI^{\bullet-}$  (with rate constant  $k_{rec1}$ )
- (7)  $NDI^{2-} + asc^+ \rightarrow NDI^{\bullet-} + asc$  (with rate constant  $k_{rec1b}$ )
- (8)  $NDI^{\bullet-} + asc^+ \rightarrow NDI + asc$  (with rate constant  $k_{rec2}$ )

The system of dynamic equations characterizing the time evolution of the concentrations for different species is given as following:

$$\frac{d[Ru^*]}{dt} = -k_0[Ru^*] - k_q[asc][Ru^*]$$

$$\frac{d[Ru^I]}{dt} = k_q[asc][Ru^*] - k_{et1}[NDI][Ru^I] - k_{et2}[NDI^{\bullet-}][Ru^I] - k_{rec}[asc^+][Ru^I]$$

$$\frac{d[NDI]}{dt} = -k_{et1}[NDI][Ru^I] + k_{rec2}[asc^+][NDI^{\bullet-}] - k_{rec1}[NDI][NDI^{2-}]$$

$$\frac{d[NDI^{-}]}{dt} = k_{et1}[NDI][Ru^I] - k_{et2}[NDI^{-}][Ru^I] + k_{rec1b}[asc^+][NDI^{2-}] - k_{rec2}[asc^+][NDI^{-}] + 2k_{rec1}[NDI][NDI^{2-}]$$

$$\frac{d[NDI^{2-}]}{dt} = k_{et2}[NDI^{-}][Ru^I] - k_{rec1b}[asc^+][NDI^{2-}] - k_{corr}[NDI][NDI^{2-}]$$

$$\frac{d[asc]}{dt} = -k_q[asc][Ru^*] + k_{rec1b}[asc^+][NDI^{2-}] + k_{rec2}[asc^+][NDI^{-}]$$

$$\frac{d[asc^+]}{dt} = k_q[asc][Ru^*] - k_{rec1b}[asc^+][NDI^{2-}] - k_{rec2}[asc^+][NDI^{-}] - k_{rec}[asc^+][Ru^I]$$

with the initial condition at the beginning of these reactions (t=0):

$$[Ru^*]_0, [NDI]_0, [asc]_0, [Ru^+]_0 = 0, [NDI^{-}]_0 = 0, [NDI^{2-}]_0 = 0, [asc^+]_0 = 0$$

The above system of ordinary differential equations (ODE) can be solved numerically for a given set of rate constants and a given set of initial values of the concentration. In this paper, we employed the standard ODE method implemented within the Scipy library. This method consists of estimating the vector of derivative of the concentrations as well as the Jacobian of the right-hand side of the equations. Using the analytical formula of these quantities, we can propagate the numerical solution of the concentrations on a given grid of time. In order to better fit the data, we define a time grid with the equivalent timestep to experimental data.

Once the numerical solution can be obtained with the above implementation, we fitted the numerical solution to the data using the least square optimization in order to obtain the best rate constants. Let us denote  $\mathbf{y}_t = (y_t^i)$  with  $i = 1 \dots n$ , the numerical solution of the vector of concentrations for a given set of rate constants  $(k_1, k_2, \dots, k_n)$  and  $\mathbf{c}_t = (c_t^i)$  with  $i = 1 \dots n$ , the  $n$  measured concentrations from the pump-pump-probe experiment. Hence the set of concentration is obtained by the following optimization program:

$$\min \sum_{i=1}^n [y_t^i(k_1, k_2, \dots, k_n) - c_t^i]^2$$

In the figures below, we present the result of our fitting process with the experimental data described in the paper. With different samples, we obtain a very similar set of the rate constants allowing to fit the experimental data from very small time scale (sub  $\mu$ s) to very large time scale (5000  $\mu$ s).

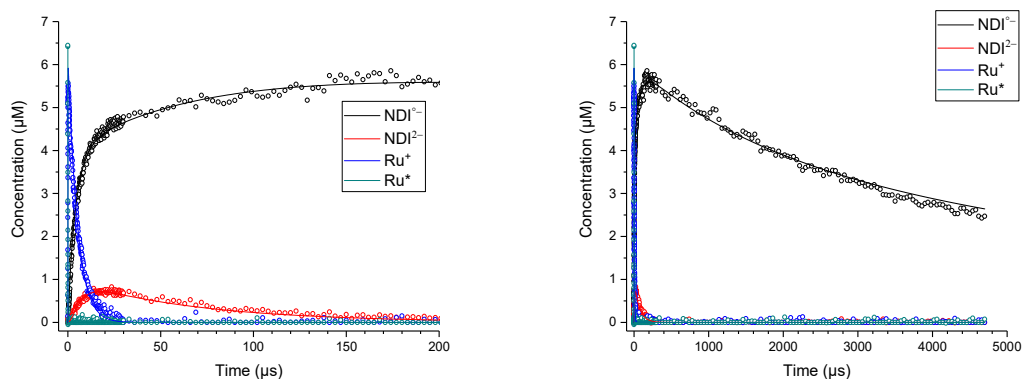


**Figure S10.** Numerical fit to obtain the rate constants of different reactions from (1) to (8).

The set of rate constants obtained from the fit is the following:

$$k_0 = (1.3 \pm 0.1) \times 10^6 \text{ s}^{-1},$$

$$k_q = (2.7 \pm 0.3) \times 10^8 \text{ M}^{-1}\text{s}^{-1},$$

$$k_{rec} = (2.8 \pm 0.3) \times 10^9 \text{ M}^{-1}\text{s}^{-1},$$

$$k_{et1} = (5.8 \pm 0.5) \times 10^9 \text{ M}^{-1}\text{s}^{-1},$$

$$k_{et} = (8 \pm 2) \times 10^9 \text{ M}^{-1}\text{s}^{-1},$$

$$k_{rec1b} = (0 \pm 0.2) \times 10^9 \text{ M}^{-1}\text{s}^{-1},$$

$$k_{rec1} = (5 \pm 1) \times 10^8 \text{ M}^{-1}\text{s}^{-1},$$

$$k_{rec2} = (4.5 \pm 0.3) \times 10^7 \text{ M}^{-1}\text{s}^{-1}$$

## REFERENCES

1. Hammarström, L., Accumulative Charge Separation for Solar Fuels Production: Coupling Light-Induced Single Electron Transfer to Multielectron Catalysis. *Accounts of Chemical Research*. **2015**, *48* (3), 840-850.
2. Barber, J., Photosynthetic energy conversion: natural and artificial. *Chemical Society Reviews*. **2009**, *38* (1), 185-196.
3. Fujita, E., Photochemical carbon dioxide reduction with metal complexes. *Coordination Chemistry Reviews* **1999**, *185-186*, 373-384.

#### Chapter 4. Charge accumulation on multicomponent systems

4. Yamazaki, Y.; Takeda, H.; Ishitani, O., Photocatalytic reduction of CO<sub>2</sub> using metal complexes. *Journal of Photochemistry and photobiology C: photochemistry reviews*. **2015**, *25*, 106-137.
5. Tamaki, Y.; Ishitani, O., Supramolecular photocatalysts for the reduction of CO<sub>2</sub>. *ACS Catalysis* **2017**, *7* (5), 3394-3409.
6. Kimura, E.; Bu, X.; Shionoya, M.; Wada, S.; Maruyama, S., *Inorganic chemistry*. **1992**, *31*, 4542.
7. Schulz, M.; Karnahl, M.; Schwalbe, M.; Vos, J. G., The role of the bridging ligand in photocatalytic supramolecular assemblies for the reduction of protons and carbon dioxide. *Coordination Chemistry Reviews* **2012**, *256* (15), 1682-1705.
8. Juris, A.; Balzani, V.; Barigelletti, F.; Campagna, S.; Belser, P.; von Zelewsky, A., Ru(II) polypyridine complexes: photophysics, photochemistry, electrochemistry, and chemiluminescence. *Coordination Chemistry Reviews*. **1988**, *84*, 85-277.
9. Pellegrin, Y.; Odobel, F., Sacrificial electron donor reagents for solar fuel production. *Comptes Rendus Chimie* **2017**, *20* (3), 283-295.
10. Yonemoto, E. H.; Saupe, G. B.; Schmehl, R. H.; Hubig, S. M.; Riley, R. L.; Iverson, B. L.; Mallouk, T. E., Electron-Transfer Reactions of Ruthenium Trisbipyridyl-Viologen Donor-Acceptor Molecules: Comparison of the Distance Dependence of Electron Transfer-Rates in the Normal and Marcus Inverted Regions. *Journal of the American Chemical Society* **1994**, *116* (11), 4786-4795.
11. Königstein, C., Some aspects of photochemical systems for direct light-induced hydrogen production. *Journal of Photochemistry and Photobiology A: Chemistry* **1995**, *90* (2), 141-152.
12. Lomoth, R.; Häupl, T.; Johansson, O.; Hammarström, L., Redox-Switchable Direction of Photoinduced Electron Transfer in an Ru(bpy)<sub>3</sub><sup>2+</sup>-Viologen Dyad. *Chemistry A European Journal*. **2002**, *8* (1), 102-110.
13. Greenfield, S. R.; Svec, W. A.; Gosztola, D.; Wasielewski, M. R., Multistep Photochemical Charge Separation in Rod-like Molecules Based on Aromatic Imides and Diimides. *Journal of the American Chemical Society*. **1996**, *118* (28), 6767-6777.
14. Angadi, M. A.; Gosztola, D.; Wasielewski, M. R., Characterization of photovoltaic cells using poly(phenylenevinylene) doped with perylene diimide electron acceptors. *Journal of applied physics* **1998**, *83* (11), 6187-6189.
15. Gosztola, D.; Niemczyk, M. P.; Svec, W.; Lukas, A. S.; Wasielewski, M. R., Excited Doublet States of Electrochemically Generated Aromatic Imide and Diimide Radical Anions. *Journal of Physical Chemistry A*. **2000**, *104* (28), 6545-6551.
16. Viehbeck, A.; Goldberg, M. J.; Kovac, C. A., Electrochemical Properties of Polyimides and Related Imide Compounds. *Journal of The Electrochemical Society*. **1990**, *137* (5), 1460-1466.
17. Tran, T.-T.; Ha-Thi, M.-H.; Pino, T.; Quaranta, A.; Lefumeux, C.; Leibl, W.; Aukauloo, A., Snapshots of Light Induced Accumulation of Two Charges on Methylviologen using a Sequential Nanosecond Pump-Pump Photoexcitation. *Journal of Physical Chemistry Letters*. **2018**, *9*, 1086-1091.

#### Chapter 4. Charge accumulation on multicomponent systems

18. Marcus, R. A.; Sutin, N., Electron transfers in chemistry and biology. *Biochimica et Biophysica Acta (BBA) - Biomembranes*. **1985**, *811* (3), 265-322.
19. Lewis, N. S.; Nocera, D. G., Powering the planet: Chemical challenges in solar energy utilization. *Proceedings of the National Academy of Sciences*. **2006**, *103* (43), 15729-15735.
20. Balzani, V.; Credi, A.; Venturi, M., Photochemical Conversion of Solar Energy. *ChemSusChem* **2008**, *1* (1-2), 26-58.
21. Meyer, T. J., Chemical approaches to artificial photosynthesis. *Accounts of chemical research*. **1989**, *22* (5), 163-170.
22. Concepcion, J. J.; House, R. L.; Papanikolas, J. M.; Meyer, T. J., Chemical approaches to artificial photosynthesis. *Proceedings of the National Academy of Sciences*. **2012**, *109* (39), 15560-15564.
23. Kärkäs, M. D.; Verho, O.; Johnston, E. V.; Åkermark, B., Artificial Photosynthesis: Molecular Systems for Catalytic Water Oxidation. *Chemical reviews*. **2014**, *114* (24), 11863-12001.
24. Kuss-Petermann, M.; Oraziatti, M.; Neuburger, M.; Hamm, P.; Wenger, O. S., Intramolecular Light-Driven Accumulation of Reduction Equivalents by Proton-Coupled Electron Transfer. *Journal of the American Chemical Society*. **2017**, *139* (14), 5225-5232.
25. Oraziatti, M.; Kuss-Petermann, M.; Hamm, P.; Wenger, O. S., Light-Driven Electron Accumulation in a Molecular Pentad. *Angewandte Chemie International Edition*. **2016**, *55* (32), 9407-9410.
26. Imahori, H.; Hasegawa, M.; Taniguchi, S.; Aoki, M.; Okada, T.; Sakata, Y., Synthesis and Photophysical Properties of Porphyrin-Tetracyanoanthraquinodimethane-Porphyrin Triad: Photon-Dependent Molecular Switching. *Chemistry letters*. **1998**, *27* (8), 721-722.
27. O'Neil, M. P.; Niemczyk, M. P.; Svec, W. A.; Gosztola, D.; Gaines, G. L.; Wasielewski, M. R., Picosecond Optical Switching Based on Biphotonic Excitation of an Electron Donor-Acceptor-Donor Molecule. *Science* **1992**, *257* (5066), 63-65.
28. Konduri, R.; Ye, H.; MacDonnell, F. M.; Serroni, S.; Campagna, S.; Rajeshwar, K., Ruthenium Photocatalysts Capable of Reversibly Storing up to Four Electrons in a Single Acceptor Ligand: A Step Closer to Artificial Photosynthesis. *Angewandte Chemie International Edition*. **2002**, *114* (17), 3317-3319.
29. Karlsson, S.; Boixel, J.; Pellegrin, Y.; Blart, E.; Becker, H.-C.; Odobel, F.; Hammarström, L., Accumulative Charge Separation Inspired by Photosynthesis. *Journal of the American Chemical Society*. **2010**, *132* (51), 17977-17979.
30. Rao, H.; Schmidt, L. C.; Bonin, J.; Robert, M., Visible-light-driven methane formation from CO<sub>2</sub> with a molecular iron catalyst. *Nature* **2017**, *548* (7665), 74-77.
31. Bonin, J.; Maurin, A.; Robert, M., Molecular catalysis of the electrochemical and photochemical reduction of CO<sub>2</sub> with Fe and Co metal based complexes. Recent advances. *Coordination Chemistry Reviews*. **2017**, *334* (Supplement C), 184-198.

32. Herrero, C.; Quaranta, A.; Leibl, W.; Rutherford, A. W.; Aukauloo, A., Artificial photosynthetic systems. Using light and water to provide electrons and protons for the synthesis of a fuel. *Energy & Environmental Science*. **2011**, *4* (7), 2353-2365.
33. Khnayzer, R. S.; Thoi, V. S.; Nippe, M.; King, A. E.; Jurss, J. W.; El Roz, K. A.; Long, J. R.; Chang, C. J.; Castellano, F. N., Towards a comprehensive understanding of visible-light photogeneration of hydrogen from water using cobalt(ii) polypyridyl catalysts. *Energy & Environmental Science*. **2014**, *7* (4), 1477-1488.
34. Mendes Marinho, S.; Ha-Thi, M.-H.; Pham, V.-T.; Quaranta, A.; Pino, T.; Lefumeux, C.; Chamaille, T.; Leibl, W.; Aukauloo, A., Time-resolved interception of multiple charge accumulation in a sensitizer-acceptor dyad. *Angewandte Chemie International Edition*. **2017**, *56* (50), 15936-15940.
35. Skaisgirski, M.; Guo, X.; Wenger, O. S., Electron Accumulation on Naphthalene Diimide Photosensitized by [Ru(2,2'-Bipyridine)<sub>3</sub>]<sup>2+</sup>. *Inorganic chemistry*. **2017**, *56* (5), 2432-2439.
36. Bird, C. L.; Kuhn, A. T., Electrochemistry of the viologens. *Chemical Society Reviews*. **1981**, *10* (1), 49-82.
37. Striepe, L.; Baumgartner, T., Viologens and Their Application as Functional Materials. *Chemistry A European Journal*. **2017**, *23* (67), 16924-16940.
38. Kitamoto, K.; Sakai, K., Tris(2,2'-bipyridine)ruthenium Derivatives with Multiple Viologen Acceptors: Quadratic Dependence of Photocatalytic H<sub>2</sub> Evolution Rate on the Local Concentration of the Acceptor Site. *Chemistry A European Journal*. **2016**, *22* (35), 12381-12390.
39. Kitamoto, K.; Ogawa, M.; Ajayakumar, G.; Masaoka, S.; Kraatz, H.-B.; Sakai, K., Molecular photo-charge-separators enabling single-pigment-driven multi-electron transfer and storage leading to H<sub>2</sub> evolution from water. *Inorganic chemistry frontiers*. **2016**, *3* (5), 671-680.
40. Lachmanová, Š.; Dupeyre, G.; Tarábek, J.; Ochsenbein, P.; Perruchot, C.; Ciofini, I.; Hromadová, M.; Pospíšil, L.; Lainé, P. P., Kinetics of Multielectron Transfers and Redox-Induced Structural Changes in N-Aryl-Expanded Pyridiniums: Establishing Their Unusual, Versatile Electrophoric Activity. *Journal of the American Chemical Society*. **2015**, *137* (35), 11349-11364.
41. Goren, Z.; Willner, I., Photochemical and chemical reduction of vicinal dibromides via phase transfer of 4,4'-bipyridinium radical: the role of radical disproportionation. *Journal of the American Chemical Society*. **1983**, *105* (26), 7764-7765.
42. Maidan, R.; Goren, Z.; Becker, J. Y.; Willner, I., Application of multielectron charge relays in chemical and photochemical debromination processes. The role of induced disproportionation of N,N'-dioctyl-4,4'-bipyridinium radical cation in two-phase systems. *Journal of the American Chemical Society*. **1984**, *106* (21), 6217-6222.
43. Muller, P.; Brettel, K., [Ru(bpy)<sub>3</sub>]<sup>2+</sup> as a reference in transient absorption spectroscopy: differential absorption coefficients for formation of the long-lived 3MLCT excited state. *Photochemical & Photobiological Sciences*. **2012**, *11* (4), 632-636.

44. Watanabe, T.; Honda, K., Measurement of the extinction coefficient of the methyl viologen cation radical and the efficiency of its formation by semiconductor photocatalysis. *Journal of Physical Chemistry*. **1982**, *86* (14), 2617-2619.
45. Winograd, N.; Kuwana, T., Evaluation of fast homogeneous electron-exchange reaction rates using electrochemistry and reflection spectroscopy. *Journal of the American Chemical Society*. **1970**, *92* (1), 224-226.
46. Rosseinsky, D. R.; Monk, P. M. S., Kinetics of comproportionation of the bipyridilium salt p-cyanophenyl paraquat in propylene carbonate studied by rotating ring-disc electrodes. *Journal of the Chemical Society, Faraday Transactions*. **1990**, *86* (21), 3597-3601.
47. Kuss-Petermann, M.; Wenger, O. S., Pump-Pump-Probe Spectroscopy of a Molecular Triad Monitoring Detrimental Processes for Photoinduced Charge Accumulation. *Helvetica Chimica Acta* **2017**, *100* (1), e1600283.
48. Renger, G.; Renger, T., Photosystem II: The machinery of photosynthetic water splitting. *Photosynthesis research*. **2008**, *98* (1), 53-80.
49. McEvoy, J. P.; Brudvig, G. W., Water-Splitting Chemistry of Photosystem II. *Chemical reviews*. **2006**, *106* (11), 4455-4483.
50. Concepcion, J. J.; Jurss, J. W.; Brennaman, M. K.; Hoertz, P. G.; Patrocinio, A. O. T.; Murakami Iha, N. Y.; Templeton, J. L.; Meyer, T. J., Making Oxygen with Ruthenium Complexes. *Accounts of Chemical Research*. **2009**, *42* (12), 1954-1965.
51. Ashford, D. L.; Gish, M. K.; Vannucci, A. K.; Brennaman, M. K.; Templeton, J. L.; Papanikolas, J. M.; Meyer, T. J., Molecular Chromophore-Catalyst Assemblies for Solar Fuel Applications. *Chemical reviews*. **2015**, *115* (23), 13006-13049.
52. Pannwitz, A.; Wenger, O. S., Proton-coupled multi-electron transfer and its relevance for artificial photosynthesis and photoredox catalysis. *Chemical communications*. **2019**.
53. Herrero, C.; Lassalle-Kaiser, B.; Leibl, W.; Rutherford, A. W.; Aukauloo, A., Artificial systems related to light driven electron transfer processes in PSII. *Coordination Chemistry Reviews*. **2008**, *252* (3), 456-468.
54. Tamaki, Y.; Ishitani, O., Supramolecular Photocatalysts for the Reduction of CO<sub>2</sub>. *ACS Catal*. **2017**, *7* (5), 3394-3409.
55. Kimura, E.; Bu, X.; Shionoya, M.; Wada, S.; Maruyama, S., A new nickel(II) cyclam (cyclam = 1,4,8,11-tetraazacyclotetradecane) complex covalently attached to tris(1,10-phenanthroline)ruthenium(2+). A new candidate for the catalytic photoreduction of carbon dioxide. *Inorganic chemistry*. **1992**, *31* (22), 4542-4546.
56. Dempsey, J. L.; Brunschwig, B. S.; Winkler, J. R.; Gray, H. B., Hydrogen Evolution Catalyzed by Cobaloximes. *Accounts of Chemical Research*. **2009**, *42* (12), 1995-2004.
57. Artero, V.; Chavarot-Kerlidou, M.; Fontecave, M., Splitting Water with Cobalt. *Angewandte Chemie International Edition*. **2011**, *50* (32), 7238-7266.

58. Windle, C. D.; Perutz, R. N., Advances in molecular photocatalytic and electrocatalytic CO<sub>2</sub> reduction. *Coordination Chemistry Reviews*. **2012**, *256* (21), 2562-2570.
59. Sala, X.; Maji, S.; Bofill, R.; García-Antón, J.; Escriche, L.; Llobet, A., Molecular Water Oxidation Mechanisms Followed by Transition Metals: State of the Art. *Accounts of Chemical Research*. **2014**, *47* (2), 504-516.
60. Pannwitz, A.; Wenger, O. S., Proton-coupled multi-electron transfer and its relevance for artificial photosynthesis and photoredox catalysis. *Chemical communications*. **2019**, *55* (28), 4004-4014.
61. Pellegrin, Y.; Odobel, F., Molecular devices featuring sequential photoinduced charge separations for the storage of multiple redox equivalents. *Coordination Chemistry Reviews*. **2011**, *255* (21), 2578-2593.
62. Molnar, S. M.; Nallas, G.; Bridgewater, J. S.; Brewer, K. J., Photoinitiated Electron Collection in a Mixed-Metal Trimetallic Complex of the Form  $\{[(\text{bpy})_2\text{Ru}(\text{dpb})]_2\text{IrCl}_2\}(\text{PF}_6)_5$  (bpy = 2,2'-Bipyridine and dpb = 2,3-Bis(2-pyridyl)benzoquinoline). *Journal of the American Chemical Society*. **1994**, *116* (12), 5206-5210.
63. Rangan, K.; Arachchige, S. M.; Brown, J. R.; Brewer, K. J., Solar energy conversion using photochemical molecular devices: photocatalytic hydrogen production from water using mixed-metal supramolecular complexes. *Energy & Environmental Science*. **2009**, *2* (4), 410-419.
64. Konduri, R.; Ye, H.; MacDonnell, F. M.; Serroni, S.; Campagna, S.; Rajeshwar, K., Ruthenium Photocatalysts Capable of Reversibly Storing up to Four Electrons in a Single Acceptor Ligand: A Step Closer to Artificial Photosynthesis. *Angewandte Chemie International Edition*. **2002**, *41* (17), 3185-3187.
65. Konduri, R.; de Tacconi, N. R.; Rajeshwar, K.; MacDonnell, F. M., Multielectron Photoreduction of a Bridged Ruthenium Dimer,  $[(\text{phen})_2\text{Ru}(\text{tatpp})\text{Ru}(\text{phen})_2][\text{PF}_6]_4$ : Aqueous Reactivity and Chemical and Spectroelectrochemical Identification of the Photoproducts. *Journal of the American Chemical Society*. **2004**, *126* (37), 11621-11629.
66. Wouters, K. L.; de Tacconi, N. R.; Konduri, R.; Lezna, R. O.; MacDonnell, F. M., Driving Multi-electron Reactions with Photons: Dinuclear Ruthenium Complexes Capable of Stepwise and Concerted Multi-electron Reduction. *Photosynthesis research*. **2006**, *87* (1), 41-55.
67. Matt, B.; Fize, J.; Moussa, J.; Amouri, H.; Pereira, A.; Artero, V.; Izzet, G.; Proust, A., Charge photo-accumulation and photocatalytic hydrogen evolution under visible light at an iridium(III)-photosensitized polyoxotungstate. *Energy & Environmental Science*. **2013**, *6* (5), 1504-1508.
68. Elliott, K. J.; Harriman, A.; Le Pleux, L.; Pellegrin, Y.; Blart, E.; Mayer, C. R.; Odobel, F., A porphyrin-polyoxometallate bio-inspired mimic for artificial photosynthesis. *Physical chemistry chemical physics*. **2009**, *11* (39), 8767-8773.
69. Bonn, A. G.; Wenger, O. S., Photoinduced charge accumulation by metal ion-coupled electron transfer. *Physical chemistry chemical physics*. **2015**, *17* (37), 24001-24010.

#### Chapter 4. Charge accumulation on multicomponent systems

70. Ghaddar, T. H.; Wishart, J. F.; Thompson, D. W.; Whitesell, J. K.; Fox, M. A., A Dendrimer-Based Electron Antenna: Paired Electron-Transfer Reactions in Dendrimers with a 4,4'-Bipyridine Core and Naphthalene Peripheral Groups. *Journal of the American Chemical Society*. **2002**, *124* (28), 8285-8289.
71. Nomrowski, J.; Wenger, O. S., Exploiting Potential Inversion for Photoinduced Multielectron Transfer and Accumulation of Redox Equivalents in a Molecular Heptad. *Journal of the American Chemical Society*. **2018**, *140* (16), 5343-5346.
72. Chen, H.-Y.; Ardo, S., Direct observation of sequential oxidations of a titania-bound molecular proxy catalyst generated through illumination of molecular sensitizers. *Nature chemistry*. **2017**, *10*, 17.
73. Young, R. M.; Jensen, S. C.; Edme, K.; Wu, Y.; Krzyaniak, M. D.; Vermeulen, N. A.; Dale, E. J.; Stoddart, J. F.; Weiss, E. A.; Wasielewski, M. R.; Co, D. T., Ultrafast Two-Electron Transfer in a CdS Quantum Dot-Extended-Viologen Cyclophane Complex. *Journal of the American Chemical Society* **2016**, *138* (19), 6163-6170.
74. Bhosale, S. V.; Jani, C. H.; Langford, S. J., Chemistry of naphthalene diimides. *Chemical Society Reviews*. **2008**, *37* (2), 331-342.
75. Lu, C.; Fujitsuka, M.; Sugimoto, A.; Majima, T., Dual Character of Excited Radical Anions in Aromatic Diimide Bis(radical anion)s: Donor or Acceptor? *Journal of physical chemistry C*. **2017**, *121* (8), 4558-4563.
76. Lakowicz, J. R., Principles of Fluorescence Spectroscopy *Springer US, Boston, MA* **2006**.
77. Ha-Thi, M. H.; Pham, V. T.; Pino, T.; Maslova, V.; Quaranta, A.; Lefumeux, C.; Leibl, W.; Aukauloo, A., Photoinduced electron transfer in a molecular dyad by nanosecond pump-pump-probe spectroscopy. *Photochemical & Photobiological Sciences*. **2018**, *17* (7), 903-909.

# Chapter 5. Photoinduced charge transfer processes on Tetraphenylporphyrins as a catalyst for CO<sub>2</sub> photoreduction and a porphyrin dyad as models for photosystem II

This chapter presents the investigations on charge transfer processes on different porphyrin molecules. Indeed such molecular systems play important roles in practical photocatalytic systems for CO<sub>2</sub> reduction. Photosensitizer, acceptor molecule, model for photosystem II, and all photocatalysts have been synthesized and provided by the team of Pr. Ally Aukauloo at Institut de Chimie Moléculaire et des Matériaux d'Orsay, thanks to a close collaboration with this group.

## **5.1 Introduction**

One of the main reasons behind climate change, which our planet is currently facing, is the increase in atmospheric CO<sub>2</sub> concentration due to overuse of fossil fuels. Energy demand is increasing continuously, while fossil resources are more and more exhausted. These problems have to be solved in terms of both limiting CO<sub>2</sub> emission and finding renewable energy sources to replace fossil fuels. It is a difficult task for the near future. Reduction of CO<sub>2</sub> to fuels using solar energy offers a promising method to recycle CO<sub>2</sub> and takes advantage of solar light as a renewable energy source. To implement this goal, there are different methods that can be used, such as electrocatalytic, photocatalytic,<sup>1-2</sup> and thermocatalytic<sup>3</sup> techniques. In this thesis, photocatalytic systems for CO<sub>2</sub> reduction in homogeneous solutions are the focus.

It is extremely unfavourable to reduce CO<sub>2</sub> by one electron to form CO<sub>2</sub><sup>•-</sup> with a reduction potential of -1.9 V versus normal hydrogen electrode (NHE).<sup>4</sup> Alternatively, reduction of CO<sub>2</sub> through proton-assisted multiple electron transfer is more favourable, as shown in Table 4.1

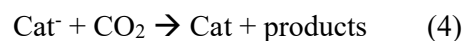
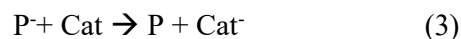
chapter 4. Therefore, a practical photocatalytic reduction system of CO<sub>2</sub> requires a multi-electron redox system.

This chapter focuses on studying kinetics and mechanisms of photoinduced processes on photocatalytic systems, which are still not well understood.

## 5.2 Metal complex approach to photocatalytic systems

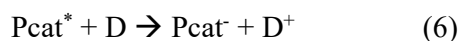
Photocatalytic reduction of CO<sub>2</sub> using metal complexes has been extensively studied, thanks to their variety of accessible oxidation states.<sup>2,4-7</sup> According to the review of Fujita *et al.*,<sup>7</sup> they divided photocatalytic systems of CO<sub>2</sub> into two types.

**Type 1:** Catalysis type 1 can be considered as a photosensitized CO<sub>2</sub> reduction process with the solution involving photosensitizer (P), catalyst (Cat), and sacrificial donor (D). Upon light excitation, the photosensitizer is excited (equation 1), and then is quenched by a sacrificial amine donor to produce a reduced sensitizer and an oxidized amine donor (equation 2). It should be noted that the oxidized amine can reduce a second photosensitizer.<sup>7</sup> The reduced state of the sensitizer continuously reduces the catalyst, and that product then reduces CO<sub>2</sub> (equation 3 and 4).<sup>8</sup>



The type 1 catalyst component generally uses transition-metal tetraaza-macro-cyclic compounds.<sup>8</sup> Catalyst can also be supramolecular complexes, which are composed of a sensitizer that is covalently attached to a coordination compound.<sup>6,9-10</sup> One of the most frequently used catalysts for selective reduction of CO<sub>2</sub> to CO is Re(bpy)(CO)<sub>3</sub>X (X = Cl, Br).

**Type 2:** Catalyst type 2 can be composed with one single compound, which can act as both the photosensitizer and the catalyst, with a sacrificial amine donor. Similarly to the catalyst type 1, the photocatalyst compound (Pcat) is excited under visible light (equation 5), and then is quenched by the electron donor (equation 6). The oxidized amine donor can reduce a second photocatalyst compound. The reduced state of photocatalyst directly interacts with CO<sub>2</sub> (equation 7)



Metalloporphyrins and related metallomacrocycles play an important role in photocatalytic type 2 reduction of CO<sub>2</sub>. Figure 5.1 presents molecular structures of metalloporphyrins (MP), metallocorrins (MN), metallophthalocyanines (MPc), and metallocorroles (MC), where M is Fe or Co.

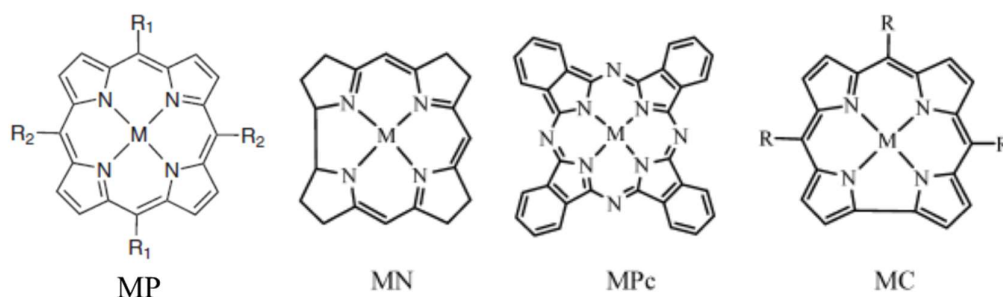


Figure 5.1. Metal porphyrin derivatives studied for reduction of CO<sub>2</sub>: metalloporphyrins (MP)<sup>5</sup>, metallocorrins (MN), metallophthalocyanines (MPc), and metallocorroles (MC)<sup>7</sup>.

It is worth noting that all photocatalysts of type 2 can also act as a catalyst for type 1 with an appropriate photosensitizer. It is also important to note that each of these catalysts requires more than a single reduction process to generate the catalytically active state. Evidence for the formation of the catalytically active state by direct light excitation has not been observed to date. Therefore, further study about the reaction mechanism of the photocatalytic reaction of CO<sub>2</sub> is needed to get a better understanding and improve the efficiency of reduction of CO<sub>2</sub>.

In this chapter, the reaction mechanisms of photocatalytic systems based on porphyrin complexes were studied using nanosecond transient absorption (TA) spectroscopy.

## 5.3 Photophysical study of iron porphyrin complexes in photocatalytic systems

### 5.3.1 Introduction

To develop catalytic systems for practical devices, it should be emphasized that catalytic systems have to be constructed based on cheap and Earth-abundant elements instead of precious metals.<sup>11</sup> Among different metal complexes, which are created for catalytic systems, iron

porphyrin complexes have been employed as an efficient and selective molecular catalyst for converting CO<sub>2</sub> to CO.<sup>12-15</sup> Iron porphyrins and their derivatives possess Fe centers, which may exist from the +III to 0 oxidation states. Additionally, the standard redox potential of the Fe<sup>I</sup>/Fe<sup>0</sup> is quite acceptable for photocatalytic reactions ( $E^0 = -1.50$  V versus saturated calomel electrode (SCE) in dimethylformamide).<sup>14</sup> Thus, iron porphyrins are shown to be one of the most suitable candidates for photochemical reduction of CO<sub>2</sub>.

Photocatalytic CO<sub>2</sub> reduction by using metal complexes in general, and iron porphyrins in particular, have obtained certain success. To properly elucidate the mechanism of those reactions, further spectroscopic investigations are strongly required. Better understanding of the mechanism will support improvement of efficient catalytic systems. In the framework of this thesis, electron transfer processes of iron tetraphenylporphyrin (FeTPPCl) and iron tetra-2,6-difluorophenylporphyrin hydroxide FeTPPF<sub>8</sub>OH (Figure 5.2) were studied by using nanosecond transient absorption (TA) in the presence of a reversible electron donor, 5,6-isopropylidene-L-ascorbate (denoted as iAscH<sup>-</sup>). iAscH<sup>-</sup> were prepared by addition of one equivalent 1,8-biazabicyclo(5.4.0) undec-7-ene (denoted as DBU) into solution of 5,6-isopropylidene-L-ascorbic acid (denoted as iAscH<sub>2</sub>).

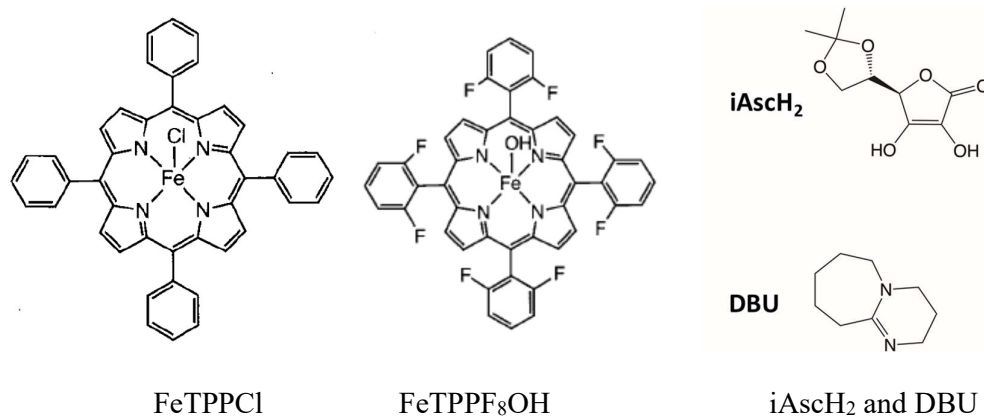


Figure 5.2. Iron porphyrins and iAscH<sup>-</sup> (reversible electron donor) studied for nanosecond transient absorption.

### 5.3.2 Results and discussion

#### Electrochemical studies.

The cyclic voltammetry measurements of FeTPPCl and FeTPPF<sub>8</sub>OH are shown in Figure 5.3. These iron porphyrins show clear standard redox potential of Fe<sup>III/II</sup>, Fe<sup>II/I</sup>, Fe<sup>I/0</sup> couples

(Table 5.1). Costentin *et al.*<sup>16</sup> indicated that the reduced state of iron porphyrins, Fe<sup>0</sup>, in an aprotic solvent, is a very efficient and robust catalyst to reduce CO<sub>2</sub>. However, explanation of the mechanism of interaction between Fe<sup>0</sup> with CO<sub>2</sub> requires further spectroscopic study.

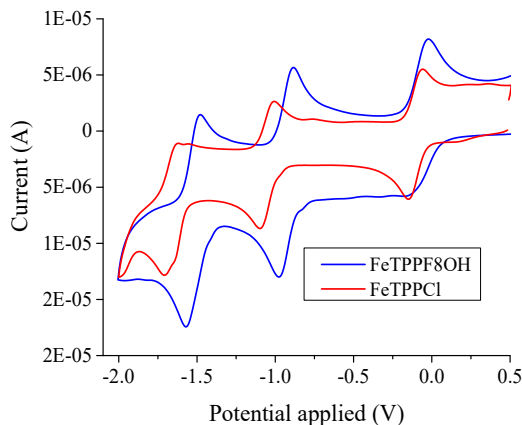


Figure 5.3. Cyclic voltammograms of 1mM of FeTPP8OH (red) and FeTPPF<sub>8</sub>OH (blue) in argon-degassed acetonitrile containing 0.1 M [Bu<sub>4</sub>N]PF<sub>6</sub> at 25 °C and recorded using a glassy carbon working electrode, a platinum mesh as the counter electrode and a saturated calomel electrode (SCE) as the reference electrode.

Table 5.1. Standard redox potentials in V versus SCE of Figure 5.3.

Complex	Fe <sup>III/II</sup>	Fe <sup>II/I</sup>	Fe <sup>I/0</sup>
FeTPP8OH	-0.12	-1.05	-1.65
FeTPPF <sub>8</sub> OH	-0.07	-0.9	-1.55

**Nanosecond transient absorption study.** With the purpose to clarify the reaction mechanism of photoinduced electron transfer processes in the catalytic system, nanosecond TA spectroscopy was studied for a homogeneous solution containing iron porphyrin and a reversible electron donor (iAscH<sup>-</sup>) in argon-saturated acetonitrile, as the initial step for further study in a system involving CO<sub>2</sub>.

*FeTPPF<sub>8</sub>OH complex and iAscH<sup>-</sup> in argon-saturated acetonitrile:*

The homogeneous solutions including iAscH<sup>-</sup> (100 mM) and FeTPPF<sub>8</sub>OH (0.02 mM) in acetonitrile were prepared separately, degassed, and then mixed together. Figure 5.4 shows the absorption spectra in the comparison between FeTPPF<sub>8</sub>OH and FeTPPF<sub>8</sub>OH- iAscH<sup>-</sup>. The

electronic absorption spectrum of FeTPPF<sub>8</sub>OH (inset Figure) shows an absorption band at 408 nm (Soret band) and Q-bands spanning the region between 500 and 700 nm (502, 573, and 646 nm) corresponding to the oxidation state of Fe<sup>III</sup>. After mixing FeTPPF<sub>8</sub>OH with iAscH<sup>-</sup>, the absorption indicates changes in Q-bands with 2 main new Q-bands at 535 and 605 nm. This may be explained by the immediate reaction between FeTPPF<sub>8</sub>OH and iAscH<sup>-</sup> due to low potential of Fe<sup>III</sup>/Fe<sup>II</sup> to create the first reduced state of Fe<sup>III</sup> (Fe<sup>II</sup>). These characteristic bands show a good match with the spectroelectrochemical reported by Neta *et al.*<sup>17</sup>.

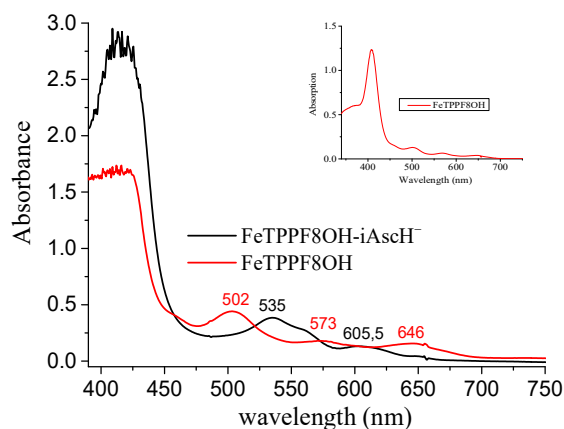


Figure 5.4. Absorption spectra of FeTPPF<sub>8</sub>OH (0.02 mM)- iAscH<sup>-</sup> (100 mM) (black curve) and FeTPPF<sub>8</sub>OH-0.02 mM (red curve) in argon-saturated acetonitrile. Inset: spectrum of FeTPPF<sub>8</sub>OH (9 μM).

This solution was measured by nanosecond TA under excitation at 430 nm, at the rising edge of the Soret band. In this case, FeTPPF<sub>8</sub>OH is considered as both a photosensitizer and a catalyst. Figure 5.5 shows the TA spectra of FeTPPF<sub>8</sub>OH- iAscH<sup>-</sup> at the indicated delay times. At short delay times (Figure 5.5a), negative bands at 650 nm can be attributed to emission spectra of FeTPPF<sub>8</sub>OH.<sup>18</sup> The appearance of positive bands at 429 and 524 nm could be due to the triplet-excited state of FeTPPF<sub>8</sub>OH. Figure 5.5b presents the formation of the new bands at 437 and 562 nm simultaneously with the decrease of the band at 524 nm. The bleaching band at 535 nm indicates the good match with the electronic absorption spectrum of FeTPPF<sub>8</sub>OH- iAscH<sup>-</sup> in Figure 5.4.

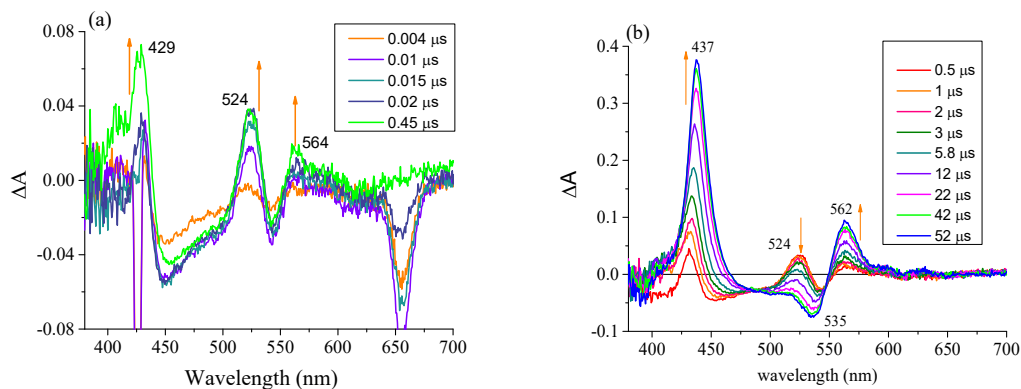


Figure 5.5. Nanosecond TA spectra at the indicated delay times of the  $FeTPPF_8OH$  (0.02 mM) –  $iAscH^-$  (100 mM) in argon-saturated acetonitrile,  $\lambda_{exc}$  430 nm.

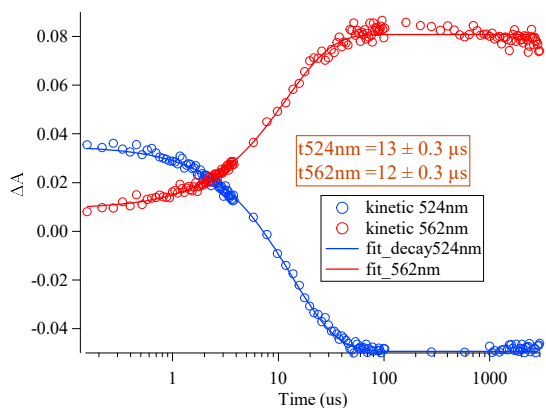


Figure 5.6. Kinetic traces and their fits at 524 and 562 nm of the  $FeTPPF_8OH$  (0.02 mM) –  $iAscH^-$  (100 mM) in argon-saturated acetonitrile,  $\lambda_{exc}$  430 nm.

Therefore, under laser excitation, the second reduced state of  $Fe^{III}$  was obtained with the Soret band at approximately 437 nm and the Q-band at 562 nm. The rising times at 437 and 562 nm are similar at  $12 \pm 0.3 \mu s$  corresponding to an apparent rate constant of  $k_{app} = 8.3 (\pm 0.2) \times 10^4 s^{-1}$ . The decay of this reduced state cannot be observed in several millisecond timescales. The efficiency of charge transfer to create  $Fe^I$  is estimated to be approximately 20 ( $\pm 1$ ) % based on the magnitude of the bleaching at 535 nm ( $\Delta A = -0.075 \pm 0.003$ ) in comparison with the ground-state absorption at 535 nm ( $A = 0.38 \pm 0.001$ ). To examine the ability for stepwise reduction of  $Fe^I$  to  $Fe^0$ , further excitation at 430 nm was implemented in this solution, expecting to excite the  $Fe^I$  state. Unfortunately, this study did not show any change in spectral characteristics. This can potentially be explained by high absorption of the ground state in competition with that of the reduced  $Fe^I$  upon excitation at this wavelength.

*FeTPPCL complex and  $i\text{AscH}^-$  in argon-saturated acetonitrile:*

Identically, the homogeneous solution composed of FeTPPCL (0.15 mM) and  $i\text{AscH}^-$  (100 mM) in argon-saturated acetonitrile was studied by using nanosecond TA spectroscopy. Figure 5.7 shows the absorption spectra of FeTPPCL-  $i\text{AscH}^-$  and FeTPPCL in argon-saturated acetonitrile. One has to note that the spectrum of FeTPPCL-  $i\text{AscH}^-$  could not be recorded under stable conditions due to a slight photodegradation of ascorbate solution. Thus, a clear change of the absorption spectrum of mixed FeTPPCL and  $i\text{AscH}^-$  was not obtained, as compared with FeTPPF8. However, Figure 5.7b shows the enlargement of the Q-band region with a new shoulder band at 543 nm and a band at 604 nm of the FeTPPCL-  $i\text{AscH}^-$  spectrum. This may also be due to immediate reaction between FeTPPCL and  $i\text{AscH}^-$  to create  $\text{Fe}^{\text{II}}$ .

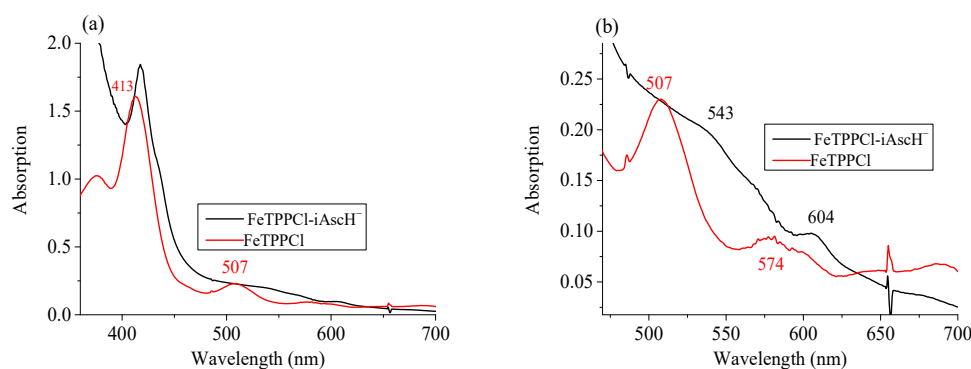


Figure 5.7. (a) Absorption spectra of FeTPPCL (0.15 mM)– $i\text{AscH}^-$  (100 mM) (black curve) and FeTPPCL (red curve) in argon-saturated acetonitrile; (b) Zoom Q- region.

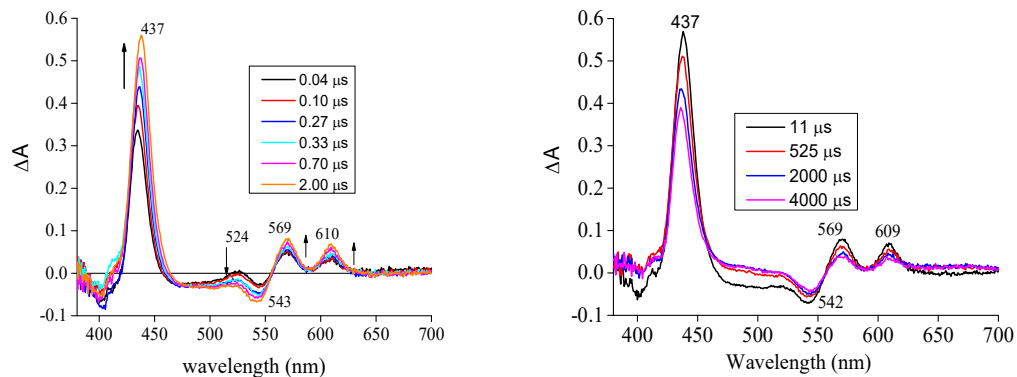


Figure 5.8. Nanosecond TA spectra at the indicated delay times of FeTPPCL (0.15 mM)– $i\text{AscH}^-$  (100 mM) in argon-saturated acetonitrile,  $\lambda_{\text{exc}}$  430 nm

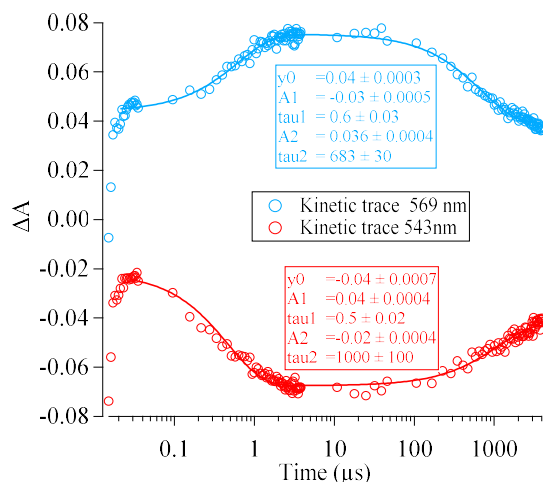


Figure 5.9 Kinetic traces and their fits at 569 and 543 nm of FeTPPCL (0.15 mM)–iAscH<sup>−</sup> (100 mM) in argon-saturated acetonitrile,  $\lambda_{exc}$  430 nm.

The TA spectra of FeTPPCL–iAscH<sup>−</sup> indicates a similar behavior in comparison with the solution FeTPPF<sub>8</sub>OH–iAscH<sup>−</sup>. The rising bands at 437, 569 and 610 nm appear simultaneously with the bleaching band at 543 nm with a time constant of  $\sim 0.6$   $\mu$ s (Figure 5.9), consistent with the reduction of Fe<sup>II</sup> to Fe<sup>I</sup>. The decay of Fe<sup>I</sup> state indicates a lifetime approximately 1000  $\mu$ s. This is faster than that of solution containing FeTPPF<sub>8</sub>OH–iAscH<sup>−</sup>. Further study with a second laser excitation is necessary to examine the possibility of the reduction of Fe<sup>I</sup>. Additionally, experiments on iron porphyrin–iAscH<sup>−</sup> in the presence of CO<sub>2</sub> or CO is worth attempting in order to explain the mechanism of photocatalytic reactions.

## 5.4 Photophysical study of zinc porphyrin complex in photocatalytic systems

### 5.4.1 Introduction

Among the transition-metal-based molecular complexes studied for photocatalytic reduction of CO<sub>2</sub>,<sup>6,11,12,19</sup> zinc porphyrins show that they are also one of the most promising candidates. The reasons for this are: 1) it is low-cost and abundant on Earth; 2) it also gives a high selectivity of reducing CO<sub>2</sub> to CO.<sup>20-21</sup> Furthermore, zinc porphyrins have also been reported as commonly used for porphyrin self-assembly to generate supramolecular arrays.<sup>22-28</sup> To the best of our knowledge, Zn-based molecular catalysts have been explored in electrochemical reduction of CO<sub>2</sub>, and have not been reported yet in photochemical reduction of CO<sub>2</sub>.

Figure 5.10 presents the molecular structure of zinc porphyrin (hereafter referred to as ZnTPPF20) which has been studied using TA spectroscopy for this thesis. To study photophysical properties of porphyrin systems for the reduction of CO<sub>2</sub>, ZnTPPF20 was examined in different roles such as a catalyst in the system including a photosensitizer ([Ru(bpy)<sub>3</sub>]<sup>2+</sup>) and an reversible electron donor (type I); or as a photocatalyst in systems with only electron donors (type II). The results indicate that the solutions of type II composed of only ZnTPPF20 and an electron donor are more stable in comparison with the solutions of type I which includes photosensitizer.

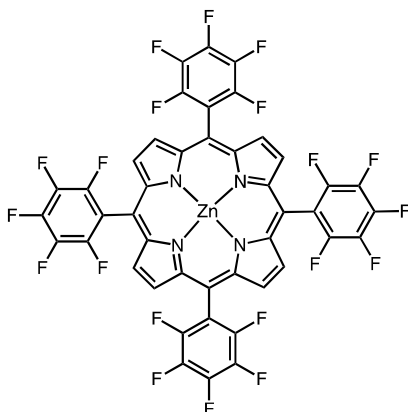


Figure 5.10. Functionalized ZnTPPF20 porphyrin studied for nanosecond transient absorption.

This chapter presents the results of studying photoinduced processes in solutions containing ZnTPPF20 and an electron donor such as diazabicyclo[2.2.2]octane (DABCO) or iAsCH<sup>-</sup> in argon-deaerated acetonitrile, using nanosecond TA.

## 5.4.2 Results and discussion

### Electrochemical studies.

The cyclic voltammetry measurements of ZnTPPF20 is shown in Figure 5.11. The potential of the first reduction peak of ZnTPPF20 (denoted hereafter as ZnTPPF20<sup>-</sup>) is about -1.0 V versus SCE, and the second one is approximately -1.4 V (denoted as ZnTPPF20<sup>2-</sup>). These potentials are quite acceptable for photocatalytic reactions.

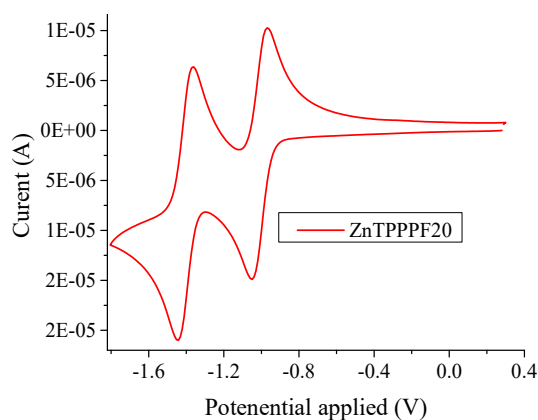


Figure 5.11. Cyclic voltammogram of 1mM of ZnTPPF20 in argon-deaerated acetonitrile containing 0.1 M  $[Bu_4N]PF_6$  at 25°C, and recorded using a glassy carbon working electrode, a platinum mesh as the counter electrode and a SCE as the reference electrode.

#### Nanosecond transient absorption study.

Systems including ZnTPPF20 and a reversible electron donor were studied by TA spectroscopy. Two solutions of ZnTPPF20 at 6.2  $\mu$ M with DABCO as an electron donor at 100 mM, and with  $iAscH^-$  at 100 mM in argon-deaerated acetonitrile were investigated.

#### Nanosecond TA of ZnTPPF20 in acetonitrile:

First, the elementary photophysical properties of ZnTPPF20 were studied. Figure 5.12 shows the absorption spectrum of ZnTPPF20 in acetonitrile with the characteristics of Zn-metallated porphyrins at 416 nm of the Soret band ( $\epsilon \approx 320000 \text{ M}^{-1}\text{cm}^{-1}$ ) and 553 nm of the Q-band ( $\epsilon \approx 20500 \text{ M}^{-1}\text{cm}^{-1}$ ).

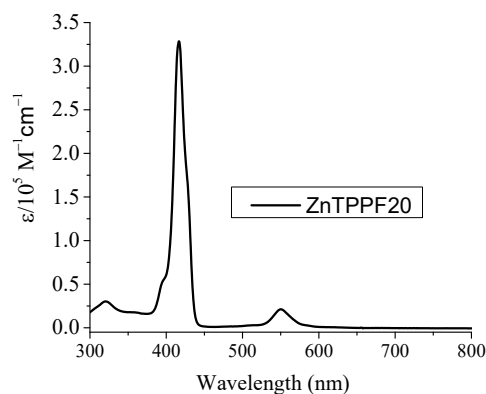


Figure 5.12. The absorption spectrum of ZnTPPF20 (6.2  $\mu$ M) in argon-saturated acetonitrile.

Then, the solution of ZnTPPF20 at 6.2  $\mu\text{M}$  was investigated in acetonitrile saturated with argon, and in air conditions by nanosecond TA spectroscopy under excitation at 430 nm. Figure 5.13a shows the TA spectra of ZnTPPF20 in acetonitrile with air. A broad positive band at 454 nm decays simultaneously with a bleaching band at 555 nm, which can be attributed to the triplet-excited state of ZnTPPF20 with a short lifetime of 0.5  $\mu\text{s}$  (Figure 5.13b). In argon-saturated acetonitrile, the same transient bands of the triplet state were observed with a longer lifetime of 21.5  $\mu\text{s}$  as showed in Figure 5.14.

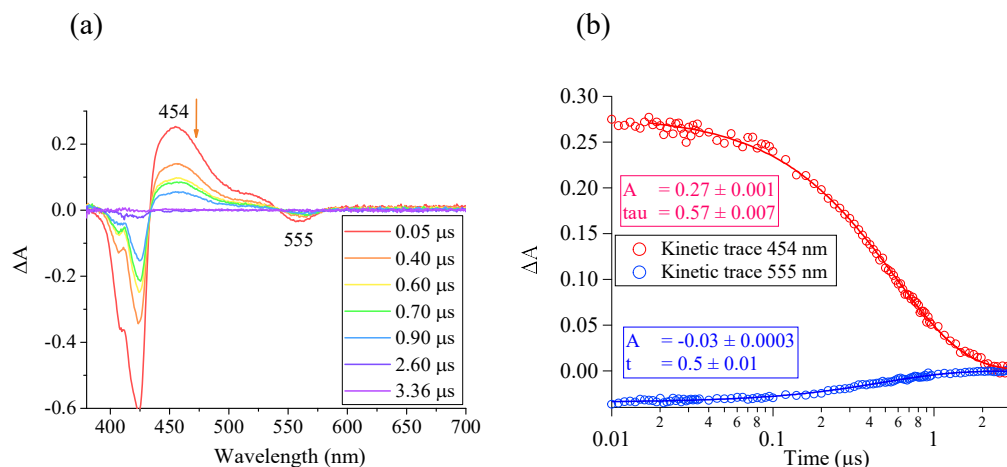


Figure 5.13 a) Nanosecond TA spectra at the indicated delay times of ZnTPPF20 (6.2  $\mu\text{M}$ ) in acetonitrile and in air,  $\lambda_{\text{exc}} = 430 \text{ nm}$ ; b) Kinetic traces and their fits at 454 and 555 nm.

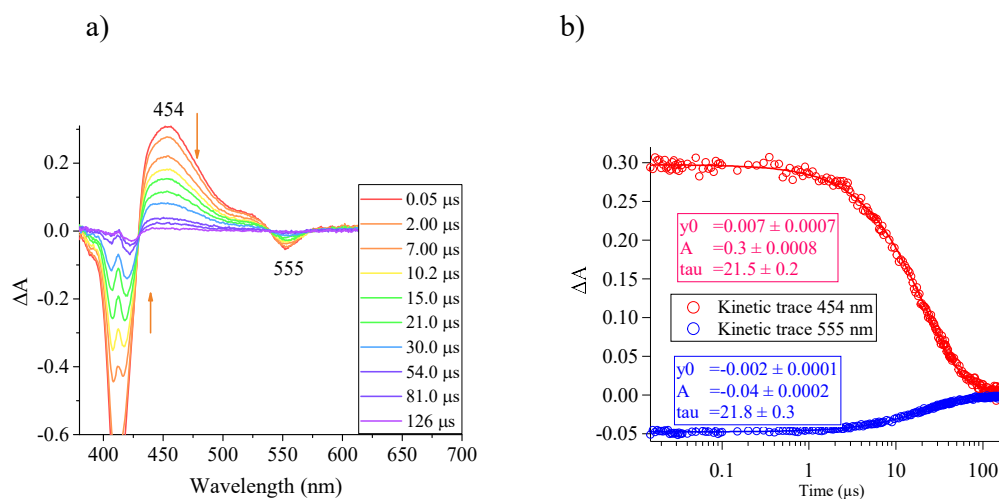


Figure 5.14. a) Nanosecond TA spectra at the indicated delay times of ZnTPPF20 in argon-saturated acetonitrile solution,  $\lambda_{\text{exc}} = 430 \text{ nm}$ , 6.2  $\mu\text{M}$ ; b) Kinetic traces and their fits at 454 and 555 nm.

*Nanosecond TA of ZnF20- iAscH<sup>-</sup> in argon-deaerated acetonitrile:*

Figure 5.15 presents the absorption spectrum of the solution containing ZnTPPF20 (6.2  $\mu\text{M}$ ) and iAscH<sup>-</sup> (100 mM), compared with the spectrum of ZnTPPF20 (6.2  $\mu\text{M}$ ), and iAscH<sup>-</sup> (100 mM) in acetonitrile. Due to the absorption of iAscH<sup>-</sup> in acetonitrile, the absorption spectrum of ZnTPPF20 is increased, and slightly redshifted. The mixture of ZnTPPF20 and iAscH<sup>-</sup> was degassed and investigated by nanosecond TA spectroscopy under 430 nm excitation.

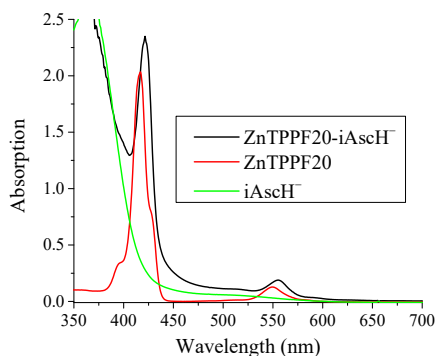


Figure 5.15. The absorption spectrum of ZnTPPF20 (6.2  $\mu\text{M}$ )– iAscH<sup>-</sup> (100 mM) (black curve) in comparison with the absorption spectrum of ZnTPPF20-6.2  $\mu\text{M}$  (red curve) and iAscH<sup>-</sup> -100 mM (green curve) in acetonitrile.

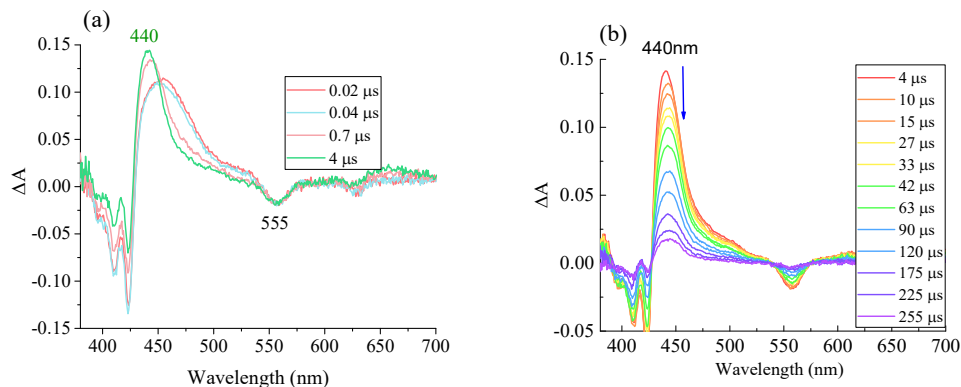


Figure 5.16. Nanosecond TA spectra of ZnTPPF20 (6.2  $\mu\text{M}$ ) and iAscH<sup>-</sup> (100 mM) in argon-saturated acetonitrile at indicated delay times,  $\lambda_{\text{exc}} = 430 \text{ nm}$ .

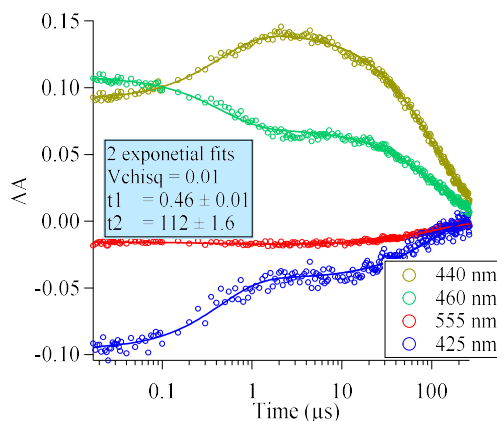


Figure 5.17. Nanosecond TA global fit kinetic traces of ZnTPPF20 (6.2  $\mu\text{M}$ ) and  $i\text{AscH}^-$  (100 mM) in argon-saturated acetonitrile,  $\lambda_{\text{exc}} = 430 \text{ nm}$ .

Figure 5.16 presents the nanosecond TA spectra of the argon-saturated solution of ZnTPPF20 and  $i\text{AscH}^-$  at indicated delay times. At short delay times (Figure 5.16a), a new band at 440 nm appears simultaneously with the disappearance of the triplet-excited state of ZnTPPF20 at 454 nm. This is assigned to a first charge transfer process from  $i\text{AscH}^-$  to the triplet-excited state of ZnTPPF20. The characteristic band at 440 nm shows a good match with the first reduced state of zinc porphyrin, which was reported by Elizabeth *et al.*<sup>29</sup> using spectroelectrochemistry. The charge recombination process of ZnTPPF20<sup>-</sup> and oxidized  $i\text{AscH}^-$  ( $i\text{AscH}^\bullet$ ) is described in Figure 5.16b. Global fitting was implemented for 4 characteristic wavelengths with two exponential times of 0.46 and 112  $\mu\text{s}$  (Figure 5.17). The efficiency of the first charge-separated state is estimated at approximately 14 ( $\pm 1$ )% by using the value of the bleaching state at 555 nm ( $\Delta A \approx -0.017$ ) in comparison with the ground state (absorption  $\sim 0.12$ ).

*Nanosecond TA of ZnTPPF20 and DABCO in argon-deaerated acetonitrile:*

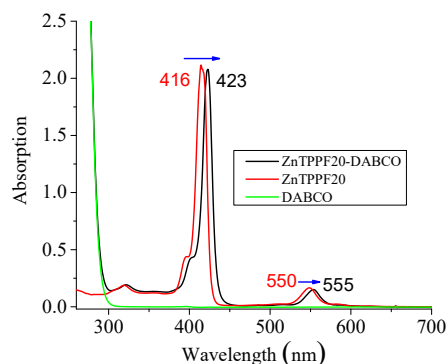


Figure 5.18. The absorption spectrum of ZnTPPF20 (6.2  $\mu\text{M}$ ) and DABCO (100 mM) (black curve) in comparison with the absorption spectrum of ZnTPPF20-6.2  $\mu\text{M}$  (red curve) and DABCO-100 mM (green curve) in acetonitrile.

The absorption spectrum of the solution of ZnTPPF20 6.2  $\mu\text{M}$  and DABCO (100 mM), shows a red shift in comparison with ZnTPPF20. It should be noted that DABCO does not show any absorption band in a range of 300-700 nm. A plausible explanation for the redshift of the ZnTPPF20 DABCO solution is the coordination of DABCO with the  $\text{Zn}^{\text{II}}$  center of the ZnTPPF20 as reported in literature.<sup>22-23</sup> Therefore, this mixing solution of ZnTPPF20 and DABCO can be expected to be as a dyad system with rapid photoinduced electron transfer processes.

As predicted, nanosecond TA spectra in Figure 5.19a indicate a faster formation of the first reduced state of ZnTPPF20 with the band at 444 nm (0.17  $\mu\text{s}$ ) in comparison with the solution of ZnTPPF20 and  $\text{iAscH}^-$  (0.46  $\mu\text{s}$ ). Thereby, the observed charge recombination (Figure 5.19b) is also more rapid. Again, global fitting was implemented and two time constants of 0.17 and 22.2  $\mu\text{s}$  were obtained (Figure 5.20). The efficiency of the first charge transfer is also evaluated at approximately 17 ( $\pm 1$ ) %. This value is slightly higher than that of ZnTPPF20 in the presence of  $\text{iAscH}^-$  donor. This can be attributed to the better redox potential of DABCO as compared with  $\text{iAscH}^-$  ( $\text{DABCO}^+/\text{DABCO} = 0.056 \text{ V vs. SCE in acetonitrile}$ <sup>30</sup> vs  $\text{iAscH}^*/\text{iAscH}^- = -0.01 \text{ vs SCE}$ )

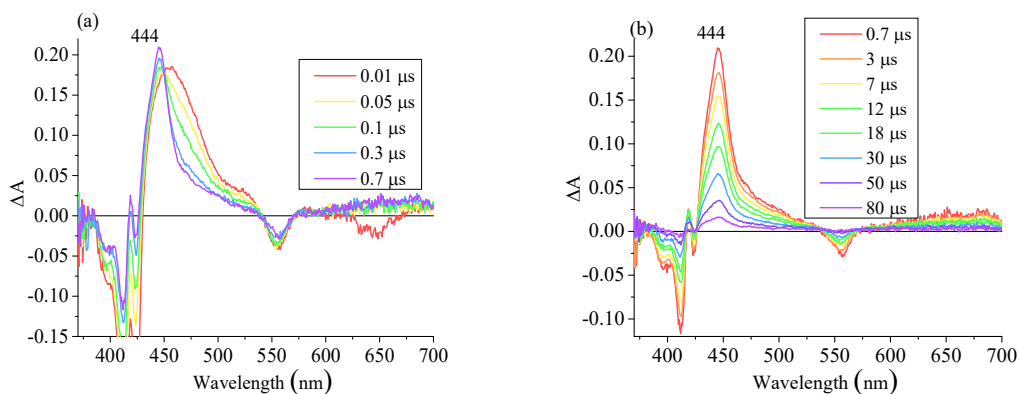


Figure 5.19. Nanosecond TA spectra of ZnTPPF20(6.2  $\mu\text{M}$ )– DABCO (100 mM) in argon-saturated acetonitrile at indicated delay times,  $\lambda_{\text{exc}} = 430 \text{ nm}$ .

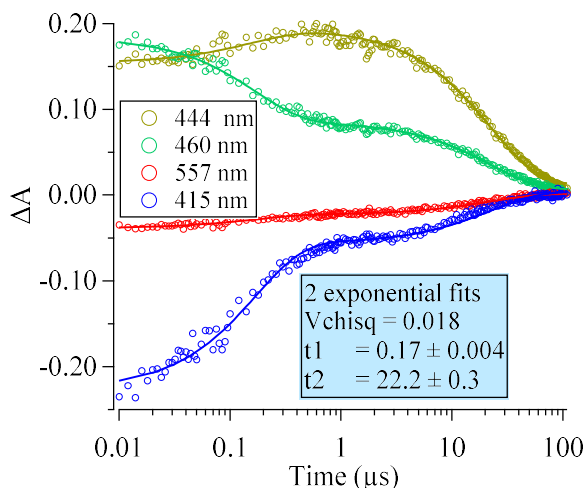


Figure 5.20. Nanosecond TA global fit kinetic traces of ZnTPPF20 (6.2  $\mu\text{M}$ )–DABCO (100 mM) in argon-saturated acetonitrile,  $\lambda_{\text{exc}} = 430 \text{ nm}$ .

Further excitation with a second laser pulse at 450 nm was used to investigate ZnTPPF20–DABCO to study the possibility of the charge accumulation on ZnTPPF20. The second laser was applied 0.8  $\mu\text{s}$  after the first laser excitation with a purpose to excite the highest concentration of first charge-separated state of ZnTPPF20. Laser excitation at 450 nm is absorbed predominantly by the first charge-separated state of ZnTPPF20 with  $\Delta A_{450 \text{ nm}} = 0.2$  versus the absorption of the ground state  $\sim 0.07$ .

To prepare for pump-pump laser excitation study, single pump experiment at 450 nm excitation was performed for ZnTPPF20–DABCO under the same conditions. Figure 5.21 shows the nanosecond TA spectra of ZnTPPF20–DABCO under excitation at 450 nm. Unexpectedly, the TA spectra indicate slower formation (0.23  $\mu\text{s}$ ) as well as relaxation (175  $\mu\text{s}$ ) of ZnTPPF20<sup>-</sup> in comparison with excitation at 430 nm (Figure 5.22). This result indicate a dependence of charge transfer process on excitation wavelengths. This can be tentatively explained by difference coordination modes of DABCO on the porphyrine center. Further experiments at other excitation wavelengths are needed for further clarification.

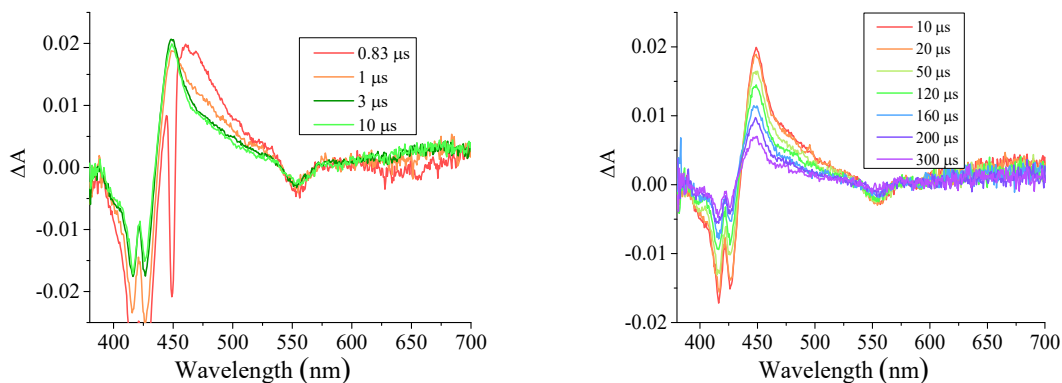


Figure 5.21. Nanosecond TA spectra of ZnTPPF20 (6.2  $\mu\text{M}$ )– DABCO (100 mM) in argon-saturated acetonitrile at indicated delay times,  $\lambda_{\text{exc}} = 450 \text{ nm}$ .

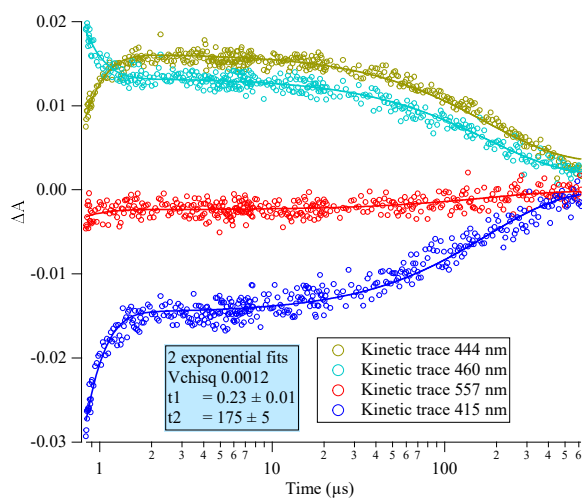


Figure 5.22. Nanosecond TA global fit kinetic traces of ZnTPPF20 (6.2  $\mu\text{M}$ )– DABCO (100 mM) in argon-saturated acetonitrile, single pulse excitation  $\lambda_{\text{exc}} = 450 \text{ nm}$ .

Double-pulse excitation was implemented with the second pulse at 450 nm and a frequency of 20 Hz to excite the first reduced state of ZnTPPF20. With this operation mode, results are giving information only on the second pulse excitation dynamics. The experiment was measured repeatedly 10 times and calculated averagely to limit noise contribution. Figure 23a presents the original TA spectra of the ZnTPPF20–DABCO using double-pulse excitation. A bleaching band at  $\sim 450 \text{ nm}$  appears rapidly simultaneously with a positive band at  $\sim 418 \text{ nm}$ . These bands indicate that the first reduced state of ZnTPPF20 is effectively excited by the second laser pulse. It is important to note that the characteristics of the original spectra (Figure 23a) results from the excitation of both ZnTPPF20<sup>-</sup> and the remaining proportion of molecules

in their ground state. Thus, the spectra in Figure 23a are corrected from the contribution of the ground state excitation of the second laser. It should be noted that the efficiency of production of the first charge-separated state is  $\sim 17 (\pm 1) \%$ , meaning that the ground state concentration decreased by  $\sim 17\%$ . Therefore, the correction is calculated approximately by the formula:  $\Delta A_{\text{Double-pulse}} - 0.83 \times \Delta A_{\text{second-pulse}}$ . The corrected spectra of double-pulse excitation are shown in Figure 23b.

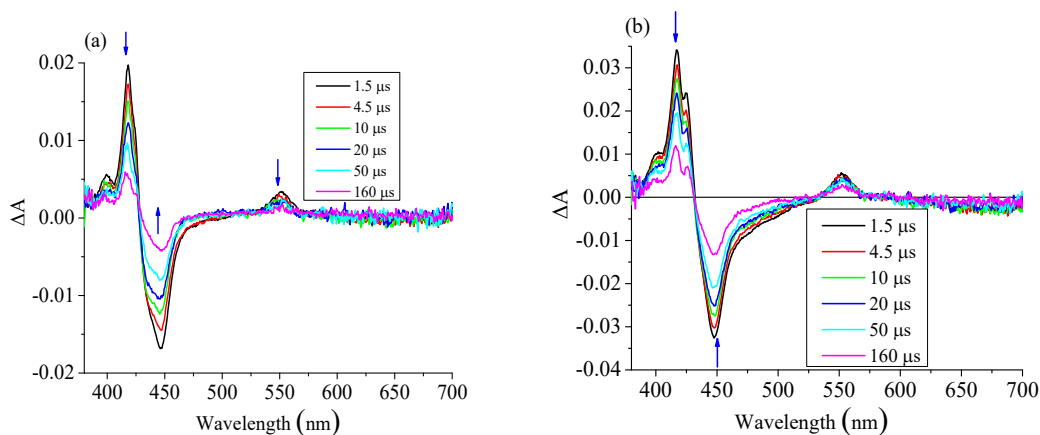
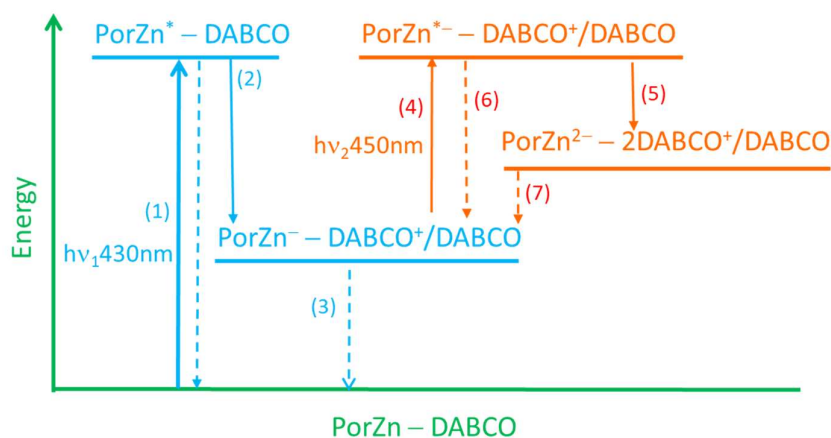


Figure 5.23. TA spectra (a) and corrected TA spectra (b) of the solution ZnTPPF20 ( $6.2 \mu\text{M}$ )–DABCO ( $100 \text{ mM}$ ) in argon-deaerated acetonitrile, upon double-pulse excitation: first pulse at  $430 \text{ nm}$ ,  $20 \text{ Hz}$  and second pulse at  $450 \text{ nm}$ ,  $10 \text{ Hz}$ ; separated by  $0.8 \mu\text{s}$ .

Figure 5.23b presents the spectra after correction. The ground-state bleaching of ZnTPPF20<sup>-</sup> at  $450 \text{ nm}$  indicates the formation of approximately 15% excited state of ZnTPPF20<sup>-</sup> ( $\Delta A_{\text{first-pulse}} \approx 0.2$  versus  $\Delta A_{\text{double-pulse}} \approx -0.03$ ).

To clarify photoinduced processes under double-pulse excitation, global fits for the corrected TA kinetic traces were successfully implemented by using bi-exponential functions with two lifetimes  $3 (\pm 0.1)$  and  $132 (\pm 2.3) \mu\text{s}$  (Figure 5.24a). It is worth emphasizing that the global fits for the single-pulse excitation were satisfactorily obtained by considering only one decay time corresponding to recombination between ZnTPPF20<sup>-</sup> and oxidized DABCO (process 3 in scheme 1). Therefore, one of two kinetic decays in double-pulse excitation can be attributed to the relaxation process of ZnTPPF20<sup>-</sup> and oxidized DABCO ( $123 \mu\text{s}$ ). There are different possibilities that can be advocated for shorter decay time as processes 6 or 7 in Scheme 1.



Scheme 1. Energy diagram and relaxation pathways for photoinduced processes in the ZnTPPF20–DABCO. Abbreviation: ZnTPPF20\* = excited state of ZnTPPF20, ZnTPPF20<sup>-</sup> = first reduced state of ZnTPPF20, DABCO<sup>+</sup> = oxidized state of DABCO, ZnTPPF20\*<sup>-</sup> = excited state of the first reduced state of ZnTPPF20, ZnTPPF20<sup>2-</sup> = second reduced state of ZnTPPF20.

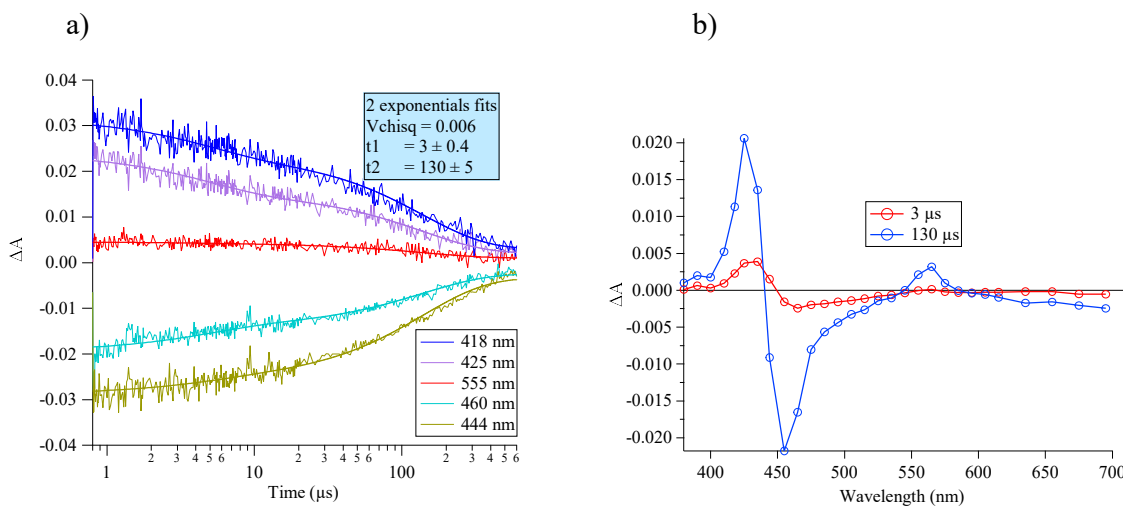


Figure 5.24. a) Nanosecond TA global fit kinetic traces of ZnTPPF20-DABCO in argon-saturated acetonitrile, double-pulse excitation  $\lambda_{exc1} = 430$  nm,  $\lambda_{exc2} = 450$  nm. b) Decay associated different spectra (DADS) obtained from global fits.

DADS are plotted for two decay times of 3 and 130  $\mu$ s, as indicated in Figure 5.24b. As expected, the blue curve describes the characteristic reverse band of the first reduced state of ZnTPPF20 and presents for the relaxation process to the ground state. Surprisingly, the red curve corresponding to the decay spectrum of 3  $\mu$ s shows an appearance of a new band at 435 nm, which is blue-shifted to the first reduced state and red-shifted to the ground state of

ZnTPPF20. This characteristic seems to be similar to the reports about the second electron reduction of zinc porphyrins.<sup>29</sup> Therefore, the second decay time may be attributed to the decay of the relaxation between the second reduced state of ZnTPPF20 and oxidized state of DABCO (process 7 in Scheme 1). To confirm the formation of this state, further optimizing data treatment in short delay times ( $< 1 \mu\text{s}$ ) are required.

This section concentrated on studying and discussing photoinduced processes in TPP porphyrin derivatives in the presence of electron donor, which play the roles as photocatalyst system. The next section will introduce and study photoinduced processes of a model of photosystem II, which play an important role in mimicking artificial photosynthesis.

## **5.5 Photoinduced processes in a porphyrin-imidazole-phenol compound**

### **5.5.1 Porphyrin-imidazole-phenol – a model of photosystem II**

As discussed in section 1.3.1, photoinduced mechanisms of photosystem II is a source of inspiration for the creation of artificial photosynthesis. Photoinduced processes of biomimetic models of TyrZ/His<sub>190</sub> have been reported as resulting in multisite proton-coupled electron transfer (PCET).<sup>31-36</sup> Those systems are biomimetic models of hydrogen-bonded TyrZ/His<sub>190</sub> covalently attached to chromophore molecules, which are the most precise representations of photosystem II. Thus, those biomimetic systems were designed with the purpose of observation of the PCET oxidation of hydrogen-bonded phenols. However, studying the precise mechanism of PCET in biomimetic models is a challenge. It is due to the fact that the PCET reaction is often poised to occur in one of many different mechanisms, such as: stepwise with electron transfer then proton transfer or vice versa, or by a concerted proton-coupled electron transfer, in which electron and proton transfer simultaneously. Therefore, data analysis is also complicated.

Mimicking the operation of photosystem II, a model compound involving a porphyrin sensitizer covalently attached to a hydro-bonded imidazole-phenol, which play a role as a biomimetic model for the P<sub>680</sub><sup>+</sup>/Tyr/His<sub>190</sub> in photosystem II, was synthesized and studied (Figure 5.25).<sup>36</sup> In this compound, the porphyrin macrocycle is chosen to act as P<sub>680</sub><sup>+</sup>, hydrogen-bonded imidazole-phenol serves as the TyrZ-His<sub>190</sub> pair. This model has presented successfully one-electron two-proton couple transfer with the presence of the water molecule.<sup>36</sup>

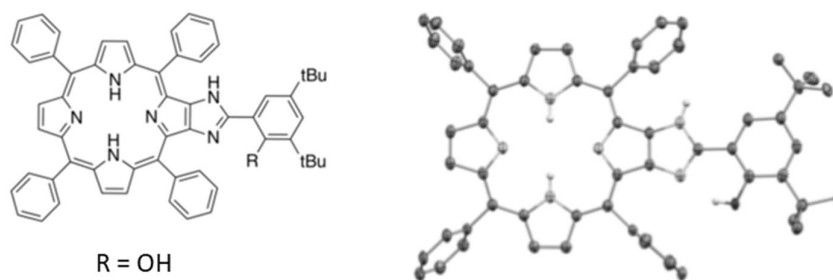


Figure 5.25. Left: Molecular drawing of porphyrin-imidazole-phenol (denoted as P-Im-ArOH), right X-ray crystal structure of P-Im-ArOH<sup>36</sup>.

The electro- and spectroelectrochemical properties of this model photosystem has also been well studied (Figure 5.26).<sup>36</sup> In Figure 5.26a, the cyclic voltammogram of P-Im-ArOH indicates two quasi-reversible oxidation processes at 0.98 and 1.40 V versus SCE. It was reported that the first oxidation process at 0.98 V is attributed to simultaneous electron oxidation of the porphyrin ring and phenol moieties. This characteristic is an interesting suggestion for us to implement an experiment with double pulse TA excitation: the expectation is to accumulate two positive charges on P-Im-Ar-OH.

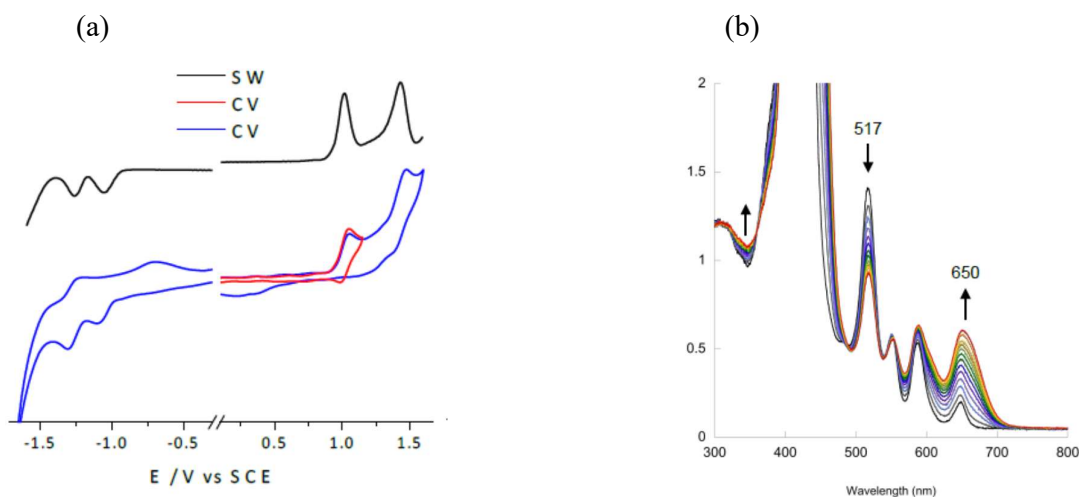
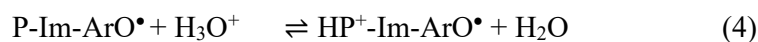
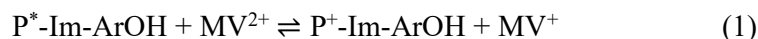


Figure 5.26. Cyclic (CV) and square wave (SW) voltammograms (a) and spectroelectrochemistry in benzonitrile/tetrabutylammonium hexafluorophosphate (0.1 M) of P-Im-ArOH<sup>38</sup>.

Indeed, photophysical processes studied by single-pulse TA spectroscopy of P-Im-ArOH with the presence of methyl viologen ( $MV^{2+}$ ), shown in the report of Aukauloo *et al* are complicated competing processes. Equations (1-5) present reaction possibilities which were

suggested by Aukauloo *et al.*<sup>37</sup>, and TA spectra could not reveal distinguishably those processes in either dry solution or wet solution.



Their study in dry solvent could indicate the formation of the  $P-\text{ImH}^+-\text{ArO}^\bullet$ . However, this result is not in accordance with the recent report of Concepcion *et al.*<sup>36</sup>, who reported a quite similar biomimetic model, using TA spectroscopy. Concepcion *et al.* have presented phenol PCET oxidation to generate  $\text{Ru}^{\text{II}}$  and  $\text{ImH}^+-\text{PhO}^\bullet$ . This was done in dry acetonitrile with  $\text{Ru}$ -phen- $\text{Im}$ - $\text{PhOH}$  model in the presence of  $\text{MV}^{2+}$ . It is important to emphasize that rigorously dry solvents are unusually implemented. The different observations in the two cited models suggested us to do experiments with thorough control conditions such as dry solvents for the expected observation of  $P-\text{ImH}^+-\text{ArO}^\bullet$  state.  $P-\text{ImH}^+-\text{ArO}^\bullet$  state will facilitate further study with second pulse laser excitation to investigate the possibility of positive charge accumulation on  $P-\text{Im}-\text{ArOH}$ .

## 5.5.2 Results and discussion

### Steady-state absorption spectroscopy

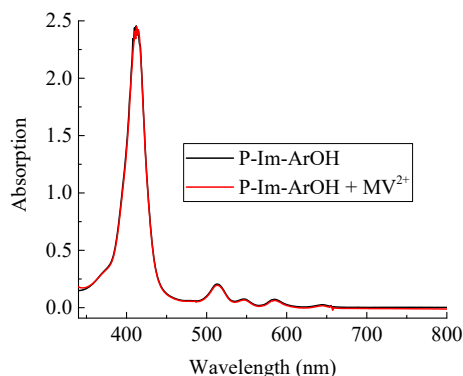


Figure 5.27. Absorption spectra of  $P-\text{Im}-\text{ArOH}$   $11 \mu\text{M}$  and  $P-\text{Im}-\text{ArOH}$  ( $11 \mu\text{M}$ ) +  $\text{MV}^{2+}$  ( $10 \text{mM}$ ) in dry argon-saturated acetonitrile.

Figure 5.27 shows the steady-state absorption spectra of P-Im-ArOH and P-Im-ArOH +  $MV^{2+}$  in dry acetonitrile. Noted that the stock solution of P-Im-ArOH was dissolved in dry benzonitrile. The absorption of P-Im-ArOH +  $MV^{2+}$  shows the identical spectral feature of P-Im-ArOH with a Soret band at 422 nm and the Q-bands at 517, 553, and 587 nm.

### Nanosecond TA spectroscopy

#### Nanosecond TA of P-Im-ArOH

Nanosecond TA study of P-Im-ArOH in dry argon-saturated acetonitrile is shown in Figure 5.28. The triplet excited state of P-Im-ArOH is presented by a band at 455 nm and the decay was fitted with a lifetime  $33 (\pm 0.6) \mu\text{s}$ .

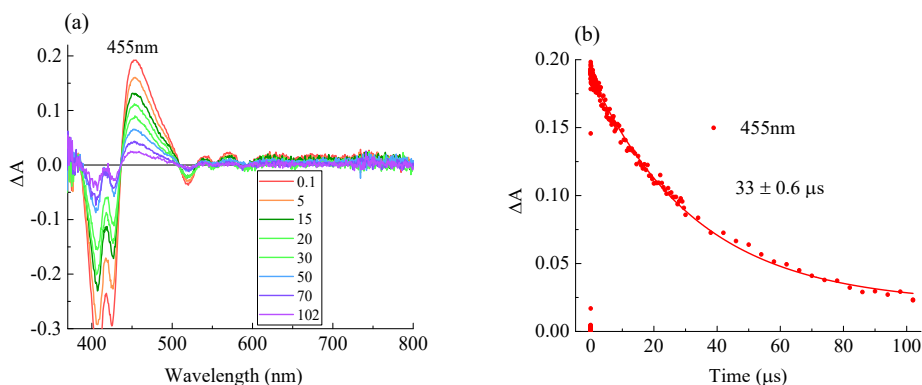


Figure 5.28. Nanosecond TA spectra (a) and kinetic trace at 455 nm (b) of P-Im-ArOH  $11 \mu\text{M}$  in dry argon-saturated acetonitrile. Absorbance of the initial solution  $A_{517 \text{ nm}} = 0.2$ ,  $\lambda_{\text{exc}} = 517 \text{ nm}$ .

#### Nanosecond TA of P-Im-ArOH and $MV^{2+}$

Nanosecond TA spectroscopy was investigated for the solution including P-Im-ArOH ( $11 \mu\text{M}$ ) and  $MV^{2+}$  ( $10 \text{ mM}$ ) in dry argon-saturated acetonitrile. Figure 5.29 describes the nanosecond TA spectra at the indicated delay times, under excitation at 517 nm. Figure 5.29a shows the characteristic band at 455 nm of the triplet excited state of P-Im-ArOH ( $^3P^3\text{-Im-ArOH}$ ) at very early delay times. This state turns to the first oxidation state of porphyrin ( $P^+\text{-Im-ArOH}$ ) simultaneously with the appearance of the first reduced state of  $MV^{2+}$  ( $MV^+$ ) at 390 and 610 nm at latter delay times ( $\approx 300 \text{ ns}$ ). Figure 5.29b indicates the bleaching band recovery at 420 nm concomitant with the decay of  $P^+\text{-Im-ArOH}$  state. The inset figure shows the comparison between the spectrum at delay time  $1 \mu\text{s}$  and the normalized spectrum at 610 nm, at delay time  $10 \mu\text{s}$ . At  $1 \mu\text{s}$ ,  $MV^+$  completely reaches its highest concentration as observed at

390 and 610 nm. The comparison of the spectra indicates that the growths of the absorption at 390 and 420 nm of the spectrum at 10  $\mu\text{s}$  are consistent with phenoxyl radical formation.<sup>36</sup> The appearance of these bands with the absence of the ground state bleach of P-Im-ArOH is similar to what was observed in the system of Ru-phen-Im-PhOH model and  $\text{MV}^{2+}$  in dry acetonitrile, reported by Concepcion *et al.*<sup>36</sup> Therefore, it is interpreted as a PCET with an oxidation of the phenol to regenerate the ground state of porphyrin and the  $\text{ImH}^+\text{-ArO}^\bullet$  phenoxyl radical in our system.

Figure 5.29c shows the relaxation of  $\text{MV}^+$ . Unexpectedly, spectra at the long delay times (Figure 5.29d) indicate the formation of mono-protonated porphyrin with the characteristic band at 430 nm<sup>37</sup>. One has to note here is that all the processes, which are described above, can be repeated in different times, except for the last stage which cannot be repeated (stage presentation in Figure 5.29d). The product of this stage can be either mono-protonated or di-protonated porphyrin, and it occurs out of our control. The appearance of protonated-porphyrin can be explained by the presence of few water molecules which are already present in the P-Im-ArOH and  $\text{MV}^{2+}$  solid. Therefore, the formation of mono- or di-protonated porphyrin is out of our control for the last stage.

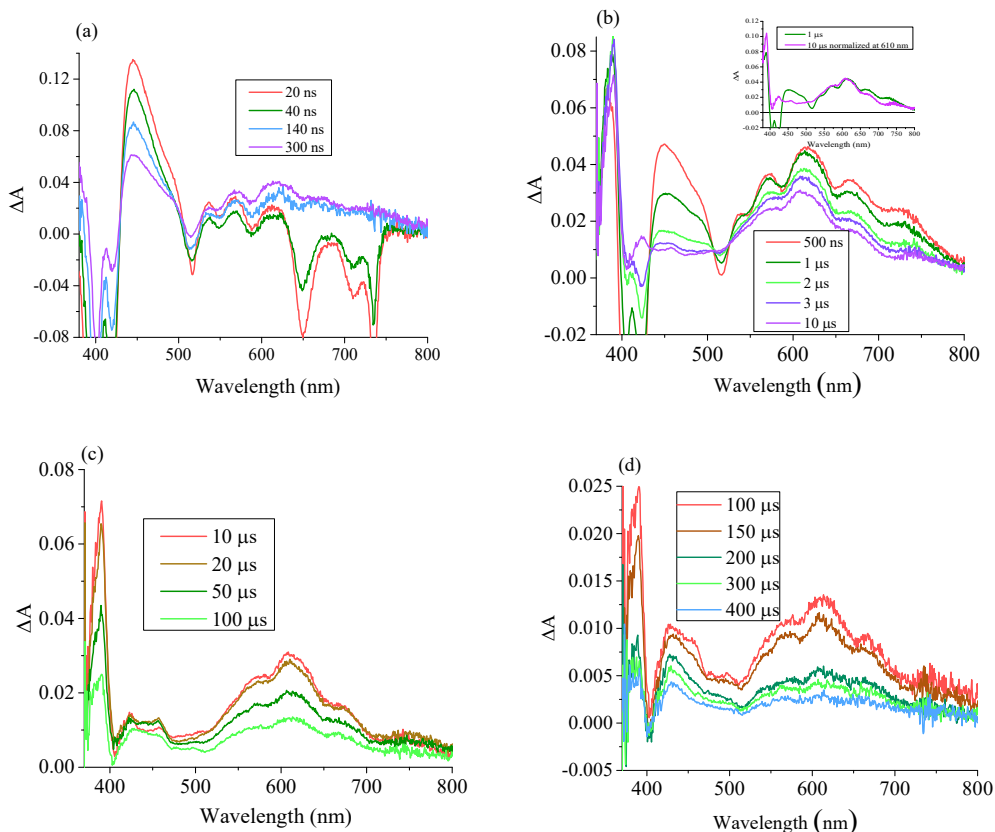
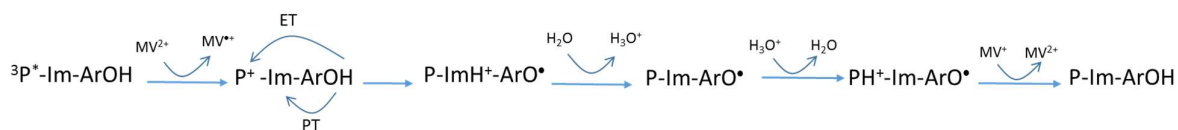


Figure 5.29. Nanosecond TA spectra of P-Im-ArOH (11  $\mu\text{M}$ ) +  $\text{MV}^{2+}$  (10 mM) in dry argon-saturated acetonitrile at indicated delay times,  $\lambda_{\text{exc}} = 517 \text{ nm}$ . Inset: normalized spectrum at 10  $\mu\text{s}$  in comparison with spectrum at 1  $\mu\text{s}$ .

Photoinduced processes of P-Im-ArOH and  $\text{MV}^{2+}$  are described in Scheme 2. Mechanism of PCET can occur in different pathways. It is not simple to precisely examine one mechanism. In this work, this question has not yet been solved.



Scheme 2. Possibilities for photoinduced processes in P-Im-ArOH +  $\text{MV}^{2+}$  in dry argon-saturated under excitation at 517 nm. Abbreviation: ET= electron transfer, PT = proton transfer

The efficiency of P-ImH<sup>+</sup>-ArO<sup>•</sup> formation can be approximately estimated to 20 % (using the concentration of  $\text{MV}^{•+}$  remaining at  $\sim 10 \mu\text{s}$ ;  $\Delta A_{605 \text{ nm}} \approx 0.03$ ,  $\epsilon_{605 \text{ nm}} \approx 1300 \text{ M}^{-1}\text{cm}^{-1}$ ). Further study by second pulse excitation at 517 nm was studied with the expectation to observe the second positive charge accumulation on P-ImH<sup>+</sup>-ArO<sup>•</sup>. Unfortunately, the results have not shown any difference between spectra of single pulse and double-pulse excitation.

In conclusion, P-Im-ArOH with the presence of electron acceptor  $\text{MV}^{2+}$  in dry argon-saturated presents a PCET process to create P-ImH<sup>+</sup>-ArO<sup>•</sup> under excitation of the porphyrin. The formation of protonated porphyrin results in the presence of a few water molecules, which are out of our control. The double-pulse excitation experiment has not indicated the accumulation of two positive charges on P-ImH<sup>+</sup>-ArOH.

## Conclusion

In summary, this chapter investigated the photoinduced processes in the photocatalyst systems of FeTPPcI, FeTPPF8OH, and ZnTPPF20 complexes and a model of photosystem II (porphyrin-Imidazole-phenol) using nanosecond TA spectroscopy. Further study with double-pulse excitation in optimized conditions needs to be done for systems involving FeTPP and  $\text{iAscH}^-$ . Spectroelectrochemistry study for ZnTPPF20 is also required to advocate for the result

observed in the pump-pump-probe experiment. Additionally, further experiments of ZnTPPF20–DABCO solution under different excitation wavelengths also has to be considered.

## REFERENCES

1. Windle, C. D.; Perutz, R. N., Advances in molecular photocatalytic and electrocatalytic CO<sub>2</sub> reduction. *Coordination Chemistry Reviews*. **2012**, *256* (21), 2562-2570.
2. Takeda, H.; Ishitani, O., Development of efficient photocatalytic systems for CO<sub>2</sub> reduction using mononuclear and multinuclear metal complexes based on mechanistic studies. *Coordination Chemistry Reviews* **2010**, *254* (3), 346-354.
3. Chueh, W. C.; Falter, C.; Abbott, M.; Scipio, D.; Furler, P.; Haile, S. M.; Steinfeld, A., High-Flux Solar-Driven Thermochemical Dissociation of CO<sub>2</sub> and H<sub>2</sub>O Using Nonstoichiometric Ceria. *Science* **2010**, *330* (6012), 1797-1801.
4. Fujita, E., Photochemical carbon dioxide reduction with metal complexes. *Coordination Chemistry Reviews* **1999**, *185-186*, 373-384.
5. Manbeck, G. F.; Fujita, E., A review of iron and cobalt porphyrins, phthalocyanines and related complexes for electrochemical and photochemical reduction of carbon dioxide. *Journal of Porphyrins and Phthalocyanines* **2015**, *19* (01-03), 45-64.
6. Tamaki, Y.; Ishitani, O., Supramolecular photocatalysts for the reduction of CO<sub>2</sub>. *ACS Catalysis* **2017**, *7* (5), 3394-3409.
7. Morris, A. J.; Meyer, G. J.; Fujita, E., Molecular Approaches to the Photocatalytic Reduction of Carbon Dioxide for Solar Fuels. *Accounts of chemical research*. **2009**, *42* (12), 1983-1994.
8. Tinnemans, A. H. A.; Koster, T. P. M.; Thewissen, D. H. M. W.; Mackor, A., Tetraaza-macrocyclic cobalt(II) and nickel(II) complexes as electron-transfer agents in the photo(electro)chemical and electrochemical reduction of carbon dioxide. *Recueil des Travaux Chimiques des Pays-Bas* **1984**, *103* (10), 288-295.
9. Gholamkhash, B.; Mametsuka, H.; Koike, K.; Tanabe, T.; Furue, M.; Ishitani, O., Architecture of Supramolecular Metal Complexes for Photocatalytic CO<sub>2</sub> Reduction: Ruthenium–Rhenium Bi- and Tetranuclear Complexes. *Inorganic Chemistry* **2005**, *44* (7), 2326-2336.
10. Sato, S.; Koike, K.; Inoue, H.; Ishitani, O., Highly efficient supramolecular photocatalysts for CO<sub>2</sub> reduction using visible light. *Photochemical & Photobiological Sciences* **2007**, *6* (4), 454-461.
11. Takeda, H.; Cometto, C.; Ishitani, O.; Robert, M., Electrons, Photons, Protons and Earth-Abundant Metal Complexes for Molecular Catalysis of CO<sub>2</sub> Reduction. *ACS Catal.* **2017**, *7* (1), 70-88.
12. Bonin, J.; Maurin, A.; Robert, M., Molecular catalysis of the electrochemical and photochemical reduction of CO<sub>2</sub> with Fe and Co metal based complexes. Recent advances. *Coordination Chemistry Reviews*. **2017**, *334* (Supplement C), 184-198.

13. Azcarate, I.; Costentin, C.; Robert, M.; Savéant, J.-M., Through-Space Charge Interaction Substituent Effects in Molecular Catalysis Leading to the Design of the Most Efficient Catalyst of CO<sub>2</sub>-to-CO Electrochemical Conversion. *Journal of the American Chemical Society*. **2016**, *138* (51), 16639-16644.
14. Costentin, C.; Robert, M.; Savéant, J.-M.; Tatin, A., Efficient and selective molecular catalyst for the CO<sub>2</sub>-to-CO electrochemical conversion in water. *Proceedings of the National Academy of Sciences*. **2015**, *112* (22), 6882-6886.
15. Rao, H.; Schmidt, L. C.; Bonin, J.; Robert, M., Visible-light-driven methane formation from CO<sub>2</sub> with a molecular iron catalyst. *Nature* **2017**, *548* (7665), 74-77.
16. Costentin, C.; Passard, G.; Robert, M.; Savéant, J.-M., Ultraefficient homogeneous catalyst for the CO<sub>2</sub>-to-CO electrochemical conversion. *Proceedings of the National Academy of Sciences* **2014**, *111* (42), 14990-14994.
17. Dhanasekaran, T.; Grodkowski, J.; Neta, P.; Hambright, P.; Fujita, E., p-Terphenyl-Sensitized Photoreduction of CO<sub>2</sub> with Cobalt and Iron Porphyrins. Interaction between CO and Reduced Metalloporphyrins. *The Journal of Physical Chemistry A* **1999**, *103* (38), 7742-7748.
18. Shediach, R.; Gray, M. H. B.; Uyeda, H. T.; Johnson, R. C.; Hupp, J. T.; Angiolillo, P. J.; Therien, M. J., Singlet and Triplet Excited States of Emissive, Conjugated Bis(porphyrin) Compounds Probed by Optical and EPR Spectroscopic Methods. *Journal of the American Chemical Society* **2000**, *122* (29), 7017-7033.
19. Rao, H.; Bonin, J.; Robert, M., Non-sensitized selective photochemical reduction of CO<sub>2</sub> to CO under visible light with an iron molecular catalyst. *Chemical Communications* **2017**, *53* (19), 2830-2833.
20. Wu, Y.; Jiang, J.; Weng, Z.; Wang, M.; Broere, D. L. J.; Zhong, Y.; Brudvig, G. W.; Feng, Z.; Wang, H., Electroreduction of CO<sub>2</sub> Catalyzed by a Heterogenized Zn-Porphyrin Complex with a Redox-Innocent Metal Center. *ACS Central science*. **2017**, *3* (8), 847-852.
21. Sonoyama, N.; Kirii, M.; Sakata, T., Electrochemical reduction of CO<sub>2</sub> at metal-porphyrin supported gas diffusion electrodes under high pressure CO<sub>2</sub>. *Electrochemistry Communications* **1999**, *1* (6), 213-216.
22. Sakuma, T.; Sakai, H.; Araki, Y.; Wada, T.; Hasobe, T., Control of local structures and photophysical properties of zinc porphyrin-based supramolecular assemblies structurally organized by regioselective ligand coordination. *Physical Chemistry Chemical Physics* **2016**, *18* (7), 5453-5463.
23. Danger, B. R.; Bedient, K.; Maiti, M.; Burgess, I. J.; Steer, R. P., Photophysics of Self-Assembled Zinc Porphyrin-Bidentate Diamine Ligand Complexes. *The Journal of Physical Chemistry A* **2010**, *114* (41), 10960-10968.
24. Liu, X.; Tripathy, U.; Bhosale, S. V.; Langford, S. J.; Steer, R. P., Photophysics of Soret-Excited Tetrapyrroles in Solution. II. Effects of Perdeuteration, Substituent Nature and Position, and Macrocycle

Structure and Conformation in Zinc(II) Porphyrins. *The Journal of Physical Chemistry A* **2008**, *112* (38), 8986-8998.

25. Hwang, I.-W.; Cho, H. S.; Jeong, D. H.; Kim, D.; Tsuda, A.; Nakamura, T.; Osuka, A., Photophysical Properties of a Three-Dimensional Zinc(II) Porphyrin Box. *The Journal of Physical Chemistry B* **2003**, *107* (37), 9977-9988.

26. Cho, H. S.; Jeong, D. H.; Cho, S.; Kim, D.; Matsuzaki, Y.; Tanaka, K.; Tsuda, A.; Osuka, A., Photophysical Properties of Porphyrin Tapes. *Journal of the American Chemical Society* **2002**, *124* (49), 14642-14654.

27. Kim, Y. H.; Jeong, D. H.; Kim, D.; Jeoung, S. C.; Cho, H. S.; Kim, S. K.; Aratani, N.; Osuka, A., Photophysical Properties of Long Rodlike Meso–Meso-Linked Zinc(II) Porphyrins Investigated by Time-Resolved Laser Spectroscopic Methods. *Journal of the American Chemical Society* **2001**, *123* (1), 76-86.

28. Cho, H. S.; Song, N. W.; Kim, Y. H.; Jeoung, S. C.; Hahn, S.; Kim, D.; Kim, S. K.; Yoshida, N.; Osuka, A., Ultrafast Energy Relaxation Dynamics of Directly Linked Porphyrin Arrays. *The Journal of Physical Chemistry A* **2000**, *104* (15), 3287-3298.

29. Galván-Miranda, E. K.; Castro-Cruz, H. M.; Arturo Arias-Orea, J.; Iurlo, M.; Valenti, G.; Marcaccio, M.; Macías-Ruvalcaba, N. A., Synthesis, photophysical, electrochemical and electrochemiluminescence properties of A2B2 zinc porphyrins: the effect of  $\pi$ -extended conjugation. *Physical Chemistry Chemical Physics* **2016**, *18* (22), 15025-15038.

30. Jonsson, M.; Houmam, A.; Jocys, G.; D. M. Wayner, D., Solvent effects on redox properties of radical ions I. *Journal of the Chemical Society, Perkin Transactions 2* **1999**, (3), 425-430.

31. Zhang, M.-T.; Irebo, T.; Johansson, O.; Hammarström, L., Proton-Coupled Electron Transfer from Tyrosine: A Strong Rate Dependence on Intramolecular Proton Transfer Distance. *Journal of the American Chemical Society* **2011**, *133* (34), 13224-13227.

32. Lachaud, F.; Quaranta, A.; Pellegrin, Y.; Dorlet, P.; Charlot, M.-F.; Un, S.; Leibl, W.; Aukauloo, A., A Biomimetic Model of the Electron Transfer between P680 and the TyrZ–His190 Pair of PSII. *Angewandte Chemie International Edition* **2005**, *44* (10), 1536-1540.

33. Hammarström, L.; Styring, S., Proton-coupled electron transfer of tyrosines in Photosystem II and model systems for artificial photosynthesis: the role of a redox-active link between catalyst and photosensitizer. *Energy & Environmental Science* **2011**, *4* (7), 2379-2388.

34. Megiatto, J. D.; Antoniuk-Pablant, A.; Sherman, B. D.; Kodis, G.; Gervaldo, M.; Moore, T. A.; Moore, A. L.; Gust, D., Mimicking the electron transfer chain in photosystem II with a molecular triad thermodynamically capable of water oxidation. *Proceedings of the National Academy of Sciences* **2012**, *109* (39), 15578-15583.

35. Manbeck, G. F.; Fujita, E.; Concepcion, J. J., Proton-Coupled Electron Transfer in a Strongly Coupled Photosystem II-Inspired Chromophore–Imidazole–Phenol Complex: Stepwise Oxidation and Concerted Reduction. *Journal of the American Chemical Society* **2016**, *138* (36), 11536-11549.

## Chapter 5

36. Chararalambidis, G.; Das, S.; Trapali, A.; Quaranta, A.; Orio, M.; Halime, Z.; Fertey, P.; Guillot, R.; Coutsolelos, A.; Leibl, W.; Aukauloo, A.; Sircoglou, M., Water Molecules Gating a Photoinduced One-Electron Two-Protons Transfer in a Tyrosine/Histidine (Tyr/His) Model of Photosystem II. *Angewandte Chemie International Edition*. **2018**, 57 (29), 9013-9017.

# Chapter 6. Time-resolved resonance Raman spectroscopic study of charge transfer reaction from Ruthenium (II) tris-bipyridine to Methyl viologen

## 6.1 Introduction

Photoinduced processes play pivotal roles in photosynthesis reactions and artificial photosynthesis system. Monitoring photoinduced processes is an essential requirement in the investigation of the kinetics and mechanism involved in artificial photosynthesis systems. To date, there is a range of different techniques which have deployed to track kinetic traces of the reactions of photosynthesis systems. Transient absorption spectroscopies have been proved as one of the best techniques in observing intermediate states utilizing information from changes in electronic structure. Using TA spectroscopies in studying mechanism of photochemical reactions are a common choice. However, in some reactions, it is tricky to get the information on different intermediates by this technique since the electronic structure changes does not accompanied by distinguishable absorption features. In those cases, time-resolved vibrational spectroscopies can provide more insight into the electronic density and structural rearrangements of the intermediate states in chemical reactions.<sup>1-2</sup> Dynamic chemical reactions can be investigated by following the modification of vibrational bands observable in Raman spectroscopy. In this chapter, another technique of time-resolved spectroscopy, nanosecond time-resolved resonance Raman spectroscopy (TR3), was then exploited to investigate vibrational structure changes due to photoinduced processes. This method is complementary to UV/Vis transient absorption and will bring new perspective to fully study the mechanism of photocatalytic reactions. To date, explanation for the mechanism reaction of photocatalytic systems still remains unclear. Using TR3 is expected to get more insight into those mechanism reactions.

At first, a model of an artificial photosynthesis system containing Ruthenium(II) Tris-bipyridine and Methylviologen in water was studied using TR3. We have succeeded in monitoring in time the vibrational structure changes in the electron transfer reaction of this system. Additionally, density functional theory (DFT) calculations were implemented using the Gaussian software suite to assist with the interpretation of the laboratory data.

**6.2 Time-resolved resonance Raman spectroscopy of the photo-induced electron transfer from Ruthenium (II) tris-bipyridine to Methylviologen (Manuscript prepared)**

Time Resolved Resonant Raman Spectroscopy  
of the Photo-induced Electron Transfer from  
Ruthenium (II) Tris-bipyridine to Methyl  
Viologen

Mark Hammond,<sup>†</sup> Thu-Trang Tran,<sup>‡</sup> Yen Hoang Hai Tran,<sup>†</sup> Minh-Huong Ha-Thi,<sup>\*†</sup> and  
Thomas Pino<sup>\*†</sup>

<sup>†</sup> *Institut des Sciences Moléculaires d'Orsay (ISMO), CNRS, Univ. Paris Sud, Université  
Paris-Saclay, 91405 Orsay, France*

<sup>‡</sup> *Faculty of Physics and Technology, Thai Nguyen University of Science, Thai Nguyen,  
Vietnam*

E-mail: minh-huong ha-thi; [thomas.pino@u-psud.fr](mailto:thomas.pino@u-psud.fr)

**Abstract**

We report the first time resolved observations of photo-induced charge transfer, measured using time resolved resonant Raman (TR3) spectroscopy, from [Ru(bpy)<sub>3</sub>]<sup>2+</sup> to methyl viologen in

Chapter 6. TR3 spectroscopic study of charge transfer reaction from  
[Ru(bpy)<sub>3</sub>]<sup>2+</sup> to MV<sup>2+</sup>

aqueous solution, showing variations in observed vibrational structure. The presence of singly charged methyl viologen in solution is noted by the appearance of several spectroscopic lines which are visible in the spectra following subtraction of reagent molecules. Assignments are confirmed using both density functional theory (DFT) calculations and literature values, and are shown to be consistent with transient absorption spectroscopy data. This presents proof-of-concept for the application of TR3 in mechanistic studies of photocatalytic systems.

### Introduction

Humanity is currently facing the threefold problem of needing to tackle climate change and the steadily increasing levels of anthropogenic CO<sub>2</sub> in Earth's atmosphere and oceans<sup>3</sup>, cease the use of fossil fuel energy sources, and produce sufficient amounts of energy for steadily increasing global demands with negligible CO<sub>2</sub> emissions<sup>4-5</sup>. Artificial photosynthesis is one of the best prospective methods for addressing all of these problems at once, but these systems are, to date, somewhat simplistic compared to the natural mechanisms which they are aiming to emulate<sup>6</sup>. While most artificial photosynthetic systems consist of little more than a photosensitizer and catalytic unit undergoing a single charge transfer at a time,<sup>7</sup> the supramolecular photosystem II mechanism used by plants is significantly more complex and efficient.<sup>8</sup> One goal in attempting to improve the efficiency of artificial photosynthesis is synchronisation of catalyst photoactivation and its consequent charge separation with reactions at the catalytic site which require multiple charge accumulations and/or transfers.<sup>9-11</sup> In order to accomplish this, a comprehensive understanding is required of the kinetics of photo-induced charge transfer and subsequent recombination of the charge transfer reaction products, and the respective timescales of these reactions.

One of the most effective and well studied photocatalysts found to date is Ruthenium (II) Tris-bipyridine [Ru(bpy)<sub>3</sub>]<sup>2+</sup>, the potential of which was first noted by Creutz and Sutin<sup>12</sup>, which shows a strong optical wavelength absorption at λ<sub>452 nm</sub>, which is attributed to a metal to ligand charge transfer (MLCT) transition. Following photoexcitation to a singlet excited state with a brief lifetime of ~ 40 fs,<sup>13</sup> the molecule may undergo intersystem crossing, trapping the excited electron in a triplet state and causing a charge separation with a significantly longer lifetime, on the order of 600 ns in aqueous media,<sup>14-15</sup> consistent with results using TR3 spectra by Henry et al.<sup>16</sup> This relatively long lived excited state is often studied in conjunction with an electron acceptor, the methyl viologen dication, in a photo-induced charge transfer reaction,<sup>17</sup> thus;



*Chapter 6. TR3 spectroscopic study of charge transfer reaction from  $[Ru(bpy)_3]^{2+}$  to  $MV^{2+}$*

The methyl viologen dication, also known as N,N0-dimethyl-4,40-bipyridinium or  $(C_6H_7N)_2^{2+}$  and referred to hereafter as  $MV^{2+}$ , has long been of interest in photochemical systems as an electron relay,<sup>18</sup> and functionalised forms of it have been used effectively in some artificial photosynthesis systems.<sup>19</sup> Also interesting is its singly charged radical cation form, which can be easily identified in optical studies due to its strong absorption bands at 398 and 603 nm,<sup>20</sup> allowing an easy way to monitor the concentration of  $MV^+$  in solution with respect to time using transient absorption spectroscopy, a technique which is very useful in monitoring energy transfer in molecular systems.<sup>21</sup> Further charge accumulation on  $MV^+$  has also been successfully investigated using a pump-pump-probe technique, to create  $MV^0$ .<sup>22</sup> The basic reaction in equation 1, while seemingly straightforward, has a strong competing factor in the form of a rapid back reaction between  $MV^+$  and  $[Ru(bpy)_3]^{3+}$ , making observation of  $MV^+$  challenging under non-ideal conditions.<sup>23</sup> Therefore, to be useful in a real world scenario, the addition of a sacrificial electron donor is required to replenish the oxidised catalyst and prevent electron transfer from proceeding in the reverse direction, though this is considered a cumbersome solution,<sup>24</sup> and better mechanisms are being sought out.

Photoinduced processes play a pivotal role in photosynthesis, and consequently in the artificial photosynthesis which seeks to emulate it. Monitoring these processes to help understand their dynamics and mechanisms is vital to a comprehensive understanding of how artificial photosynthesis systems work and may be improved. To date, numerous techniques have been employed to this effect, including time resolved transient absorption spectroscopy which has proven to be very useful in tracking the kinetic changes occurring in reaction mixtures. However, transient absorption spectroscopy necessarily uses electronic transitions which tend to be broad and structureless in solution, which do not give sufficient information to investigate structural changes and/or intermediate states. Time resolved vibrational spectroscopy techniques are an ideal way of finding this required information, giving observation of changes in molecular structures over time.

To date, the precise mechanism of photocatalytic systems still requires further study for a definitive understanding. This work studies the aqueous reaction mixture of  $[Ru(bpy)_3]^{2+}$  with  $MV^{2+}$  under laser irradiation, using nanosecond time resolved resonant Raman (TR3) spectroscopy to investigate changes in vibrational structure due to photoinduced processes. This has the potential to be a very powerful technique in the study of photocatalytic reaction mechanisms.

*Chapter 6. TR3 spectroscopic study of charge transfer reaction from  
[Ru(bpy)<sub>3</sub>]<sup>2+</sup> to MV<sup>2+</sup>*

Spectra are presented of the reaction in progress, acquired using a pump-probe setup (with  $\lambda_{\text{pump}} = 460$  nm and  $\lambda_{\text{probe}} = \sim 355$  nm) to measure the reaction at several intervals on microsecond timescales. These spectra show changes in vibrational structure of the spectra as a function of time, highlighting the electron transfer dynamics of this system. In addition, density functional theory (DFT) calculations were performed using the Gaussian software suite<sup>25</sup> to assist with interpretation of the laboratory data. Further details on both experimental and theoretical techniques are available as supplementary information.

## **Results**

Time-Resolved Resonant Raman (TR3) data are presented in figure 1, following background removal (subtraction of baseline and H<sub>2</sub>O spectrum). Two other sets of experimental data are also used in this study, and these are available as supporting information. The 2800–3700 cm<sup>-1</sup> region of these spectra has a significantly reduced signal-to-noise ratio following subtraction of the broad and extremely high intensity water band, and consequently this region is not considered in this analysis. MV<sup>2+</sup> is at high concentration in the solution being examined, dominating the remaining spectra of the reaction mixture, with the strongest bands found at 660, 838, 1194, 1236, 1302, 1541, 1658, 2836, and 2974 cm<sup>-1</sup>. Alongside these expected bands, several other small bands are seen to rise and fall over time, most notably at 739, 1428, and 2876 cm<sup>-1</sup>, attributed to molecular species being created and destroyed during the course of the reaction. These bands of interest are observed to rise in intensity, reaching maxima around  $\sim 0.5 - 3$   $\mu\text{s}$ .

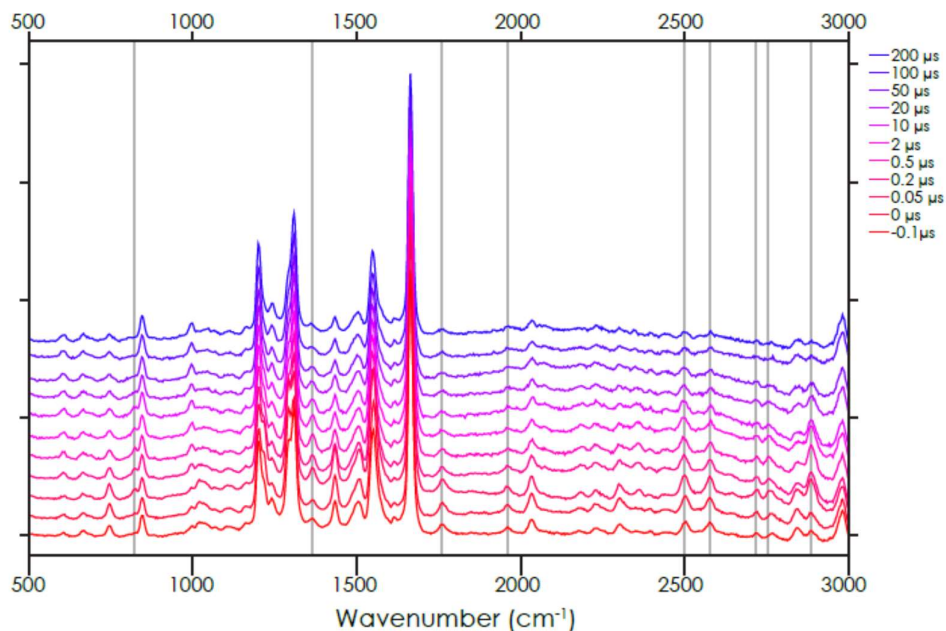
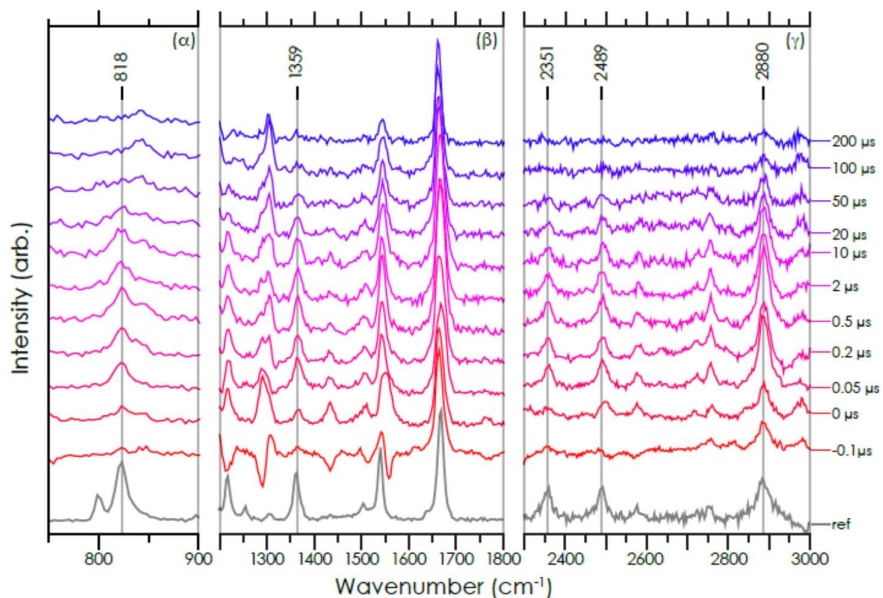


Figure 1: Time-Resolved Resonant Raman (TR3) spectra ( $\lambda_{\text{pump}} = 460 \text{ nm}$  and  $\lambda_{\text{probe}} = \sim 55 \text{ nm}$ ) on an aqueous solution of  $[Ru(bpy)_3]^{2+}$  ( $\sim 42 \mu\text{M}$ ) and  $MV^{2+}$  ( $\sim 20 \text{ mM}$ ), taken at a series of microsecond-timescale intervals following excitation. Presented here is dataset c (high resolution,  $-0.1$ – $200 \mu\text{s}$ ), with datasets a and b available as supporting information. The spectra are dominated by strong bands arising due to  $MV^{2+}$ , but some clear evolution over time is apparent in some weaker bands, which have been highlighted for clarity.

### Singly charged methyl viologen



*Chapter 6. TR3 spectroscopic study of charge transfer reaction from  
[Ru(bpy)<sub>3</sub>]<sup>2+</sup> to MV<sup>2+</sup>*

Figure 2: Time resolved bands assigned to MV<sup>+</sup> at 818, 1359, 2351, 2489, and 2880 cm<sup>-1</sup>. A laboratory reference spectrum of MV<sup>+</sup> is also included for comparison.

The behavior of MV<sup>+</sup> is the main point of interest in this study, and several Raman bands due to this molecule can be seen in the data recorded. The spectra presented in figure 2 are shown following subtraction of the MV<sup>2+</sup> spectrum at t = 0, and the [Ru(bpy)<sub>3</sub>]<sup>2+</sup> spectrum at the same respective time intervals. Unfortunately, a perfect subtraction is not feasible with these data, and regions underlying the strong MV<sup>2+</sup> bands are not reliably free of contamination.

Five highlighted bands at 818, 1359, 2351, 2489, and 2880 cm<sup>-1</sup> are unambiguously assigned to MV<sup>+</sup> using a combination of literature reference values and DFT calculations; these values are mean averages taken over three laboratory experiments. See table 1. Also presented in figure 2 is a resonant Raman spectrum of pure MV<sup>+</sup>, acquired from a chemically reduced sample of MV<sup>2+</sup>.

Table 1: Peaks observed in laboratory recorded TR3 spectra assigned to MV<sup>+</sup>, with scaled DFT values for comparison, calculated at O3LYP/cc-pVTZ. Bands in the TR3 data with minimal contamination are highlighted in bold, with wavenumber values from datasets a, b, and c. Literature values, for comparison, are taken from <sup>α</sup>Feng & Cotton (1986),<sup>β</sup>Forster et al (1982),<sup>γ</sup>Poizat et al (1984).<sup>δ</sup> All values are given in wavenumbers (cm<sup>-1</sup>).

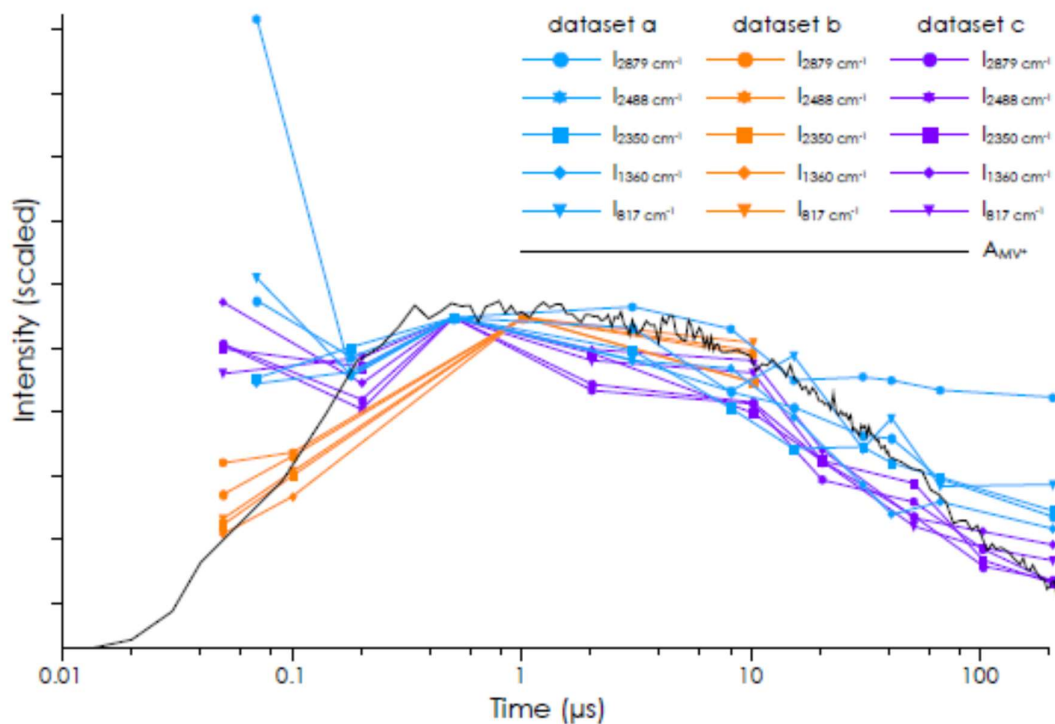
Singly Charged Methyl Viologen, MV <sup>+</sup>				
TR3	DFT	Lab ref	Lit ref	Assignment
685	669	688	682 <sup>α,β,δ</sup>	Axial whole molecule
817 <sup>a</sup> , 814 <sup>b</sup> , 823 <sup>c</sup>	806	800,824	818 <sup>α,β,δ</sup>	stretch ring breathing
1214	1189,1198	1219	1212 <sup>α,β</sup> ,1210 <sup>δ</sup>	N-CH3 str
1282	1237	1255,1307	1250 <sup>δ</sup>	C-H in plane bend
<b>1360<sup>a</sup>, 1351<sup>b</sup>, 1365<sup>c</sup></b>	1333, 1339	1363	1363 <sup>β</sup> , 1357 <sup>δ</sup>	C-C central str
1425	1440	1435	1430 <sup>α,δ</sup>	C-N stretch
1502	1493	1505	1499 <sup>α</sup>	C-C out of plane bend
1545	1511	1541	1534 <sup>α,β,δ</sup>	C-H in plane stretch
1658	1656	1669	1662 <sup>α,β</sup> , 1660 <sup>δ</sup>	C-C sym str
<b>2350<sup>a</sup>, 2344<sup>b</sup>, 2358<sup>c</sup></b>		2355		N-CH3 (overtone)
<b>2488<sup>a</sup>, 2484<sup>b</sup>, 2886<sup>c</sup></b>		2491		C-H in plane (overtone)
<b>2879<sup>a</sup>,2874<sup>b</sup>, 2886<sup>c</sup></b>	2914	2886		C-H aliph sym
3016	3072	3025		C-H arom str

Further support for the assignment of the four specific bands to MV<sup>+</sup> can be made by comparing their observed intensities with transient absorption data. Figure 3 presents a measured transient absorption curve recorded in the optical wavelength range, using the broad absorption band centred at approximately ~600 nm. This shows variation of absorption (and

*Chapter 6. TR3 spectroscopic study of charge transfer reaction from  $[\text{Ru}(\text{bpy})_3]^{2+}$  to  $\text{MV}^{2+}$*

therefore concentration) of  $\text{MV}^+$  over time. Also presented on this figure are measured TR3 intensities for the five bands assigned to methyl viologen, from the three separate datasets, with intensities scaled to the datapoint closest to 0.5  $\mu\text{s}$ .

Overall, a good match is seen between the Raman and optical intensities. Some discrepancy is noted in dataset (a), shown in blue, at longer timescales, particularly the longest at 200  $\mu\text{s}$ . This is particularly the case for the combination band at 2488  $\text{cm}^{-1}$ . This is due to the weak intensities of these bands at timescales where only a very small concentration of  $\text{MV}^+$  remains in solution. Dataset (c), shown in violet, shows the same reaction with improved signal-to-noise, eliminating this problem. Another discrepancy seen in datasets (a) and (c) is excess emission at very short timescales, 0.07  $\mu\text{s}$  and 0.05  $\mu\text{s}$ , respectively. The reason for this is not entirely clear, but it is possibly due to some contribution from excited forms of  $[\text{Ru}(\text{bpy})_3]^{2+}$  at these short timescales. This is consistent with the measured fluorescence lifetime for  $[\text{Ru}(\text{bpy})_3]^{2+}$  of 850 ns.<sup>29</sup> This does not appear to be the case for dataset (b), for which the discrepancy observed in the peak intensities at 0.05  $\mu\text{s}$  are due to relatively weak band intensities, as with dataset (a) at 200  $\mu\text{s}$ .



Chapter 6. TR3 spectroscopic study of charge transfer reaction from  
[Ru(bpy)<sub>3</sub>]<sup>2+</sup> to MV<sup>2+</sup>

Figure 3. Transient absorption curve plotted against varying intensities of the MV<sup>+</sup> bands taken from the three datasets. Band intensities are measured from bands at 818, 1359, 2351, 2489, and 2880 cm<sup>-1</sup>, as shown in figure 2.

### Discussion

Definitive spectroscopic assignments in this study are challenging, but the molecules being observed have certain structural differences which give rise to characteristic spectroscopic features. For example, all [Ru(bpy)<sub>3</sub>]<sup>n+</sup> complexes show a broad band at ~1000 cm<sup>-1</sup> due to stretching modes of the Ru–N bond, and all forms of methyl viologen show clear features in the ~2800-2900 cm<sup>-1</sup> region due to aliphatic C–H stretches from methyl groups. Density Functional Theory (DFT) calculations (O3LYP/cc-pVTZ) on the two charge states of interest of methyl viologen, MV<sup>2+</sup> and MV<sup>+</sup>, also show a clear structural difference in that the MV<sup>2+</sup> molecule is found to have a twisted structure (consistent with existing literature<sup>30-31</sup>) with the two component pyridine rings being offset by a dihedral angle of approximately 45°, while the MV<sup>+</sup> molecule is planar. Consequently, there are some notable differences in the spectra of the two different charge states of methyl viologen, though not all of these differences are easy to discern in the TR3 data. The spectrum of MV<sup>+</sup> is also seen to have a higher Raman activity than that of MV<sup>2+</sup>, in both calculated and laboratory spectra, assisting in its identification despite lower concentrations.

The bands assigned here as unambiguously due to MV<sup>+</sup> are found to be a good match with laboratory data of MV<sup>+</sup> and are not coincident with any other species in the reaction mixture. Other MV<sup>+</sup> bands may show some contamination from other molecular species present in solution and/or are weak enough to be indiscernible above the level of noise. For example, a weak band of MV<sup>+</sup> at 1026 cm<sup>-1</sup> has been previously observed in aqueous solution,<sup>22</sup> but in the data presented here, this band cannot be distinguished from the Ru–N band of [Ru(bpy)<sub>3</sub>]<sup>n+</sup> at ~1021 cm<sup>-1</sup>. All bands assigned to MV<sup>+</sup> are presented in table 1. Using DFT calculations, the band at ~1359 cm<sup>-1</sup> (figure 2α) is assigned to a stretching mode of the central C–C bond of the molecule, and the 2880 cm<sup>-1</sup> band (figure 2γ) is due to symmetric C–H stretching on the methyl groups. The latter band is not observed in the laboratory spectrum of pure MV<sup>2+</sup> where the two aliphatic C–H stretching modes lie at 2836 and 2969 cm<sup>-1</sup>. The other two bands at 2351 and 2489 cm<sup>-1</sup> (figure 2β) are not fundamental vibrational transitions, as none are predicted in any methyl viologen molecule between ~1700-2800 cm<sup>-1</sup>. These two bands can therefore be

*Chapter 6. TR3 spectroscopic study of charge transfer reaction from  
[Ru(bpy)<sub>3</sub>]<sup>2+</sup> to MV<sup>2+</sup>*

tentatively assigned as overtone bands of the N–CH<sub>3</sub> stretch at 1214 cm<sup>-1</sup> and the C–H in plane bending mode at 1282 cm<sup>-1</sup> respectively.

The [Ru(bpy)<sub>3</sub>]<sup>3+</sup> molecule is predicted to also be present in the reaction mixture, existing simultaneously with MV<sup>+</sup>. DFT calculations (X3LYP/3-21G) provide a good match with laboratory spectra after scaling, but also predict very little difference between the spectra of [Ru(bpy)<sub>3</sub>]<sup>2+</sup> and [Ru(bpy)<sub>3</sub>]<sup>3+</sup> making definitive assignments of the latter molecule a challenge. The main difference between the calculated spectra of these molecules is that [Ru(bpy)<sub>3</sub>]<sup>3+</sup> appears to show fewer vibrational modes, with nearly all being weaker in Raman intensity. However, this theory level is quite low in order for calculations to complete in a feasible amount of time, and only fundamental vibrations can be calculated. A few bands are present in the recorded spectra, at 753, 1021, 1107, 1214, 1658, and 3071 cm<sup>-1</sup>, which do not appear to match those of any other molecule expected to be present. Weak bands at 1107 and 3071 cm<sup>-1</sup> appear to be due to [Ru(bpy)<sub>3</sub>]<sup>3+</sup>. Both [Ru(bpy)<sub>3</sub>]<sup>2+</sup> and [Ru(bpy)<sub>3</sub>]<sup>3+</sup> are expected to contribute to the broad, weak band at ~1022 cm<sup>-1</sup>, due to Ru–N stretching modes (together with some contribution from MV<sup>+</sup>, as mentioned above). Additionally, weak bands observed at 753, 1214, and 1658 cm<sup>-1</sup> have a fair match with DFT calculated values. These bands are difficult to observe, however, due to [Ru(bpy)<sub>3</sub>]<sup>3+</sup> having much lower Raman intensities than MV<sup>+</sup>.

Also worth noting is that the calculated spectrum of [Ru(bpy)<sub>3</sub>]<sup>2+\*</sup> (i.e. [Ru(bpy)<sub>3</sub>]<sup>2+</sup> in its triplet excited state) shows both several differences and significantly higher Raman activity when compared with the spectra of other ruthenium tris-bipyridine complexes. This spectrum has a high density of states, and is dominated by two very strong bands, the Ru–N stretch predicted at 962 cm<sup>-1</sup> and the C–C asymmetric stretch predicted at 1488 cm<sup>-1</sup>. These most likely contribute to the broad 1022 cm<sup>-1</sup> complex, and the strong complex of bands in the 1400-1700 cm<sup>-1</sup> range. No distinct bands can be discerned from the data recorded in this study, but this molecule may contribute to the increased intensity of these regions observed at the shortest timescales.

The timescales and kinetics of charge transfer in this study can be inferred from the weak bands in the spectrum which vary over time. Using the transient absorption curve in figure 3, we can deduce that bands which follow this behaviour, with maxima around 0.5-3 μs, are products of the charge transfer reaction shown in equation 1, i.e. between MV<sup>+</sup> and [Ru(bpy)<sub>3</sub>]<sup>3+</sup>. At timescales longer than ~3 μs, the MV<sup>+</sup> bands are seen to decrease in intensity, coincident with its expected recombination into MV<sup>2+</sup>, via the back reaction;

*Chapter 6. TR3 spectroscopic study of charge transfer reaction from [Ru(bpy)<sub>3</sub>]<sup>2+</sup> to MV<sup>2+</sup>*



DFT energy calculations (X3LYP/3-21G) corrected using the conductor-like polarized continuum model (CPCM) and adjusted for thermal effects can confirm the energetics of these reaction. The reaction in equation 1 is predicted to be weakly exothermic, with  $\Delta E = -0.5497$  eV. The back reaction in equation 2 returns the  $[\text{Ru}(\text{bpy})_3]^{2+}$  molecule to its singlet ground state, predicted to be 2.1307 eV lower in energy than the excited triplet state in the initiating reaction, and consequently this second reaction is more strongly exothermic with  $\Delta E = -1.4721$  eV. This back reaction is therefore likely to occur readily wherever possible. The physical quantity of  $\text{MV}^+$  created in this experiment can be calculated using the Beer-Lambert law in combination with the unscaled transient absorption data (see figure 3). Taking the molar extinction coefficient,  $\epsilon$ , for  $\text{MV}^+$  to be  $13700 \text{ M}^{-1}\text{cm}^{-1}$  in water, the maximum concentration formed during this experiment is calculated to be  $47.43 \mu\text{M}$  at  $\sim 0.4 \mu\text{s}$  reducing in concentration exponentially over time, until a concentration approaching zero is observed by  $\sim 300 \mu\text{s}$ . This relatively slow decay indicates that the back reaction occurs on much longer timescales, approximately 2.5 orders of magnitude greater than the excitation time. It can be rationalized by the highly dilute quantity of  $\text{MV}^+$  produced during the reaction and the diffusion-limited nature of the back reaction process.

This study gives firm confirmation of the photoinduced charge transfer process from ruthenium (II) tris-bipyridine ( $[\text{Ru}(\text{bpy})_3]^{2+}$ ) to methyl viologen under pump-probe laboratory conditions, and helps to elucidate upon the kinetics of this process. We find that the reduced form of methyl viologen,  $\text{MV}^+$ , is at its highest concentration near  $0.5\text{--}3 \mu\text{s}$ , while recombination is an order of magnitude slower, due to the process being diffusion limited. This molecule can be easily detected due to the high Raman activity of its molecular vibrations. The other component in this reaction,  $[\text{Ru}(\text{bpy})_3]^{3+}$ , is much harder to detect due to its weaker spectrum. No evidence is found of any other molecular species resulting from this reaction. Our results provide a powerful method for investigation of photocatalytic processes, from simple mechanisms to potentially much more complex molecular systems. As research on photocatalytic systems, particularly in the context of artificial photosynthesis and solar energy production, is currently an area of intensive research, this technique may prove extremely useful in future studies, where time resolved observations of vibrational structures are required.

### **Acknowledgement**

*Chapter 6. TR3 spectroscopic study of charge transfer reaction from  
[Ru(bpy)<sub>3</sub>]<sup>2+</sup> to MV<sup>2+</sup>*

We acknowledge the use of the computing center MÃalsoLUM of the LUMAT research federation (FR LUMAT 2764). T.-T.T. is grateful to the Vietnamese government for the scholarship (2016-2019). M.H. is grateful for financial support through the "Make Our Planet Great Again" French program, supported by the Centre National de la Recherche Scientifique (CNRS)

**Supporting Information Available**

The following files are available free of charge.

- Experimental and Theoretical Methods, and Additional Data

**SUPPORTING INFORMATION**

**Laboratory Methods and Data**

**Experimental Setup**

Time resolved resonant Raman (TR3) spectroscopy is an excellent technique for analysing vibrational dynamics and structure in chemical and biological systems. A TR3 pump-probe setup has been constructed for these experiments, capable of nanosecond time resolution. A pulsed Nd:YAG optical parametric oscillator (OPO) laser is used as the pump, operating at 10Hz and tunable between 210 – 2500 nm with a pulse duration of ~4 ns and timing jitter of < 2 ns. For the probe, a pulsed InnoLas SpitLight Standard 600 laser is used, with a pulse duration of 6 – 7 ns and a repetition rate of 10Hz, set to an excitation wavelength of 355 nm. The timing of these lasers, independently variable, is synchronised by electronic control so the probe can achieve maximum efficiency. Scattered light from the probe is gathered using a charge-coupled device (CCD) detector. The separate wavelengths of the two lasers allow optimisation to achieve the best resonance enhancement for the collected Raman signal, with the pump causing excitation and generating intermediate species and charge transfer products, which are then recorded using the probe. For each sample, a probe-only measurement is made to obtain a ground state Raman spectrum, and a pump-only measurement is made to obtain and subtract background fluorescence of the sample being examined. A pump-probe spectrum is then acquired for each time interval.

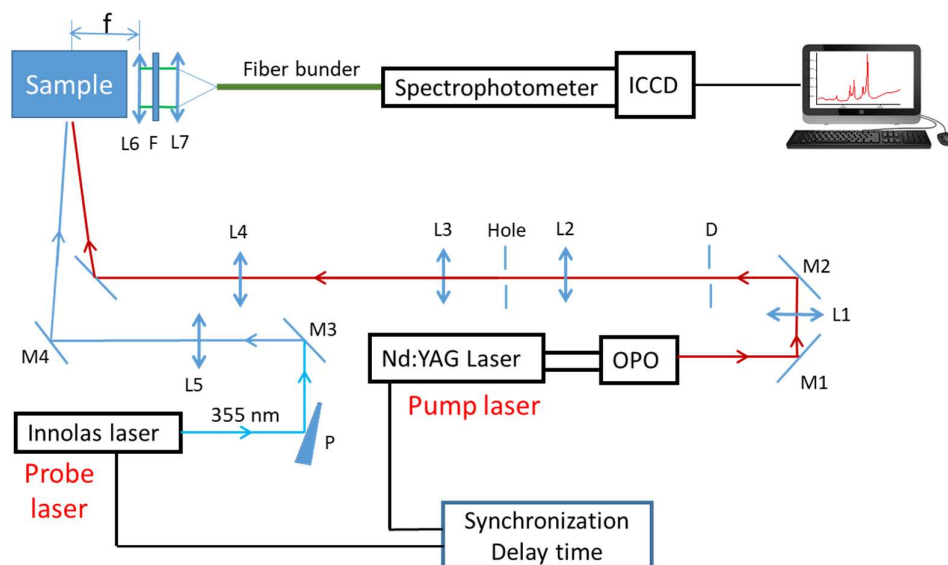


Figure 1: Schematic diagram of the experimental setup, as described in the text.

A schematic of the experimental setup is given in figure 1. In this configuration, the pump laser is reflected off mirror M1 through lens L1 to collimate the beam. This then reflects off mirror M2 and through a diaphragm, D, into lens L2 to obtain a homogeneous beam. This beam is then passed through lenses L3 and L4 to enter the sample. The probe laser is reflected off a prismatic window, P, reflecting 4% of the total laser power. This then reflects off mirror M3 (with a reflectance maximum at 355 nm), before being focussed through lens L5 and reflected off mirror M4 into the sample. The two beams are aligned to overlap on the sample, and scattered light is collected using a fibre coupled spectrophotometer.

#### Data Analysis

Data acquired from the laboratory apparatus were analysed using the QTIplot1 and fityk2 software packages. Each dataset consists of two resonance spectra (water, and  $\text{MV}^{2+}$  in water), and two sets of time resolved spectra  $[\text{Ru}(\text{bpy})_3]^{2+}$  in water, and  $[\text{Ru}(\text{bpy})_3]^{2+}$  and  $\text{MV}^{2+}$  in water). The same procedure was used to treat each spectrum. First, the x-axis is converted from wavelength units to wavenumber units using a spectroscopic measurement of the laser wavelength as a reference. Baseline removal is then performed by subtracting a spline function, fit to clean regions of the spectrum at 470, 920, 1850, and 4470  $\text{cm}^{-1}$ . Finally, the y-axis is scaled to match the peak intensity of the water band at 3447  $\text{cm}^{-1}$ , before subtracting the water signal. This provides a resonance Raman spectrum of pure  $\text{MV}^{2+}$  and time resolved spectra of  $[\text{Ru}(\text{bpy})_3]^{2+}$ , and  $[\text{Ru}(\text{bpy})_3]^{2+}$  with  $\text{MV}^{2+}$  (including spectroscopic features of any

*Chapter 6. TR3 spectroscopic study of charge transfer reaction from  $[\text{Ru}(\text{bpy})_3]^{2+}$  to  $\text{MV}^{2+}$*

photoproducts). At each time interval, the spectrum of  $[\text{Ru}(\text{bpy})_3]^{2+}$  is then subtracted from  $[\text{Ru}(\text{bpy})_3]^{2+}$  with  $\text{MV}^{2+}$ , leaving a time resolved set of spectra for  $\text{MV}^{2+}$  with photoproducts. Finally, the resonance Raman spectrum of  $\text{MV}^{2+}$  is subtracted from these time resolved spectra, yielding a residual spectrum showing bands which are due to photoproducts, such as  $\text{MV}^+$  and  $[\text{Ru}(\text{bpy})_3]^{3+}$ , showing several bands in common with the spectrum of pure  $\text{MV}^+$ , as shown in figure 11.

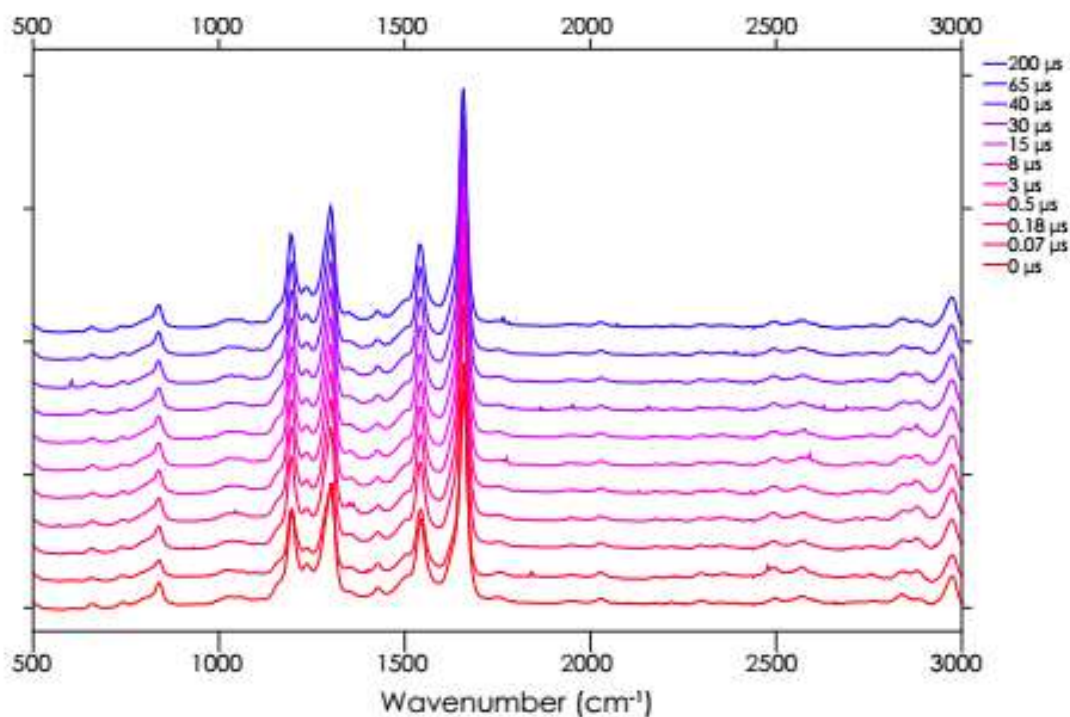


Figure 2: TR3 spectra of the full reaction mixture for dataset a.

Chapter 6. TR3 spectroscopic study of charge transfer reaction from  $[Ru(bpy)_3]^{2+}$  to  $MV^{2+}$

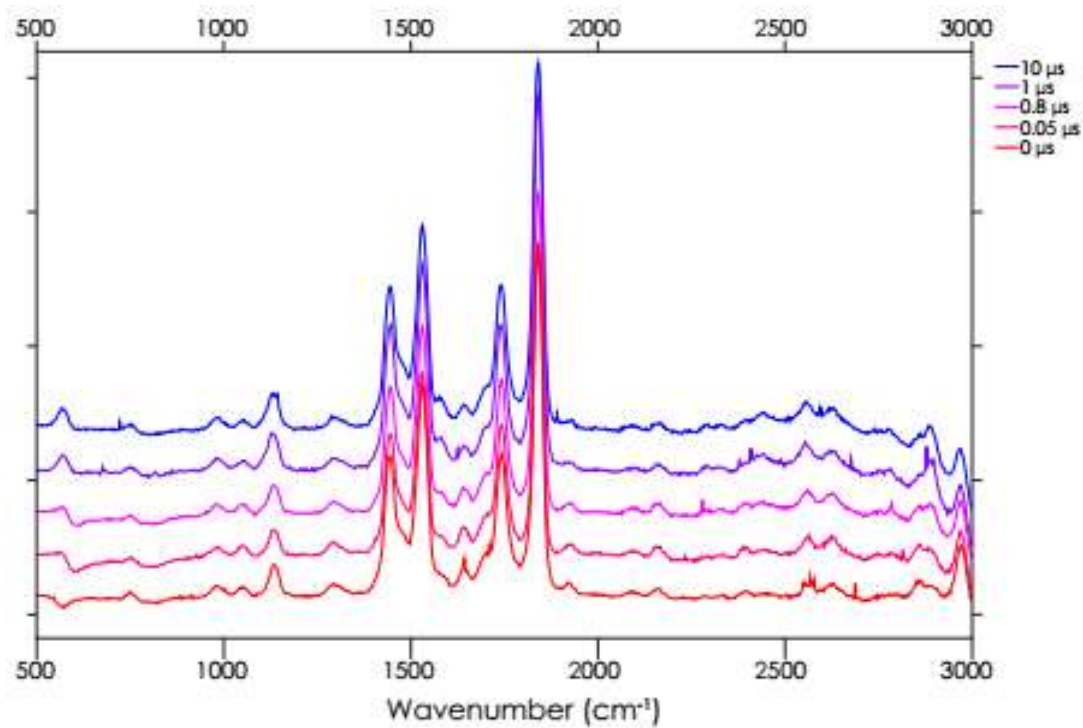


Figure 3: TR3 spectra of the full reaction mixture for dataset b.

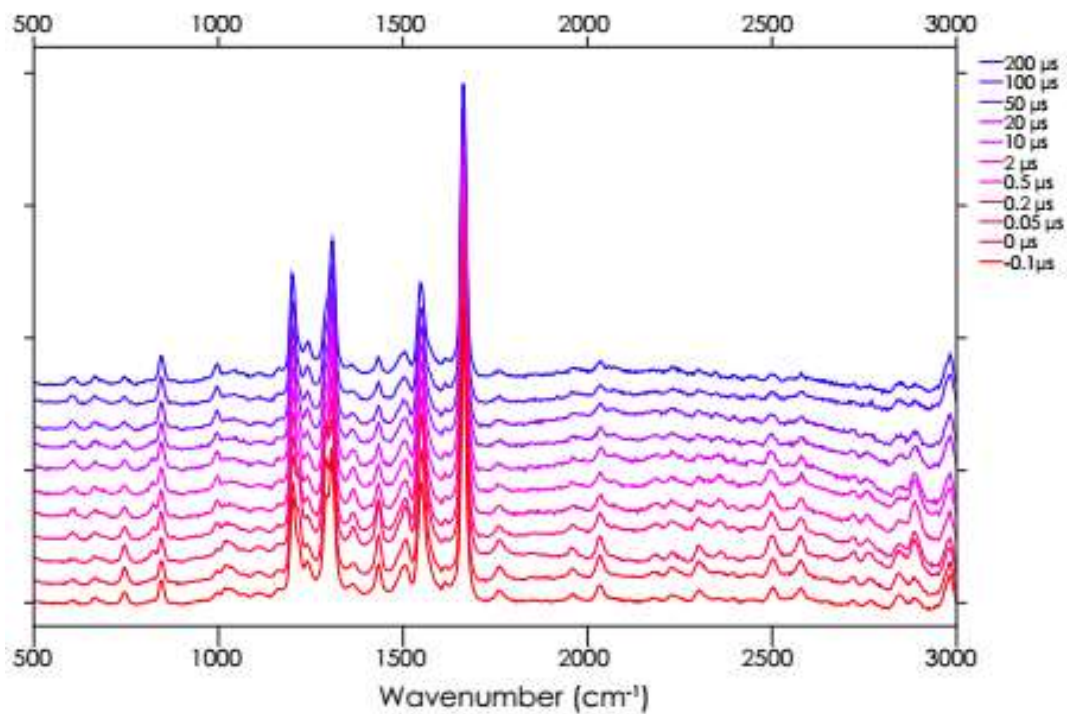


Figure 4: TR3 spectra of the full reaction mixture for dataset c

Chapter 6. TR3 spectroscopic study of charge transfer reaction from  $[Ru(bpy)_3]^{2+}$  to  $MV^{2+}$

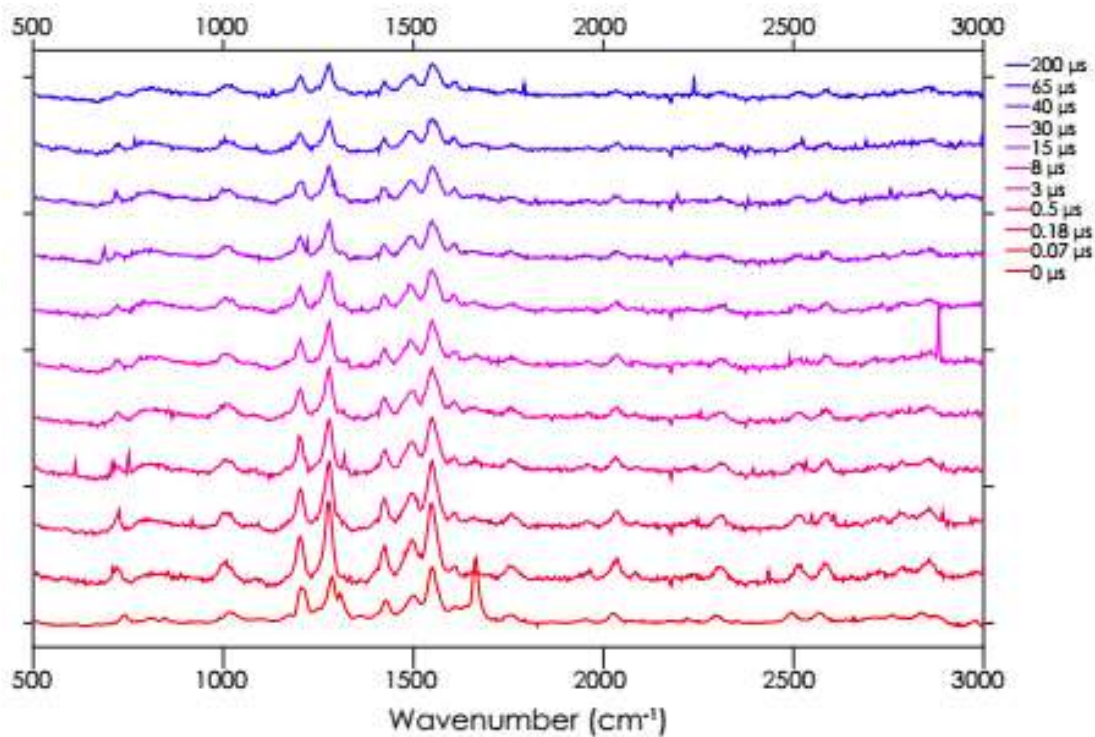


Figure 5: TR3 spectra of  $[Ru(bpy)_3]^{2+}$  for dataset a

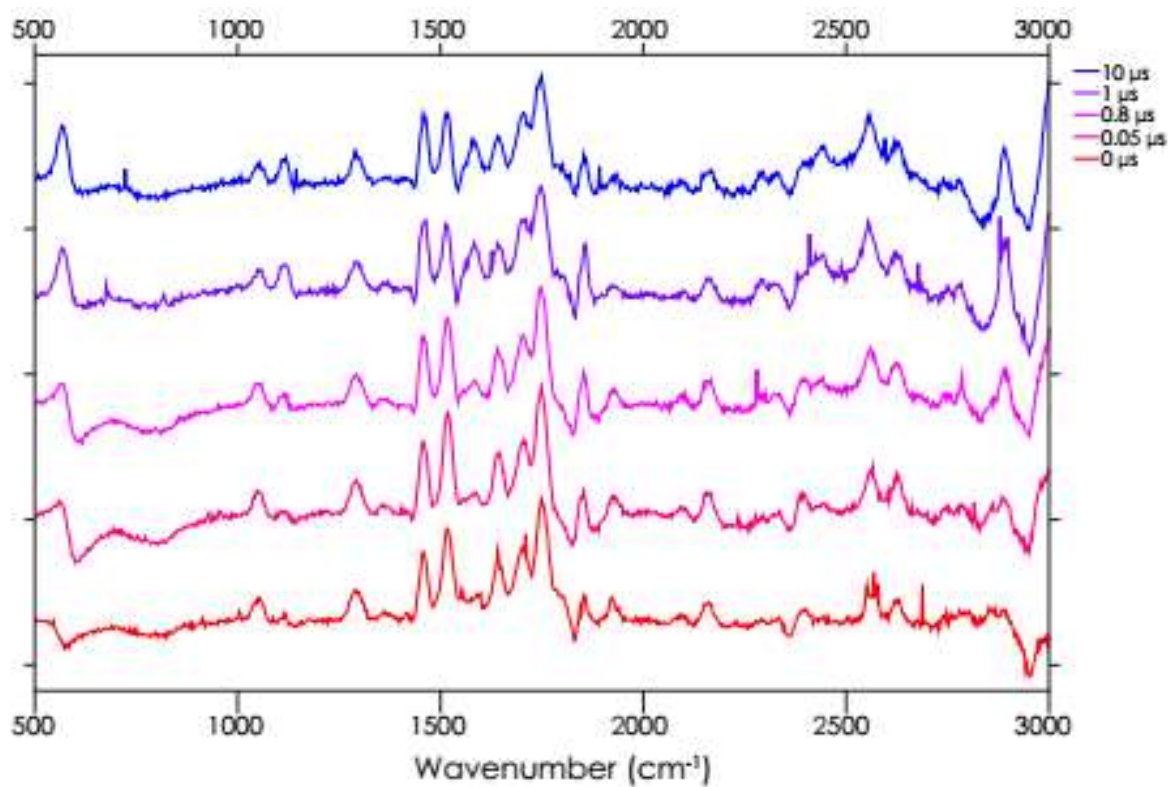


Figure 6: TR3 spectra of  $[Ru(bpy)_3]^{2+}$  for dataset b

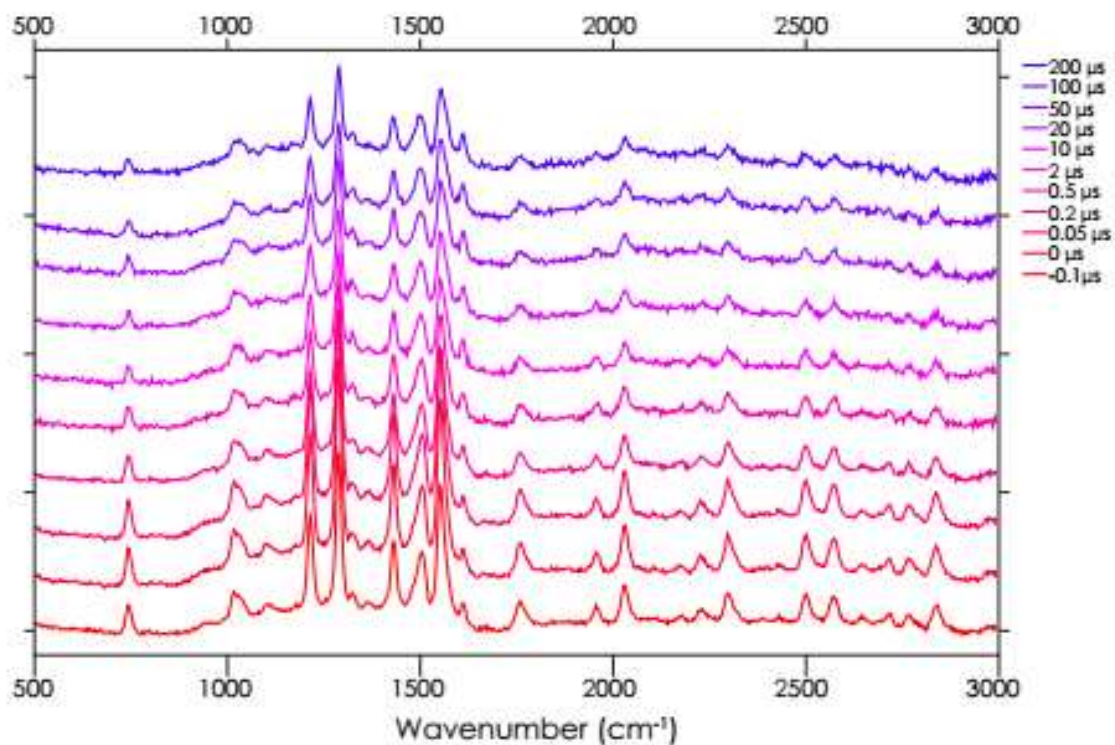


Figure 7: TR3 spectra of  $[\text{Ru}(\text{bpy})_3]^{2+}$  for dataset c.

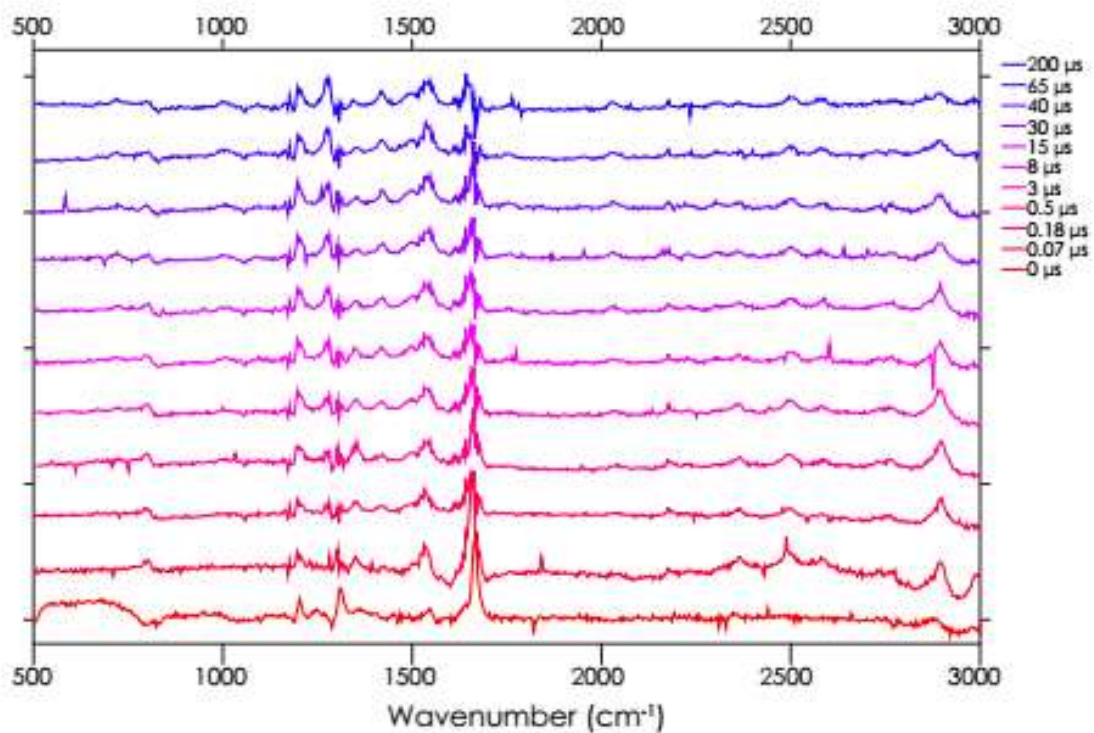


Figure 8: TR3 spectra of the residuals, following subtraction of time resolved  $[\text{Ru}(\text{bpy})_3]^{2+}$  spectra and resonant Raman spectrum of  $\text{MV}^{2+}$ , for dataset a.

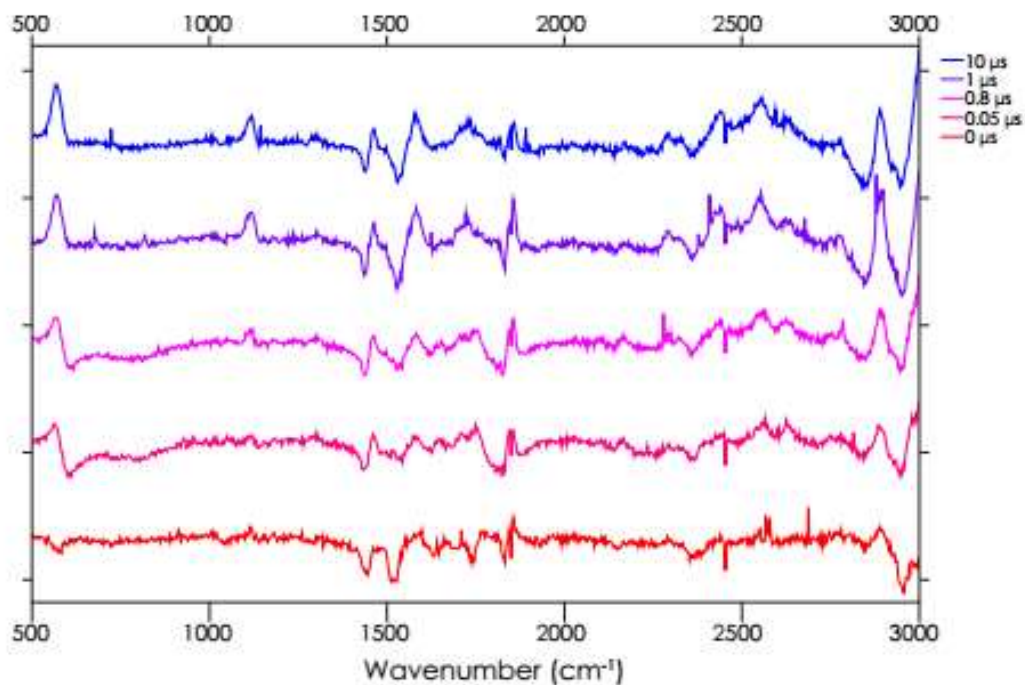


Figure 9: TR3 spectra of the residuals, following subtraction of time resolved  $[\text{Ru}(\text{bpy})_3]^{2+}$  spectra and resonant Raman spectrum of  $\text{MV}^{2+}$ , for dataset b.

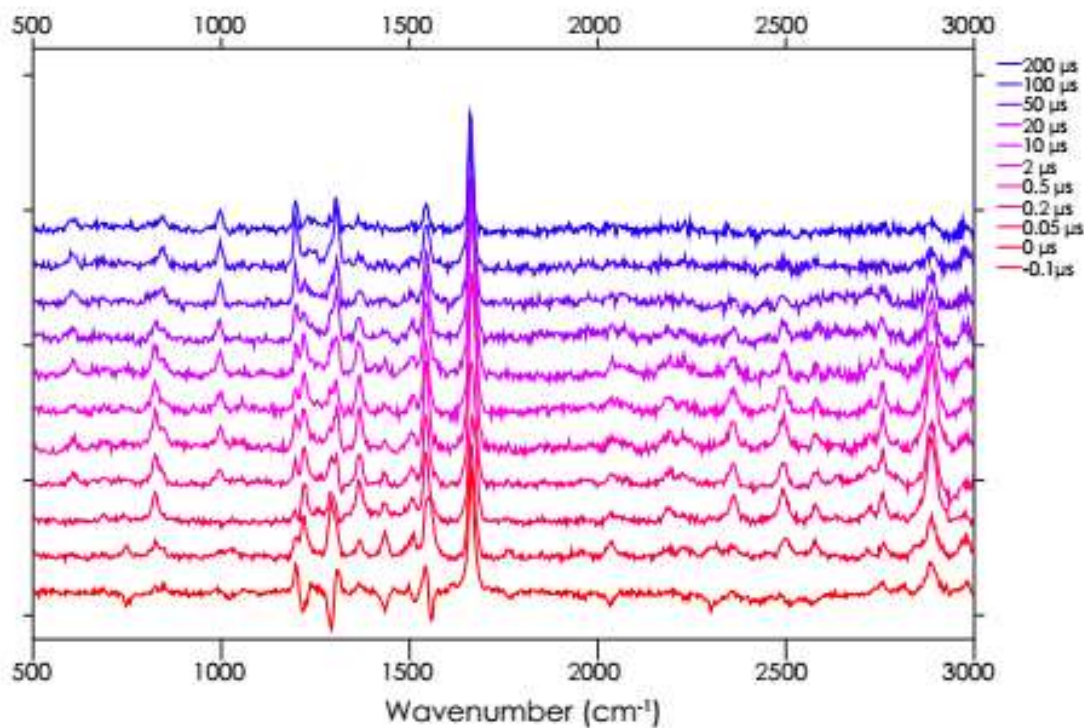


Figure 10: TR3 spectra of the residuals, following subtraction of time resolved  $[\text{Ru}(\text{bpy})_3]^{2+}$  spectra and Raman spectrum of  $\text{MV}^{2+}$ , for dataset c.

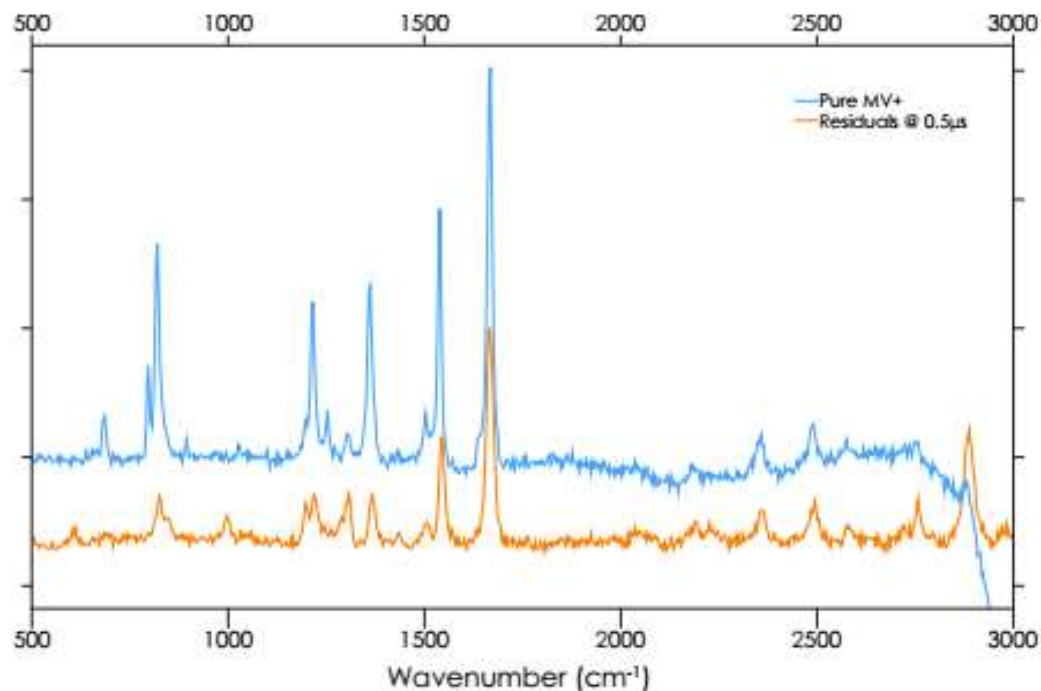


Figure 11: Comparison of the residual spectrum at 0.5  $\mu$ s from dataset c with a pure chemical sample of  $MV^+$ .

## Theoretical Methods and Calculations

### Theoretical Methods

To interpret the laboratory data, several density functional theory (DFT) calculations are necessary, performed using the Gaussian suite of software, version 09, revision A.02.3. Molecular structures are generated using Avogadro version 1.2.0.4 and results are analysed and compared using Gabedit 2.5.05 and fityk 1.3.1.<sup>32</sup>

These calculations are challenging to accomplish, due to the relatively high charge density resulting from a double positive charge on a relatively small molecule in the case of methyl viologen, and due to the large number of orbitals present in the  $[Ru(bpy)_3]^{n+}$  molecules. To explore functional/basis set combinations, several test calculations have been performed on the pyridine molecule due to its structural similarities with the compounds under investigation. Two theory levels are determined to be suitable for use in this study.

For computational efficiency, structures are optimised incrementally. First, a low level optimisation is performed at the X3LYP/3-21G level of theory,<sup>33-34</sup> which yields results of fair accuracy with short computational times. Following this, a high level optimisation is performed at the O3LYP/cc-pVTZ theory level,<sup>35-36</sup> providing improved accuracy without excessive

computational expense. These optimised structures are then used for O3LYP/ccpVTZ vibrational frequency calculations, to obtain predicted Raman wavenumbers and activities. Due to computational time constraints, calculations for the [Ru(bpy)<sub>3</sub>]<sup>n+</sup> molecules are only obtained at the X3LYP/3-21G level of theory, and these results are discussed, with the caveat that they are of lower accuracy than those acquired for methyl viologen molecules. For discussion of reaction kinetics, X3LYP/3-21G calculations are adjusted using the conductor-like polarizable continuum model (CPCM) to compensate for solvent effects, and thermally corrected energy values are used.

For methyl viologen, Raman spectra for various different charge states and excited states are calculated. Excited state calculations are performed by first optimising the geometry to the target excited state using Time-Dependent Density Functional Theory (TDDFT) at the O3LYP/cc-pVTZ theory level, and then performing vibrational calculations on those optimised structures at the same level. While the final analysis of experimental data appears to show only MV<sup>2+</sup> and MV<sup>+</sup> in the laboratory spectra, these additional calculations are included here for completeness.

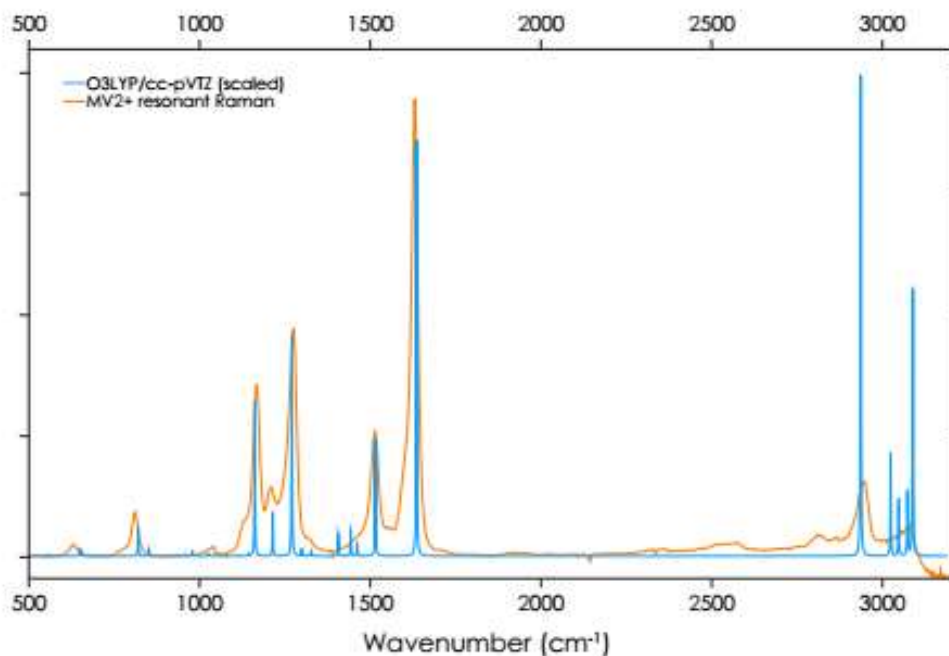


Figure 12: Comparison of the scaled DFT Raman spectrum (O3LYP/cc-pVTZ) of MV<sup>2+</sup> with the laboratory recorded resonant Raman spectrum of MV<sup>2+</sup>

*Chapter 6. TR3 spectroscopic study of charge transfer reaction from [Ru(bpy)<sub>3</sub>]<sup>2+</sup> to MV<sup>2+</sup>*

DFT is well known to overestimate the wavenumber of calculated vibrational frequencies so this work also requires scaling factors. These are deduced for both methyl viologen and [Ru(bpy)<sub>3</sub>]<sup>n+</sup> molecules by comparison with laboratory acquired spectra. Two scaling factors are found for MV<sup>2+</sup> at the O3LYP/cc-pVTZ theory level. For  $\bar{\nu} < \sim 2000$  cm<sup>-1</sup>, frequencies are scaled by 0.9569, and for  $\bar{\nu} > \sim 2000$  cm<sup>-1</sup>, a factor of 0.9718 is used, and these are applied to all forms of methyl viologen. The [Ru(bpy)<sub>3</sub>]<sup>2+</sup> molecule similarly requires two scaling factors, at 1.0502 for  $\bar{\nu} < \sim 900$  cm<sup>-1</sup> and 0.95204  $\bar{\nu} > \sim 900$  cm<sup>-1</sup>, which are applied to all [Ru(bpy)<sub>3</sub>]<sup>n+</sup> molecules. It should be noted that due to anharmonicity, DFT calculated values in the C–H stretching region around 3000 cm<sup>-1</sup>, overestimate both vibrational wavenumber and oscillator strength, causing uncertainty in this spectroscopic region even after scaling.

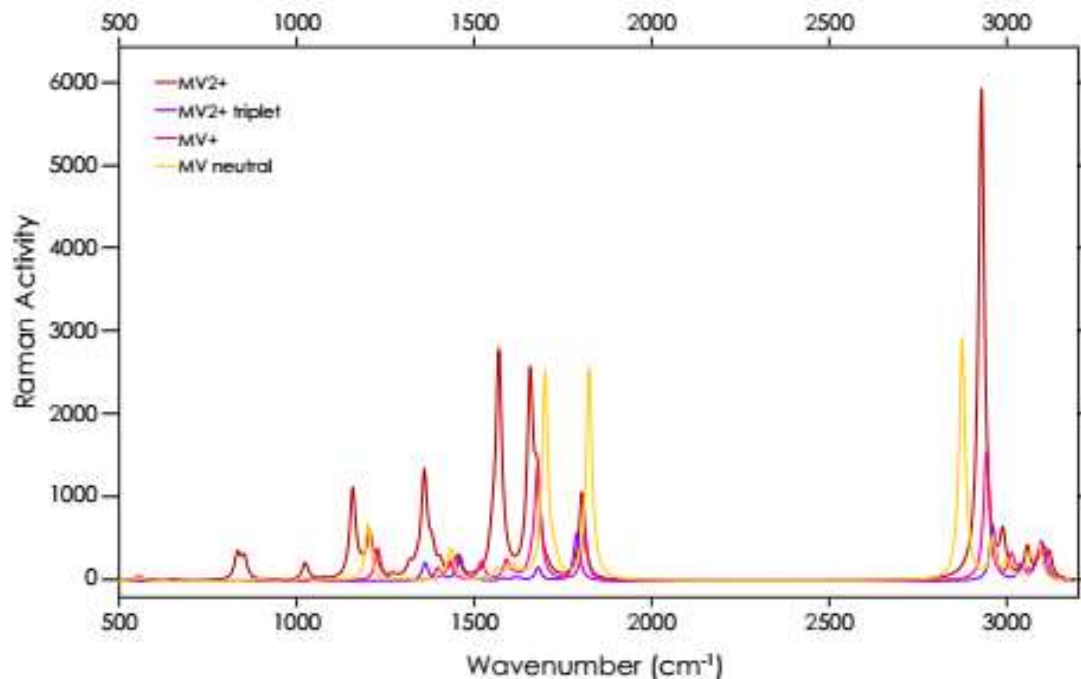


Figure 13: Scaled DFT Raman spectra (O3LYP/cc-pVTZ) of four charge states of methyl viologen – neutral, singly charged, double charged, and doubly charged triplet state.

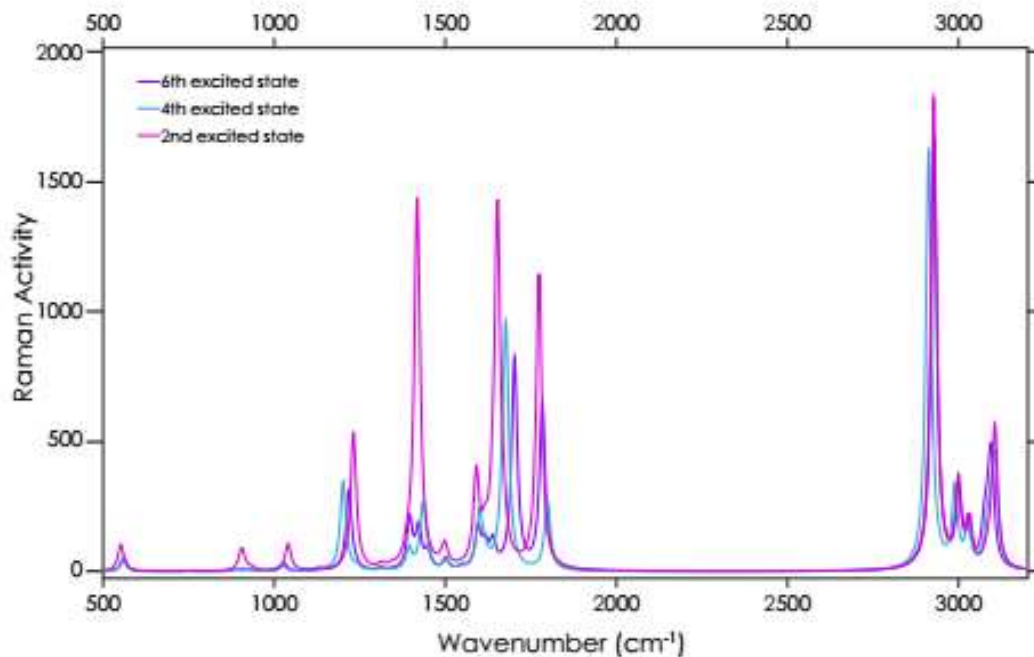


Figure 14: Scaled DFT Raman spectra (O3LYP/cc-pVTZ), optimized using TDDFT (O3LYP/cc-pVTZ) of three accessible excited states of  $MV^{2+}$

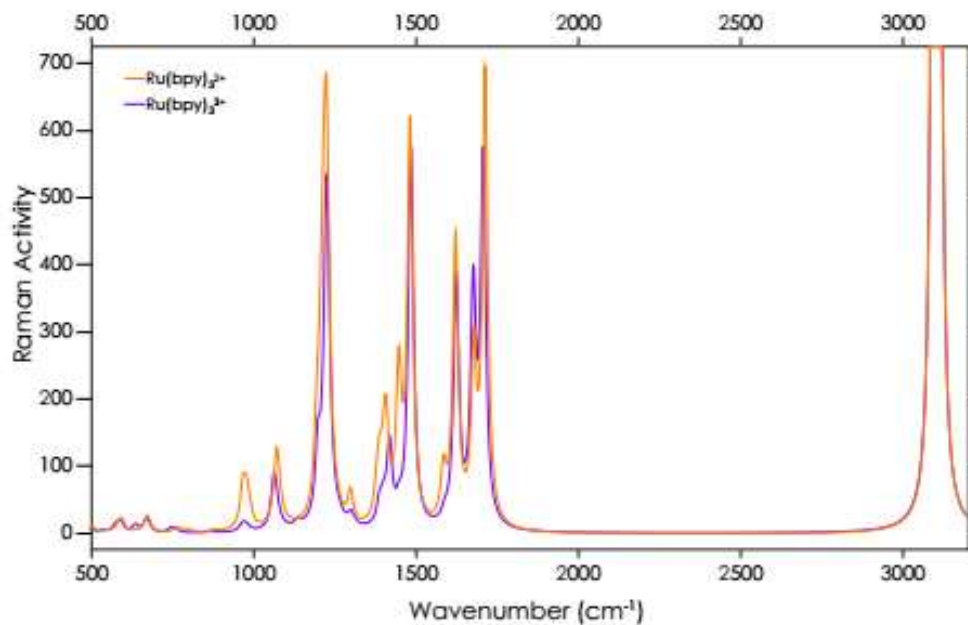


Figure 15: Scaled DFT Raman spectra (X3LYP/3-21G) of  $[Ru(bpy)_3]^{2+}$  and  $[Ru(bpy)_3]^{3+}$ .

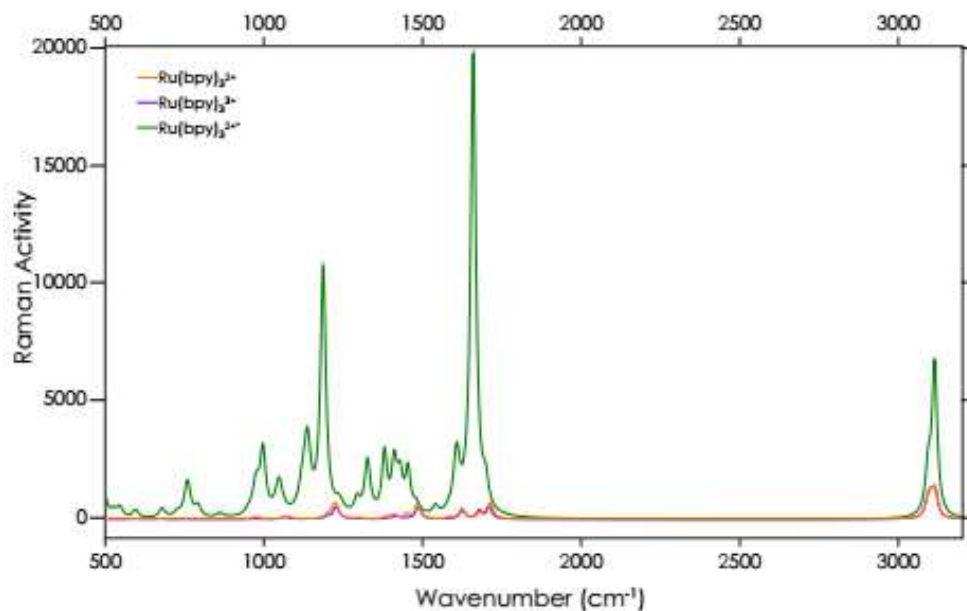


Figure 16: Scaled DFT Raman spectra (X3LYP/3-21G) of the triplet state of  $[Ru(bpy)_3]^{2+}$  compared with the far weaker spectra of  $[Ru(bpy)_3]^{2+}$  and  $[Ru(bpy)_3]^{3+}$

## REFERENCES

1. Sahoo, S. K.; Umaphathy, S.; Parker, A. W., Time-Resolved Resonance Raman Spectroscopy: Exploring Reactive Intermediates. *Applied Spectroscopy* **2011**, *65* (10), 1087-1115.
2. An Introduction to Time-Resolved Resonance Raman Spectroscopy and Its Application to Reactive Intermediates. In *Reviews of Reactive Intermediate Chemistry*, pp 121-182.
3. Woosley, R. J.; Millero, F. J.; Wanninkhof, R., Rapid anthropogenic changes in CO<sub>2</sub> and pH in the Atlantic Ocean: 2003–2014. *Global Biogeochemical Cycles* **2016**, *30* (1), 70-90.
4. Gattuso, J.-P.; Magnan, A.; Billé, R.; Cheung, W. W. L.; Howes, E. L.; Joos, F.; Allemand, D.; Bopp, L.; Cooley, S. R.; Eakin, C. M.; Hoegh-Guldberg, O.; Kelly, R. P.; Pörtner, H.-O.; Rogers, A. D.; Baxter, J. M.; Laffoley, D.; Osborn, D.; Rankovic, A.; Rochette, J.; Sumaila, U. R.; Treyer, S.; Turley, C., Contrasting futures for ocean and society from different anthropogenic CO<sub>2</sub> emissions scenarios. *Science* **2015**, *349* (6243), aac4722.
5. Audoly, R.; Vogt-Schilb, A.; Guivarch, C.; Pfeiffer, A., Pathways toward zero-carbon electricity required for climate stabilization. *Applied Energy* **2018**, *225*, 884-901.
6. Gust, D.; Moore, T. A.; Moore, A. L., Solar Fuels via Artificial Photosynthesis. *Accounts of Chemical Research* **2009**, *42* (12), 1890-1898.
7. Hammarström, L.; Styring, S., Coupled electron transfers in artificial photosynthesis. *Philosophical Transactions of the Royal Society B: Biological Sciences* **2008**, *363* (1494), 1283-1291.

Chapter 6. TR3 spectroscopic study of charge transfer reaction from  
[Ru(bpy)<sub>3</sub>]<sup>2+</sup> to MV<sup>2+</sup>

8. Shen, J.-R., The Structure of Photosystem II and the Mechanism of Water Oxidation in Photosynthesis. *Annual Review of Plant Biology* **2015**, *66* (1), 23-48.
9. Mendes Marinho, S.; Ha-Thi, M.-H.; Pham, V.-T.; Quaranta, A.; Pino, T.; Lefumeux, C.; Chamaille, T.; Leibl, W.; Aukauloo, A., Time-resolved interception of multiple charge accumulation in a sensitizer-acceptor dyad. *Angew. Chem. Int. Ed.* **2017**, *56* (50), 15936-15940.
10. Karlsson, S.; Boixel, J.; Pellegrin, Y.; Blart, E.; Becker, H.-C.; Odobel, F.; Hammarström, L., Accumulative Charge Separation Inspired by Photosynthesis. *J. Am Chem. Soc.* **2010**, *132* (51), 17977-17979.
11. Pannwitz, A.; Wenger, O. S., Proton-coupled multi-electron transfer and its relevance for artificial photosynthesis and photoredox catalysis. *Chemical Communications*. **2019**.
12. Creutz, C.; Sutin, N., Reaction of tris(bipyridine)ruthenium(III) with hydroxide and its application in a solar energy storage system. *Proceedings of the National Academy of Sciences* **1975**, *72* (8), 2858-2862.
13. Bhasikuttan, A. C.; Suzuki, M.; Nakashima, S.; Okada, T., Ultrafast Fluorescence Detection in Tris(2,2'-bipyridine)ruthenium(II) Complex in Solution: Relaxation Dynamics Involving Higher Excited States. *Journal of the American Chemical Society*. **2002**, *124*, 8398-8405.
14. Bradley, P. G.; Kress, N.; Hornberger, B. A.; Dallinger, R. F.; Woodruff, W. H., Vibrational spectroscopy of the electronically excited state. 5. Time-resolved resonance Raman study of tris(bipyridine)ruthenium(II) and related complexes. Definitive evidence for the "localized" MLCT state. *Journal of the American Chemical Society* **1981**, *103* (25), 7441-7446.
15. Creutz, C.; Chou, M.; Netzel, T. L.; Okumura, M.; Sutin, N., Lifetimes, spectra, and quenching of the excited states of polypyridine complexes of iron(II), ruthenium(II), and osmium(II). *Journal of the American Chemical Society* **1980**, *102* (4), 1309-1319.
16. Henry, W.; Coates, C. G.; Brady, C.; Ronayne, K. L.; Matousek, P.; Towrie, M.; Botchway, S. W.; Parker, A. W.; Vos, J. G.; Browne, W. R.; McGarvey, J. J., The Early Picosecond Photophysics of Ru(II) Polypyridyl Complexes: A Tale of Two Timescales. *The Journal of Physical Chemistry A* **2008**, *112* (20), 4537-4544.
17. Mabrouk, P. A.; Wrighton, M. S., Transient Raman detection of excited state electron, transfer to methyl viologen from photoexcited molecular reagents in fluid solution and anchored to SiO<sub>2</sub>. *Spectrochimica Acta Part A: Molecular Spectroscopy* **1989**, *45* (1), 17-22.
18. Ebbesen, T. W.; Levey, G.; Patterson, L. K., Photoreduction of methyl viologen in aqueous neutral solution without additives. *Nature* **1982**, *298* (5874), 545-548.
19. Ikeyama, S.; Katagiri, T.; Amao, Y., The improvement of formic acid production from CO<sub>2</sub> with visible-light energy and formate dehydrogenase by the function of the viologen derivative with carbamoylmethyl group as an electron carrier. *Journal of Photochemistry and Photobiology A: Chemistry* **2018**, *358*, 362-367.

Chapter 6. TR3 spectroscopic study of charge transfer reaction from  
 $[Ru(bpy)_3]^{2+}$  to  $MV^{2+}$

20. Scaiano, J. C.; Tanner, M.; Weir, D., Exploratory study of the intermolecular reactivity of excited diphenylmethyl radicals. *Journal of the American Chemical Society* **1985**, *107* (15), 4396-4403.
21. Patmore, N. J., Photophysical properties of metal complexes. *Annual Reports Section "A" (Inorganic Chemistry)* **2008**, *104* (0), 498-528.
22. Tran, T.-T.; Ha-Thi, M.-H.; Pino, T.; Quaranta, A.; Lefumeux, C.; Leibl, W.; Aukauloo, A., Snapshots of Light Induced Accumulation of Two Charges on Methylviologen using a Sequential Nanosecond Pump-Pump Photoexcitation. *Journal of Physical Chemistry Letters*. **2018**, *9*, 1086-1091.
23. Okura, I.; Nakamura, S.; Kim-Thuan, N.; Nakamura, K.-I., Kinetics and mechanism of methyl viologen reduction and hydrogen generation by visible light with tris (2,2'-bipyridine) ruthenium dication. *Journal of Molecular Catalysis* **1979**, *6* (4), 261-267.
24. Pellegrin, Y.; Odobel, F., Sacrificial electron donor reagents for solar fuel production. *Comptes Rendus Chimie* **2017**, *20* (3), 283-295.
25. Frisch, M. J., Gaussian 09 Revision A.02.2009; Gaussian Inc. Wallingford CT 2009.
26. Feng, Q.; Cotton, T. M., A surface-enhanced resonance Raman study of the photoreduction of methylviologen on a p-indium phosphide semiconductor electrode. *The Journal of Physical Chemistry* **1986**, *90* (6), 983-987.
27. Forster, M.; Girling, R. B.; Hester, R. E., Infrared, Raman and resonance Raman investigations of methylviologen and its radical cation. *Journal of Raman Spectroscopy*. **1982**, *12* (1), 36-48.
28. Poizat, O.; Sourisseau, C.; Mathey, Y., Vibrational study of the methyl viologen dication  $MV^{2+}$  and radical cation  $MV^{\cdot+}$  in several salts and as an intercalate in some layered MPS3 compounds. *Journal of the Chemical Society, Faraday Transactions 1: Physical Chemistry in Condensed Phases* **1984**, *80* (12), 3257-3274.
29. Rajkumar, E.; Rajagopal, S., Photoinduced electron transfer reaction of tris(4,4'-dicarboxyl-2,2'-bipyridine)ruthenium(ii) ion with organic sulfides. *Photochemical & Photobiological Sciences* **2008**, *7* (11), 1407-1414.
30. Hohenstein, E. G., Mechanism for the Enhanced Excited-State Lewis Acidity of Methyl Viologen. *Journal of the American Chemical Society* **2016**, *138* (6), 1868-1876.
31. Romanova, J.; Liégeois, V.; Champagne, B., Resonant Raman spectra of molecules with diradical character: multiconfigurational wavefunction investigation of neutral viologens. *Physical Chemistry Chemical Physics* **2014**, *16* (39), 21721-21731.
32. Wojdyr, M., Fityk: a general-purpose peak fitting program. *Journal of Applied Crystallography* **2010**, *43* (5-1), 1126-1128.
33. Xu, X.; Goddard, W. A., The X3LYP extended density functional for accurate descriptions of nonbond interactions, spin states, and thermochemical properties. *Proceedings of the National Academy of Sciences of the United States of America* **2004**, *101* (9), 2673-2677.

Chapter 6. TR3 spectroscopic study of charge transfer reaction from  
 $[Ru(bpy)_3]^{2+}$  to  $MV^{2+}$

34. Binkley, J. S.; Pople, J. A.; Hehre, W. J., Self-consistent molecular orbital methods. 21. Small split-valence basis sets for first-row elements. *Journal of the American Chemical Society* **1980**, *102* (3), 939-947.
35. Cohen, A. J.; Handy, N. C., Dynamic correlation. *Molecular Physics* **2001**, *99* (7), 607-615.
36. Jr., T. H. D., Gaussian basis sets for use in correlated molecular calculations. I. The atoms boron through neon and hydrogen. *The Journal of Chemical Physics* **1989**, *90* (2), 1007-1023.

# Chapter 7. Conclusions and perspectives

## 7.1 Conclusions

In this thesis, photophysical properties of electron transfer in different dyad systems composed of BDP's derivatives and fullerene were investigated using fast and ultrafast transient absorption spectroscopies. Under selective excitation of the BDP moiety in BDP-C<sub>60</sub> dyad, two ultrafast photoinduced electron transfer mechanisms were demonstrated for the conformer with donor-acceptor distance of 8.8 Å.<sup>1</sup> Further excitation at 380 nm was also studied to examine the possibility of hole transfer due to excitation of both donor and acceptor moieties. However, it seems that there is no charge transfer from C<sub>60</sub> to BDP moiety. For both the dyad-peptide and dyad alkyl, photoinduced electron transfer from the BDP excited state to the fullerene competes with energy transfer under excitation at 527 nm using femtosecond and nanosecond TA spectroscopies in visible region. To get more understanding of photoinduced processes in these systems, femtosecond UV-vis-NIR TA measurements are under progress.

The second objective of this thesis is studying multi-electron transfer in different systems using pump-pump-probe transient absorption spectroscopy. It is the first time that the charge accumulation was successfully demonstrated in two different multicomponent systems. The first system is composed of [Ru(bpy)<sub>3</sub>]<sup>2+</sup> and MV<sup>2+</sup> in the presence of ascorbate as reversible electron donor. The sequential accumulation of two electron on MV<sup>2+</sup> was observed upon sequential excitation of the [Ru(bpy)<sub>3</sub>]<sup>2+</sup>. We have reached a fairly good global yield of approximately 9% for the two-charge accumulation.<sup>2</sup>

The second multicomponent systems contained NDI molecules instead of MV<sup>2+</sup> in the first one. Unexpectedly, double charge accumulation on NDI molecules was obtained with only the first pump laser excitation of [Ru(bpy)<sub>3</sub>]<sup>2+</sup>. The appearance of NDI<sup>2-</sup> in single pulse excitation can be attributed to efficient electron transfer between NDI<sup>-</sup> and [Ru(bpy)<sub>3</sub>]<sup>2+</sup> molecules. The formation quantum yield of the NDI<sup>2-</sup> from NDI after the single pulse excitation is 2.2 (±0.1) % and with a quantum yield close to 1 for the electron transfer between [Ru(bpy)<sub>3</sub>]<sup>2+</sup> and NDI. The second lasers was applied to study the possibility of charge accumulation due to

## *Chapter 7. Conclusions and perspectives*

sequential single-photon absorption. The formation of the  $\text{NDI}^{2-}$  which was induced by the second pulse excitation is demonstrated. In total, the quantum yield of  $\text{NDI}^{2-}$  formed is 4.2%.<sup>3</sup>

Efforts to study charge accumulation in photocatalyst molecules in multicomponent configuration, were implemented using pump-pump-probe TA spectroscopy. The solution of Iron porphyrins in the presence of  $\text{iAscH}^-$  indicates the good formation of the second reduced state of iron ( $\text{Fe}^{I+}$ ) with the efficiency approximately 20% under single pulse excitation. However, using double pulse excitation, the formation of  $\text{Fe}^0$  could not be observed for the solution  $\text{FeTPPF8OH}$  and  $\text{iAscH}^-$ . Studying double pulse excitation for the solution  $\text{FeTPPCL}$  and  $\text{iAscH}^-$  should be done in the future to complement this series of experiments. Furthermore, experiments in the presence of  $\text{CO}$  or  $\text{CO}_2$  are worth to be attempted in the next steps to explore the photocatalytic cycle and extend the study beyond catching the intermediates of the photocatalysts.

Charge transfer in a system composed of Zinc porphyrin and an electron donor ( $\text{iAscH}^-$  or DABCO) was also investigated. The solution with DABCO electron donor expresses a better efficiency of first electron transfer ( $\approx 17\%$ ) and stability as compared with  $\text{iAscH}^-$  electron donor. Double pulse excitation experiments were performed to examine the possibility of second charge accumulation on zinc porphyrin. The result indicates a decay ( $3 \mu\text{s}$ ) of a new species at 435 nm. It seems consistent with the characteristic of second reduced state of zinc porphyrin, which was reported in the literature. To strengthen our assignment, spectroelectrochemistry of  $\text{ZnTPP20}$  needs to be performed.

The light-driven charge separation in porphyrin-imidazole-phenol, a model molecule of photosystem II, was investigated. A good control experiment without the presence of water indicates that PCET processes result in the efficient formation of  $\text{P-ImH}^+-\text{ArO}^\bullet$  (20%). This result encouraged us to study double pulse excitation with expectation that second positive charge will be accumulated on porphyrin to create  $\text{P}^+-\text{Im-ArO}^\bullet$ . Unfortunately, the state of  $\text{P}^+-\text{Im-ArO}^\bullet$  could not observe under second pulse excitation.

Studying photoinduced processes using nanosecond TR3 was investigated for a model system of artificial photosynthesis,  $[\text{Ru}(\text{bpy})_3]^{2+}$  and  $\text{MV}^{2+}$ . The result indicates success in monitoring the kinetic traces of the first reduced state of  $\text{MV}^{2+}$  through characteristic of structure changes. DFT calculations at the X3LYP/3-21G theory level provide a good match with laboratory spectra.<sup>4</sup> This result paves a powerful approach to investigate more sophisticated photoinduced processes in photocatalytic systems, an intense research theme.

To summarize, this thesis investigated different photosystems as dyads, a model of multicomponent or photocatalyst systems with the purpose to find out the best-approach systems to gain high efficiency of double charge transfer. All approaching systems possess their advantages and disadvantages. We suggest here some discussion and strategy optimize the efficiency of second charge transfer for each step after second light excitation. We offer different conditions that should be optimized from the initial state after the second photon excitation by related fundamental knowledge, which is discussed in chapter 1 and the different photosystems which we studied.

We consider the system, including acceptor (A) and photosensitizer (P) can be linked together (dyad system) or separated (as multicomponent system) in the presence of electron donor (D). After the first laser excitation, the first reduced state of the acceptor is not frequently difficult to achieve ( $A^-$ ). Much more challenge starts after the second laser excitation to accumulate charge on acceptor by re-excitation photosensitizer. An assumption that under second laser excitation, what we expect is in accordance with the processes (1) and (2) in Figure 7.1(a).

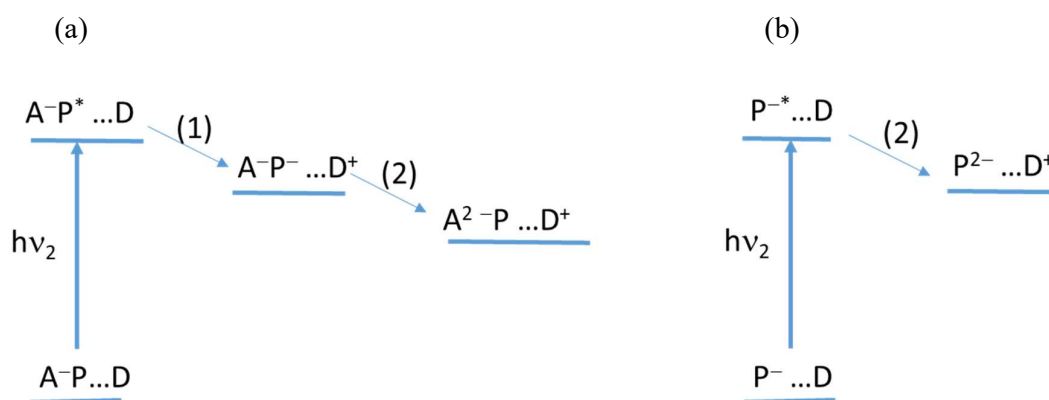


*Figure 7.1 Scheme of second charge transfer on photosystems (a) photosensitizer – acceptor and donor, (b) photocatalyst and donor*

Under second laser excitation, the photosensitizer is re-excited in expectation to be quenched by electron donor to perform reaction (1). In fact, at this step, different photosystems show different behavior. Integrated systems (dyad, triad) generally suffer from more unproductive channel pathways than with multicomponent systems, such as reverse electron transfer to form  $A-P^-$  or energy transfer between  $P^*$  and  $A^-$ . These disadvantages were evidenced in a dyad system of  $NDI-[Ru(bpy)_3]^{2+}$  in the presence of ascorbate as resulting in low efficiency of the second charge populated on NDI.<sup>2</sup> However, it is a different story in the multicomponent which were composed by the same those species with better efficiency of the second charge transfer<sup>3</sup> ( $\approx 1\%$  in dyad system versus  $4.2\%$  in multicomponent system). In fact, the formation of the

## *Chapter 7. Conclusions and perspectives*

first charge separated state (CSS1) in the dyad is evidently more efficient ( $k_{app1} = 3.8 (\pm 0.7) \times 10^7 \text{ s}^{-1}$  for the dyad vs.  $k_{app1} = 2.2 (\pm 0.1) \times 10^5 \text{ s}^{-1}$  vs. for the multicomponent system), thanks to the close distance of the photosensitizer and the NDI unit. Thus, once the photosensitizer is reduced to form  $\text{Ru}^{\text{I}}\text{-NDI}$ , the only efficient pathways is to form the singly reduced state  $\text{Ru-NDI}^{\bullet-}$  and the doubly reduced  $\text{Ru-NDI}^{2-}$  (CSS2) was thus not be observed in the single-pulse experiments. In the case of multicomponent systems, the formation of the accumulative charge separation state was shown be more efficient since the reduced photosensitizer  $\text{Ru}^{\text{I}}$  formed after excitation can participate immediately to the formation of the CSS2 without any reaction with the ground state of NDI, in particular when the CSS1 is already generated by the first pump excitation. Furthermore, counter-productive reaction such as reverse electron transfer from the reduced electron acceptor to the excited sensitizer is largely suppressed in the multicomponent system due to the increased distance. Using double-pulse excitation, we improve the efficiency of charge accumulation on the NDI moiety in comparison with that of using single-pulse excitation (4.2% versus 2.2%, respectively). The main cause, which leads to this result, is the higher concentration of the singly reduced species already created by the first pump. It is worth to note that despite being a multicomponent system, our results show a higher efficiency of second charge accumulation (4.2%) in comparison with ~1% in the case of Ru-NDI dyad system.<sup>14</sup> This result can be explained thanks to the higher distance between molecules in the multicomponent system which helps to limit unproductive reactions. In general, our studies in multicomponent systems indicate a fairly good efficiency of second charge transfer. It somehow proves the power of an approach using multicomponent systems. Here, we will also suggest some strategies to minimize the contribution of the unproductive pathways to optimize the reaction (1).

Electron transfer in reaction 1 ( $K_{ET1}$ ) is in competition with energy transfer between  $A^-$  and  $P^*$  ( $K_{EN}$ ). Therefore, it should be that  $K_{ET1}$  has to be higher than  $K_{EN}$  ( $K_{EN} < K_{ET1}$ ). In this case, we have electron transfer between  $P^*$  and D is generally limited by the diffusion rate. Thus,  $K_{ET1}$  might be improved by only the presence of a high potential electron donor. On the other side,  $K_{EN}$  can give more choices to minimize this value. A long-distance between  $A^-$  and P should be the right choice to decrease the effect of Dexter energy transfer. In that case, our approach by using multicomponent indicates an advantage in comparison with dyad systems, which frequently suffer from Dexter energy transfer due to a short distance. To minimize the contribution of FRET, what we suggest is choosing photosensitizers which possess a narrow fluorescence region to limit the overlap electronic absorption spectrum of  $A^-$  and emission of

the photosensitizer. For our multicomponent systems, although fluorescence of  $[\text{Ru}(\text{bpy})_3]^{2+}$  covers on a large range of visible regions, FRET should be inefficient for this system because of the large distance between photosensitizer and acceptor (multicomponent). However, in the dyad system  $[\text{Ru}(\text{bpy})_3]^{2+}$ -NDI, the FRET competes with the charge transfer. It is thus one of the possible reason for the lower efficiency of charge accumulation of  $[\text{Ru}(\text{bpy})_3]^{2+}$ -NDI dyad (~1%) in comparison with multicomponent (~4.2%).

For designing dyad systems, we also recommend two main characteristics which are needed considering to limit unproductive pathways: (1) the distance between acceptor and photosensitizer, in general, it should be larger than 10 Å to limit the effect of Dexter energy transfer. (2) Alongside with choosing a proper photosensitizer, acceptor and photosensitizer should be designed in a rigid conformation to take control FRET contribution.

To gain two charges accumulation on acceptor, we have to optimize the electron transfer of reaction between  $\text{A}^-$  and  $\text{P}^-$  (reaction 2 in Figure 7.1 a). The factors which are decided to the efficiency of the second charge transfer can be involved electronic coupling  $V_{\text{DA}}$ , reorganization energy ( $\lambda$ ), and driving force  $\Delta G$  of reaction between  $\text{A}^-$  and  $\text{P}^-$ . Noted that  $V_{\text{DA}}$  between the states of  $\text{A}^-$  and  $\text{P}^-$  should be strong in this case. Here, we suggest a strategy to favor electron transfer through optimization the relation between driving force and reorganization. As discussed in section 1.4.1.2, single electron transfer will be barrierless if  $\Delta G^0 = -\lambda$ . It means that electron transfer reaction can proceed in a highly favorable process with a low reorganization of the acceptor, do not require a high value of  $-\Delta G^0$  electron transfer. For example, fullerene is one of the best candidates for electron acceptor with the low reorganization. In our Por-Im-ArOH dyad system, estimation values of driving force and reorganization energy should be important to explain precisely the mechanism of PCET.

The reaction (1) will not have to pay attention if acceptor and photosensitizer are unique. Another approach using photocatalyst molecules act as both photosensitizer and acceptor in the presence of an electron donor. For those systems, our investigations also indicate better stable solution as well as higher efficiency of first charge transfer under laser irradiation in comparison with the case involving photosensitizer. Thus, it seems that this approach manifest some good points at initial steps. Furthermore, we can exclude the handicaps which have to face as involving both acceptor and photosensitizer. Therefore, we only need to consider the optimization of the second reaction in Figure 7.1 (b). One requirement here to optimize the efficiency of second charge transfer is the long excited-state lifetime of  $\text{P}^{*-}$  to support for an

efficiency the second reductive quenching process. It should be the same order of diffusion rate. Our studies using iron porphyrin photocatalyst systems under second laser excitation show no change that can be observed. It could be due to short lifetime of excited state of FeTPPF8<sup>-</sup> and/or competition with absorption between ground state and reduced state. In the case of using ZnTPPF20 with DABCO – electron donor, we observed apparently the bleaching signal of the first reduced state of ZnTPPF20. In this case, the absorption of the ground state contributes as a small proportion in comparison with the first reduced state. Thus, this characteristic is an advantage for the study double charge transfer in this system. The global fit indicates two decay times corresponding with two different species, which are obtained in DADS. It is consistent with the appearance of a new species. This study can be the first report in monitoring photocatalytic reaction by using flash photolysis.

## **7.2 Perspectives**

Studying photoinduced processes in BDP-C<sub>60</sub>-peptide and BDP-C<sub>60</sub>-alkyl indicate that electron transfer can occur better with the helical peptide, as a good electron mediator. These results are a good initial step for future work on self-assembled monolayers on gold surface for practical molecular photovoltaic devices. This goal will be done in strong collaboration with Dr Allard and his co-workers at Institut Lavoisier de Versailles.

An extension of this research is to study charge accumulation on photocatalytic systems using pump-pump probe transient absorption experiment. The next steps, using nanosecond pump-pump-probe time-resolved resonance Raman will be deployed.

For further plan, to access to molecular devices for photocatalysis, we have interested in the heterogeneous solution containing TiO<sub>2</sub> nanostructure conjugated to an assembling chromophore-catalyst. TiO<sub>2</sub> gives much attraction because of its properties as electron acceptor, photostability, and light dispersion. The systems containing TiO<sub>2</sub> nanostructure conjugated to assembling chromophore-catalyst have been used in dye-sensitized photoelectrosynthesis cells (DSPECs) to generate highly energetic molecules such as: methanol or hydrogen.<sup>5-6</sup> However, there are few fundamental studies to explain mechanism of photoinduced processes in those systems. Therefore, the fundamental study of photoinduced charge accumulation in TiO<sub>2</sub> nanoparticle functionalized by different assembling chromophore-catalysts will help to better understand the multielectronic photocatalytic processes, an essential step for the production of solar fuels.

## REFERENCES

1. Tran, T.-T.; Rabah, J.; Ha-Thi, M.-H.; Allard, E.; Nizinski, S.; Burdzinski, G.; Aloïse, S.; Fensterbank, H.; Baczko, K.; Clavier, G.; Miomandre, F.; Pino, T.; Méallet-Renault, R., Photoinduced electron transfer in a BODIPY-Fullerene dyad. *Article in preparation*.
2. Tran, T.-T.; Ha-Thi, M.-H.; Pino, T.; Quaranta, A.; Lefumeux, C.; Leibl, W.; Aukauloo, A., Snapshots of Light Induced Accumulation of Two Charges on Methylviologen using a Sequential Nanosecond Pump–Pump Photoexcitation. *Journal of Physical Chemistry Letters*. **2018**, *9*, 1086-1091.
3. Tran, T.-T.; Ha-Thi, M.-H.; Pino, T., Watching intermolecular light induced charge accumulation on Naphthalene Diimide by Tris(bipyridyl)ruthenium(II) photosensitizer. *Article In preparation*.
4. Hammonds, M.; Tran, T.-T.; Ha-Thi, M.-H.; Tran-Hoang, H.-Y.; Pino, T., Time resolved resonant Raman spectroscopy of the photoinduced electron transfer from Ruthenium(II) Tris-bipyridine to Methylviologen. *Article In preparation*.
5. Zheng, B.; Sabatini, R. P.; Fu, W.-F.; Eum, M.-S.; Brennessel, W. W.; Wang, L.; McCamant, D. W.; Eisenberg, R., Light-driven generation of hydrogen: New chromophore dyads for increased activity based on Bodipy dye and Pt(diimine)(dithiolate) complexes. *Proceedings of the National Academy of Sciences* **2015**, *112* (30), E3987-E3996.
6. Pho, T. V.; Sheridan, M. V.; Morseth, Z. A.; Sherman, B. D.; Meyer, T. J.; Papanikolas, J. M.; Schanze, K. S.; Reynolds, J. R., Efficient Light-Driven Oxidation of Alcohols Using an Organic Chromophore–Catalyst Assembly Anchored to TiO<sub>2</sub>. *ACS Applied Materials & Interfaces* **2016**, *8* (14), 9125-9133.

**Titre :** Caractérisation des processus électroniques et multi-électroniques par spectroscopies laser résolues en temps dans des photosystèmes moléculaires, vers la production de fuel solaire par photosynthèse artificielle.

**Mots clés :** Photocatalytiques, Résolues en temps, Photolysis

**Résumé :** La demande énergétique de l'humanité augmente rapidement et ne montre aucun signe de ralentissement. Parallèlement à cette problématique, l'utilisation abusive de combustibles fossiles est l'une des principales causes d'augmentation de la concentration de CO<sub>2</sub> dans l'atmosphère. Ces problèmes doivent être résolus en termes de limitation des émissions de CO<sub>2</sub> et de recherche de sources d'énergie renouvelables pour remplacer les combustibles fossiles. De nos jours, l'énergie solaire est l'une des sources d'énergie renouvelables les plus efficaces. La conversion de l'énergie de la lumière solaire en électricité dans le photovoltaïque ou en énergie chimique par le biais de processus photocatalytiques implique invariablement un transfert d'énergie photo-induit et un transfert d'électrons. Dans ce contexte, l'objectif de la thèse est d'étudier les processus photo-induits dans les photosystèmes moléculaires utilisant la photolyse par flash laser.

Le premier thème de cette thèse porte sur l'étude du transfert monoélectronique dans des systèmes de dyades donneur-accepteur en vue d'optimiser l'efficacité de la séparation des charges et de son application dans la cellule solaire organique photovoltaïque.

Le deuxième thème de cette thèse porte sur l'étude de deux systèmes modèles de photosynthèse artificielle étudiés pour la possibilité d'une accumulation de charge par étapes. Ensuite, différents systèmes photocatalytiques, développés pour la photoréduction du CO<sub>2</sub>, ont été étudiés. La compréhension des processus photo-induits devraient permettre l'amélioration de l'efficacité de la réduction du CO<sub>2</sub> dans les systèmes photocatalytiques pratiques.

**Titre:** Electron and Multielectron reaction characterizations in molecular photosystems by laser flash photolysis, towards energy production by artificial photosynthesis.

**Keywords:** Photocatalytic, Time resolution, photolysis

**Abstract:** The energy demand of humanity is increasing rapidly, and shows no signs of slowing. Alongside this issue, abuse using fossil fuels is one of the main reasons which leads to an increase in atmospheric CO<sub>2</sub> concentration. These problems have to be solved in terms of both limiting CO<sub>2</sub> emission and finding renewable energy sources to replace fossil fuels. Nowadays, solar energy appears as one of the most effective renewable energy sources. Conversion of solar light energy to electricity in photovoltaics or to chemical energy through photocatalytic processes invariably involves photoinduced energy transfer and electron transfer. In this context, the aim of the thesis focuses on studying photoinduced processes in molecular photosystems using laser flash photolysis.

The first theme of this thesis focus on studying single electron transfer in Donor-Acceptor Dyad systems towards optimization efficiency of charge separation and application in the photovoltaic organic solar cell.

In the second theme of this thesis, two model systems of artificial photosynthesis were investigated to assess the possibility of stepwise charge accumulation on model molecules. A fairly good global yield of approximately 9% for the two charge accumulation on MV<sup>2+</sup> molecule was achieved. Then, different photocatalytic systems, which have developed for CO<sub>2</sub> reduction, were studied. Understanding of the photoinduced processes is an important step toward improving the efficiency of reduction of CO<sub>2</sub> in practical photocatalytic systems.